Astrophysics and Space Science Proceedings 33

Manfred P. Leubner
Zoltán Vörös *Editors*

Multi-scale Dynamical Processes in Space and Astrophysical Plasmas

Springer

Astrophysics and Space Science Proceedings
Volume 33

For further volumes:
http://www.springer.com/series/7395

Multi-scale Dynamical Processes in Space and Astrophysical Plasmas

Editors

Manfred P. Leubner
Zoltán Vörös

Springer

Editors
Manfred P. Leubner
Zoltán Vörös
Inst. of Astro- and Particle Physics
University of Innsbruck
Innsbruck
Austria

ISSN 1570-6591 ISSN 1570-6605 (electronic)
ISBN 978-3-642-30441-5 ISBN 978-3-642-30442-2 (eBook)
DOI 10.1007/978-3-642-30442-2
Springer Heidelberg New York Dordrecht London

Library of Congress Control Number: 2012944404

© Springer-Verlag Berlin Heidelberg 2012
This work is subject to copyright. All rights are reserved by the Publisher, whether the whole or part of the material is concerned, specifically the rights of translation, reprinting, reuse of illustrations, recitation, broadcasting, reproduction on microfilms or in any other physical way, and transmission or information storage and retrieval, electronic adaptation, computer software, or by similar or dissimilar methodology now known or hereafter developed. Exempted from this legal reservation are brief excerpts in connection with reviews or scholarly analysis or material supplied specifically for the purpose of being entered and executed on a computer system, for exclusive use by the purchaser of the work. Duplication of this publication or parts thereof is permitted only under the provisions of the Copyright Law of the Publisher's location, in its current version, and permission for use must always be obtained from Springer. Permissions for use may be obtained through RightsLink at the Copyright Clearance Center. Violations are liable to prosecution under the respective Copyright Law.
The use of general descriptive names, registered names, trademarks, service marks, etc. in this publication does not imply, even in the absence of a specific statement, that such names are exempt from the relevant protective laws and regulations and therefore free for general use.
While the advice and information in this book are believed to be true and accurate at the date of publication, neither the authors nor the editors nor the publisher can accept any legal responsibility for any errors or omissions that may be made. The publisher makes no warranty, express or implied, with respect to the material contained herein.

Printed on acid-free paper

Springer is part of Springer Science+Business Media (www.springer.com)

Preface

Magnetized plasmas in the universe exhibit complex dynamical behavior over a huge range of scales. The fundamental mechanisms of energy transport, redistribution, and conversion almost always occur in a multi-scale manner, while the driving mechanisms often include energy accumulation, free energy excited relaxation processes, dissipation and self-organization. The plasma processes associated with energy conversion, transport, and self-organization, such as magnetic reconnection, instabilities, linear and nonlinear waves, wave-particle interactions, dynamo processes, turbulence, heating, diffusion, or convection, represent fundamental physical ingredients of similar dynamical behavior occurring in the near-Earth space, at the Sun, in the heliosphere, or in astrophysical environments.

The International Astrophysics Forum (IAFA 2011) held in "Europe's most beautiful flower village," in the Tyrolean Alpbach in June 2011, reviewed the state of the art of space and astrophysical plasma research and identified the key problems to be addressed in the coming years. Merging new ideas in an interdisciplinary manner, the IAFA 2011 conference also provided a forum for promoting future international collaboration and research programs in theory, experiment, and numerical simulations with regard to space and astrophysical environments. Science topics addressed included the following:

- Magnetic field topology and reconnection
- Scaling and turbulence
- Wave-particle interactions
- Statistical physics and entropy approaches
- Shocks and nonlinear structures
- Multi-scale complexity, self-organization and relaxation
- Heliogeophysics

The scientific sessions were organized into a few consecutive reviews of related principal topics, followed by a 15-min long informal forum discussion. The result of these enthusiastic discussions is the IAFA 2011 Proceedings book. We warmly thank all the participants of IAFA 2011 who contributed to the Proceedings or presented their talks during the meeting.

Finally, we appreciate the support provided by the International Advisory Committee, the Local Organizing Committee, the numerous referees, and the Management of Congress Center Alpbach for their valuable help.

Innsbruck, Austria

Manfred P. Leubner
Zoltán Vörös

Acknowledgments

The editors take the opportunity to thank the following participants for their contribution: Alexeev Igor (Moscow State University), Amano Takanobu (The University of Tokyo), Arregui Iñigo and Ballester Jose (Universitat de les Illes Balears), Balogh Andre (International Space Science Institute, Bern), Bárta Miroslav (Astronomical Institute Ondřejov), Belenkaya Elena (Moscow State University), Belmont Gerard (Ecole Polytechnique, Paris), Boldyrev Stanislav (University of Wisconsin, Madison), Browning Philippa (University of Manchester), Bruno Roberto (Instituto Nationale di Astrofisica, Roma), Büchner Jörg (Max-Planck-Institut, Katlenburg-Lindau), Chapman Sandra (University of Warwick), Chen Christopher (University of California, Berkeley), Cho Jungyeon (Chungnam National University, Daejeon), Consolini Giuseppe (Istituto di Fisica dello Spazio Interplanetario, Roma), Daughton William (Los Alamos National Laboratory), Egedal-Pedersen (Massachusetts Institute of Technology), Erdelyi Robertus (University of Sheffield), Fujimoto Masaki (Institute of Space and Astronautical Science, Kanagawa), Greco Antonella (University of Calabria), Hau Lin-Ni (National Central University, Jhongli City), Hornig Gunnar (University of Dundee), Hoshino Masahiro (The University of Tokyo), Jacobs Carla (Katholieke Universiteit Leuven), Jatenco-Pereira Vera (University of Sao Paulo), Ji Hantao (Princeton Plasma Physics Laboratory), Joshi Bhuwan (Udaipur Solar Observatory), Karimabadi Homa (University of California, San Diego), Karlický Marian (Academy of Sciences of the Czech Republic, Ondřejov), Kasper Justin (Harvard-Smithsonian Center of Astrophysics), Kendl Alexander (University of Innsbruck), Khodachenko Maxim (Space Research Institute, Graz), Lazar Marian (Ruhr University, Bochum), Lazarian Alexander (University of Wisconsin), Leubner Manfred (University of Innsbruck), Livadiotis George (Southwest Research Institute, San Antonio), Loureiro Nuno (Instituto Superior Tecnico, Lisbon), Lu Quanming (University of Science and Technology of China, Hefei), Medvedev Mikhail (University of Kansas, Lawrence), Mozer Forrest (University of California, Berkeley), Nemecek Zdenek (Charles University, Prague), Nishizuka Naoto (Japan Aerospace Exploration Agency, Kanagawa), Parker Eugene (University of Chicago), Podesta John (Los Alamos National Laboratory), Popel Sergey (Institute for Dynamics of Geospheres, RAS, Moscow), Retino Alessandro

(Laboratoire de Physique des Plasmas, CNRS), Rypdal Kristoffer (University of Tromso), Sahraoui Fouad (Ecole Polytechnique, Paris), Sauvaud Jean-Andre (Centre d' Etude Spatiale des Rayonnements, Toulouse), Schekochihin Alexander (University of Oxford), Shimizu Toshifumi (Institute of Space and Astronautical Science, Kanagawa), Shivamoggi Bhimsen (University of Central Florida, Orlando), Shukla Padma (Ruhr University, Bochum), Stasiewicz Kristof (Swedish Institute of Space Physics, Uppsala), Taroyan Youra (Aberystwyth University), Valdivia Juan Alejandro (University of Santiago, Chile), Uzdensky Dmitri (University of Colorado, Boulder), Vlahos Loukas (Aristotle University of Thessaloniki), Voitenko Yuriy (Belgian Institute for Space Aeronomy, Brussels), Vörös Zoltán (University of Innsbruck), Watkins Nicholas (British Antarctic Survey, Cambridge), Weygand James (University of California, Los Angeles), Yoon Peter (University of Maryland), Yordanova Emiliya (Swedish Institute of Space Physics, Uppsala), and Zimbardo Gaetano (University of Calabria, Cosenza).

Contents

Contributors

Igor I. Alexeev Scobeltsyn Institute of Nuclear Physics, Lomonosov Moscow State University, Leninskie Gory, Moscow, Russia

Takanobu Amano Department of Physics, Nagoya University, Nagoya, Japan

Max-Planck-Institut für Kernphysik, Heidelberg, Germany

Iñigo Arregui Departament de Física, Universitat de les Illes Balears, Palma de Mallorca, Spain

Jose Luis Ballester Departament de Física, Universitat de les Illes Balears, Palma, Spain

Michael R. Bareford School of Mathematical Sciences, University of St. Andrews, St. Andrews, UK

Miroslav Bárta Astronomical Institute of the Academy of Sciences of the Czech Republic, Ondřejov, Czech Republic

Elena S. Belenkaya Scobeltsyn Institute of Nuclear Physics, Lomonosov Moscow State University, Leninskie Gory, Moscow, Russia

Philippa K. Browning Jodrell Bank Centre for Astrophysics, University of Manchester, Manchester, UK

Jörg Büchner MPS Lindau, Katlenburg-Lindau, Germany

Jungyeon Cho Chungnam National University, Daejeon, Korea

Giuseppe Consolini INAF-Istituto di Astrofisica e Planetologia Spaziali, Via del Fosso del Cavaliere, Roma, Italy

Bengt Eliasson International Centre for Advanced Studies in Physical Sciences and Institute for Theoretical Physics, Faculty of Physics and Astronomy, Ruhr University Bochum, Bochum, Germany

Mykola Gordovskyy Jodrell Bank Centre for Astrophysics, University of Manchester, Manchester, UK

M.S. Grigoryan Scobeltsyn Institute of Nuclear Physics, Lomonosov Moscow State University, Leninskie Gory, Moscow, Russia

B. Gouveia dal Pino Instituto de Astronomia, Geofísica e Ciências Atmosféricas, Universidade de São Paulo, São Paulo/SP, Brazil

Masahiro Hoshino Department of Earth and Planetary Science, University of Tokyo, Tokyo, Japan

Shinsuke Imada Institute of Space and Astronautical Science, Japan Aerospace Exploration Agency, Chuo, Sagamihara, Kanagawa, Japan

Vera Jatenco-Pereira Institute of Astronomy, Geophysics and Atmosferic Sciences, University of São Paulo, São Paulo, Brazil

Bhuwan Joshi Udaipur Solar Observatory, Physical Research Laboratory, Udaipur, Rajasthan, India

Marian Karlický Astronomical Institute of the Academy of Sciences of the Czech Republic, Ondřejov, Czech Republic

Alexander Kendl Institute for Ion Physics and Applied Physics, University of Innsbruck, Innsbruck, Austria

Maxim L. Khodachenko Space Research Institute, Austrian Academy of Sciences, Graz, Austria

Grzegorz Kowal Instituto de Astronomia, Geofísica e Ciências Atmosféricas, Universidade de São Paulo, São Paulo/SP, Brazil

M. Lazar Institut für Theoretische Physik, Lehrstuhl IV: Weltraum- und Astrophysik, Ruhr-Universität Bochum, Bochum, Germany

Alexandre Lazarian Astronomy Department, University of Wisconsin, Madison, WI, USA

P.K. Manoharan Radio Astronomy Centre, Tata Institute of Fundamental Research, Udhagamandalam (Ooty), Tamil Nadu, India

Eugene N. Parker Department of Physics, University of Chicago, Chicago, IL, USA

Silvia Perri Università della Calabria, Ponte P. Bucci, Arcavacata di Rende, Italy

V. Pierrard Belgian Institute for Space Aeronomy, Space Physics, Brussels, Belgium

John J. Podesta Los Alamos National Laboratory, Los Alamos, NM, USA

S. Poedts Centre for Plasma Astrophysics, Leuven, Belgium

Sergey I. Popel Institute for Dynamics of Geospheres RAS, Moscow, Russia

Andrei Runov Institute of Geophysics and Planetary Physics, University of California, Los Angeles, CA, USA

Kristoffer Rypdal Department of Physics and Technology, University of Tromsø, Tromsø, Norway

Martin Rypdal Department of Mathematics and Statistics, University of Tromsø, Tromsø, Norway

R. Schlickeiser Institut für Theoretische Physik, Lehrstuhl IV: Weltraum- und Astrophysik, Ruhr-Universität Bochum, Bochum, Germany

Toshifumi Shimizu Institute of Space and Astronautical Science, Japan Aerospace Exploration Agency, Chuo, Sagamihara, Kanagawa, Japan

Bhimsen K. Shivamoggi University of Central Florida, Orlando, FL, USA

Padma Kant Shukla International Centre for Advanced Studies in Physical Sciences and Institute for Theoretical Physics, Faculty of Physics and Astronomy, Ruhr University Bochum, Bochum, Germany

Department of Mechanical and Aerospace Engineering and Center for Energy Research, University of California San Diego, La Jolla, CA, USA

Jan Skála Faculty of Science, UJEP, Ústí nad Labem, Czechia

Roberto Soler Department of Mathematics, Centre for Plasma Astrophysics, Katholieke Universiteit Leuven, Leuven, Belgium

Boris V. Somov Astronomical Institute, Moscow State University, Moscow, Russia

Lennart Stenflo Department of Physics, Linköping University, Linköping, Sweden

Youra Taroyan IMAPS, Aberystwyth University, Wales, UK

Astrid Veronig IGAM/Institute of Physics, University of Graz, Graz, Austria

Aline de Almeida Vidotto SUPA, School of Physics and Astronomy, University of St. Andrews, North Haugh, St. Andrews, UK

Ethan T. Vishniac Department of Physics and Astronomy, McMaster University, Hamilton, Canada

Zoltán Vörös Institute of Astro- and Particle Physics, University of Innsbruck, Innsbruck, Austria

Peter H. Yoon Institute for Physical Science and Technology, University of Maryland, College Park, MD, USA

Gaetano Zimbardo Università della Calabria, Ponte P. Bucci, Arcavacata di Rende, Italy

Part I
Magnetic Field Topology and Reconnection

Field Line Topology and Rapid Reconnection

Eugene N. Parker

Abstract Consider a magnetic field extending through an infinitely conducting fluid between end plates $z = 0$, $z = L$, with arbitrary interlacing of the field lines throughout. The field is fixed in both endplates and is allowed to relax to an equilibrium described by the force-free equilibrium equation $\nabla \times \mathbf{B} = \alpha \mathbf{B}$. The divergence of this field equation yields $\mathbf{B} \cdot \nabla d = 0$, requiring that the torsion coefficient α be constant along each individual field line, and showing that the field lines represent a family of real characteristics of the equilibrium field equation. So the field line topology plays a direct role in determining the nature of the equilibrium field. For an arbitrarily prescribed interlacing field line topology a continuous field generally cannot provide an α that is constant along field lines. Yet with the field fixed at both ends it is obvious that every topology has an equilibrium. So there must be a mathematical solution to the field equation for each and every topology. This dilemma is resolved by the fact that the field lines represent a family of real characteristics, so that surfaces of discontinuity (current sheets) can form along the flux surfaces. In almost all field line topologies, then, the continuous field is cut up by surfaces of tangential discontinuity between regions of continuous field.

1 The Force-Free Field Equation

The familiar force-free field equation

$$\nabla \times \mathbf{B} = \alpha \mathbf{B} \tag{1}$$

has both real and complex characteristics, providing unusual analytic properties, as we shall soon see. In particular, the continuous solutions to Eq. (1) prove to be

E.N. Parker (✉)
Department of Physics, University of Chicago, Chicago, IL, USA
e-mail: parker@oddjob.uchicago.edu

Parker, E.N.: *Field Line Topology and Rapid Reconnection*.
Astrophys Space Sci Proc. **33**, 3–9 (2012)
DOI 10.1007/978-3-642-30442-2_1, © Springer-Verlag Berlin Heidelberg 2012

incompatible with almost all field line topologies. This contradiction can be resolved only through recognition that the family of real characteristics (the magnetic field lines) provides for discontinuities. So the topology of the field lines dictates the structure of the solutions of the equilibrium equation (1). The result is that for almost all field line topologies, there are surfaces of tangential discontinuity partitioning off regions of continuous field [1–3].

Note, then, that the curl of the field equation is

$$\mathbf{B} \times \nabla\alpha = \nabla^2\mathbf{B} + \alpha^2\mathbf{B} \tag{2}$$

The Laplacian indicates two families of complex characteristics for this quasilinear equation. The divergence of either Eq. (1) or (2) leads to

$$\mathbf{B} \cdot \nabla\alpha = 0 \tag{3}$$

requiring that the torsion coefficient α be constant along each field line. Obviously the field lines represent a family of real characteristics. Hence the field line topology plays a prominent role in determining the nature of the associated equilibrium field, described by Eq. (1). The field line topology is invariant in the presence of an infinitely conducting fluid, but the precise shape of the field lines can be determined only along with the equilibrium solution **B**.

The torsion coefficient $\alpha(\mathbf{r})$ at any point P represents the ratio of the magnetic circulation $\oint d\mathbf{s} \cdot B$ around any small closed contour circling **B** at P divided by the magnetic flux $\int d\mathbf{s} \cdot B$ through that contour. Note then that the field equation is linear in **B** if $\alpha(\mathbf{r})$ is specified. However, we are concerned here with the field extending through an infinitely conducting fluid from $z = 0$ to $z = L$ and anchored at both ends. The field lines are subject to arbitrary interlacing throughout $0 < z < L$, so that the field line topology, but not $\alpha(\mathbf{r})$, is known. The invariant topology of the field lines is sufficient to provide a unique equilibrium **B(r)** and the related $\alpha = \mathbf{B}\cdot\nabla\times\mathbf{B}/B^2$. Thus the problem is not linear, because α is an unknown function related to **B**, and the precise field equation is not known ahead of its solution for a specified topology.

2 The Generic Magnetic Field Problem

Consider an initial uniform magnetic field B_0 extending in the z-direction between the infinitely conducting plane boundaries $z = 0$ and $z = L$. The space $0 < z < L$ is filled with an infinitely conducting incompressible fluid so that the field moves precisely with the fluid. At time $t = 0$ the fluid and the upper end plate $z = L$ are set in the 2D incompressible motion

$$v_x = +\nu kz\frac{\partial\psi}{\partial y}, \quad v_y = -\nu kz\frac{\partial\psi}{\partial x}, \quad v_z = 0, \tag{4}$$

where $\psi = \psi(x, y, kzt)$ represents a bounded, smooth, continuous, differentiable stream function. After a time t the magnetic field is given by

$$B_x = +B_0\, \nu kt \frac{\partial \psi}{\partial y}, \quad B_y = -B_0\, \nu kt \frac{\partial \psi}{\partial x}, \quad B_z = B_0. \tag{5}$$

We suppose that ψ represents a general chaotic swirling motion fed into the system through $z = L$, while the footpoints at $z = 0$ are held fixed. The characteristic transverse (x, y) scale of the swirling is denoted by $l(\ll L)$. The fluid motion is shut off at a time $t = T$, when the transverse field components B_x and B_y are comparable in magnitude to the mean field B_0 and there is a succession of L/l uncorrelated eddies or swirls along any given field line. This interlacing topology is determined by the function $\psi(x, y, kzt)$, and the field given by Eq. (5) is not in equilibrium, i.e. not in the lowest available energy state for the given topology, of course.

We wish to know the equilibrium field configuration for the specified topology. The force free Eq. (1) is difficult to work with, so to facilitate the calculation, it is convenient to stretch (dilate) the field in the z-direction by the large factor $N(\gg 1)$. The upper end plate moves to $z = NL$, and the field described by Eq. (5) becomes

$$B_x = +\left(\frac{B_0}{N}\right) \nu kT \frac{\partial \psi}{\partial y}, \quad B_y = -\left(\frac{B_0}{N}\right) \nu kT \frac{\partial \psi}{\partial x}, \quad B_z = B_0, \tag{6}$$

where now $\psi(x, y, kzT)$ is replaced by $\psi(x, y, kzT/N)$. The field line topology is preserved and the transverse field components are now small compared to the longitudinal z-component by the factor $1/N$.

The next step is to hold fixed the footpoints of the field at $z = 0, L$ while releasing the fluid throughout $0 < z < L$ so that the magnetic field described by Eq. (6) can relax to the lowest available energy state. A small viscosity is introduced into the fluid so that the free energy of the field can be removed by viscous dissipation. The end plates are assumed to maintain a uniform fluid pressure at both $z = 0$ and $z = L$, which will generally involve fluid motion across the end plates. It is evident that a final stable equilibrium exists because the field is held fixed at both ends and the fluid pressure remains uniform. The system relaxes exponentially to the final static equilibrium state, which conforms to Eq. (1). The boundary conditions during this relaxation are $B_z = B_0$ and $v_x = v_y = 0$ at $z = 0, L$. The final equilibrium state is uniquely determined by the invariant field line topology.

Using the small ordering parameter $\epsilon = O(1/N) \ll 1$, the final equilibrium state can be written in the form

$$B_x = \epsilon B_0 b_x, \quad B_y = \epsilon B_0 b_y, \quad B_z = B_0(1 + \epsilon b_z). \tag{7}$$

The torsion is reduced by the expansion of the transverse components, so let

$$\alpha = \epsilon a \tag{8}$$

The stretched field varies slowly in the z-direction, so write

$$\frac{\partial}{\partial z} = \epsilon \frac{\partial}{\partial \zeta} \tag{9}$$

Thus $\partial/\partial x$, $\partial/\partial y$, and $\partial/\partial\zeta$ are all $O(1/l)$.

The components of the field Eq. (1) become

$$\epsilon \frac{\partial b_z}{\partial y} - \epsilon^2 \frac{\partial b_y}{\partial \zeta} = \epsilon^2 a b_x, \tag{10}$$

$$\epsilon^2 \frac{\partial b_x}{\partial \zeta} - \epsilon \frac{\partial b_z}{\partial x} = \epsilon^2 a b_y, \tag{11}$$

$$\epsilon \frac{\partial b_y}{\partial x} - \epsilon \frac{\partial b_x}{\partial y} = \epsilon a (1 + \epsilon b_z). \tag{12}$$

The divergence condition is

$$\epsilon \frac{\partial b_x}{\partial x} + \epsilon \frac{\partial b_y}{\partial y} + \epsilon^2 \frac{\partial b_z}{\partial \zeta} = 0, \tag{13}$$

and Eq. (3) reduces to

$$\epsilon^2 b_x \frac{\partial a}{\partial x} + \epsilon^2 b_y \frac{\partial a}{\partial y} + (1 + \epsilon b_z)\epsilon^2 \frac{\partial a}{\partial \zeta} = 0. \tag{14}$$

It is evident from Eqs. (10) and (11) that b_z is small $O(\epsilon)$ compared to b_x and b_y. So Eq. (13) reduces to

$$\frac{\partial b_x}{\partial x} + \frac{\partial b_y}{\partial y} = 0 \tag{15}$$

upon neglecting terms second order in ϵ compared to one. It follows that there exists a function $\theta(x, y, \zeta)$ such that

$$b_x = +\frac{\partial \theta}{\partial y}, \quad b_y = -\frac{\partial \theta}{\partial x}. \tag{16}$$

It follows from Eq. (12) that

$$a = -\left(\frac{\partial^2 \theta}{\partial x^2} + \frac{\partial^2 \theta}{\partial y^2} \right), \tag{17}$$

and Eq. (14) becomes

$$\frac{\partial a}{\partial \zeta} = \frac{\partial \theta}{\partial x}\frac{\partial a}{\partial y} - \frac{\partial \theta}{\partial y}\frac{\partial a}{\partial x}. \tag{18}$$

The equilibrium field is described by Eqs. (16)–(18). These equations are identical in form to the vorticity equation for a 2D ideal incompressible inviscid fluid. For the fluid analog replace b_x and b_y by v_x and v_y, respectively, and the torsion a by the vorticity ω. The vorticity equation (18) has been studied at great length over many years [4] and it can be shown that the entrophy cascades to large wave numbers and the kinetic energy cascades to small wave numbers with the passage of time. That is to say, a^2 evolves along the z-direction to successively smaller transverse scales while the magnetic energy $b_x^2+b_y^2$ evolves into successively larger transverse scales. That is the nature of the lowest available energy state of the interlaced field topology. There are infinitely many different interlaced field line topologies providing the vorticity-like evolution along the field. However this special evolution does not span the topology of the general interlaced field, which has no such special evolution of the topology along the field lines. To put it differently, the vorticity-like field Eq. (18) admits a topological set of vortex fields with measure zero compared to all possible interlaced field line topologies described by $\psi(x, y, kzt)$.

We are faced with a seeming contradiction. We know that a stable equilibrium exists for all field line topologies, because the field is tied at both ends, $z = 0$ and $z = L$. On the other hand, the field equation describing the equilibrium state admits only vorticity-like equilibrium topologies – a set of measure zero.

3 Discussion and Conclusion

What is it, then, that constrains the solutions of the field equation so that they cannot provide the equilibrium for the general interlaced field line topology? The difficulty is expressed by Eq. (3), asserting that the torsion coefficient α is constant along each field line all the way from $z = 0$ to $z = NL$. Recall that almost all elemental flux bundles writhe and twist on a transverse scale $O(l)$ through successive unrelated interlacing patterns, with each pattern extending a distance $O(Nl)$ along the field. Each field line encounters $O(L/l)$ uncorrelated patterns on the way from $z = 0$ to $z = NL$. The torsion must be adjusted so that any given flux bundle fits smoothly to the surrounding field as it extends through each independent swirling pattern along its length. In almost all interlacing field line topologies that cannot be accomplished with a single value for the twist (the torsion coefficient α) along each elemental flux bundle, so long as the field is everywhere continuous. It takes a very special interlacing topology to make this possible, and the vorticity-like field Eq. (18) spells out that special form of the topology for which Eq. (3) is satisfied and the field is continuous throughout.

The general interlacing field line topologies built into the field by $\psi(x, y, kzt)$ generally do not conform to the special vorticity analog. So we expect that the individual flux bundles do not all fit smoothly and continuously to-gether everywhere throughout the field region $z = 0$ to $z = L$. The family of real characteristics of Eq. (1) allows for exactly this condition, providing surfaces of tangential discontinuity (current sheets) along flux surfaces in the magnetic field.

The surfaces of tangential discontinuity represent flux surfaces across which the direction of field changes discontinuously (i.e. the surface is a current sheet) while the field magnitude (i.e. the magnetic pressure) is continuous. The essential point is that the magnetic field is not defined on a surface of tangential discontinuity (TD), nor is the torsion coefficient α defined. So Eq. (3) is not applicable to a TD, across which the shear or torsion is therefore unrestricted. In this way, each flux bundle, with an α that is uniform along the length of the flux bundle, may interlace through any sequence of patterns along its length without fitting continuously into the diverse local field patterns along the way. So, any field line topology introduced by $\psi(x, y, kzt)$ can settle into equilibrium accompanied by a suitable array of TD's. It would appear that each successive independent swirl of the field would create its own set of TD's along the length of the field, suggesting that passage through L/l uncorrelated swirls along the length L would provide L/l distinct sets of TD's. Indeed, it is not known whether a finite or an infinite number of TD's is required for equilibrium within a single swirl.

In summary, the field Eq. (18) represents the solutions that are everywhere continuous. Such continuous fields exist only in the special vorticity-like interlacing topology. For the general interlacing topology described by $\psi(x, y, kzt)$, Eq. (3) is satisfied in regions between TD's, and the TD's take up the shear in the field that would otherwise violate Eq. (3).

Note, then, that a TD can end only at the boundaries $z = 0, z = NL$, so a TD re-quired for equilibrium in an independent region anywhere along the field extends in both directions from the region to the boundaries, spreading out and becoming less intense with distance along the field. Meeting TD's from other uncorrelated regions along the way, the TD's form a complex and irregular honeycomb structure with continuous field throughout each cell of the honeycomb [2]. It follows that the continuous field within each cell is a solution of the vorticity-like equilibrium Eq. (18) within the writhing boundaries of the cell.

Lacking a comprehensive analytic theory of field and field line topology, it appears that a quantitative illustration of the discontinuous equilibrium solutions might best be pursued through numerical methods. Simulations of the relaxation of 2D magnetic fields show the trend toward current sheets of declining thickness, subject to the limitations imposed by magnetic Reynolds numbers limited to 10^3 [5, 6]. The 3D problem requires much greater computing capacity of course, but it is essential for developing the theory in the physical world. A recent example is a numerical simulation carried out by Wilmot-Smith et al. [7]. They use a Lagrangian formulation to follow the initial braided magnetic field as it re-laxes toward equilibrium. Their numerical experiment shows nothing that resembles a direct evolution toward TD's or current sheets, but shows a tendency for striations in the current with thickness d diminishing exponentially, $d \approx 10^{-n/2}$, with the number n of braiding loops along the field. They remark, "It is possible, as with any numerical relaxation experiment, that the force free-state of E^3 has additional properties not seen in the numerical approximation." Here E^3 refers to their braided field of three pairs of positive and negative loops.

This brings us back to the problem posed by an equilibrium field without internal discontinuities. The equilibrium field lacking discontinuities in any finite region of space conforms to the vorticity Eq. (18) throughout that region. So if a numerical result correctly relaxes to a continuous equilibrium configuration when stretched out in the z-direction, that configuration must conform to Eq. (18). However, the vorticity equation does not admit of continuous solutions with braided topology E^3. So if the numerical solution for the braided topology is relaxing toward a final equilibrium while showing no signs of developing discontinuities, there must be a problem with the numerical scheme, which brings us back to the concern expressed by Wilmot-Smith et al. In particular, if it turns out that a single loop or swirl requires a large number of TD's for equilibrium, a numerical experiment with adequate resolution becomes problematical even for a topology as simple as E^3.

References

1. Parker, EN 1972, Astrophys. J. 174, 499.
2. Parker, EN 1994, Spontaneous Current Sheets in Magnetic Fields, Oxford University Press, New York.
3. Parker, EN 2007, Conversations on Electric and Magnetic Fields in the Cosmos, Princeton University Press, Princeton.
4. Kraichnan, RH and Montgomery, D 1980, Rep. Prog. Phys. 43, 549.
5. Matthaeus, WH and Montgomery, D 1980, Annals NY Acad. Sci. 367, 203.
6. Biskamp, D and Welter, H 1989, Phys. Fluids B 1, 1964.
7. Wilmot-Smith, AL, Hornig, G, and Pontin, DI 2009, Astrophys. J. 696, 1339.

Acceleration of Energetic Particles through Reconnection of Weakly Stochastic Magnetic Field

Alexandre Lazarian, Grzegorz Kowal, B. Gouveia dal Pino, and Ethan T. Vishniac

Abstract Astrophysical media are turbulent and therefore reconnection should be treated in the presence of pre-existing turbulence. We consider the model of fast magnetic reconnection in Lazarian and Vishniac (Astrophys J 517:700–718, 1999) which predicts that the rate of reconnection is controlled by the intensity and the injection scale of turbulent motions. We provide new evidence of successful testing of the model and argue that the model presents a generic set up for astrophysical reconnection events. We study particle acceleration that takes place in volumes of driven turbulence as well turbulent volumes in the presence of large scale reconnection. We show that in the latter case the acceleration is of the first order Fermi type thus supporting the model of acceleration proposed in Gouveia dal Pino and Lazarian (Astron Astrophys 44:845–853, 2005)

1 Introduction

Astrophysical fluids are turbulent and this changes the physics of many processes. It has been long accepted that this dramatically alters the nature of the cosmic ray propagation and acceleration (see [32]), the research during the last decade also testifies that the nature of the reconnection process is being radically changed

A. Lazarian (✉)
Astronomy Department, University of Wisconsin, Madison, WI 53706, USA
e-mail: alazarian@facstaff.wisc.edu

G. Kowal · B.G. dal Pino
Instituto de Astronomia, Geofísica e Ciências Atmosféricas, Universidade de São Paulo, Rua do Matão, 1226 – Cidade Universitária, CEP 05508-090, São Paulo/SP, Brazil
e-mail: kowal@astro.iag.usp.br; dalpino@astro.iag.usp.br

E.T. Vishniac
Department of Physics and Astronomy, McMaster University, Hamilton, ON L8S, 4M1, Canada
e-mail: ethan@mcmaster.ca

Lazarian, A. et al.: *Acceleration of Energetic Particles through Reconnection of Weakly Stochastic Magnetic Field*. Astrophys Space Sci Proc. **33**, 11–21 (2012)
DOI 10.1007/978-3-642-30442-2_2, © Springer-Verlag Berlin Heidelberg 2012

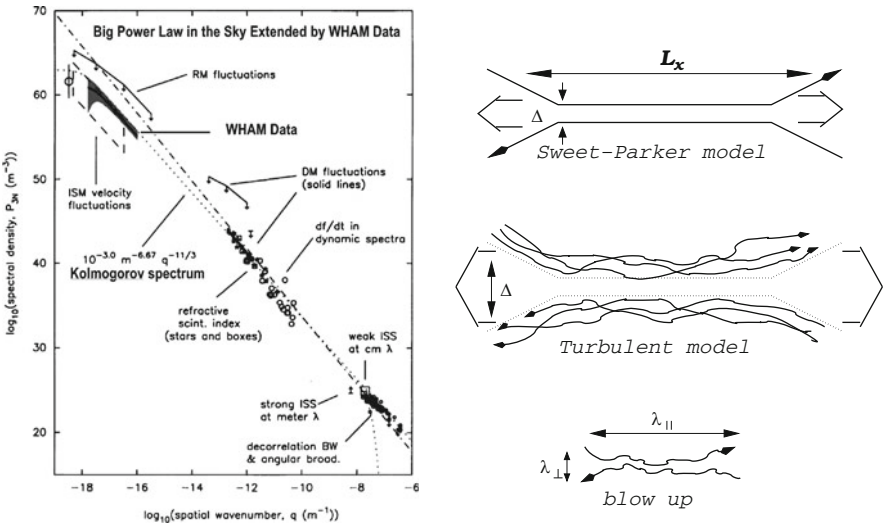

Fig. 1 *Left panel*: Turbulence in the interstellar gas as revealed by electron density fluctuations. "Big Power Law in the Sky" in Armstrong et al. [2] extended using WHAM data. The slope corresponds to that of Kolmogorov turbulence (Modified from [5]). *Right Panel*: Sweet-Parker model versus the model in LV99. Turbulence makes the outflow region much wider and independent of resistivity (From Lazarian et al. [28])

([26], henceforth LV99, [18, 19]). Reconnection in turbulent media was invoked by de Gouveia dal Pino and Lazarian ([8], henceforth GL05) in the model of the first order Fermi acceleration of cosmic rays in reconnection sites. This paper discusses new testings of the LV99 model as well as new results on energetic particle acceleration in the regions of reconnection of weakly turbulent magnetic field.

Astrophysical turbulence, in general, is *not* caused by reconnection. Therefore, while dealing with problems of reconnection and related particle acceleration it is proper to treat the turbulence as pre-existing. For instance, it has been known for decades that interstellar medium (ISM) is driven by violent supernovae explosions (McKee and Ostriker 1977). By now it has been accepted that the ISM is turbulent on scales ranging from AUs to kpc (see [2, 14, 24]. Figure 1 shows the turbulent power density plotted against the inverse of the scale length, with data at large scales, i.e. at small wavenumbers q expanded using the Wisconsin H_α Mapper (WHAM) data on electron density fluctuations [5]. Another example is turbulence is solar wind (see [31]).

The problem of magnetic reconnection is a long standing one. It is generally believed that a magnetic field embedded in a highly conductive fluid preserves its topology for all time due to the magnetic fields being frozen-in (see [1]). At the same time, although ionized astrophysical objects, like stars and galactic disks, are almost perfectly conducting, they show indications of changes in topology [38],

"magnetic reconnection", on dynamical time scales (see [37]). Reconnection can be observed directly in the solar corona [43], but can also be inferred from the existence of large-scale dynamo activity inside stellar interiors [39]. Solar flares are usually associated with magnetic reconnection. More recent research shows that γ-ray busts can also have a similar origin [27,44].[1] At the same time, a lot of previous work has concentrated on showing how reconnection can be rapid in plasmas with very small collisional rates (see [12,13]). We feel that this substantially constrains astrophysical applications of the corresponding reconnection models.

Magnetic reconnection presents a known example of flux freezing violation. but it is conceivable that it was not taken seriously due to the unclear nature of fast reconnection (see [46] and references therein). Indeed, for years it was considered that fast reconnection required some special physical conditions and therefore "flux freezing" is fulfilled everywhere apart from some special zones.

The understanding of flux freezing in turbulent astrophysical environments has been challenged relatively recently and not all the consequences of this radical change have been evaluated so far. LV99 identified magnetic field wandering, which is the inherent property of magnetized turbulent plasma, as the cause of fast, i.e. independent of resistivity, magnetic reconnection. They showed that in turbulent fluids magnetic fields should undergo constant reconnection and change their identity all the time. This implies that magnetic fields are not any more frozen into a perfectly conducting fluid if this fluid is turbulent as was explicitly stated first in Vishniac and Lazarain (1999). Later, the challenge to the concept of "flux freezing" came from another side, i.e. from more formal mathematical studies of turbulent magnetic fields (see Eyink et al. 2011). Eyink et al. ([15], henceforth ELV11) showed the consistency of these two approaches and established the equivalence of the LV99 treatment with that in more recent mathematical papers.

While the idea that turbulence can change the reconnection rates has been discussed in a number of earlier papers, the LV99 model was radically different from its predecessors. For instance, Mathaeus and Lamkin [35, 36] performed 2D numerical simulations of turbulence and provided arguments in favor of magnetic reconnection getting fast. However, the physics of the processes that they considered was very different from that in LV99. For instance, the key process of field wandering of the LV99 model was been considered in Mathaeus and Lamkin [35, 36]. On the contrary, the components of their approach, e.g. X-point and possible effects of heating and compressibility are not ingredients of the LV99 model. Other papers, e.g. [17,41] explore the changes of the microscopic properties of the plasma induced by turbulence and consider how these changes can accelerate magnetic reconnection. LV99 shows that the microscopic plasma properties are irrelevant for their model of reconnection (see testing in [18] and more discussion of plasma effects in ELV11).

[1] LV99 model of reconnection predicts the bursty character of reconnection when the initial state of magnetic field is close to the laminar one.

In what follows, we discuss the LV99 model in Sect. 2, present new numerical tests of the LV99 model in Sect. 3, demonstrate the efficiency of energetic particle acceleration in turbulent reconnection regions in Sect. 4. In Sect. 5 we present astrophysical settings where we identified the acceleration of particles in reconnection layers, in Sects. 6 and 7 we, respectively, provide the discussion and summary of our results.

2 Reconnection of Weakly Turbulent Magnetic Field

To deal with strong, dynamically important magnetic fields LV99 proposed a model of fast reconnection in the presence of sub-Alfvénic turbulence. It is important to stress that unlike laboratory controlled settings, in astrophysical situations turbulence is preexisting, arising usually from the processes different from reconnection itself [6]. In fact, any modeling of astrophysical reconnection should account for the turbulent state of fluids and in most cases the turbulence does not arise from magnetic reconnection. The analogy here can be as follows: turbulence that is experienced by the airplane does not arise from the airplane motion, but preexist in the atmosphere.

LV99 identified stochastic wandering of the magnetic field-lines as the most critical property of MHD turbulence which permits fast reconnection and obtained analytical relations between the reconnection rate and the turbulence intensity and the turbulence injection scale.

LV99 revealed a very intimate relation between turbulence and magnetic reconnection and this connection was deepened by later research (ELV11, [22]). First of all, LV99 showed that reconnection was a necessary ingredient of MHD turbulence, this was the process that made the currently accepted picture of MHD turbulence in [16] self-consistent. Moreover, further research in ELV11 revealed that the expressions of reconnection rate in LV99 can be obtained from the concept of Richardson diffusion, which is the basic concept of fluid turbulence.

3 Numerical Testing of LV99 Model

Testing of LV99 model of reconnection was performed in [18,19]. Below we present some of the results obtained. In Fig. 2 we see the results for varying amounts of input power, for fixed resistivity and injection scale as well as for the case of no turbulence at all. The line drawn through the simulation points is for the LV99 predicted scaling, i.e. $V_{rec} \sim P^{1/2}$, where P is the power of injected turbulence. We also see the results obtained with a new way of real space turbulence driving (see more in [19]). This driving is different from the Fourier space in [18]. The results with both types of driving support LV99 model. In addition, Kowal et al. [18]

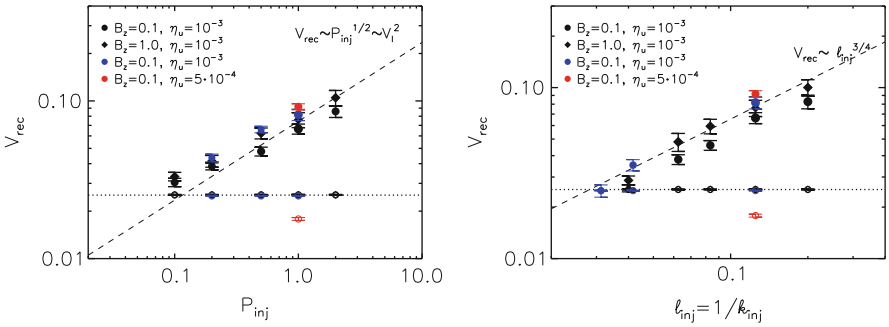

Fig. 2 New and old testing of LV99 model. *Left Panel*: The dependence of the reconnection speed V_{rec} on P_{inj}. *Blue symbols* show models with new driving in which the eddies where injected in magnetic field instead of velocity, as in the previous models (*black symbols*). A unique *red symbol* shows the reconnection rates from model with new driving in velocity performed with higher resolution ($512 \times 1024 \times 512$) and resistivity coefficient reduced to $\eta_u = 5 \cdot 10^{-4}$. *Right Panel*: The dependence of the reconnection speed V_{rec} on l_{inj} with additional models in which turbulence was driven in a new way as we describe in the text. Error bars represent the time variance of V_{rec}. The size of symbols corresponds to the error of V_{rec} (From Kowal et al. [19])

confirmed the predicted independence of the rate of reconnection on both Ohmic and anomalous resistivities, supporting LV99 conclusion that the reconnection is determined only by the properties of the turbulent flow.

4 Reconnection and Particle Acceleration

Magnetic reconnection results in shrinking of magnetic loops which induces the charged particles entrained on magnetic loops to get accelerated (see Fig. 3). This process was proposed in GL05 for the LV99 reconnection and then was adopted for the collisionless reconnection in [13]. The physics of the acceleration is the same although GL05 appealed to the 3D magnetic bundles (see Fig. 3), while [13] considered 2D shrinking islands. The latter is an artifact of the constrained 2D geometry. The difference in dimensions affects the acceleration efficiency according to [20]. GL05 claimed that the acceleration is of the first order Fermi type. This was confirmed in [21]. Below we descibe the numerical set up and the results of calculations.

In order to integrate the test particle trajectories we freeze in time a data cube obtained from the MHD models of reconnection in [18] and inject test thermal particles in the domain with random initial positions and directions. For each particle we solve the relativistic motion equation

$$\frac{d}{dt}\left(\gamma m \boldsymbol{u}\right) = q\left(\boldsymbol{E} + \boldsymbol{u} \times \boldsymbol{B}\right), \tag{1}$$

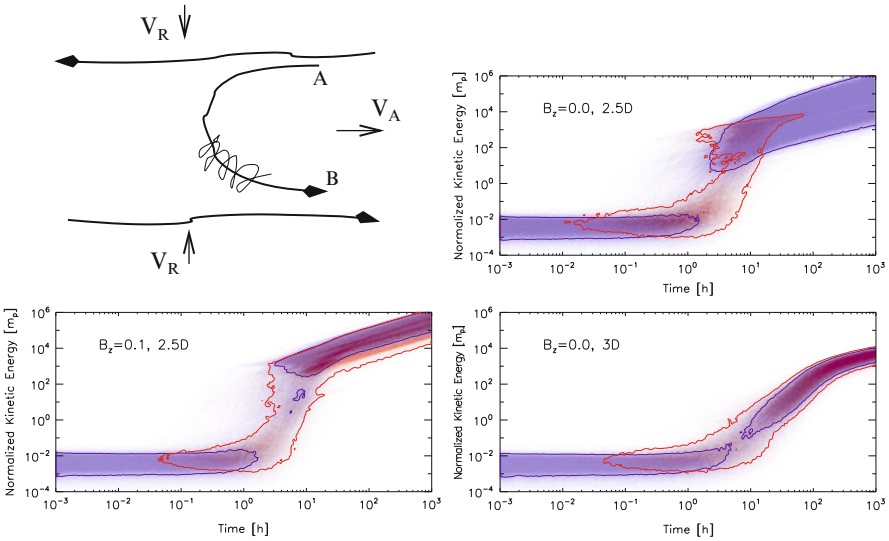

Fig. 3 *Left upper corner*: Schematic of the first order Fermi acceleration in the process of reconnecting turbulent magnetic field (From Lazarian 2005). *Other panels*. Numerical studies of particle acceleration. Kinetic energy evolution of a group of 10^4 protons in 2D models of reconnection with a guide field $B_z = 0.0$ and 0.1. In the *right bottom panel* a fully 3D model with initial $B_z = 0.0$ is presented. The colors show how the parallel (*red*) and perpendicular (*blue*) components of the particle velocities increase with time. The contours correspond to values 0.1 and 0.6 of the maximum number of particles for the parallel and perpendicular accelerations, respectively. The energy is normalized by the rest proton mass energy. The background magnetized flow with multiple current sheet layers is at time 4.0 in Alfvén time units (From Kowal et al. [20])

where m, q and $\boldsymbol{u}$ are the particle mass, electric charge and velocity, respectively, $\boldsymbol{E}$ and $\boldsymbol{B}$ are the electric and magnetic fields, respectively, $\gamma \equiv \left(1 - u^2/c^2\right)^{-1}$ is the Lorentz factor, and c is the speed of light. The electric field $\boldsymbol{E}$ is taken from the MHD simulations $\boldsymbol{E} = -\boldsymbol{v} \times \boldsymbol{B} + \eta \boldsymbol{J}$, where $\boldsymbol{v}$ is the plasma velocity, $\boldsymbol{J} \equiv \nabla \times \boldsymbol{B}$ is the current density, and η is the Ohmic resistivity coefficient. We neglect the resistive term above since its effect on particle acceleration is negligible [20].

In Fig. 3, we present the time evolution of the kinetic energy of the particles which have their parallel and perpendicular (red and blue points, respectively) velocity components accelerated for three models of reconnection. The upper left panel shows the energy evolution for a 2D model without the guide field. Initially, the particles pre-accelerate by increasing their perpendicular velocity component only. Later we observe an exponential growth of energy mostly due to the acceleration of the parallel component which stops after the energy reaches values of 10^3–$10^4\, m_p$ (where m_p is the proton rest mass energy). Further on, particles accelerate their perpendicular component only with smaller linear rate in a log–log diagram. In 2.5D case, there is also an initial slow acceleration of the perpendicular component followed by the exponential acceleration of the parallel velocity component. Due

to the presence of a weak guide field, the parallel component accelerates further to higher energies at a similar rate as the perpendicular one. This implies that the presence of a guide field removes the restriction seen in the 2D model without a guide field and allows the particles to increase their parallel velocity components as they travel along the guide field, in open loops rather than in confined 2D islands. This result is reassured by the 3D model in the bottom panel of Fig. 3, where no guide field is necessary as the MHD domain in fully three-dimensional. In this case, we clearly see a continuous increase of both components, which suggests that the particle acceleration behavior changes significantly when 3D effects are considered, where open loops replace the closed 2D reconnecting islands.

5 Reconnection and Acceleration: Astrophysical Examples

Lazarian and Opher [25] identified the origin of anomalous cosmic rays measured by Voyagers as arising from magnetic reconnection in heliosheath. As magnetic field lines of the magnetic spiral (arising from solar rotation) present in the solar wind get closer together magnetic reconnection is expected. In view of solar wind being turbulent, the LV99 model of reconnection is relevant.[2]

To explain the excess of the cosmic ray arrival from the direction towards heliotail Lazarain and Desiati (2010) considered magnetic reconnection in heliotail. The accumulation of magnetic flux of opposite polarities in heliotail arises from solar magnetic field reversals within 11 year cycle. Magnetic fields in heliotail are expected to be turbulent. The mechanism provides an attractive alternative to those discussed in the literature.

Magnetic reconnection in clusters of galaxies present an interesting way of accelerating energetic particles there (see Lazarian and Brunetti 2011). The large scale reversals of magnetic fields in galaxy clusters are expected as a result of accretion flows, instabilities and galactic jets. Acceleration in reconnection regions may present an appealing alternative to the acceleration of cosmic rays by the intracluster magnetic turbulence. Further work on the quantitative elaboration of the predictions of this and other astrophysical models that appeal to the acceleration of cosmic rays in reconnection sites are necessary [23].

6 Discussion

First of all, we would like to stress that the LV99 model is not in conflict with the studies of magnetic reconnection in collisionless plasmas that have been a major thrust of the plasma physics community (e.g. Daughton et al. [9]). Unlike latter

[2]Drake (2001) followed with a model appealing to the collisionless reconnection for which turbulence is not directly involved.

studies, LV99 deals with turbulent environments. It is demonstrated in LV99, the local reconnection rates are influenced by plasma effects, e.g. kinetic effects of Hall effects, but the overall or global reconnection rate, i.e. the rate at which magnetic flux tubes reconnect, is determined by the turbulent broadening of the reconnection region. Thus, in the turbulent astrophysical media the rate of reconnection is not going to be affected by additional mechanisms.

Over the last decade, more traditional approaches to reconnection have changed considerably. At the time of its introduction, the models competing with LV99 were modifications of the single X-point collisionless reconnection scheme first introduced by Petschek [40]. Those models had point-wise localized reconnection regions which were stabilized via plasma effects so that the outflow opened up on larger scales. Such configurations would be difficult to sustain in the presence of random forcing, which would be expected to collapse the reconnection layer. Moreover, [7] argued that observations of solar flares were inconsistent with single X-point reconnection.

In response to these objections, more recent models of collisionless reconnection have acquired several features in common with the LV99 model. In particular, they have moved to consideration of volume-filling reconnection, (although it is not clear how this volume filling is achieved in the presence of a single reconnection layer (see [13])). While much of the discussion still centers around magnetic islands produced by reconnection, in three dimensions these islands are expected to evolve into contracting 3D loops or ropes due to tearing-type instabilities in electron-current layers [10, 11]. This is broadly similar to what is depicted in Fig. 1, at least in the sense of introducing stochasticity to the reconnection zone. At the same time, although the 3D PIC simulation studies are described as "turbulent", they do not exhibit the inertial-range power-law spectra observed in the magnetosphere and do not take into account either the pre-existing turbulence found in many of its regions (due to temperature anisotropy, velocity shear, Kelvin-Helmholtz instability, etc.) or inertial-range turbulence generated as a consequence of reconnection itself [45].

The above remarks apply to the recent 3D PIC study [4], which observes micro-turbulence in the electron current layer during reconnection. The authors identify the source of this "turbulence" as a filamentation instability driven by current gradients, very similar to a related instability in the Electron MHD (EMHD) model. The key aim of this work was to identify the term in the generalized Ohm's law which supplies the reconnection electric field to break the "frozen-in" condition. However, this study ignores the ambient inertial-range turbulence observed in the magnetosphere and other astrophysical plasmas, which may strongly modify laminar instabilities and reconnection process.

We believe that in most astrophysical situations one has to deal with the *pre-existing turbulence*, which is the inevitable consequence of the high Reynolds number of astrophysical fluids and for which abundant empirical evidence exists. Such turbulence may modify or suppress instabilities, e.g. the tearing mode instability invoked in many studies [3, 33]. At the same time, LV99 model induces fast reconnection on dynamical time scales.

Our study shows that the acceleration of energetic particles in LV99-type reconnection layers provides first order Fermi acceleration first described in de GL05. The studies in [19, 20] confirm the promise of this way of accelerating of particles in various environments.

7 Summary

The results of our studies can be very briefly summarized as follows:

1. Advances in the understanding of magnetic reconnection in the MHD regime, in particular, related to the LV99 model of turbulent magnetic reconnection motivate the studies of whether the reconnection in this regime can accelerate energetic particles. New higher resolution testing of the LV99 model as well as simulations with a different type of driving confirm that the reconnection is fast.
2. Contracting magnetic loops in magnetic reconnection in 2D, in the MHD regime, provide the acceleration analogous to that observed in PIC simulations, which proves that the acceleration in reconnection regions is a universal process which is not determined by the details of plasma physics. This confirms that the process of acceleration in GL05 and Drake et al. (2006) has the same nature.
3. Acceleration of energetic particles in 2D and 3D shows substantial differences, which call for focusing on realistic 3D geometries of reconnection. Our study also shows that the first order Fermi acceleration dominates the second order Fermi that is also present in turbulent reconnection layers.

Acknowledgements The research of AL is supported by the Center for Magnetic Self-Organization in Laboratory and Astrophysical Plasmas. AL also acknowledged Humboldt Award at the Universities of Cologne and Bochum, as well as the hospitality of the International Institute of Physics (Brazil) and the Vilas Associate Award. GK and EMGDP acknowledge the support by the FAPESP grants no. 2006/50654-3 and 2009/50053-8, and the CNPq grant no. 300083/94-7. This research was also supported by the project TG-AST080005N through TeraGrid resources provided by Texas Advanced Computing Center (http://www.tacc.utexas.edu).

References

1. Alfvén, H., *Existence of Electromagnetic-Hydrodynamic Waves*, Nature, 1942, 150, 405–406
2. Armstrong, J. W., Rickett, B. J., & Spangler, S. R., *Electron density power spectrum in the local interstellar medium*, 1995, ApJ, 443, 209–221
3. Bhattacharjee, A., Huang, Y.-M., Yang, H. & Rogers, B. 2009, *Fast reconnection in high-Lundquist-number plasmas due to the plasmoid Instability*, Phys. Plasmas, 16, 112102
4. Che, H., Drake, J. F., & Swisdak, M. 2011, *A current filamentation mechanism for breaking magnetic field lines during reconnection*, Nature, 474, 184
5. Chepurnov, A. & Lazarian, A., *Extending the Big Power Law in the Sky with Turbulence Spectra from Wisconsin Hα Mapper Data*, 2010, ApJ, 710, 853–858

6. Cho, J. and Lazarian, A., *Compressible magnetohydrodynamic turbulence: mode coupling, scaling relations, anisotropy, viscosity-damped regime and astrophysical implications*, 2003, MNRAS, 345, 325–339
7. Ciaravella, A., & Raymond, J. C. 2008, ApJ, 686, 1372
8. de Gouveia dal Pino, E. M., & Lazarian, A., *Production of the large scale superluminal ejections of the microquasar GRS 1915+105 by violent magnetic reconnection*, A&A, 2005, 441, 845–853
9. Daughton, W., Scudder, J., & Karimabadi, H. 2006, Physics of Plasmas, 13, 072101
10. Daughton, W., Roytershteyn, V., Albright, B. J., Bowers, K., Yin, L., & Karimabadi, H. 2008, AGU Fall Meeting Abstracts, A1705
11. Daughton, W., Roytershteyn, V., Karimabadi, H., Yin, L., Albright, B. J., Bergen, B., & Bowers, K., 2011, Nature Physics, in press.
12. Drake, J. F., *Magnetic explosions in space*, 2001, Nature, 410, 525–526
13. Drake, J. F., Swisdak, M., Schoeffler, K. M., Rogers, B. N., & Kobayashi, S., *Formation of secondary islands during magnetic reconnection*, 2006, GeoRL, 33, 13105.
14. Elmegreen, B. G., & Scalo, J. 2004, Annual Review Astronomy & Astrophysics, 42, 211
15. Eyink, G. L., Lazarian, A., & Vishniac, E. T., *Fast Magnetic Reconnection and Spontaneous Stochasticity*, 2011, ApJ, 743, 51
16. Goldreich, P. & Sridhar, S., *Toward a theory of interstellar turbulence. 2: Strong alfvenic turbulence*, 1995, ApJ, 438, 763–775
17. Jacobson, A. R., *A possible plasma-dynamo mechanism driven by particle transport*, 1984, Physics of Fluids, 27, 7–9
18. Kowal, G., Lazarian, A., Vishniac, E. T., & Otmianowska-Mazur, K., *Numerical Tests of Fast Reconnection in Weakly Stochastic Magnetic Fields*, 2009, ApJ, 700, 63–85
19. Kowal, G., Lazarian, A., Vishniac, E. T., & Otmianowska-Mazur, K., *Reconnection Studies under Different Types of Turbulent Driving*, 2012, Nonlin. Process Geophysics, submitted
20. Kowal, G., de Gouveia Dal Pino, E. M., & Lazarian, A., *Magnetohydrodynamic Simulations of Reconnection and Particle Acceleration: Three-dimensional Effects*, 2011, ApJ, 735, 102
21. Kowal, G., de Gouveia Dal Pino, E. M., & Lazarian, A., *Acceleration in Turbulence and Weakly Stochastic Reconnection*, 2012, Physical Review Letters, in press
22. Lazarian, A., Eyink G., & Vishniac, E. 2012, Physics of Plasmas, 19, 012105
23. Lazarian, A., *Theoretical approaches to particle propagation and acceleration in turbulent intergalactic medium*, 2006, Astronomische Nachrichten, 327, 609
24. Lazarian, A., *Obtaining Spectra of Turbulent Velocity from Observations*, 2009, Space Science Review, 143, 357–385
25. Lazarian, A., & Opher, M. 2009, ApJ, 703, 8
26. Lazarian & Vishniac, *Reconnection in a Weakly Stochastic Field*, 1999, ApJ, 517, 700–718
27. Lazarian, A., Petrosian, V., Yan, H., & Cho, J., *Physics of Gamma-Ray Bursts: Turbulence, Energy Transfer and Reconnection*, 2003, arXiv:astro-ph/0301181
28. Lazarian, A., Vishniac, E. T., & Cho, J., *Magnetic Field Structure and Stochastic Reconnection in a Partially Ionized Gas*, 2004, ApJ, 603, 180–197
29. Lazarian, A., & Desiati, P., *Magnetic reconnection as the cause of cosmic ray excess from the heliospheric tail*, 2010, ApJ, 722, 188–196
30. Lazarian, A., & Brunetti, G., *Turbulence, reconnection and cosmic rays in galaxy clusters*, 2011, Mem.S.A.It., 82, 636–647
31. Leamon, R. J., Smith, C. W., Ness, N. F., Matthaeus, W. H., & Wong, H. K., *Observational constraints on the dynamics of the interplanetary magnetic field dissipation range*, 1998, JGR, 103, 4775
32. Longair, M. S. 2011, High Energy Astrophysics by Malcolm S. Longair. Cambridge University Press, 2011. ISBN: 9780521756181,
33. Loureiro, N. F., Uzdensky, D. A., Schekochihin, A. A., Cowley, S. C. & Yousef, T. A., *Turbulent magnetic reconnection in two dimensions*, 2009, MNRAS, 399, L146–L150
34. McKee, Ch.F. & Ostriker, J.P., *A theory of interstellar medium*, 1977, Astrophys. J., 218, 148–169

35. Matthaeus, W. H. & Lamkin, S. L., *Rapid magnetic reconnection caused by finite amplitude fluctuations*, 1985, Physics of Fluids, 28, 303–307
36. Matthaeus, W. H. & Lamkin, S. L., *Turbulent magnetic reconnection*, Physics of Fluids, 1986, 29, 2513–2534
37. Parker, E. N., *The Generation of Magnetic Fields in Astrophysical Bodies. I. The Dynamo Equations*, ApJ, 1970, 162, 665–673.
38. Parker, E. N., *Cosmical magnetic fields: Their origin and their activity*, 1979, Oxford Clarendon Press; New York, Oxford University Press
39. Parker, E. N., *A solar dynamo surface wave at the interface between convection and nonuniform rotation*, 1993, ApJ, 408, 707–719
40. Petschek, H.E. 1964, The Physics of Solar Flares, AAS-NASA Symposium (NASA SP-50), ed. W. H. Hess (Greenbelt, MD: NASA), 425
41. Speiser, T. W., *Conductivity without collisions or noise*, 1970, Planetary and Space Science, 18, 613
42. Vishniak, E.T. & Lazarian, A., *Reconnection in the interstellar medium*, 1999, Astrophys. J., 511, 193–203
43. Yokoyama, T. & Shibata, K., *Magnetic reconnection as the origin of X-ray jets and Hα surges on the Sun*, 1995, Nature, 375, 42–44
44. Zhang, B. and Yan, H., *The Internal-collision-induced Magnetic Reconnection and Turbulence (ICMART) Model of Gamma-ray Bursts*, 2011, ApJ, 726, 90
45. Zimbardo, G., Greco, A., Sorriso-Valvo, L., Perri, S., Vörös, Z., Aburjania, G., Chargazia, K., & Alexandrova, O. 2010, Space Science Review, 156, 89
46. Zweibel, E. G., & Yamada, M. 2009, Annual Review of Astronomy & Astrophysics, 47, 291

Dynamical Behaviors of the Solar Chromosphere Observed with Hinode Dynamics in Sunspot Light Bridges and Magnetic Reconnection Processes

Toshifumi Shimizu and Shinsuke Imada

Abstract The *Hinode*'s Solar Optical Telescope has revealed that the solar chromosphere is full of dynamical nature, which is much more dynamic than our thought. Observations of chromospheric dynamics in sunspot light bridges provides a new insight on the magnetic field topology for causing magnetic reconnection in the solar atmosphere and the process to supply the twisted flux to the solar surface.

1 Hinode's Chromospheric Observations

High spatial and cadence Ca II H observations carried out by Solar Optical Telescope (SOT) [4, 12, 16, 17] onboard *Hinode* [7] have revealed that the solar chromosphere is full of dynamical nature including transient brightenings and plasma ejections [11]. The main driver for the chromospheric dynamics is believed to be magnetic reconnection. However, we have not yet observationally determined the field topology for reconnection events in the chromosphere and the process to reach the topology.

In the paper, we focus on the field topology of reconnection events observed in sunspot light bridges. The magnetic reconnection at the field topology suggested by light bridge events may be called *component reconnection* and the similar topology is also observationally suggested to other chromospheric dynamics, such as penumbral micro-jets [5]. In the field topology suggested, the reconnection process occurs between non-antiparallel fields, and unlike the reconnection for exactly antiparallel fields, it is only the component of the field perpendicular to

T. Shimizu (✉) · S. Imada
Institute of Space and Astronautical Science, Japan Aerospace Exploration Agency,
3-1-1 Yoshinodai, Chuo, Sagamihara, Kanagawa 252-5210, Japan
e-mail: shimizu@solar.isas.jaxa.jp; imada.shinsuke@jaxa.jp

Shimizu, T. and Imada, S.: *Dynamical Behaviors of the Solar Chromosphere Observed with Hinode Dynamics in Sunspot Light Bridges and Magnetic Reconnection Processes*. Astrophys Space Sci Proc. **33**, 23–28 (2012)
DOI 10.1007/978-3-642-30442-2_3, © Springer-Verlag Berlin Heidelberg 2012

the separator (guide field) that actually reconnects. This type of reconnection is sometimes referred to as *component reconnection* or *component merging* [15].

2 Chromospheric Dynamics in Sunspot Light Bridges

Light bridges are one of the fundamental magnetic structures in sunspots, which separates dark umbra into two portions. The umbral fields at both sides of light bridges have the same magnetic polarity. Magnetic fields in light bridges have lower field strength and are sparser and more horizontal than in the neighboring umbrae [9]. Recent observations have revealed that some types of light bridges are accompanied by remarkable long-lasting plasma ejections or surge activities in the chromosphere [1]. Moreover, a constant brightness enhancement may be observed over light bridges in chromospheric images [2].

2.1 Magnetic Field Configuration Revealed with Hinode

Hinode SOT observations have for the first time provided high-resolution chromospheric movies of light bridges with precise measurements of magnetic field vectors at the photospheric level [13]. The chromospheric movie shows chromospheric plasma ejections intermittently and recurrently for a fairly long duration (more than 1 day in case of the light bridge in the well-developed large sunspot of active region NOAA 10953 on April 30, 2007). The field vector measurement revealed obliquely oriented magnetic fields with vertical electric current density higher than 100 mA m^{-2} along the light bridge (Fig. 1), suggesting that current-carrying highly twisted magnetic flux tubes are trapped below a cusp-shaped magnetic structure along the light bridge (Fig. 2). The presence of trapped current-carrying flux tubes is essential for causing long-lasting chromospheric plasma ejections at the interface with pre-existing vertically oriented umbral fields. A bidirectional jet was clearly detected [13], suggesting magnetic reconnections occurring at very low altitudes, i.e., upper photosphere and lower chromosphere.

Chromospheric plasma ejections are observed for a fairly long duration in a light bridge, but it is a part of the entire life of the light bridge. We tracked how magnetic and dynamical properties change with time for the entire life (3.5 days) [14]. The most significant change was observed in morphology; Photospheric G-band intensity features morphologically changed from cellular or patchy to filamentary, and ejections were dominantly observed in the period when cellular or patchy features were dominantly observed. Note that there were only small changes in the magnetic flux density and inclination at the photospheric level, when the morphology changed from cellular or patchy to filamentary (1,000–1,200 G vs. 1,500–1,600 G and 130–140° vs. 110–120°). This observation demonstrates that

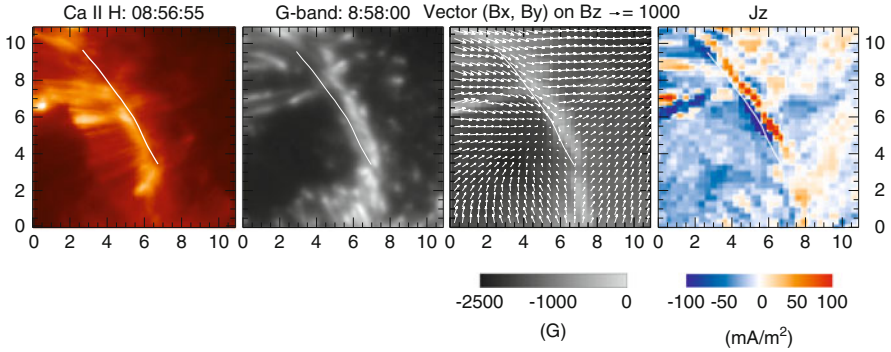

Fig. 1 Observations of photospheric magnetic fields at a sunspot light bridge, which was accompanied by long-lasting chromospheric plasma ejections. From the *left*, chromospheric Ca II H intensity, photospheric G-band intensity, magnetic field vectors, and vertical electrical current density. The field of view is 11 × 11 arcsec (Adapted from [13])

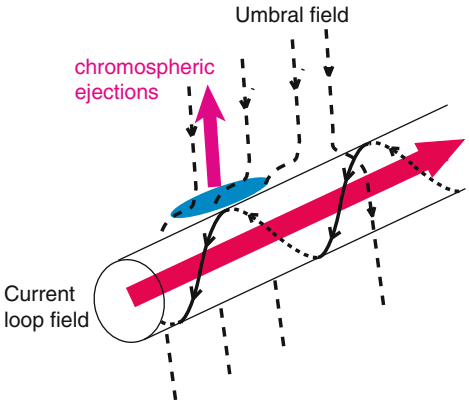

Fig. 2 Magnetic field configuration of a sunspot light bridge inferred from *Hinode* observations. A current-carrying helical magnetic flux tube is trapped below a cusp-shaped vertically oriented umbral field

chromospheric activity is related to the change of morphology in the photosphere. Chromospheric activity may be controlled mainly by dynamical properties at the photosphere where the plasma β is high.

2.2 *Supply of Twisted Magnetic Flux to Light Bridges*

One of questions is why plasma ejections are intermittently continued for a long duration in light bridges. Observations have suggested twisted magnetic flux is trapped along light bridges. With the magnetic field strength and dimension [14], the

magnetic energy involved in the trapped flux is in order of 10^{29} ergs. The pitch angle of the magnetic field lines in the twisted flux tube is 0.2–0.9 for the full 8 arcsec length of the light bridge [13]. As suggested in Fig. 2, only a part of the trapped field which is anti-parallel to the ambient umbral field is an energy source of explosions for producing plasma ejections. Thus, the magnetic energy available for producing plasma ejections may be slightly smaller than 10^{29} ergs. On the other hand, the kinetic energy of each plasma ejection is roughly estimated to be 6×10^{26} ergs on average, with observed upward speed (100 km s^{-1} on average) and the volume (width and length of 1 arcsec) with an assumption of gas density (10^{14} cm^{-3}, a value at low chromosphere). This means only about 200 ejections can be produced with the magnetic energy involved in the light bridge. Since much more than ejections were observed in this light bridge, it should be required to supply the magnetic energy to the light bridge.

We have not yet understood how helical twisted flux tubes are created along light bridges. During light bridge formation, a lot of umbral dots are emerged along the area where a light bridge will be formed, and the light bridge structure rapidly intrudes from the leading edge of penumbral filaments into the umbra [6]. The highly inclined twisted fields in light bridges may be emerged from below the photosphere. As a possibility, a mechanism for creating twisted flux might be formed below the photosphere and a portion of sunspot umbral fields below the photosphere may be used for creating twisted fields along the light bridge. Otherwise, unknown mechanism at the surface may add twist to trapped fields.

2.3 Suggestion from Reconnection at Dayside Magnetopause

Three dimensional nature of magnetic fields has been measured in magnetosphere observations, which may give theoretical ideas to the interpretation of dynamical phenomena in the Sun. One remarkable example is flux transfer events (FTE) [10], which changed concept of the dayside magnetopause reconnection from the traditional two-dimensional configuration to a specific three-dimensional one. Magnetic field measurements in the vicinity of the magnetopause near local noon on a typical pass when the magnetosheath field is southward clearly show evidence for patchy impulsive reconnection. The magnetic field lines in a number of FTE flux tubes have been found to be helical.

One of theoretical models for FTE, called multiple x-line FTE model, suggested that FTEs can result from a tearing instability or simultaneous formation of multiple x-lines in the dayside magnetopause current layer [8]. The reconnected field lines in the multiple x-line reconnection are inherently helical when the y-component of the interplanetary magnetic field is non-zero. Note that recent THEMIS spacecraft observations show that an FTE was generated by multiple x-line reconnection [3].

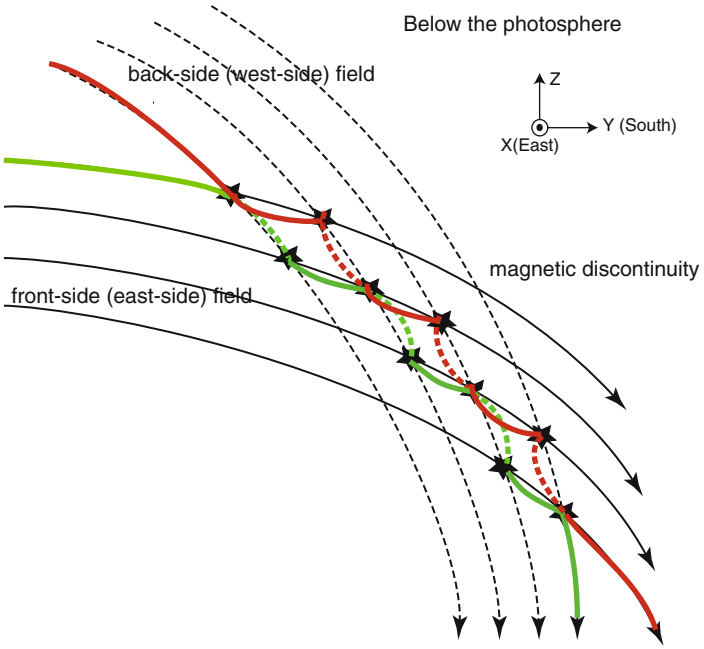

Fig. 3 Field discontinuity formed between differently inclined fields along the light bridge. Reconnection along multiple X-lines creates the helical twisted field lines, which may appear along the light bridge

2.4 A Scenario for Continuous Supply of Twisted Flux Tubes

The multiple x-line model can give a hint on the formation of helical twisted magnetic flux appearing along sunspot light bridges. The current density map in Fig. 1 tells that the umbra at the east-side of the light bridge is more twisted globally than the umbra at the west-side. Two umbral flux tubes separated by the light bridge may be tilted differently, forming a field discontinuity below the photosphere (Fig. 3). If reconnection takes place at multiple positions in the discontinuity, the reconnected field lines are helically twisted. Note that Fig. 3 shows reconnected field lines when reconnection takes place along two X-lines. Twisted flux is emerged toward the photosphere, maybe due to magnetic tension and buoyancy. This process can continuously supply twisted and horizontally oriented flux to the light bridge.

Acknowledgements Hinode is a Japanese mission developed and launched by ISAS/JAXA, with NAOJ as domestic partner and NASA and STFC (UK) as international partners. It is operated by these agencies in co-operation with ESA and NSC (Norway). This work was partially supported by KAKENHI 23540278 and the JSPS Core-to-Core Program 22001.

References

1. Asai, A., Ishii, T.T., & Kurokawa, H. 2001, ApJ, 555, L65
2. Berger, T.E. & Berdyugina, S.V. 2003, ApJ, 589, L117
3. Hasegawa, H. et al. 2010, Geophys. Res. Lett., 37, L16101
4. Ichimoto, K. et al. 2008, Solar Physics, 249, 233
5. Katsukawa, Y. et al. 2007, Science, 318, 1594
6. Katsukawa, Y. et al. 2007, PASJ, 59, S577
7. Kosugi, T. et al. 2007, Sol. Phys., 243, 3
8. Lee, L.C. & Fu, Z. 1985, Geophys. Res. Lett., 12, 105
9. Leka, K.D. 1997, ApJ, 484, 900
10. Russel, C.T. & Elphic, R.C. 1979, Geophys. Res. Lett., 6, 1
11. Shibata, K. et al. 2007, Science, 318, 1591
12. Shimizu, T. et al. 2008, Solar Physics, 249, 221
13. Shimizu, T. et al. 2009, ApJ, 696, L66
14. Shimizu, T. 2011, ApJ, 738, 83
15. Sonnerup, B.U.Ö. et al. 1981, J. Geophys. Res., 86, 10049
16. Suematsu, Y. et al. 2008, Solar Physics, 249, 197
17. Tsuneta, S. et al. 2008, Solar Physics, 249, 167

Signatures of Magnetic Reconnection in Solar Eruptive Flares: A Multi-wavelength Perspective

Bhuwan Joshi, Astrid Veronig, P.K. Manoharan, and Boris V. Somov

Abstract In this article, we review some key aspects of a multi-wavelength flare which have essentially contributed to form a standard flare model based on the magnetic reconnection. The emphasis is given on the recent observations taken by the Reuven Ramaty High Energy Solar Spectroscopic Imager (RHESSI) on the X-ray emission originating from different regions of the coronal loops. We also briefly summarize those observations which do not seem to accommodate within the canonical flare picture and discuss the challenges for future investigations.

1 Introduction

Solar flares are the most striking explosive form of solar activity. A flare is characterized by a sudden catastrophic release of energy in the solar atmosphere. In tens of minutes energy in excess of 10^{32} erg is released. Mostly flares occur in solar active regions; being more frequent at the locations where the active region is

B. Joshi (✉)
Udaipur Solar Observatory, Physical Research Laboratory, Udaipur 313 004, Rajasthan, India
e-mail: bhuwan@prl.res.in

A. Veronig
IGAM/Institute of Physics, University of Graz, Universitätsplatz 5, A-8010 Graz, Austria
e-mail: astrid.veronig@uni-graz.at

P.K. Manoharan
Radio Astronomy Centre, Tata Institute of Fundamental Research, Udhagamandalam (Ooty) 643 001, Tamil Nadu, India
e-mail: mano@ncra.tifr.res.in

B.V. Somov
Astronomical Institute, Moscow State University, Universitetskij Prospekt 13, Moscow 119992, Russia
e-mail: somov@sai.msu.ru

Joshi, B. et al.: *Signatures of Magnetic Reconnection in Solar Eruptive Flares: A Multi-wavelength Perspective*. Astrophys Space Sci Proc. **33**, 29–41 (2012)
DOI 10.1007/978-3-642-30442-2_4, © Springer-Verlag Berlin Heidelberg 2012

rapidly evolving [17]. The frequency and intensity of solar flare occurrence follow the 11-year sunspot cycle [25, 26].

Flares manifest their signatures in a wide range of electromagnetic spectrum, from radio to γ-rays, and involve substantial mass motions and particle acceleration. Emission in these wavelengths originates from the atmospheric layers of the Sun extending from the chromosphere to the corona. In general, flares are not visible in the photosphere except in some exceptionally high energy and impulsive events known as white light flares. Now it is well known that the energy released during flares is stored in the corona prior to the event in the form of stressed or non-potential magnetic fields. Magnetic reconnection has been recognized as the fundamental process responsible for the changes in the topology of magnetic fields, as well as the rapid conversion of stored magnetic energy into heat and kinetic energy of plasma and particles during a flare.

In Sect. 2, we provide an observational overview of solar flares and discuss some key aspects of flare development which form the basis for the standard flare model. With high resolution observations at temporal and spectral domains, now we have a clearer view on these multi-wavelength flare components. Recent observations, mainly inspired by Reuven Ramaty High Energy Solar Spectroscopic Imager (RHESSI) [38], have further revealed many new multi-wavelength aspects of flare emission which have changed our "standard" understanding on flares. These new results are summarized in Sect. 3.

2 Overview of Multi-wavelength Phenomena

2.1 Confined and Eruptive Flares

The very early observations of solar flares in soft X-ray (SXR) wavelengths from the *Skylab* mission in 1973–1974 established two morphologically distinct classes of flares: confined and eruptive events [53]. The confined flares show brightening in compact loop structures with little large-scale motion. They are generally modeled in terms of energy release within a single static magnetic loop and are thus referred to as single-loop, compact or point flares. The second category comprises the long duration events (LDE) which are eruptive in nature. They are accompanied by an arcade of loops and show more strong association with coronal mass ejections (CMEs). It is worth to mention that the temporal evolution of CME and flare signatures in eruptive events suggests that both phenomena have a strongly coupled relationship but not a cause-effect one [82]. The Hα observations reveal that eruptive events are almost always associated with chromospheric brightenings in the form of long, bright parallel ribbons. Therefore, LDE flares are also referred to as two-ribbon flares. This two-element classification of solar flares is also broadly reflected in the X-ray observations of stellar flares [54, 55].

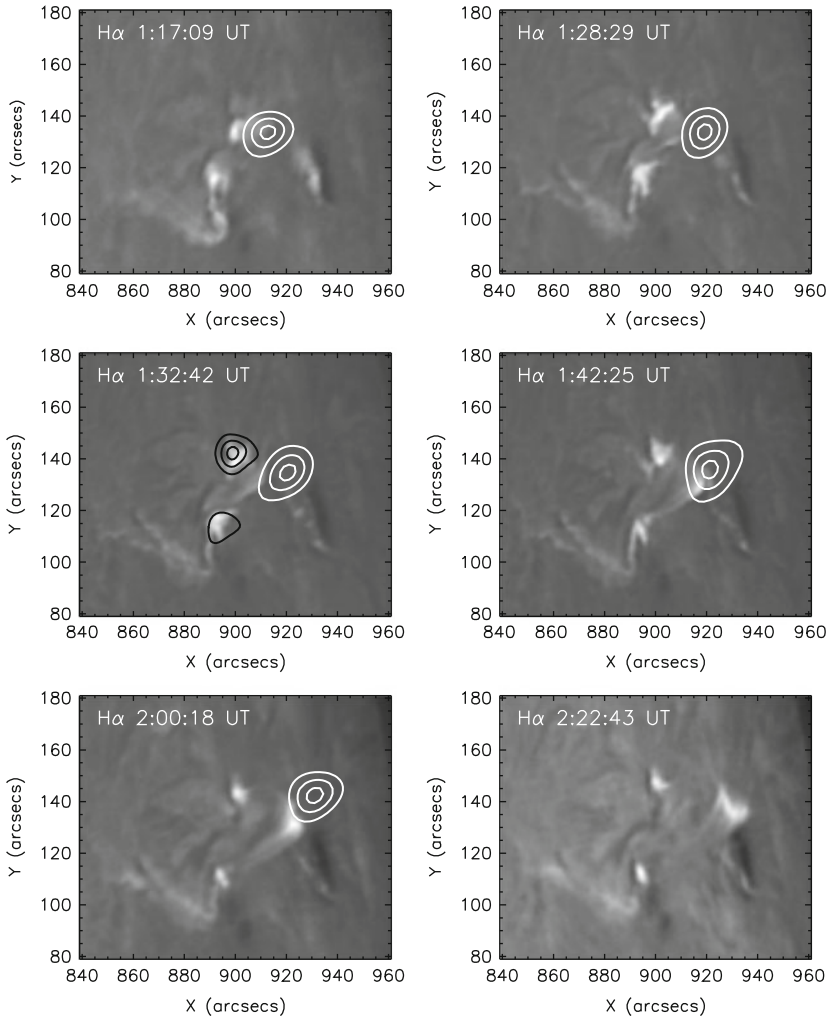

Fig. 1 Time evolution of a large eruptive flare of 2B/X2.7 class that occurred in active region NOAA 10488 on November 3, 2003 at a location N10W83, i.e., close to the west limb of the sun. The Hα filtergrams, observed from ARIES Solar Tower Telescope, are overlayed by RHESSI X-ray images at 10–15 keV (*white contours*) and 50–100 keV (*black contours*; only in the third panel) (Figure adopted from [24])

2.2 Time Evolution of an Eruptive Flare

A solar flare is a multi-wavelength phenomenon. Therefore in order to have a complete understanding of its temporal evolution we need to look at the time profiles observed at different wavelengths. The time evolution of flare emission is schematically presented in Fig. 1. However, it has been observed that there could be

subtle activities at the flare location before its onset. In the following, we discuss different aspects of flare evolution.

2.2.1 Pre-flare Activity and Precursor Phase

The pre-flare activity refers to the very earliest stage of flare which is elusive to recognize even in SXRs [28]. The activities in this initiation phase can be seen at longer wavelength such as Hα, ultraviolet (UV), and extreme ultraviolet (EUV). The observations of subtle changes in the configuration of EUV loops and localized brightenings at this early phase can provide important clues about the triggering mechanism of the eruption [9, 28]. It has been suggested that the pre-flare brightening may occur as a result of slow magnetic reconnection and provide a trigger for the subsequent large-scale eruption [9, 49].

Many flares show slow and gradual enhancement in SXRs before the onset of the impulsive energy release, referred to as the X-ray precursor phase [70]. This early phase mainly corresponds to small-scale brightening in UV to SXR wavelengths [9, 28, 29]. The precursor flare brightening mostly occurs in the neighborhood of the main flare location [12]. However, usually precursor and main flare locations do not exactly coincide [13,80]. Some studies recognize the precursor phase brightenings as the evidence for distinct, localized instances of energy release which play a significant role in destabilizing the magnetic configuration of active region leading to eruption and large-scale magnetic reorganization [9, 28].

2.2.2 Impulsive Phase

The primary energy release takes place during the impulsive phase which lasts from tens of seconds to tens of minutes. This phase is marked by emission in hard X-rays (HXR), non-thermal microwaves and in some cases also γ-rays and white-light continuum, showing evidence of strong acceleration of both electrons and ions. These radiations are further supplemented by strong enhancement of emissions in chromospheric lines (e.g., Hα), ultraviolet and extreme ultraviolet. The impulsive phase is mainly characterized by the flare signatures at chromospheric layers where the feet of magnetic loops are rooted at both sides of the polarity inversion line. Morphologically, flare brightenings at this region are termed as "footpoints" or "ribbons" detected in HXRs and Hα observations, respectively. With the upward expansion of the arcade of loops, the two parallel flare ribbons (or HXR footpoints) separate from each other during the impulsive phase and later. The HXR emission from the footpoints of flaring loops is traditionally viewed in terms of the thick-target bremsstrahlung process in which the X-ray production at the footpoints of the loop system takes place when high-energy electrons, accelerated in the coronal reconnection region, come along the guiding magnetic field lines and penetrate the denser transition region and chromospheric layers [6, 69]. During very high

energetic events, the photospheric Doppler enhancements have been reported which are co-spatial with Hα flare ribbons [35, 74].

In the impulsive phase, the time evolution of the spectral index of the non-thermal part of the photon spectrum and non-thermal flux show an interesting pattern known as *soft-hard-soft* spectral evolution. The HXR spectra of flares often initially show a steep spectral slope (soft), which flattens at the peak of the flare (hard), and then becomes steeper again (soft) in the decay phase of the flare [4]. With RHESSI data, the soft-hard-soft spectral evolution has been determined with much better accuracy. RHESSI observations clearly recognize that the spectral *soft-hard-soft* behavior in rise-peak-decay phase is followed not only in overall flare development, but even more pronounced in sub-peaks [16]. This anti-correlation between spectral index and flux is generally interpreted as a signature of the acceleration process with each non-thermal peak representing a distinct acceleration event of the electrons in the flare [16, 28]. Although the *soft-hard-soft* spectral evolution is very common, it does not apply to all flares. Some flares also exhibit *soft-hard-harder* patterns in which the spectrum continues to become harder throughout the flare evolution [10, 30]. This pattern is more commonly seen in microwave spectra than in HXR observations [61]. This is mainly reported in gradual HXR events, in particular those which are associated with solar proton events [10, 30, 59]. The *soft-hard-harder* pattern is attributed to extended phases of acceleration in large flares. Some events of this class also exhibit the long-lived high energy coronal sources [33].

2.2.3 Gradual Phase

The gradual phase of a solar flare is best described by SXR time profile. During the impulsive onset of HXR emission (see Sect. 2.2.2), the SXR gradually builds up in strength and peaks a few minutes *after* the impulsive emission. This implies that the long-lived and gradual SXR emission is a delayed effect of the impulsive onset of HXR radiation. This phase is characterized by the formation of loops (and arcade of loops in large flares) which emit in SXRs and EUV, indicating the presence of hot plasma ($\sim$10–20 MK) inside them. The process of filling of hot plasma in coronal loops is termed as *chromospheric evaporation* [39, 47, 48, 51, 52, 78]. The chromospheric plasma is rapidly heated and compelled to spread out in the coronal loops primarily by the energy deposition of energetic electrons accelerated at the magnetic reconnection site in the corona [39, 78]. Thermal conduction from the corona may also play a role in heating the chromospheric plasma [1, 3, 81]. The flare loop system exhibits a gradient in temperature with outermost loops being the hottest [14].

The *Yohkoh/ SXT* observations detected cusp-shaped structure above the hottest outer loops in many LDE flares [14, 71, 72]. The soft X-ray arcades along with the cusp resemble the general geometry of large-scale magnetic reconnection [71]. In the later stages, as the loops begin to cool, the arcade becomes visible in lower temperature emissions such as EUV and Hα [14, 60, 73, 79]. Both conduction and

radiation may contribute to the cooling process which essentially depends on flare loop length and plasma parameters [2, 11]. Another important observational feature of gradual phase is the continual downflow of lower temperature plasma observed in Hα visible along the leg of arcade. This Hα downflow (also termed as 'coronal rain') is the result of draining of cool plasma due to gravity [5].

2.3 "Sigmoid-to-Arcade" Development

Sigmoids are S-shaped (or inverse S-shaped) coronal features, mainly identified in SXR images, in the form of a region of enhanced emission [7, 45, 58]. In a few studies, sigmoid structures have been reported in EUV [41, 42] and in one of the events even in HXRs [23]. They are often composed of two opposite J-like bundles of loops which collectively form an S-shape feature [7]. Sigmoid regions are considerably more likely to be eruptive than non-sigmoidal sites [15, 19]. With the onset of an eruptive flare, the region is enveloped by arcades or cusped loops (see Sect. 2.2.3). Thus the "sigmoid to arcade" development is suggestive of large-scale magnetic reconnection driven by the eruption [50, 64].

2.4 Standard Flare Model

The standard flare model, also known as CSHKP model, recognizes that the evolution of flare loops and ribbon can be understood as a consequence of the relaxation of magnetic field lines stretched by the ejection of plasma [8, 18, 31, 65]. The magnetic reconnection has been identified as the key process which releases sufficient magnetic energy on short time scales to account for the radiative and kinetic energies observed during an eruptive event [56]. In this picture, the rise of the loop system as well as the footpoint (or ribbon) separation reflect the upward movement of the magnetic reconnection site during which field lines, rooted successively apart from the magnetic inversion line, reconnect. This picture successfully explains the apparent motions of flare loops and ribbons along with the multi-wavelength view of the loop system with the hottest one located at the outermost region.

The discovery of the HXR source located *above* the soft X-ray flare loops (known as "above-the-looptop" source) by *Yohkoh* was an important landmark in the history of solar flare observations [46]. This new kind of HXR emission raised great interest as it is believed to occur closest to the particle acceleration region associated with the magnetic reconnection site. Essentially the *Yohkoh* discoveries of the HXR above-the-looptop source along with the SXR cusp (see Sect. 2.2.3) confirmed the role of magnetic reconnection in the standard flare model. Here it is worth mentioning that the above-the-looptop source is still a rarely observed feature [20]. However, due to high sensitivity and broad energy coverage of RHESSI, the HXR emission

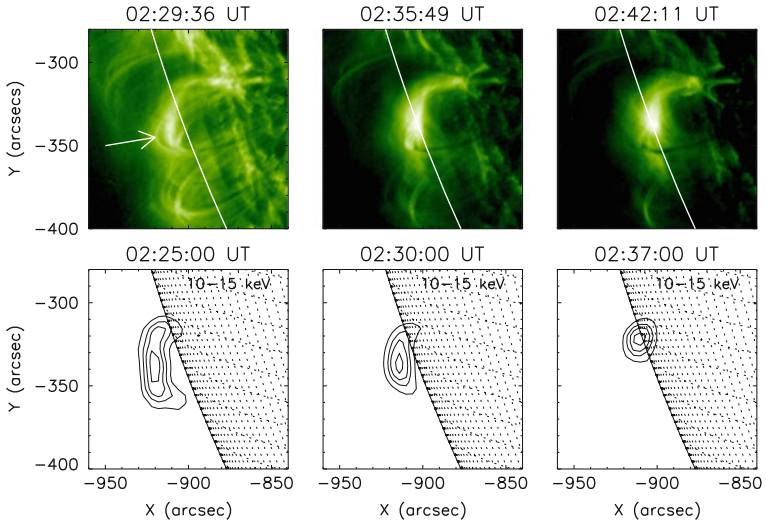

Fig. 2 Large scale contraction of coronal loops observed for ∼11 min in an M7.6 flare that occurred in active region NOAA 10486 on October 24, 2003 at a location S19E72 [27]. The contraction of coronal loops can be readily seen in TRACE EUV images at 195 Å (*top panels*) and RHESSI X-ray images at 10–15 keV (*bottom panels*)

from the looptop has now become a well known phenomenon and coronal HXR sources are detected in all phases of solar flares [32, 34]. In a few events, coronal HXR sources are even observed before flare impulsive phase [40, 77]. RHESSI observations have also identified a new class of coronal sources that show strong looptop HXR emission without significant footpoint emissions [28, 75, 76].

3 Beyond the "Standard" Observations

3.1 Contraction of Coronal Loops

RHESSI observations have discovered that during the early impulsive phase of the flare, coronal loop system undergoes an altitude decrease or contraction before showing the "standard" behavior of apparent outward expansion. This phenomenon of loop contraction or shrinkage, first reported in an M1.2 class flare on April 15, 2002 [66], has now been confirmed in several events of different classes [24, 57, 67, 77]. Motivated by these RHESSI findings, the loop contraction was examined in other wavelength images and similar kind of descending loop motion was detected in EUV [27, 37, 43] and microwave images [36]. The study of an M7.6 class flare on October 24, 2003: (Fig. 2) is perhaps the best example of the loop contraction which

was observed for ∼11 min and identified in HXRs (up to ∼25–50 keV) and EUV images [27]. Some observations also apparently imply that the contraction motion of flaring loops may be the result of the relaxation of the sheared magnetic field [21].

3.2 Converging Motion of Footpoints

In some events, the converging motion of footpoint sources (i.e., decrease in footpoint separation) has been observed at the early stage which temporally matches with the phase of contraction of coronal loops [21,22,27,28]. A detailed analysis of footpoint motions was carried out for X10 class flare on October 29, 2003 [44]. In this study it was found that the two conjugate footpoints first move toward and then away from each other, mainly parallel and perpendicular to the magnetic inversion line, respectively. Further the transition of these two phases of footpoint motions coincides with the direction reversal of the motion of the looptop source. An interpretation of this new kind of motions of looptop and footpoint sources is proposed in terms of *rainbow reconnection model* [62] which essentially builds on the idea of three-dimensional magnetic reconnection at a magnetic separator in the corona during the phase of *shear relaxation* of coronal loops [27,63].

3.3 Double Coronal Sources

The RHESSI observations of three homologous flares that occurred between April 14–16, 2002 revealed the appearance of a coronal X-ray source besides the X-ray looptop emission [66, 67] which was formed at higher altitudes. Out of these, one event clearly shows a cusp-shaped flare loop in the rise phase [66, 68]. When the impulsive rise in HXRs (>25 keV) began, the cusp part of the coronal source separated from the underlying flare loop, forming two HXR emitting sources. The two sources exhibit energy dependent structures with the emissions at higher energies coming from the inner regions between them. These observations have been interpreted as evidence for the formation of a current sheet between top of the flare loops and the second coronal source located above the flare loop top [66, 68]. The imaging spectroscopy of the two coronal sources was conducted for an M-class flare occurred on April 30, 2002 [44]. In this event, the HXR footpoints were occulted by the limb thus making conditions favorable for the imaging of relatively faint coronal sources. The parameters derived from X-ray spectroscopy of the two sources reveal that the magnetic reconnection site lies between the top of the flare loops and the second coronal source. The formation of double coronal sources, one at each side of the reconnection site, has been viewed in the framework of the stochastic acceleration model [44].

4 Summary

The multi-wavelength observations have immensely improved our understanding of various physical processes occurring in different atmospheric layers of the Sun during a solar flare. The standard flare model has been successful in broadly recognizing these physical processes as the consequence of large-scale magnetic reconnection in the corona. However, the advancement in the observational capabilities has also led to several new aspects of the flare evolution that deviate from the standard flare model. Although flares have been observed over the past 150 years, but still our understanding about them is incomplete. We have yet to understand several basic elements pertaining to pre-flare magnetic configuration, triggering mechanism, energy release site (e.g., current sheet dimensions), conversion of magnetic energy into heat and kinetic energy, particle acceleration, etc. These outstanding issues pose challenges for future investigations.

Acknowledgements This activity has been supported by the European Community Framework Programme 7, 'High Energy Solar Physics Data in Europe (HESPE)', grant agreement no.: 263086. We thank Dr. Brajesh Kumar and Dr. Anand Joshi for carefully going through the manuscript. Thanks are also due to an anonymous referee for helpful suggestions.

References

1. S. K. Antiochos and P. A. Sturrock. Evaporative cooling of flare plasma. *Astrophys. J.*, 220:1137–1143, March 1978.
2. M. J. Aschwanden and D. Alexander. Flare Plasma Cooling from 30 MK down to 1 MK modeled from Yohkoh, GOES, and TRACE observations during the Bastille Day Event (14 July 2000). *Solar Phys.*, 204:91–120, December 2001.
3. M. Battaglia, L. Fletcher, and A. O. Benz. Observations of conduction driven evaporation in the early rise phase of solar flares. *Astron. Astrophys.*, 498:891–900, May 2009.
4. A. O. Benz. Spectral features in solar hard X-ray and radio events and particle acceleration. *Astrophys. J.*, 211:270–280, January 1977.
5. J. W. Brosius. Chromospheric Evaporation and Warm Rain during a Solar Flare Observed in High Time Resolution with the Coronal Diagnostic Spectrometer aboard the Solar and Heliospheric Observatory. *Astrophys. J.*, 586:1417–1429, April 2003.
6. J. C. Brown. The Deduction of Energy Spectra of Non-Thermal Electrons in Flares from the Observed Dynamic Spectra of Hard X-Ray Bursts. *Solar Phys.*, 18:489–502, July 1971.
7. R. C. Canfield, M. D. Kazachenko, L. W. Acton, D. H. Mackay, J. Son, and T. L. Freeman. Yohkoh SXT Full-Resolution Observations of Sigmoids: Structure, Formation, and Eruption. *Astrophys. J.*, 671:L81–L84, December 2007.
8. H. Carmichael. A Process for Flares. *NASA Special Publication*, 50:451, 1964.
9. C. Chifor, D. Tripathi, H. E. Mason, and B. R. Dennis. X-ray precursors to flares and filament eruptions. *Astron. Astrophys.*, 472:967–979, September 2007.
10. E. W. Cliver, B. R. Dennis, A. L. Kiplinger, S. R. Kane, D. F. Neidig, N. R. Sheeley, Jr., and M. J. Koomen. Solar gradual hard X-ray bursts and associated phenomena. *Astrophys. J.*, 305:920–935, June 1986.
11. J. L. Culhane, J. F. Vesecky, and K. J. H. Phillips. The Cooling of Flare Produced Plasmas in the Solar Corona. *Solar Phys.*, 15:394–413, December 1970.

12. F. Fárník, H. Hudson, and T. Watanabe. Spatial Relations between Preflares and Flares. *Solar Phys.*, 165:169–179, April 1996.
13. F. Fárník and S. K. Savy. Soft X-Ray Pre-Flare Emission Studied in Yohkoh-SXT Images. *Solar Phys.*, 183:339–357, December 1998.
14. T. G. Forbes and L. W. Acton. Reconnection and Field Line Shrinkage in Solar Flares. *Astrophys. J.*, 459:330, March 1996.
15. A. Glover, N. D. R. Ranns, L. K. Harra, and J. L. Culhane. The Onset and Association of CMEs with Sigmoidal Active Regions. *Geophys. Res. Lett.*, 27:2161, July 2000.
16. P. C. Grigis and A. O. Benz. The spectral evolution of impulsive solar X-ray flares. *Astron. Astrophys.*, 426:1093–1101, November 2004.
17. M. J. Hagyard, D. Teuber, E. A. West, and J. B. Smith. A quantitative study relating observed shear in photospheric magnetic fields to repeated flaring. *Solar Phys.*, 91:115–126, March 1984.
18. T. Hirayama. Theoretical Model of Flares and Prominences. I: Evaporating Flare Model. *Solar Phys.*, 34:323–338, February 1974.
19. H. S. Hudson, J. R. Lemen, O. C. St. Cyr, A. C. Sterling, and D. F. Webb. X-ray coronal changes during halo CMEs. *Geophys. Res. Lett.*, 25:2481–2484, 1998.
20. S. Ishikawa, S. Krucker, T. Takahashi, and R. P. Lin. On the Relation of Above-the-loop and Footpoint Hard X-Ray Sources in Solar Flares. *Astrophys. J.*, 737:48, August 2011.
21. H. Ji, G. Huang, and H. Wang. The Relaxation of Sheared Magnetic Fields: A Contracting Process. *Astrophys. J.*, 660:893–900, May 2007.
22. H. Ji, G. Huang, H. Wang, T. Zhou, Y. Li, Y. Zhang, and M. Song. Converging Motion of Hα Conjugate Kernels: The Signature of Fast Relaxation of a Sheared Magnetic Field. *Astrophys. J.*, 636:L173–L174, January 2006.
23. H. Ji, H. Wang, C. Liu, and B. R. Dennis. A Hard X-Ray Sigmoidal Structure during the Initial Phase of the 2003 October 29 X10 Flare. *Astrophys. J.*, 680:734–739, June 2008.
24. B. Joshi, P. K. Manoharan, A. M. Veronig, P. Pant, and K. Pandey. Multi-Wavelength Signatures of Magnetic Reconnection of a Flare-Associated Coronal Mass Ejection. *Solar Phys.*, 242:143–158, May 2007.
25. B. Joshi and P. Pant. Distribution of Hα flares during solar cycle 23. *Astron. Astrophys.*, 431:359–363, February 2005.
26. B. Joshi, P. Pant, and P. K. Manoharan. North-South Distribution of Solar Flares during Cycle 23. *Journal of Astrophysics and Astronomy*, 27:151–157, September 2006.
27. B. Joshi, A. Veronig, K.-S. Cho, S.-C. Bong, B. V. Somov, Y.-J. Moon, J. Lee, P. K. Manoharan, and Y.-H. Kim. Magnetic Reconnection During the Two-phase Evolution of a Solar Eruptive Flare. *Astrophys. J.*, 706:1438–1450, December 2009.
28. B. Joshi, A. M. Veronig, J. Lee, S.-C. Bong, S. K. Tiwari, and K.-S. Cho. Pre-flare Activity and Magnetic Reconnection during the Evolutionary Stages of Energy Release in a Solar Eruptive Flare. *Astrophys. J.*, 743:195, December 2011.
29. S. Kim, Y.-J. Moon, Y.-H. Kim, Y.-D. Park, K.-S. Kim, G. S. Choe, and K.-H. Kim. Preflare Eruption Triggered by a Tether-cutting Process. *Astrophys. J.*, 683:510–515, August 2008.
30. A. L. Kiplinger. Comparative Studies of Hard X-Ray Spectral Evolution in Solar Flares with High-Energy Proton Events Observed at Earth. *Astrophys. J.*, 453:973, November 1995.
31. R. A. Kopp and G. W. Pneuman. Magnetic reconnection in the corona and the loop prominence phenomenon. *Solar Phys.*, 50:85–98, October 1976.
32. S. Krucker, M. Battaglia, P. J. Cargill, L. Fletcher, H. S. Hudson, A. L. MacKinnon, S. Masuda, L. Sui, M. Tomczak, A. L. Veronig, L. Vlahos, and S. M. White. Hard X-ray emission from the solar corona. *A&A Rev.*, 16:155–208, October 2008.
33. S. Krucker, G. J. Hurford, A. L. MacKinnon, A. Y. Shih, and R. P. Lin. Coronal γ-Ray Bremsstrahlung from Solar Flare-accelerated Electrons. *Astrophys. J.*, 678:L63–L66, May 2008.
34. S. Krucker and R. P. Lin. Hard X-Ray Emissions from Partially Occulted Solar Flares. *Astrophys. J.*, 673:1181–1187, February 2008.

35. B. Kumar and B. Ravindra. Analysis of Enhanced Velocity Signals Observed during Solar Flares. *Journal of Astrophysics and Astronomy*, 27:425–438, December 2006.
36. Y. P. Li and W. Q. Gan. The Shrinkage of Flare Radio Loops. *Astrophys. J.*, 629:L137–L139, August 2005.
37. Y. P. Li and W. Q. Gan. The Oscillatory Shrinkage in TRACE 195 Å Loops during a Flare Impulsive Phase. *Astrophys. J.*, 644:L97–L100, June 2006.
38. R. P. Lin, B. R. Dennis, and G. J. Hurford et al. The Reuven Ramaty High-Energy Solar Spectroscopic Imager (RHESSI). *Solar Phys.*, 210:3–32, November 2002.
39. R. P. Lin and H. S. Hudson. Non-thermal processes in large solar flares. *Solar Phys.*, 50:153–178, October 1976.
40. R. P. Lin, S. Krucker, G. J. Hurford, D. M. Smith, H. S. Hudson, G. D. Holman, R. A. Schwartz, B. R. Dennis, G. H. Share, R. J. Murphy, A. G. Emslie, C. Johns-Krull, and N. Vilmer. RHESSI Observations of Particle Acceleration and Energy Release in an Intense Solar Gamma-Ray Line Flare. *Astrophys. J.*, 595:L69–L76, October 2003.
41. C. Liu, J. Lee, V. Yurchyshyn, N. Deng, K.-S. Cho, M. Karlický, and H. Wang. The Eruption from a Sigmoidal Solar Active Region on 2005 May 13. *Astrophys. J.*, 669:1372–1381, November 2007.
42. R. Liu, C. Liu, S. Wang, N. Deng, and H. Wang. Sigmoid-to-flux-rope Transition Leading to a Loop-like Coronal Mass Ejection. *Astrophys. J.*, 725:L84–L90, December 2010.
43. R. Liu, H. Wang, and D. Alexander. Implosion in a Coronal Eruption. *Astrophys. J.*, 696:121–135, May 2009.
44. W. Liu, V. Petrosian, B. R. Dennis, and Y. W. Jiang. Double Coronal Hard and Soft X-Ray Source Observed by RHESSI: Evidence for Magnetic Reconnection and Particle Acceleration in Solar Flares. *Astrophys. J.*, 676:704–716, March 2008.
45. P. K. Manoharan, L. van Driel-Gesztelyi, M. Pick, and P. Demoulin. Evidence for Large-Scale Solar Magnetic Reconnection from Radio and X-Ray Measurements. *Astrophys. J.*, 468:L73, September 1996.
46. S. Masuda, T. Kosugi, H. Hara, S. Tsuneta, and Y. Ogawara. A loop-top hard X-ray source in a compact solar flare as evidence for magnetic reconnection. *Nature*, 371:495–497, October 1994.
47. R. O. Milligan, P. T. Gallagher, M. Mathioudakis, D. S. Bloomfield, F. P. Keenan, and R. A. Schwartz. RHESSI and SOHO CDS Observations of Explosive Chromospheric Evaporation. *Astrophys. J.*, 638:L117–L120, February 2006.
48. R. O. Milligan, P. T. Gallagher, M. Mathioudakis, and F. P. Keenan. Observational Evidence of Gentle Chromospheric Evaporation during the Impulsive Phase of a Solar Flare. *Astrophys. J.*, 642:L169–L171, May 2006.
49. R. L. Moore and G. Roumeliotis. Triggering of Eruptive Flares - Destabilization of the Preflare Magnetic Field Configuration. In Z. Svestka, B. V. Jackson, & M. E. Machado, editor, *IAU Colloq. 133: Eruptive Solar Flares*, volume 399 of *Lecture Notes in Physics, Berlin Springer Verlag*, page 69, 1992.
50. R. L. Moore, A. C. Sterling, H. S. Hudson, and J. R. Lemen. Onset of the Magnetic Explosion in Solar Flares and Coronal Mass Ejections. *Astrophys. J.*, 552:833–848, May 2001.
51. W. M. Neupert. Comparison of Solar X-Ray Line Emission with Microwave Emission during Flares. *Astrophys. J.*, 153:L59, July 1968.
52. S. Nitta, S. Imada, and T. T. Yamamoto. Clear Detection of Chromospheric Evaporation Upflows with High Spatial/Temporal Resolution by Hinode XRT. *Solar Phys.*, page 398, November 2011.
53. R. Pallavicini, S. Serio, and G. S. Vaiana. A survey of soft X-ray limb flare images - The relation between their structure in the corona and other physical parameters. *Astrophys. J.*, 216:108–122, August 1977.
54. R. Pallavicini, G. Tagliaferri, and L. Stella. X-ray emission from solar neighbourhood flare stars - A comprehensive survey of EXOSAT results. *Astron. Astrophys.*, 228:403–425, February 1990.

55. J. C. Pandey and K. P. Singh. A study of X-ray flares - II. RS CVn-type binaries. *Mon. Not. R. Astron. Soc.*, 419:1219–1237, January 2012.
56. E. R. Priest and T. G. Forbes. The magnetic nature of solar flares. *A&A Rev.*, 10:313–377, 2002.
57. V. E. Reznikova, V. F. Melnikov, H. Ji, and K. Shibasaki. Dynamics of the Flaring Loop System of 2005 August 22 Observed in Microwaves and Hard X-rays. *Astrophys. J.*, 724:171–181, November 2010.
58. D. M. Rust and A. Kumar. Evidence for Helically Kinked Magnetic Flux Ropes in Solar Eruptions. *Astrophys. J.*, 464:L199, June 1996.
59. R. Saldanha, S. Krucker, and R. P. Lin. Hard X-ray Spectral Evolution and Production of Solar Energetic Particle Events during the January 2005 X-Class Flares. *Astrophys. J.*, 673:1169–1173, February 2008.
60. B. Schmieder, P. Heinzel, J. E. Wiik, J. Lemen, B. Anwar, P. Kotrc, and E. Hiei. Relation between cool and hot post-flare loops of 26 June 1992 derived from optical and X-ray (SXT-Yohkoh) observations. *Solar Phys.*, 156:337–361, February 1995.
61. A. V. R. Silva, H. Wang, and D. E. Gary. Correlation of Microwave and Hard X-Ray Spectral Parameters. *Astrophys. J.*, 545:1116–1123, December 2000.
62. B. V. Somov. Non-neutral current sheets and solar flare energetics. *Astron. Astrophys.*, 163:210–218, July 1986.
63. B. V. Somov. Interpretation of the observed motions of hard X-ray sources in solar flares. *Astronomy Letters*, 36:514–519, July 2010.
64. A. C. Sterling, H. S. Hudson, B. J. Thompson, and D. M. Zarro. Yohkoh SXT and SOHO EIT Observations of Sigmoid-to-Arcade Evolution of Structures Associated with Halo Coronal Mass Ejections. *Astrophys. J.*, 532:628–647, March 2000.
65. P. A. Sturrock. Model of the High-Energy Phase of Solar Flares. *Nature*, 211:695–697, August 1966.
66. L. Sui and G. D. Holman. Evidence for the Formation of a Large-Scale Current Sheet in a Solar Flare. *Astrophys. J.*, 596:L251–L254, October 2003.
67. L. Sui, G. D. Holman, and B. R. Dennis. Evidence for Magnetic Reconnection in Three Homologous Solar Flares Observed by RHESSI. *Astrophys. J.*, 612:546–556, September 2004.
68. L. Sui, G. D. Holman, S. M. White, and J. Zhang. Multiwavelength Analysis of a Solar Flare on 2002 April 15. *Astrophys. J.*, 633:1175–1186, November 2005.
69. S. I. Syrovatskii and O. P. Shmeleva. Heating of Plasma by High-Energy Electrons, and Nonthermal X-Ray Emission in Solar Flares. *Soviet Astron.*, 16:273–282, September 1972.
70. S. J. Tappin. Do all solar flares have X-ray precursors? *A&AS*, 87:277–302, February 1991.
71. S. Tsuneta. Structure and Dynamics of Magnetic Reconnection in a Solar Flare. *Astrophys. J.*, 456:840, January 1996.
72. S. Tsuneta, H. Hara, T. Shimizu, L. W. Acton, K. T. Strong, H. S. Hudson, and Y. Ogawara. Observation of a solar flare at the limb with the YOHKOH Soft X-ray Telescope. *PASJ*, 44:L63–L69, October 1992.
73. W. Uddin, B. Joshi, R. Chandra, and A. Joshi. Dynamics of Limb Flare and Associated Primary and Secondary Post Flare Loops. *Bulletin of the Astronomical Society of India*, 31:303–308, March 2003.
74. P. Venkatakrishnan, B. Kumar, and W. Uddin. Co-spatial evolution of photospheric Doppler enhancements and Hα flare ribbons observed during the solar flare of 2003 October 28. *Mon. Not. R. Astron. Soc.*, 387:L69–L73, June 2008.
75. A. M. Veronig and J. C. Brown. A Coronal Thick-Target Interpretation of Two Hard X-Ray Loop Events. *Astrophys. J.*, 603:L117–L120, March 2004.
76. A. M. Veronig, J. C. Brown, and L. Bone. Evidence for a solar coronal thick-target hard X-ray source observed by RHESSI. *Advances in Space Research*, 35:1683–1689, 2005.
77. A. M. Veronig, M. Karlický, B. Vršnak, M. Temmer, J. Magdalenić, B. R. Dennis, W. Otruba, and W. Pötzi. X-ray sources and magnetic reconnection in the X3.9 flare of 2003 November 3. *Astron. Astrophys.*, 446:675–690, February 2006.
78. A. M. Veronig, J. Rybák, P. Gömöry, S. Berkebile-Stoiser, M. Temmer, W. Otruba, B. Vršnak, W. Pötzi, and D. Baumgartner. Multiwavelength Imaging and Spectroscopy of Chromospheric Evaporation in an M-class Solar Flare. *Astrophys. J.*, 719:655–670, August 2010.

79. B. Vršnak, M. Temmer, A. Veronig, M. Karlický, and J. Lin. Shrinking and Cooling of Flare Loops in a Two-Ribbon Flare. *Solar Phys.*, 234:273–299, April 2006.
80. H. P. Warren and A. D. Warshall. Ultraviolet Flare Ribbon Brightenings and the Onset of Hard X-Ray Emission. *Astrophys. J.*, 560:L87–L90, October 2001.
81. D. M. Zarro and J. R. Lemen. Conduction-driven chromospheric evaporation in a solar flare. *Astrophys. J.*, 329:456–463, June 1988.
82. J. Zhang, K. P. Dere, R. A. Howard, M. R. Kundu, and S. M. White. On the Temporal Relationship between Coronal Mass Ejections and Flares. *Astrophys. J.*, 559:452–462, September 2001.

Energy Cascades in Large-Scale Solar Flare Reconnection

Miroslav Bárta, Jan Skála, Marian Karlický, and Jörg Büchner

Abstract Very fast energy release is sometimes observed in large-scale current layers formed in astrophysical plasmas. Solar flares represent a clear example. The dissipation and changes of the magnetic field topology in the almost collisionless plasmas are inherently related to plasma-kinetic processes in very thin current sheets (CSs). Question arises, how the originally thick current layer is efficiently fragmented into these small-scale dissipative CSs. We investigated this question by means of high-resolution MHD simulations. In addition to the earlier considered chain plasmoid instability we identified other elementary process for energy transport from large to small scales – fragmenting coalescence of plasmoids. This result changes so far basically 1D picture of energy cascade in a large scale magnetic reconnection and reveals multi-dimensional nature of the fragmentation process. At the same moment it shows that plasmoid coalescence contributes – quite surprisingly – to the direct energy cascade.

1 Introduction

Magnetic reconnection is accepted as the key mechanism for energy release in solar flares and other eruptive events in astrophysical plasmas. However, direct application of magnetic-reconnection theory to the physics of flares (and other

M. Bárta (✉) · M. Karlický
Astronomical Institute ASCR, CZ-25165 Ondřejov, Czechia
e-mail: barta@asu.cas.cz; karlicky@asu.cas.cz

J. Skála
Faculty of Science, UJEP, CZ-40096 Ústí nad Labem, Czechia
e-mail: jskala@physics.ujep.cz

J. Büchner
MPS Lindau, D-37191 Katlenburg-Lindau, Germany
e-mail: buechner@mps.mpg.de

Bárta, M. et al.: *Energy Cascades in Large-Scale Solar Flare Reconnection*.
Astrophys Space Sci Proc. **33**, 43–48 (2012)
DOI 10.1007/978-3-642-30442-2_5, © Springer-Verlag Berlin Heidelberg 2012

large-scale phenomena) faced a crucial issue for a long time: All known micro-physical processes leading to the change of magnetic field topology (i.e. the reconnection) require very thin current sheets ($\approx$1 m in the solar corona). On the other hand, the typical flare current-layer width estimated from observations [6] is about six orders of magnitude larger. This duality is reflected also in the flare observations which exhibit both coherent large-scale (10^7 m) dynamics and signatures of the micro-scale, chaotic energy release, at the same moment [1]. In order to overcome this huge scale-gap [9] suggested the concept of *fractal reconnection*. Nevertheless, this ad hoc suggested scheme had no support in the analytical theory of magnetic reconnection neither has been similar effects convincingly observed in numerical experiments, and thus this interesting approach was for a quite long time mostly ignored. However, quite recently [8] discovered missed solution in the Sweet-Parker's analysis of the current-sheet stability and they found that each CS with sufficiently high aspect ratio is linearly unstable to the formation of plasmoids (plasmoid instability). Later on, Uzdensky et al. [10] have developed analytical theory of the *chain plasmoid instability*, related closely to the original Shibata's and Tanuma's idea [9].

As the analytical theory has a limited scope we focus in our paper at the research of the anticipated tearing-mode cascade in fully non-linear regime using numerical simulations. At the same moment we are looking for other mechanisms of direct energy cascade (fragmentation/filamentation) in magnetic reconnection.

2 Model

We are interested in processes of filamentation of the originally thick current layer to smaller structures. The range of scales in which these processes should operate is still far from the scales where other terms of generalised Ohm's law (from which the largest is the Hall-scale) operate. The evolution of magnetized coronal plasma can be thus adequately described by a set of compressible resistive one-fluid MHD equations, including gravity. For details of the model used see [2]. The set of MHD equations is rewritten into its conservative form and numerically integrated. In order to see anticipated filamentation of the current density the AMR technique (see, e.g., [3]) is implemented into our numerical code. The mesh is refined whenever the CS typical width drops below certain number of grid cells. The initial state has been chosen in the form of a vertical generalized Harris-type CS with the magnetic field slightly decreasing with height – see [2] for details. Calculations are performed in a symmetric box with line-tying boundary condition (BC) at the bottom and free BCs otherwise. We assume translational symmetry in the current density direction (y) and presence of the guide field B_y in this direction. Anomalous resistivity η is switched-on whenever the current (measured by current-carrier velocity) intensifies above some threshold [2, 5]; $\eta = 0$ otherwise. The threshold for the resistivity

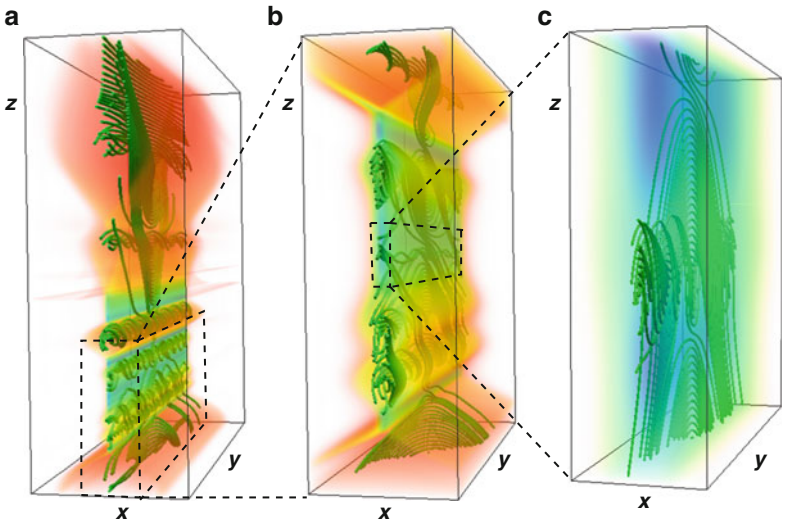

Fig. 1 Current density (color scale) and magnetic field structure at $t = 300\tau_A$. Increasing zoom reveals subsequently smaller plasmoids separated by correspondingly thinner CSs (tearing cascade)

onset leads to the minimum width of the CSs at the order of couple of cells at the highest resolution. As the ratio between the largest and smallest resolved scales in the simulation is $\approx 10^4$, the Lundquist number is of the order $\approx 10^8$. The model parameters used are the same as in [2].

3 Results

Results of our modelling are shown in Figs. 1 and 2. The figures display magnetic field structure on the background of the current density. Figure 1 shows the situation at $t = 300\tau_A$ (τ_A being the Alfvén transit time – see [2]). Subsequent zooms from panels (a) to (c) reveals smaller and smaller plasmoids formed by the tearing instability. The plasmoids are separated by consecutively thinner CSs. This picture is in line with the chain plasmoid instability [10]. Figure 2 shows formation of the CS between two *merging* larger plasmoids at $t = 365\tau_A$. As the CS become sufficiently long and thin, plasmoid instability takes place again and a new plasmoid is formed in this *transversal* CS. Situation is better visible in Fig. 2d which represents a projection of Fig. 2c into plane $y = 0$.

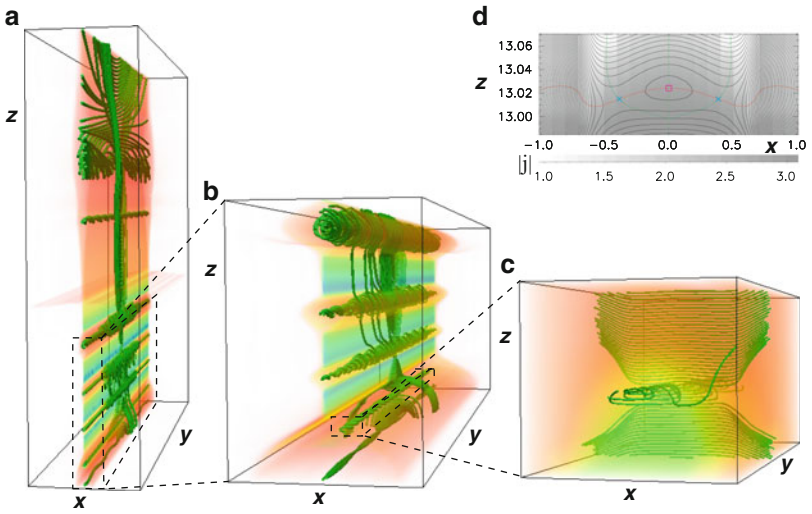

Fig. 2 Current density and magnetic field structure at $t = 365\tau_A$. Panels (**a**)–(**c**): Increasing zoom shows the micro-plasmoid formed in the CS between two merging larger plasmoids (fragmenting coalescence). Panel (**d**): 2D projection of panel (**c**) into plane $y = 0$. *Red* and *green lines* represent locations of $B_x = 0$ and $B_z = 0$, respectively, 'x' and 'o' symbols show locations of X- and O-type null lines. Note the anisotropic scales on x- and z-axis

4 Discussion and Conclusions

The huge gap between energy input and dissipation scales in large systems like solar-flare current layers represents a big challenge for application of magnetic-reconnection theory to energy release in such large-scale phenomena. The idea of fractal reconnection [9] that recently developed into theory of chain plasmoid instability [10] clearly addresses this issue. Nevertheless, its convincing confirmation by numerical experiments was not available until recently (e.g., [2, 7] and references therein). The reason why earlier numerical simulations met difficulties with finding this predicted process most likely lies in the limited resolution of previous experiments. Thanks to the AMR technique used in our simulation the domain of simulated scales spans over almost five decades. Such a wide scale-range enables investigation of the scaling law for the cascading process. In [2] the authors found for 1-D scaling of magnetic energy density along the CS the power-law $\mathscr{E}_M(k) \propto k^s$ with $s \approx -2.14$. Under some plausible assumptions it can be compared with the scaling found in analysis by Uzdensky et al. [10] for number of plasmoids of size L:

$$N(L) \propto L^{-2} . \tag{1}$$

Assuming (for simplicity) that the magnetic field strength is linearly increasing from the null-point in the center of the plasmoid towards its edge, where its reaches a typical value B_0

$$B(x) = B_0 \frac{x}{L} \tag{2}$$

we get for magnetic energy in a circular-shaped single plasmoid of size L

$$E_M^{SP}(L) = \int_{\text{plasmoid}} \frac{B^2(x)}{2\mu_o} \mathrm{d}V = \frac{1}{2\mu_o} \int_0^L B_0^2 \frac{x^2}{L^2} 2\pi x \mathrm{d}x = \frac{\pi}{4\mu_o} B_0^2 L^2 \,. \tag{3}$$

Since for magnetic energy at scale L holds

$$\mathrm{d}E_M(L) = E_M^{SP}(L) N(L) \mathrm{d}L = \mathscr{E}_M(k) \mathrm{d}k \,, \tag{4}$$

taking into account scaling law in Eq. (1) and applying relations between scale and corresponding wavenumber $k = \frac{2\pi}{L}$, $\mathrm{d}k = -\frac{2\pi}{L^2}\mathrm{d}L$, we finally arrive to power spectrum for magnetic energy density in the form

$$\mathscr{E}_M(k) \propto k^{-2} \,. \tag{5}$$

The scaling law for magnetic energy density is power-law, again, with the spectral index $s = -2$ quite close to that found in our simulated data ($s = -2.14$).

Moreover – and above all – our high-resolved simulations revealed the significance of the opposite process – the plasmoid coalescence – for further fragmentation of the current structures. We have found that the coalescence is accompanied by formation of intense, thin CSs between the merging plasmoids that may later become unstable to further plasmoid formation. Although the coalescence eventually leads to the formation of a single larger structure from the two smaller, this process is inherently connected with further fragmentation in the CS between the merging plasmoids. Consequently, also this process contributes – quite unexpectedly – to the energy transport towards small scales (direct cascade). Since these CSs are transversal to the original large-scale current layer the simulation reveals truly 2D nature of the turbulent cascade towards small scales. Similar process has been recently observed also in kinetic (PIC) simulations [4].

Acknowledgements This research was supported by the grants P209/12/0103 (GA CR), P209/10/1680 (GA CR), 5322215000801 (IGA UJEP) and the research project AV0Z10030501 of the Astronomical Institute of the Academy of Sciences.

References

1. M. J. Aschwanden. Particle acceleration and kinematics in solar flares - A Synthesis of Recent Observations and Theoretical Concepts (Invited Review). *Space Sci. Rev.*, 101:1–227, January 2002.
2. M. Bárta, J. Büchner, M. Karlický, and J. Skála. Spontaneous Current-layer Fragmentation and Cascading Reconnection in Solar Flares. I. Model and Analysis. *Astrophys. J.*, 737:24, August 2011.

3. M. J. Berger and J. Oliger. Adaptive Mesh Refinement for Hyperbolic Partial Differential Equations. *Journal of Computational Physics*, 53:484–512, March 1984.
4. M. Karlický and M. Bárta. Successive Merging of Plasmoids and Fragmentation in a Flare Current Sheet and Their X-Ray and Radio Signatures. *Astrophys. J.*, 733:107, June 2011.
5. B. Kliem, M. Karlický, and A. O. Benz. Solar flare radio pulsations as a signature of dynamic magnetic reconnection. *Astron. Astrophys.*, 360:715–728, August 2000.
6. J. Lin, J. Li, T. G. Forbes, Y.-K. Ko, J. C. Raymond, and A. Vourlidas. Features and Properties of Coronal Mass Ejection/Flare Current Sheets. *Astrophys. J.*, 658:L123–L126, April 2007.
7. N. F. Loureiro, R. Samtaney, A. A. Schekochihin, and D. A. Uzdensky. Magnetic reconnection and stochastic plasmoid chains in high-Lundquist-number plasmas. *ArXiv e-prints*, August 2011.
8. N. F. Loureiro, A. A. Schekochihin, and S. C. Cowley. Instability of current sheets and formation of plasmoid chains. *Physics of Plasmas*, 14(10):100703–+, October 2007.
9. K. Shibata and S. Tanuma. Plasmoid-induced-reconnection and fractal reconnection. *Earth, Planets, and Space*, 53:473–482, June 2001.
10. D. A. Uzdensky, N. F. Loureiro, and A. A. Schekochihin. Fast Magnetic Reconnection in the Plasmoid-Dominated Regime. *Physical Review Letters*, 105(23):235002–+, December 2010.

Plasmoids in Solar Flares and Their Radio and X-ray Signatures

Marian Karlický and Miroslav Bárta

Abstract This review summarizes our recent results connected with the theoretical and observational aspects of plasmoids in solar flares. We show that the plasmoids play a very important role in the primary flare process – in the magnetic field reconnection. It is shown how the plasmoids are formed, how they move and interact, and how the flare current sheet is fragmented due to these processes. Furthermore, we present a successive merging of the plasmoids, which not only very efficiently accelerate particles, but also it can produce large plasmoids which are sometimes observed in the X-ray emission. Considering the plasmoids the radio drifting pulsating structures (DPSs), narrowband dm-spikes and the above-the-loop-top hard X-ray sources are interpreted. Some interesting radio spectra, relevant to this topic, are added.

1 General Description of Plasmoids

The importance of plasmoids in solar flares was recognized for the first time in [1]. They studied an ejection of the plasmoid, observed during the 1992 October 5 flare in X-rays by *Yohkoh*. The same flare was studied also in [2] and it was shown that this plasmoid was associated with the drifting pulsating structure (DPS) (see Fig. 1). Similar observations were described in [3]. The model of this radio emission was proposed and further developed in [4–8]. This model assumes the vertical current sheet formed below the rising magnetic rope (Fig. 2 right side). In the current sheet, due to tearing and coalescence processes the plasmoids (in 3-D magnetic ropes) are formed and particles, especially electrons are very efficiently accelerated [9–14].

M. Karlický (✉) · M. Bárta
Astronomical Institute of the Academy of Sciences of the Czech Republic, CZ–25165, Ondřejov, Czech Republic
e-mail: karlicky@asu.cas.cz; barta@asu.cas.cz

Karlický, M. and Bárta, M.: *Plasmoids in Solar Flares and Their Radio and X-ray Signatures*. Astrophys Space Sci Proc. **33**, 49–59 (2012)
DOI 10.1007/978-3-642-30442-2_6, © Springer-Verlag Berlin Heidelberg 2012

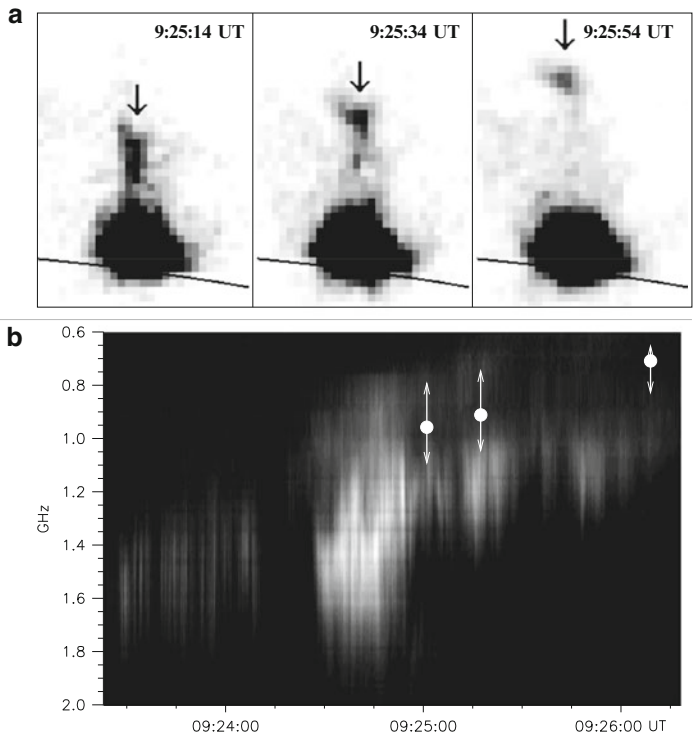

Fig. 1 (**a**) The X-ray plasmoid (*black blob* above the limb flare, see the *arrows*) ejected during the the 5 October 1992 flare, as observed by SXT/*Yohkoh* [1]. (**b**) The simultaneous radio spectrum of the drifting pulsating structure (DPS) [2]. The small *white circles* with the error bars correspond to the plasma frequency in the plasmoid as derived in [1]. These *circles* show an agreement between radio and plasma frequencies as expected in the plasma emission mechanism generating DPS

Some of the electrons are then trapped in the plasmoids (in semi-closed magnetic field structures – O-type in 2-D), where they generate Langmuir waves, which through a wave transformation to electromagnetic waves produce DPSs. The DPS is generated in the limited range of frequencies due to a limited range of plasma densities (frequencies) inside the plasmoid. In dependance on the magnetic field in the flare atmosphere the plasmoids move upwards or downwards or even stay at some height of the flaring atmosphere [7, 15] (Fig. 3). Due to a preference of divergent magnetic field lines in the upward direction, most of the plasmoids move upwards and corresponding DPSs drift towards lower frequencies. In some cases the plasmoids move downwards and interact with the underlying flare arcade, see Fig. 4 and [16, 17].

All these processes can be considered as a fragmentation of the flare current sheet. Two types of the fragmentation was suggested: (a) fragmentation due to stretching of the current sheet and the tearing-mode instabilities in narrower and narrower current sheet (cascading reconnection) [18], and (b) fragmentation

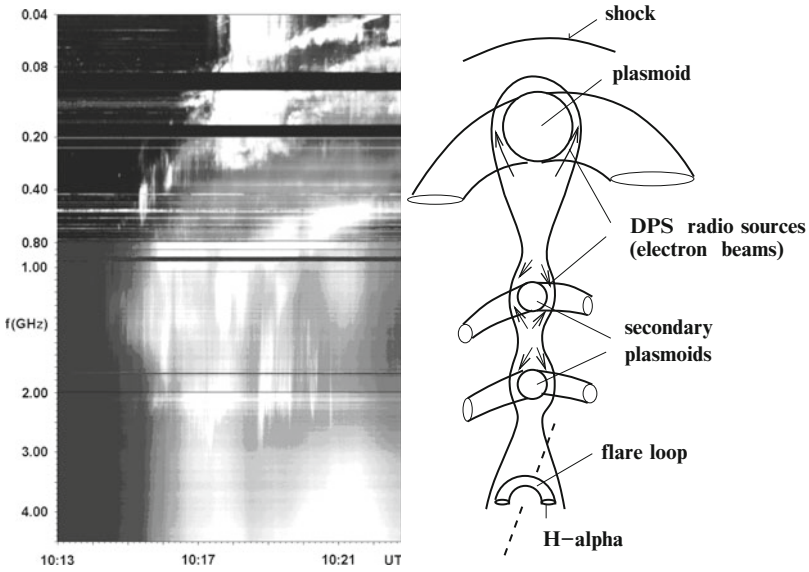

Fig. 2 *Left*: The 0.04–4.5 GHz radio spectrum observed during the 12 April 2001 flare by the Potsdam (0.04–0.8 GHz range, courtesy by A. Klassen) and the Ondřejov radiospectrographs (0.8–4.5 GHz), showing the DPS at 10:17:20–10:22:00 UT in the 0.45–1.5 GHz range and the type II radio burst (generated by shock wave) at 10:17–10:33 UT in the 0.04–300 GHz range. *Right*: Flare scenario: The rising magnetic rope (the uppermost plasmoid) generate *vertical* current sheet, where the further plasmoids (magnetic ropes) are generated due to the tearing-mode instability. Above this main rope the shock, producing type II radio burst, is generated; compare this scenario with the radio spectrum in the *left* part of the figure, for details, see [5]

between two merging plasmoids in generated current sheets in smaller and smaller spatial scales [19–21]. This concept was theoretically developed in [22, 23] as the theory of the chain plasmoid instability. The multi-scale magnetic islands was observed in the Earth's magnetotail [24] as well as in solar flares [5]. An advantage of this concept is that it explains how very narrow current sheets with high current densities (requested for the anomalous resistivity generation and fast reconnection) are generated. Moreover, many magnetic X-points in this model give sufficient volume for an acceleration of particles.

2 Successive Merging of Plasmoids

We simulated this process using a 2.5-D fully relativistic electromagnetic particle-in-cell model [6, 25, 26] with free boundary conditions. The system size was $L_x \times L_y = 600\Delta \times 4,000\Delta$, where $\Delta(= 1)$ is a grid size. We took the Harris current sheet along the line $x = 0\Delta$ with its half-width 10Δ. We considered the

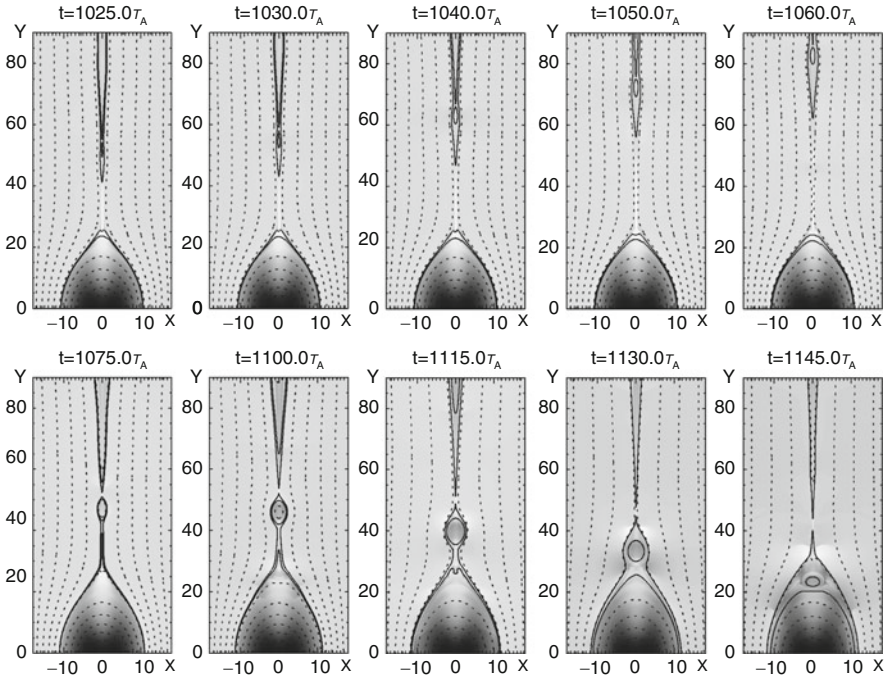

Fig. 3 Two rows show an *upward*-moving and *downward*-moving plasmoid as the result of numerical simulations of reconnection, tearing and coalescence processes in the *vertical* current sheet [15]

electron-proton plasma with the proton-electron mass ratio $m_p/m_e = 16$. In each numerical cell located far from the current sheet, we initiated $n_0 = 60$ electrons and $n_0 = 60$ protons. In the current sheet the initial number density was enhanced just to keep the pressure equilibrium. The initial electron temperature was taken to be the same in the whole numerical box as T = 10 MK and the temperature of protons was chosen the same as electrons. The plasma frequency is $\omega_{pe}\Delta t = 0.05$ (Δt is the time step which equals to 1), the electron Debye length is $\lambda_D = 0.6\ \Delta$, and the electron and proton inertial lengths are $d_e = 10\ \Delta$ and $d_i = 40\ \Delta$, respectively. We initiated a cosine perturbation of the electric current density in the sheet for a formation of ten plasmoids along the current sheet. Then we studied an evolution of this system which is shown in Fig. 5. As shown there the plasmoids started to interact and merge successively into one large plasmoid (Fig. 5f). During this process the mean energy of electrons increases 6.5 times comparing with that in the initial state. Figure 6 shows details of this evolution as well as the distribution of numerical electrons (points), having the energy greater than 40 keV, at four different times: at $\omega_{pe}t = 5{,}200$ (a), at $\omega_{pe}t = 5{,}600$ (b), at $\omega_{pe}t = 8{,}000$ (c), and at $\omega_{pe}t = 9000$ (d). As can be seen here, in each merging process electrons are very efficiently accelerated – see an increase of the number of numerical electrons

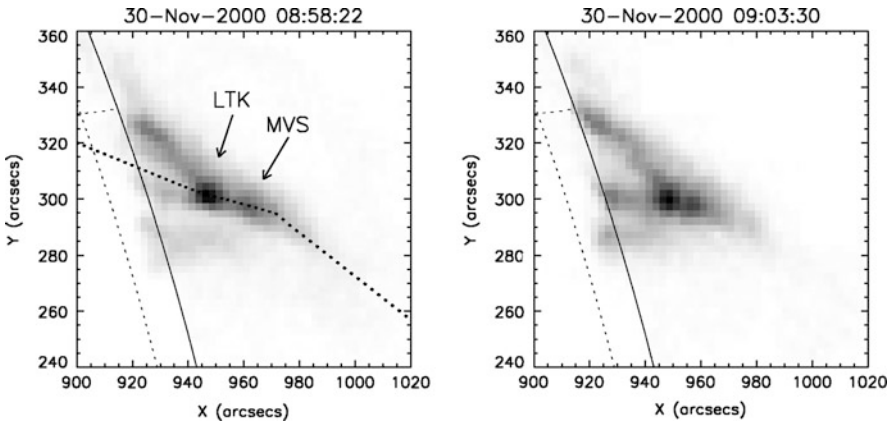

Fig. 4 Coalescence of *downward* moving plasmoid (source *MVS*) with the loop-top kernel (*LTK*) observed in X-rays by SXT/*YOHKOH* [16]; compare with the *bottom* row in Fig. 3

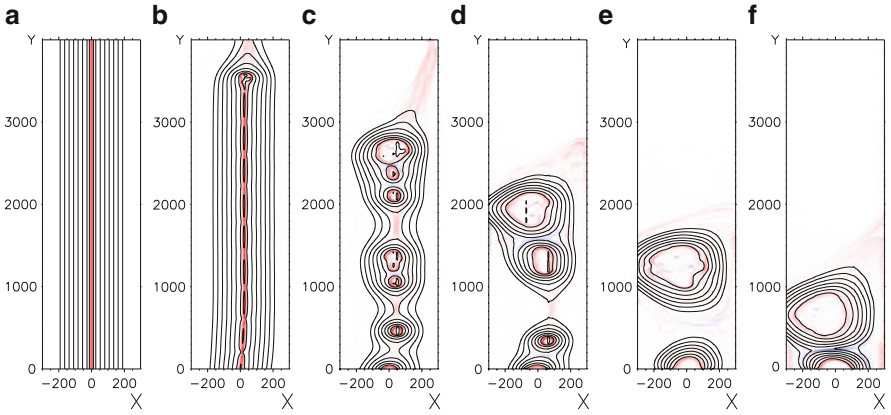

Fig. 5 Magnetic field lines and corresponding current densities, obtained by the PIC simulations, in the $x - y$ computational plane at six different times: at the initial state (**a**), at $\omega_{pe}t = 1,800$ (**b**), at $\omega_{pe}t = 3,500$ (**c**), at $\omega_{pe}t = 5,000$ (**d**), at $\omega_{pe}t = 6,500$ (**e**), and at $\omega_{pe}t = 8,000$ (**f**). The *reddish* and *blue* areas mean current densities with the initial and opposite orientation of the electric current, respectively. The x and y coordinates are expressed in grids [26]

(points) in dependence on time. Then we computed electron distribution functions in all three coordinates in the whole computational box. The most energetic electrons are accumulated between merging plasmoids. At some regions and for short times during the coalescence process the distributions deviated from the thermal ones, but very soon these distributions were thermalized by fast wave-particle processes.

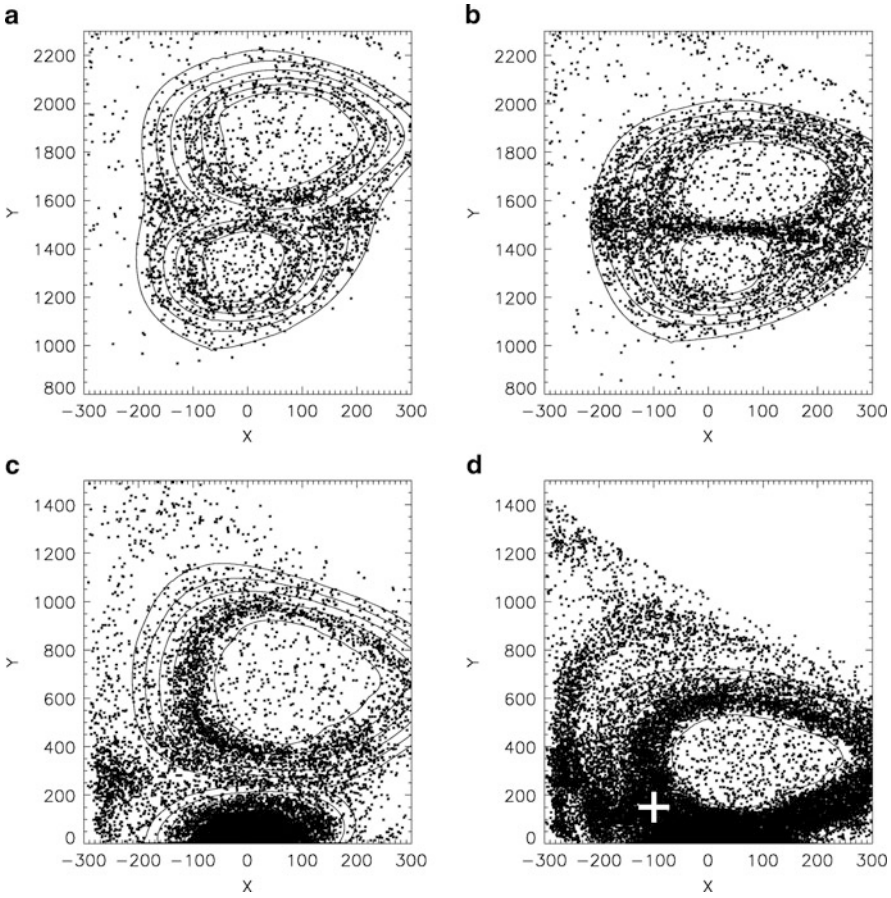

Fig. 6 The detailed view on magnetic field lines in the $x-y$ computational plane and distribution of numerical electrons (points) having the energy greater than 40 keV at four different times: at $\omega_{pe}t = 5,200$ (**a**), at $\omega_{pe}t = 5,600$ (**b**), at $\omega_{pe}t = 8,000$ (**c**), and at $\omega_{pe}t = 9,000$ (**d**). The *white cross*, located at (**d**) $x = -100$, y $= 150$, shows the region where the X-ray spectra (Fig. 7b) were computed. The x and y coordinates are expressed in grids [26]

3 X-ray and Radio Signatures of Plasmoids in Solar Flares

3.1 The Above-the-Loop-Top Hard X-ray Sources

The above-the-loop-top hard X-ray sources belong to the most discussed topics in recent years [27–30]. A very interesting example was published recently in [31]. They presented the hard X-ray source (with the energy up to ∼80 keV) which was located 6 Mm above thermal flare loops. They derived the upper limit of the plasma density and source volume as $n_e \sim 8\times10^9$ cm^{-3} and $V \sim 8\times10^{26}$ cm^3, respectively.

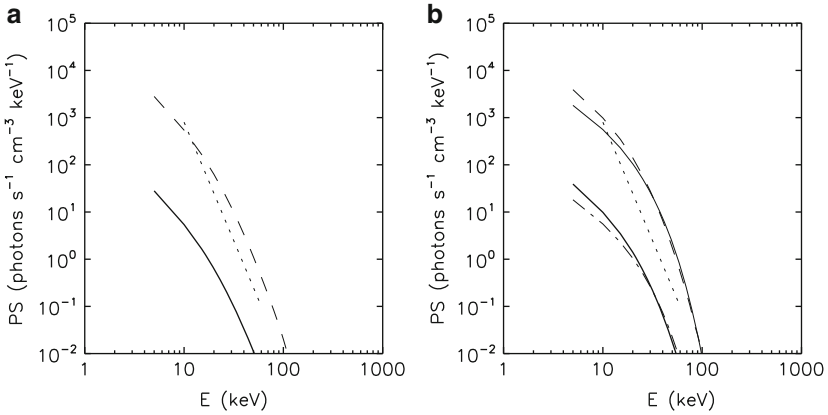

Fig. 7 The X-ray spectra (**a**, **b**) (the *full line* for the source density $n_e = 10^9$ cm^{-3}, and the *dashed line* for $n_e = 10^{10}$ cm^{-3}) computed in the whole computational box (**a**) and at the location shown in Fig. 6d by the particle integrating method. The X-ray spectra in (**b**) (the *dashed-dot line* for the source density $n_e = 10^9$ cm^{-3}, and the *dashed-dot-dot-dot line* for $n_e = 10^{10}$ cm^{-3}) computed at the location shown in Fig. 6d by the thermal method for the temperature 118.7 MK. For comparison the X-ray spectrum (*dotted line*) observed during the December 31, 2007 flare [31] is added [26]

They concluded that these hard X-ray sources have to be close to the acceleration region and the distribution function of electrons emitting hard X-rays is strongly non-thermal or the plasma in the source is very hot (up to $T_e \sim 200$ MK). We used the model of successive merging of plasmoids, as presented above, and we computed the X-ray spectra using two methods (for details, see [26]) and compared with that observed (Fig. 7). We found a good agreement between them and thus we proposed that the process of successive merging of plasmoids generates the observed above-the-loop-top hard X-ray sources.

3.2 DPSs and Narrowband dm-Spikes

As described above, on the dynamic radio spectra the most distinct signatures of plasmoids are DPSs. Usually, the DPSs are observed at the beginning of the impulsive phases of strong eruptive flares. In some cases even several DPSs were recorded indicating several plasmoids in the flare current sheets, see e.g. two positively drifting DPSs shown in Fig. 8 right part.

Besides these DPSs, there are so called the narrowband dm-spikes [32–40] which were also proposed to be connected with plasmoids. There are arguments that between two merging plasmoids many small plasmoids are generated due to a fragmentation process. These plasmoids then interact, accelerate electrons which produce plasma waves in each plasmoids, and thus generate a cloud of narrowband radio bursts – dm-spikes as observed, see e.g. Fig. 8 right part. Searching for

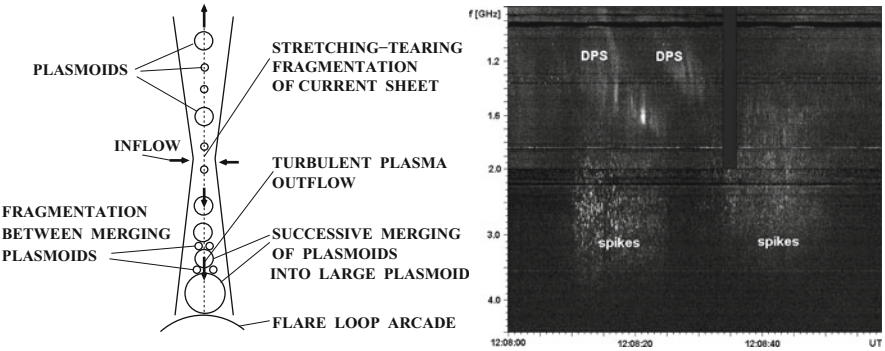

Fig. 8 *Left*: Fragmentation of the current sheet. *Right*: The radio spectrum observed during the 28 March 2001 flare by two Ondřejov radiospectrographs (0.8–2.0 and 2.0–4.5 GHz). It shows the DPSs (radio signatures of large plasmoids) which drift towards narrowband dm-spikes (signatures of the interaction of fragnented plasmoids), compare both parts

a characteristic bandwidth of individual spikes [41,42] it was found that the Fourier transform of the dynamic spectra of spikes have a power-law form with power-law indices close to $-5/3$. Based on these results it was proposed that the spikes are generated in turbulent reconnection outflows [43]. The global scenario of these processes are shown in Fig. 8 left part. This scenario summarizes several aspects of the fragmentation of the flare current sheet. Due to a stretching of the current sheet by the rising main magnetic rope (see Fig. 2) and simultaneous tearing-mode instability the plasmoids are formed. These plasmoids move and generate DPSs in the turbulent reconnection plasma outflows. The plasmoids are accumulated above the flare arcade, where they start to interact. During these interactions they are fragmented and generate the narrowband dm-spikes, compare this scenario with the DPSs and dm-spikes shown in Fig. 8 left part.

4 Conclusions

The present paper summarizes all our previous results explaining the plasmoid formation, their ejection, and corresponding DPSs. We propose that the above-the-loop-top hard X-ray source is large and stationary plasmoid, which is sufficiently dense and with a sufficient amount of energetic electrons. This model is in agreement with the conclusions in [31] that the acceleration region is close to the hard X-ray source. Namely, it enables to re-accelerate energetic electrons. Furthermore, the model can explain not only the above-the-loop-top hard X-ray sources, but also the loop-top sources because the arcade of loops is, in principle, the ‘plasmoid’ fixed in its half height at the photosphere. Considering all aspects of the associated fragmentation process (power-law spatial scales of plasmoids, effective acceleration of electrons, trapping of electrons in plasmoids, location in

the reconnection plasma outflow) we also propose that these processes explain the narrowband dm-spikes. It can be supported by the statistical finding that more than 70% of all groups of the narrowband dm-spikes are observed during the GOES-rising-flare phases [44]. However, the generation of the DPSs and narrowband dm-spikes is a very complex process, depending on many specific conditions. Thus, these bursts can be observed only in specific flares. Furthermore, in some flares these bursts can be covered by strong radio continua or some continua are in reality formed by a superposition of many narrowband dm-spikes.

Acknowledgements This research was supported by the grants P209/12/0103, P209/10/1680 (GA CR), and the research project AV0Z10030501 of the Astronomical Institute AS.

References

1. Ohyama, M., Shibata, K.: X-ray plasma ejection associated with an impulsive flare on 1992 October 5: Physical conditions of X-ray plasma ejection. Astrophys. J. **499**, 934–944 (1998)
2. Kliem, B., Karlický, M., Benz, A.O.: Solar flare radio pulsations as a signature of dynamic magnetic reconnection. Astron. Astrophys. **360**, 715–728 (2000)
3. Khan, J.I., Vilmer, N., Saint-Hilaire, P., Benz, A.O.: The solar coronal origin of a slowly drifting decimetric-metric pulsation structure. Astron. Astrophys. **388**, 363–372 (2002)
4. Karlický, M., Fárník, F., Mészárosová, H.: High-frequency slowly drifting structures in solar flares. Astron. Astrophys. **395**, 677–683 (2002)
5. Karlický, M.: Series of high-frequency slowly drifting structures mapping the flare magnetic field reconnection. Astron. Astrophys. **417**, 325–332 (2004)
6. Karlický, M., Bárta, M.: Drifting pulsating structures generated during tearing and coalescence processes in a flare current sheet. Astron. Astrophys. **464**, 735–740 (2007)
7. Bárta, M., Karlický, M., Žemlička, R.: Plasmoid dynamics in flare reconnection and the frequency drift of the drifting pulsating structure. Solar Phys. **253**, 173–189 (2008)
8. Karlický, M., Bárta, M., Rybák, J.: Radio spectra generated during coalescence processes of plasmoids in a flare current sheet. Astron. Astrophys. **514**, id.A28 (2010)
9. Drake, J.F., Shay, M.A., Thongthai, W., Swisdak, M.: Production of energetic electrons during magnetic reconnection. Phys. Rev. Letters **94**, id.095001 (2005)
10. Drake, J.F., Swisdak, M., Che, H., Shay, M. A.: Electron acceleration from contracting magnetic islands during reconnection. Nature **443**, 553–556 (2006)
11. Hoshino, M.: Electron surfing acceleration in magnetic reconnection. J. Geophys. Res. **110**, id. A10215 (2005)
12. Pritchett, P.L.: Relativistic electron production during guide field magnetic reconnection. J. Geophys. Res. **111**, id.A10212 (2006)
13. Pritchett, P.L.: Energetic electron acceleration during multi-island coalescence. Phys. Plasmas **15**, 102105-102105-9 (2008)
14. Karlický, M.: Separation of accelerated electrons and positrons in the relativistic reconnection. Astrophys. J. **674**, 1211–1216 (2008)
15. Bárta, M., Vršnak, B., Karlický, M.: Dynamics of plasmoids formed by the current sheet tearing, Astron. Astrophys. **477**, 649–655 (2008)
16. Kolomanski, S., Karlický, M.: The interaction of a plasmoid with a loop-top kernel. Astron. Astrophys. **475**, 685–693 (2007)
17. Milligan, R.O., McAteer, R.T.J., Dennis, B.R., Young, C.A.: Evidence of a plasmoid-looptop interaction and magnetic inflows during a solar flare/coronal mass ejection eruptive event. Astrophys. J. **713**, 1292–1300 (2010)

18. Shibata, K., Tanuma, S.: Plasmoid-induced-reconnection and fractal reconnection. Earth Planets Space **53**, 473–482 (2001)
19. Bárta, M., Büchner, J., Karlický, M.: Multi-scale MHD approach to the current sheet filamentation in solar coronal reconnection. Adv. Space Res. **45**, 10–17 (2010)
20. Bárta, M., Büchner, J., Karlický, M., Skála, J.: Spontaneous Current-layer Fragmentation and Cascading Reconnection in Solar Flares. I. Model and Analysis. Astrophys. J. **737**, id. 24 (2011)
21. Bárta, M., Büchner, J., Karlický, M., Kotrč, P.: Spontaneous current-layer fragmentation and cascading reconnection in solar flares. II. Relation to observations. Astrophys. J. **730**, id.47 (2011)
22. Loureiro, N.F., Schekochihin, A.A., Cowley, S.C.: Instability of current sheets and formation of plasmoid chains. Physics of Plasmas **14**, 100703–100703-4 (2007)
23. Uzdensky, D.A., Loureiro, N.F., Schekochihin, A.A.: Fast magnetic reconnection in the plasmoid-dominated regime. Physical Review Letters **105**, 235002–235002-4 (2010)
24. Hoshino, M., Nishida, A., Yamamoto, T., Kokubun, S.: Turbulent magnetic field in the distant magnetotail: Bottom-up process of plasmoid formation? Geophys. Res. Lett. **21**, 2935–2938 (1994)
25. Saito, S., Sakai, J.I.: The emission of electromagnetic waves during the coalescence of two parallel current loops in solar flares. Astrophys. J. **616**, L179–L182 (2004)
26. Karlický, M., Bárta, M.: Successive merging of plasmoids and fragmentation in a flare current sheet and their X-ray and radio signatures. Astrophys. J. **733**, id.107 (2011)
27. Masuda, S., Kosugi, T., Hara, H., Tsuneta, S., Ogawara, Y.: A loop-top hard X-ray source in a compact solar flare as evidence for magnetic reconnection. Nature **371**, 495–497 (1994)
28. Tomczak, M.: The analysis of hard X-ray radiation of flares with occulted footpoints. Astron. Astrophys. **366**, 294–305 (2001)
29. Petrosian, V., Donaghy, T.Q., McTierman, J.M.: Loop top hard X-ray emission in solar flares: Images and statistics. Astrophys. J. **569**, 459–473 (2002)
30. Krucker, S., Lin, R.P.: Hard X-ray emissions from partially occulted solar flares. Astrophys. J. **673**, 1181–1187 (2008)
31. Krucker, S., Hudson, H.S., Glesener, L., White, S.M., Masuda, S., Wuelser, J.P., Lin, R.P.: Measurements of the coronal acceleration region of a solar flare. Astrophys. J. **714**, 1108–1119 (2010)
32. Benz, A.O.: Millisecond radio spikes. Solar Phys. **104**, 99–110 (1986)
33. Karlický, M.: Narrowband dm-spikes as indication of flare mass ejection. Solar Phys. **92**, 329–342 (1984)
34. Stähli, M., Magun, A.: The microwave spectrum of solar millisecond spikes. Solar Phys. **104**, 117–123 (1986)
35. Benz, A.O., Jaeggi, M., Zlobec, P.: Fine structure near the starting frequency of solar type III radio bursts. Astron. Astrophys. **109**, 305–313 (1982)
36. Zlobec, P., Karlický, M.: Narrowband dm-spikes observed during the 15 June 1991 flare. Solar Phys. **182**, 477–496 (1998)
37. Mészárosová, H., Veronig, A., Zlobec, P., Karlický, M.: Analysis of solar narrow band dm-spikes observed at 1420 and 2695 MHz. Astron. Astrophys. **407**, 1115–1125 (2003)
38. Güdel, M., Zlobec, P.: Polarization and emission mode of solar radio spikes. Astron. Astrophys. **299**, 299–309 (1991)
39. Kuijpers, J., Van der Post, P., Slottje, C.: Runaway acceleration in a radio flare. Astron. Astrophys. **103**, 331–338 (1981)
40. Fleishman, G.D., Yastrebov, S.G.: On the harmonic structure of solar radio spikes. Solar Phys. **154**, 361–369 (1994)
41. Karlický, M., Sobotka, M., Jiřička, K.: Narrowband dm-Spikes in the 2 GHz Frequency Range and MHD Cascading Waves in Reconnection Outflows. Solar Phys. **168**, 375–383 (1996)
42. Karlický, Jiřička, K., Sobotka, M.: Power-law spectra of 1-2 GHz narrowband dm-spikes. Solar Phys., **195**, 165–174 (2000)

43. Bárta, M., Karlický, M.: Turbulent plasma model of the narrowband dm-spikes. Astron. Astrophys. **379**, 1045–1051 (2001)
44. Jiřička, K., Karlický, M., Mészárosová, H., Snížek, V.: Global statistics of 0.8-2.0 Ghz radio bursts and fine structures observed during 1992–2000 by the Ondřejov radiospectrograph. Astron. Astrophys. **375**, 243–250 (2001)

Occurrence of Magnetic Reconnection in the Deep Magnetotail: ARTEMIS Results

Zoltán Vörös, Andrei Runov, and Alexander Kendl

Abstract Using two-probe ARTEMIS magnetic field and plasma measurements we have accomplished a survey of the occurrence of magnetic reconnection signatures in the distant magnetotail between October 2010 and June 2011. We have considered highly accelerated electron and fast bulk plasma flow events during ARTEMIS tail crossings. Our findings suggest that the deep-tail region between $-60R_E < X(GSM) < -40R_E$ is rather active. Fourteen events have been found exhibiting signatures of magnetic reconnection occurrence during 29 days of plasma sheet crossings. Comparisons with mid-tail surveys of reconnection statistics indicate that the deep-tail region can play a significant role in global magnetosphere dynamics.

1 Introduction

Magnetic reconnection (MR) represents a multi-scale physical process in laboratory, space and astrophysical plasmas. It is associated with large-scale (system- and fluid-scale) reorganizations of the magnetic field topology and localized kinetic (ion- and electron-scale) processes, leading to particle energization, intense energy bursts and flows [1]. MR plays a crucial role in understanding the non-steady interaction of

Z. Vörös (✉)
Institute of Astro- and Particle Physics, University of Innsbruck, A–6020, Innsbruck, Austria
e-mail: zoltan.voeroes@uibk.ac.at

A. Runov
Institute of Geophysics and Planetary Physics, University of California, Los Angeles, CA 90095-1567, USA
e-mail: arunov@igpp.ucla.edu

A. Kendl
Institute for Ion Physics and Applied Physics, University of Innsbruck, A–6020, Innsbruck, Austria
e-mail: alexander.kendl@uibk.ac.at

Vörös, Z. et al.: *Occurrence of Magnetic Reconnection in the Deep Magnetotail: ARTEMIS Results*. Astrophys Space Sci Proc. **33**, 61–66 (2012)
DOI 10.1007/978-3-642-30442-2_7, © Springer-Verlag Berlin Heidelberg 2012

solar wind with the Earth's magnetosphere and in explaining the bursty response of magnetosphere-ionosphere system during magnetospheric storms and substorms. On the basis of previous statistical studies (e.g. [2–4]) it is suggested that, MR is preferentially initiated in the mid magnetotail (between $X = -15$ and $-30R_E$, where R_E is the Earth's radius). This region and the near-Earth magnetosphere represent key areas of energy accumulation, release and transport during substorms. However, the tail region beyond $-30R_E$ is much less explored. Occasional deep-tail observations of the Geotail probe have revealed an unsteady magnetotail beyond $X - 30R_E$ as well. It was found, that at $X \sim -60R_E$, the tailward progression and retreat of MR associated activity is highly dynamic, turbulent, characterized by complex 3D structures, multiple X-lines, appearance and dynamical evolution of acceleration centers [5]. In this paper we provide a preliminary analysis of ARTEMIS two-probe mission data (former THB and THC satellites of THEMIS) between October 2010 and June 2011. The probes were crossing the deep-tail between $X \sim -45$ and $-75R_E$. Here we investigate electron acceleration and bulk flow signatures between $10R_E > Y(GSM) > -10R_E$. Altogether, the two probes were inside of this region more than 29 days. We show that the occurrence of MR signatures in this deep-tail region is comparable to that in the mid-tail.

2 Electron Acceleration Signatures

Since MR is associated with particle acceleration, it is justified to evaluate the observed energy ranges of particle populations. In this paper electron acceleration signatures will be considered. We use the magnetic data from the Flux-Gate magnetometer [6]. Particle data are provided by the Electrostatic Analyzer (ESA, [7]), which measures electron energies over the range of 0–30 keV and by the Solid State Telescope (SST, [8]), which measures electron energies over 30 keV. As an example, Fig. 1 shows 8 h of magnetic field B_X and speed V_X data in GSM coordinates, and electron flux data observed by THB and THC probes on February 19, 2011. For this time period, the SST electron data are available from THC only. The magnetic field B_X component shows that both probes move from the southern hemisphere of the plasma sheet to the northern hemisphere between 06:30 and 08:15 UT. The neutral sheet crossing is accompanied by tailward – Earthward flow reversals ($\pm V_X$, second panel in Fig. 1) and bursts of energetic electrons observed by SST and ESA instruments (the bottom three panels for THC and two panels for THB in Fig. 1, respectively). The accelerated electrons and bulk flow signatures are associated with MR. The MR event on February 19, 2011 was accompanied by correlated flow and field reversals, Hall-effect signatures, MHD and ion-scale turbulence [9]. The bottom panels of THC and THB electron flux subplots in Fig. 1 show the time series of 5 keV and 1 keV electrons. Except for the time period of MR occurrence between 06:30 and 08:00 UT, the flux of 5 keV electrons (eflux[5 keV]) is lower than the flux of 1 keV electrons (eflux[1 keV]). It also remains valid for the fast Earthward flow dominated interval between 00:00 and 01:00 UT, where

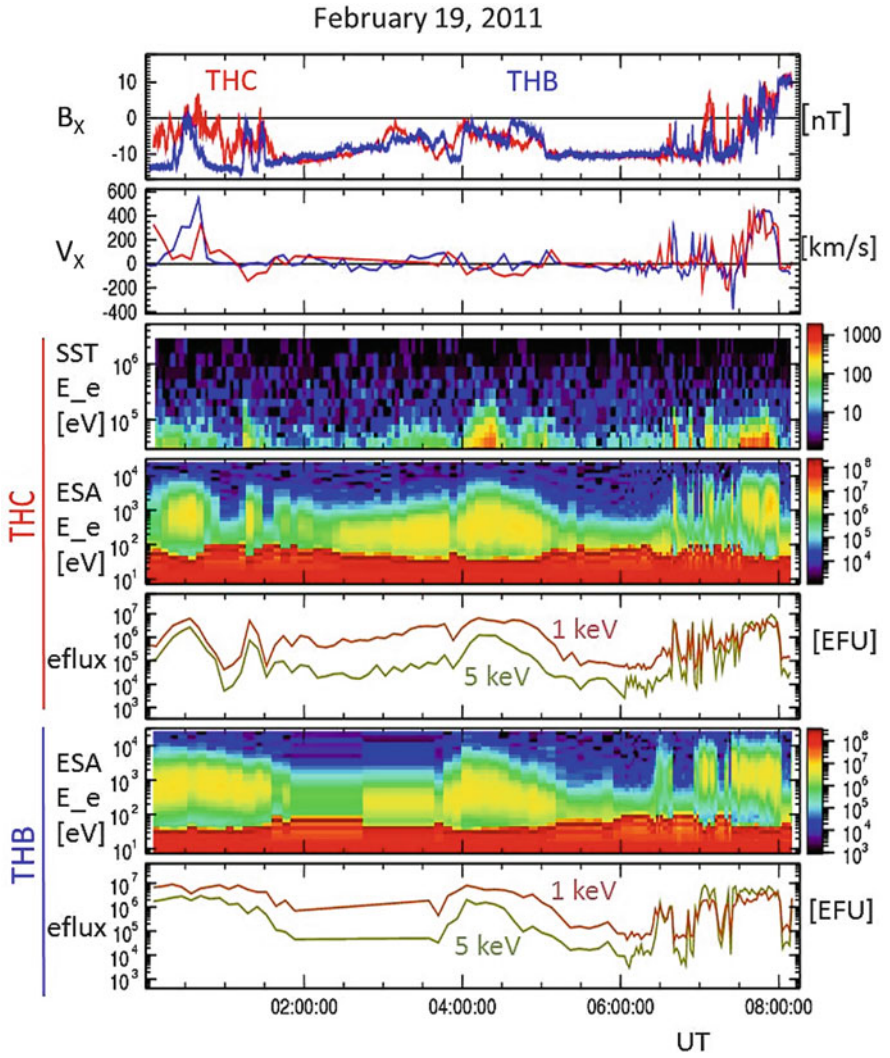

Fig. 1 ARTEMIS data on February 19, 2011; *Top*: B_X and V_X GSM components of magnetic field and plasma bulk speed for THB and THC probes; *Bottom*: THC and THB electron data; the color code and eflux data are in EFU units $[eV/cm^2.s.sr.eV]$. Magnetic reconnection signatures has been observed between 07:00 and 08:00 UT [8]

local MR signatures were not observed. In fact, statistical analysis has shown that the ratio r = eflux(5 keV)/eflux(1 keV) can serve as a proxy for the occurrence of highly accelerated electrons and MR, providing that $r > 1.5$ [3]. Although this criterion was based on low-energy electron fluxes (1–5 keV), it was good enough to find all MR and highly accelerated electron events in a larger GEOTAIL data set of 209 tailward flows between 1995 and 2003 [3]. Figure 2 shows the distribution

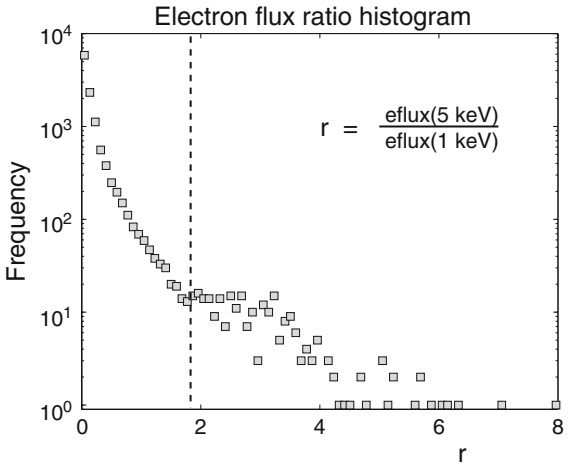

Fig. 2 Histogram of electron flux ratio

of the ratio r observed during the 29 days while ARTEMIS probes were within $10R_E > Y(GSM) > -10R_E$ in the deep tail. The threshold r = 1.9 separates two different distributions of r values. Therefore, for finding highly accelerated electron events in ARTEMIS data, the criterion $r > 1.9$ will be used.

The observed distribution of the ratio r together with the threshold r = 1.9 between the distances $-75R_E < X(GSM) < -40R_E$ is depicted in Fig. 3a. Figure 3b is showing the X(GSM) distribution of those Earthward ($+V_X$) and tailward ($-V_X$) flow events for which the plasma $\beta > 1$. This criterion guaranties that plasma sheet bulk flows are selected [10]. The vertical boxes contain the correlated highly accelerated electron and high speed bulk flow events. The corresponding MR sites (triangles) together with the trajectories of THB and THC probes in X(GSM)-Y(GSM) coordinates are depicted in Fig. 3c. The MR sites on February 19 (Fig. 1) observed by THB and THC are indicated by filled circles. The Earthward-tailward flows are rather symmetrically distributed between $-60R_E < X(GSM) < -40R_E$. There were no highly accelerated electrons beyond $-60R_E$, however, there were three tail-crossings only during the considered time period. The observed high speed flows can be associated by remote driving sources.

3 Conclusions

Previous statistical studies suggest that MR occurs in the mid-tail, preferentially beyond $-17R_E$ [2–4]. Although the location of MR depends on solar wind conditions [3], the occurrence rate of tailward/Earthward flows is increasing towards $-30R_E$ (GEOTAIL apogee) [4]. This indicates that, in terms of MR associated

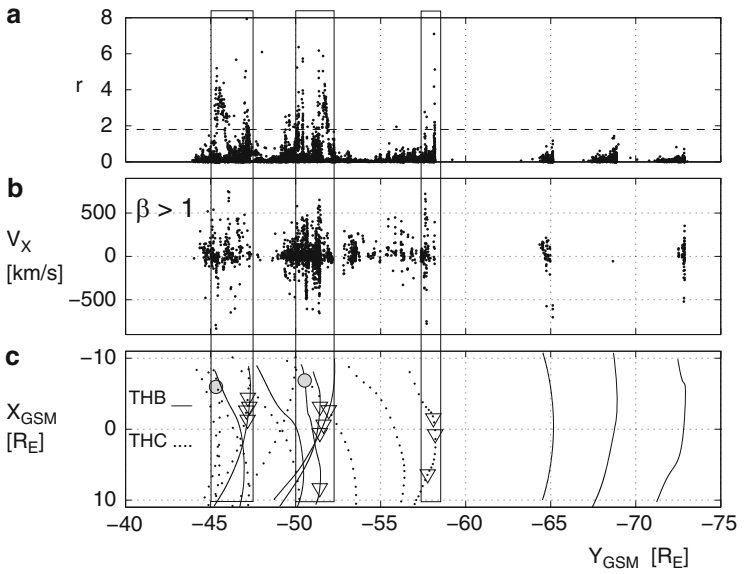

Fig. 3 Magnetic reconnection signatures; (**a**) Electron flux ratio distribution over X_{GSM}. The horizontal *dashed line* indicates the threshold for highly accelerated electron events; (**b**) Earthward-tailward fast flow distribution over X_{GSM}; (**c**) THB (*solid lines*) and THC (*dotted lines*) trajectories and the position of the observed reconnection signatures (*triangles*) in X_{GSM} - Y_{GSM} coordinates. *Filled circles* indicate the reconnection event in Fig. 1

flows, the poorly explored region immediately beyond $-30R_E$ can be rather active as well. Although in this paper we present a limited number of ARTEMIS tail crossings (nine double crossings between October 2010 and June 2011), the number of highly accelerated electron or MR events reaches 14 (Fig. 3c). Some of these events (e.g. in February 2011) were observed by both THB and THC. Between 1995 and 2003, during winter and spring seasons, GEOTAIL observed 34 highly accelerated electron events [3]. The different orbital characteristics, solar wind conditions and the uneven survey of the plasma sheet do not allow a precise comparison of these statistics. However, the large number of MR associated highly accelerated electron events beyond $-30R_E$ (ARTEMIS), in comparison with mid-tail occurrences (GEOTAIL), suggests that the deep-tail region is rather active and can play an important role in global magnetospheric physics.

Acknowledgements We acknowledge NASA contract NAS5- 02099 and V. Angelopoulos for use of data from the THEMIS Mission. Specifically, C.W. Carlson and J.P. McFadden for use of ESA data, K. H. Glassmeier, U. Auster, and W. Baumjohann for use of FGM data, A. Roux and O. LeContel for use of SCM data. This work was made with the support of the ISSI team 185 "Dispersive cascade and dissipation in collisionless space plasma turbulence: observations and simulations". The work was also supported by the Austrian Wissenschaftsfonds FWF under Grant No. Y398.

References

1. Zweibel, E.G., Yamada, M.: Magnetic reconnection in astrophysical and laboratory plasmas. Annu. Rev. Astron. Astrophys. **47**, 291–332 (2009)
2. Baumjohann, W., Paschmann, G., and Lühr, H.: Characteristics of high-speed ion flows in the plasma sheet. J. Geophys. Res. **95**, 3801–3809 (1990)
3. Nagai, T., Fujimoto, M., Nakamura, R., Baumjohann, W., Ieda, A., Shinohara, I., Machida, S., Saito, Y., and Mukai, T.: Solar wind control of the radial distance of the magnetic reconnection site in the magnetotail. J. Geophys. Res. 110, A09208, doi:10.1029/2005JA011207 (2005)
4. Zhang, L. Q., Liu, Z. X., Ma, Z. W., Baumjohann, W., Pu, Z. Y., Dunlop, M. W., Reme, H., and Wang, J.Y.: X line distribution determined from earthward and tailward convective bursty flows in the central plasma sheet. J. Geophys. Res. 115, A06218, doi:10.1029/2009JA014429 (2010)
5. Angelopoulos, V., et al.: Tailward progression of magnetotail acceleration centers: realtionship to substorm current wedge. J. Geophys. Res. **101**, 24599–24619 (1996)
6. Auster, H.U., et al.: TheTHEMISfluxgatemagnetometer. SpaceSci.Rev. **141** ,235–264 (2008)
7. McFadden, J.P., Carlson, C.W., Larson, D., Angelopolos, V., Ludlam, M., Abiad, R., Elliot, B.: TheTHEMIS ESA plasma instrument and in-flight calibration. Space Sci.Rev. **141**, 277–302 (2008)
8. Angelopoulos, V.: The THEMIS mission. SpaceSci.Rev. **141**, 5–34 (2008)
9. Vörös, Z.: Magnetic reconnection associated fluctuations in the deep magnetotail: ARTEMIS results. Nonlin. Proc. Geophys. **18**, 861–869, doi:10.5194/npg-18-861-2011 (2011)
10. Baumjohann, W., Paschmann, G., and Cattell, C. A.: Average Plasma Properties in the Central Plasma Sheet. J. Geophys. Res. **94**, 6597–6606 (1989)

Part II
Plasma Relaxation and Heating

Relaxation and Heating Triggered by Nonlinear Kink Instability: Application to Solar Flares and Coronal Heating

Philippa K. Browning, Michael R. Bareford, and Mykola Gordovskyy

Abstract Energy release and particle acceleration in kink-unstable twisted coronal loops are discussed. If the magnetic field in a coronal loop is sufficiently strongly twisted, it may become unstable to the ideal kink instability. We present results of 3D MHD simulations which show that in the nonlinear phase of the instability, current sheets form in which magnetic reconnection rapidly dissipates magnetic energy. In the later phase, the current sheet fragments. The energy release is well-modelled by a helicity conserving relaxation to a minimum energy state. We exploit this in order to calculate a distribution of energy-release events, and show how this is relevant to the solar coronal heating problem. Using test particle approach coupled with 3D MHD simulations, we also show how the electric fields associated with the fragmented currents sheet can efficiently accelerate charged particles. This has implications for the origin of high-energy particles in solar flares.

1 Introduction

Surprisingly, the temperature of the solar corona is of the order 1 MK, much hotter than the surface temperature (around 6,000 K). The corona is both highly structured and dynamic, as demonstrated by recent observations from Solar Dynamic Observatory and other space telescopes, and is strongly magnetised. Two major unsolved astrophysical problems, the high coronal temperature and understanding solar flares, may be resolved by the process of magnetic reconnection. As first

P.K. Browning (✉) · M. Gordovskyy
Jodrell Bank Centre for Astrophysics, University of Manchester, Manchester, UK
e-mail: p.browning@manchester.ac.uk

M.R. Bareford
School of Mathematical Sciences, University of St. Andrews, St. Andrews, UK
e-mail: michael.bareford@postgrad.manchester.ac.uk

Browning, P.K. et al.: *Relaxation and Heating Triggered by Nonlinear Kink Instability: Application to Solar Flares and Coronal Heating*.
Astrophys Space Sci Proc. **33**, 69–75 (2012)
DOI 10.1007/978-3-642-30442-2_8, © Springer-Verlag Berlin Heidelberg 2012

suggested by Parker [17], coronal heating may arise through the combined effect of many nanoflares, each consisting of a release of magnetic energy through magnetic reconnection. The effectiveness of this mechanism relies on nanoflares occurring sufficiently frequently; since determining the occurrence rate for nanoflares observationally has proved inconclusive so far, it is of interest to predict this theoretically.

Solar flares are dramatic releases of stored magnetic energy, almost certainly enabled by magnetic reconnection, manifested through complex signatures across the electromagnetic spectrum [4]. An important question is to explain the origin of the large numbers of high-energy non-thermal charged particles, which carry a significant fraction of the energy released [16, 19]. Electrons are observed through hard X-ray emission as they impinge on the dense chromosphere as well as (sometimes) as coronal loop-top sources, and through microwave and radio emission, whilst ions can be detected via gamma ray nuclear line emission; particles produced at a flare may also be an observed as Solar Energetic Particles in space.

We present here an overview of recent results concerned with energy-release and particle acceleration in twisted coronal loops, which are ubiquitous in the solar corona.

2 Single Heating Events and Event Distributions

We first discuss a single energy-releasing event. The coronal field is stressed by slow photospheric footpoint motions, evolving through a series of nonlinear force-free fields ($\mathbf{j} \times \mathbf{B} = 0$ or $\nabla \times \mathbf{B} = \alpha(\mathbf{r})\mathbf{B}$); this then undergoes helicity-conserving relaxation towards a minimum energy state [18], the constant-α field ($\nabla \times \mathbf{B} = \alpha \mathbf{B}$), releasing energy to heat the corona [14]. Browning and Van der Linden proposed that a trigger for this relaxation could be the onset of ideal instability, such as the kink mode in a twisted loop [8] in the nonlinear phase, current sheets form and multiple reconnections cause the field to undergo Taylor relaxation [6].

This process is investigated by considering an initially force-free cylindrical loop equilibrium, with piecewise-constant $\alpha(r)$ profile (α_1 in the inner part of the loop, α_2 in the outer), embedded within a potential field. The magnetic field, continuous at all boundaries, can be expressed in terms of Bessel functions [2, 3, 6]. The linear stability threshold (a curve in the 2D parameter space (α_1, α_2)) is determined using the CILTS code [6, 7], accounting for line-tying at the photospheric boundaries of the loop (the planes $z = 0, L$). In order to investigate how the relaxation occurs, and the validity of the Taylor model, 3D MHD simulations were undertaken [7, 15] using the Lagrangian Remap code LARE3D [1]. The initial state is a force-free equilibrium, just inside the linearly-unstable region. A stepwise current-dependent resistivity profile, with an enhanced value above a critical current density, representing anomalous resistivity, is usually used.

The loop initially deforms helically. A helical current ribbon forms at the quasi-resonant surface in the nonlinear phase of the instability, as misaligned fieldlines are

pushed together, in which fast magnetic reconnection dissipates magnetic energy. The current sheet stretches and breaks up, producing a fragmented current structure with multiple reconnection sites throughout the loop volume [7, 11, 15]. This distributed reconnection causes α to become more uniform, giving relaxation to the minimum energy state [15]. Furthermore, in the zero net-current case, the twisted field lines reconnect with the surrounding axial field, causing apparent radial loop expansion.

The loop is effectively heated throughout its volume, with intermittently-distributed regions of hot plasma up to 10^8 K (this would then cool due to radiation and conduction, not included in our simulations). Such an event may be observed as a confined microflare, in which a low-lying, almost horizontal loop transiently brightens without eruption.

3D numerical MHD simulations can only be performed for a few initial field profiles; in order to build up a distribution of events, we therefore use relaxation theory. If a loop is twisted by random photospheric motions, magnetic energy builds up until the kink instability threshold is reached, triggering relaxation and heating. The twisting persists, and the process thus repeats, leading to a sequence of heating events of different magnitudes (dependent on where threshold is reached). This is modelled using a Monte Carlo approach both for loops with and without net-current [2,3]. In order to model the latter, representing twisting by footpoint motions localised within the loop cross-section, the equilibrium field model is extended to incorporate an outer current-neutralising layer with locally-constant $\alpha = \alpha_3$; α_3 is determined by the requirement that the azimuthal field vanish at the loop edge (R_3). The linear stability threshold for line-tied loops with these profiles in shown in Fig. 1a, for a range of aspect ratios L/R_3.

The effect of slow photospheric footpoint motions is modelled as a random walk through equilibrium space (α_1, α_2), until the stability threshold is reached, where the energy release is calculated by assuming a helicity-conserving relaxation. In the zero net-current case, the stability threshold does not form a closed curve and we thus cut off the evolution if the axial field B_z reverses. The process repeats, with a new random starting equilibrium after each relaxation. Both spatially-correlated and uncorrelated random walks have been considered [3]; for the latter case, a broad distribution of energy-release sizes is produced, with smaller events being more frequent (Fig. 1b). This is a power law distribution, of the form $f(E) \approx E^{-\gamma}$, where the index γ is slightly larger than the critical value (2) required for effectiveness of nanoflare heating (see [3]). If the footpoint motions have strong spatial correlation across the loop radius, the values of α_1 and α_2 will not evolve independently, and crossing of the instability threshold tends to occur always in the same place: a much narrower distribution of energy-releases is produced. In future, the properties of the random walk through current profiles could be better constrained by using observations of photospheric footpoint motions.

The coronal heating rate can be estimated by taking the average energy release, and dividing by the typical time for the loop to be twisted until it is unstable. Heating is more efficient if the footpoint motions have a long temporal correlation, so that the loop reaches instability quickly rather than undergoing a many-step random walk.

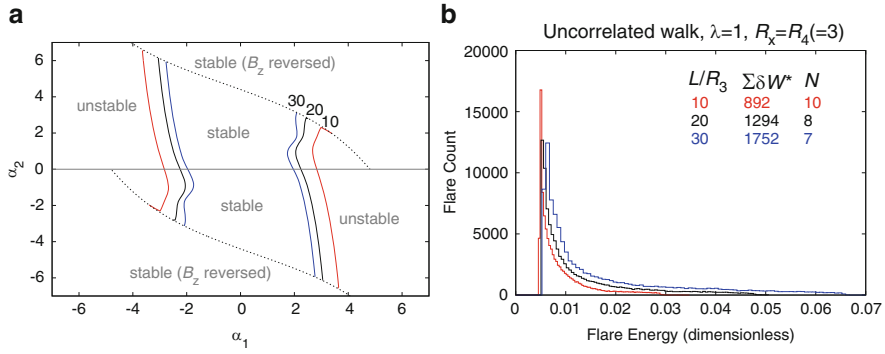

Fig. 1 (**a**) The linear stability threshold for ideal kink instability with line-tying, for zero net-current equilibria with piecewise constant α profile and a range of aspect ratios L/R_3. (**b**) The frequency distribution of heating events for different loop aspect ratios ($L/R_3 = 10, 20, 30$), assuming an uncorrelated random walk and relaxation of the full loop volume [3]

For typical coronal parameters, this gives a value of 3×10^7 erg cm^{-2} s^{-1} [3], adequate for Active Region heating.

3 Accelerated Particles

We now consider the acceleration of charged particles in unstable twisted loops, in order to understand the origin of high-energy particles in solar flares. It is likely that the strong electric fields associated with magnetic reconnection should accelerate charged particles. However, in the standard flare model with a localised acceleration site, there are some difficulties [5]: notably, how to accelerate a very large number of particles, and the extremely strong currents which would be associated with charged particle beams. A distributed acceleration site – which naturally arises if acceleration occurs in a fragmented current sheet – ameliorates these problems.

A time-dependent test particle approach is used, in which the trajectories of charged particles are integrated using the relativistic guiding-centre equations, in evolving background fields from the above MHD simulations. The local fields at a particle position are obtained by interpolation in the 4D grid of data in space and time [9, 10]. Test particles are injected into the fields of an unstable twisted loop, initially with a Maxwellian energy distribution and uniform spatial distribution. The particles undergo stepwise energy gain, with intervals of almost constant energy interspersed with short acceleration episodes when a current sheet is encountered. As a result, the loop quickly fills with high-energy protons and electrons. The results are described in more detail in [11, 12], where various initial fields are considered as well as different resistivity profiles and particle boundary conditions.

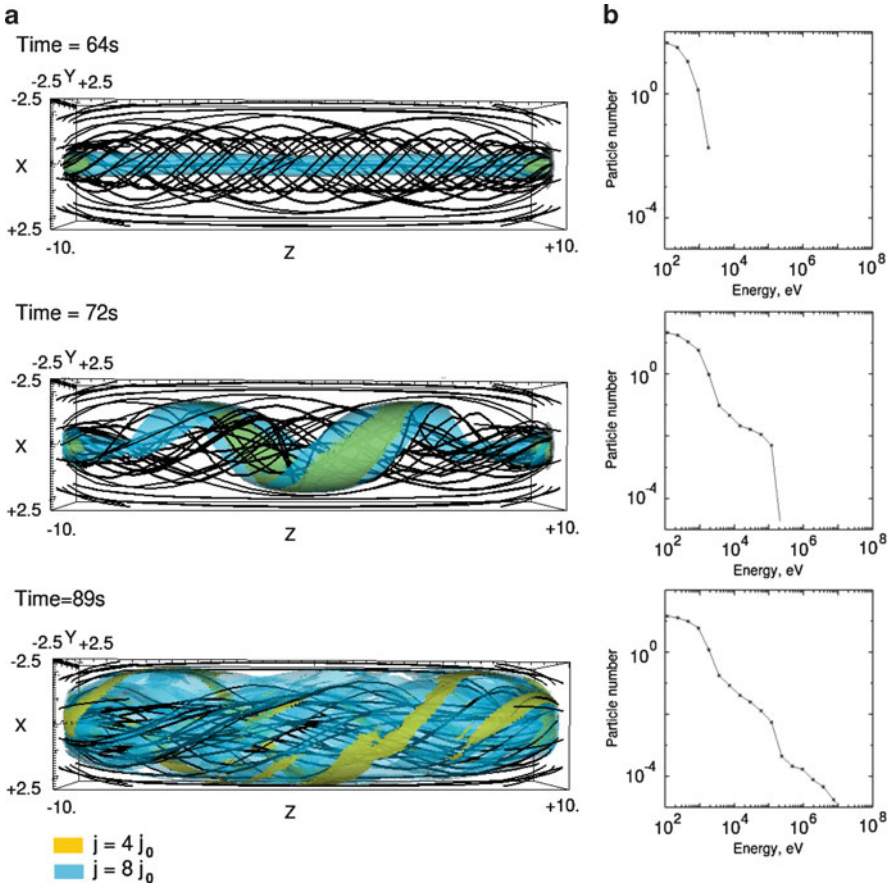

Fig. 2 (**a**) The fieldlines and current isosurfaces during the nonlinear phase of the kink instability from 3D MHD simulations of an unstable twisted loop with field line convergence, at successive times. (**b**) Energy spectra of electrons on the unstable loop at successive times

Recently, we have investigated reconnection in unstable twisted loops with field convergence towards the chromospheric footpoints, generated numerically by twisting footpoint motions applied to an initially untwisted flux tube with convergence. The field disrupts if sufficiently twisted, and forms a fragmented current sheet similar to the analytical, straight-loop model described in Sect. 2 (Fig. 2a); due to the convergence, there are stronger current concentrations near the footpoints [13].

These fields have been used as a basis for test particle simulations. Time-dependent energy spectra of both protons and electrons are calculated, which quickly develop hard non-thermal power-law tails as particles are accelerated by the electric fields within the reconnecting current sheets (Fig. 2b). Since acceleration is mainly by parallel electric fields, the pitch angle distribution of high-energy particles

is strongly collimated parallel to the magnetic field. The region of high-energy particles at the loop ends, which should correspond to observed Hard X-ray sources, expands radially as the event proceeds (due to the reconnection of the loop field with the surrounding axial field). The distribution of particles impinging on the footpoints also depends to some extent on the initial loop current profile.

Test particle models are limited in validity due to the neglect of the electromagnetic fields generated by the particles. Therefore, in future, we propose to develop self-consistent models of particle acceleration using gyro-kinetic or other approaches. Nevertheless, the effects of fields generated by the energetic particles are likely to be less significant in the models presented here (compared with localised reconnection sites) due to the almost-uniform volumetric distribution of high-energy ions and electrons – though exact current neutrality is still unlikely. The significance of the particle feedback on the fields depends also on the efficiency of the acceleration (the fraction of the energy transferred to the non-thermal particles), which depends quite strongly on the model parameters [12].

We have shown that kink-unstable twisted loops can develop fragmented current sheets in which fast magnetic reconnection dissipates magnetic energy and the field relaxes towards a lower-energy equilibrium. Reconnection heats the plasma and generates non-thermal ion and electron populations which fill the loop. Such a process may explain the origin of the large number of high-energy charged particles observed in (small) solar flares. If a loop is continually twisted by footpoint motions, the process repeats, giving a sequence of heating events of various sizes. In a simple cylindrical loop, a power-law distribution of event sizes (a nanoflare distribution) can result, whose combined heating effect is sufficient to explain the high temperature of the solar corona.

Acknowledgements We are grateful to the UK Science and Technology Facilities Council for financial support. Numerical simulations were undertaken using the UK MHD consortium facilities, funded by STFC and SRIF

References

1. Arber T D, Longbottom A W, Gerrard C L and Milne M 2001 *J. Comp. Phys.* **171** 151
2. Bareford M R, Browning P K and Van der Linden R A M 2010 *Astron. Astrophys.* **521** A70
3. Bareford M R, Browning P K and Van der Linden R A M 2011 *Sol. Phys.* **273** 93
4. Benz A 0 2008 *Living Reviews in Solar Physics* **5** 1
5. Brown J C et al 2009 *Astron. Astrophys.* **508** 993
6. Browning P K and Van der Linden R A M 2003 *Astron. Astrophys.* **400** 355
7. Browning P K et al 2008 *Astron. Astrophys.* **485** 837
8. Browning P K, Gordovskyy M, Stanier A, Hood A and Dalla S 2011 *Plas. Phys. Cont. Fus.* **53** 124030
9. Gordovskyy M, Browning P K and Vekstein GE 2010a *Astron. Astrophys.* **519** A21
10. Gordovskyy M, Browning P K and Vekstein GE 2010b *Astrophys. J.* **720** 1603
11. Gordovskyy M and Browning P K 2011a *Astrophys. J.* **729** 101
12. Gordovskyy M and Browning P K 2012 *Sol. Phys.* in press

13. Gordovskyy M, Browning P K, Bian N and Kontar E 2012 *Sol. Phys.* submitted
14. Heyvaerts J and Priest E R 1984 *Astron. Astrophys.* **137** 63
15. Hood A W, Browning P K and Van der Linden R A M 2009 *Astron. Astrophys.* **506** 913
16. Lin R P, Krucker S, Hurford G J et al 2003 *Astrophys.J.* **595** L66
17. Parker E N 1988 *Ap. J.* **330** 474
18. Taylor J B 1974 *Phys. Rev. Lett.* **33** 1139
19. Zharkova V et al 2011 *Space Sci. Rev.* **159** 357

Plasma Relaxation in Hall Magnetohydrodynamics

Bhimsen K. Shivamoggi

Abstract Parker's formulation of isotopological plasma relaxation process in magnetohydrodynamics (MHD) is extended to Hall MHD. The torsion coefficient α in the Hall MHD Beltrami condition turns out now to be proportional to the potential vorticity. The Hall MHD Beltrami condition becomes equivalent to the potential vorticity conservation equation in two-dimensional (2D) hydrodynamics if the Hall MHD Lagrange multiplier β is taken to be proportional to the potential vorticity as well. The winding pattern of the magnetic field lines in Hall MHD then appears to evolve in the same way as potential vorticity lines in 2D hydrodynamics.

1 Introduction

A significant class of exact solutions of the equations governing magnetohydrodynamics (MHD) emerges under the Beltrami condition – the local current density is proportional to the magnetic field – the *force-free* state (Lundquist [1], Lust and Schluter [2]). These Beltrami solutions turned out to correlate well with real plasma behavior (Priest and Forbes [3], Schindler [4]). Parker [5–7] showed that, in certain plasma relaxation processes, the Beltrami condition is indeed equivalent to the vorticity conservation equation in two-dimensional (2D) hydrodynamics (and the Lagrange multiplier α turned out to be proportional to vorticity).

In a high-β plasma, on length scales in the range $d_e < \ell < d_i$, where d_s is the skin depth, $d_s \equiv c/\omega_{p_s}$, $s = i, e$ (i and e referring to the ions and electrons, respectively), the electrons decouple from the ions. This results in an additional transport mechanism for the magnetic field via the Hall current (Sonnerup [8]), which is the ion-inertia contribution in Ohm's law. The Hall effect leads to the generation of whistler waves whose,

B.K. Shivamoggi (✉)
University of Central Florida, Orlando, FL 32816-1364, USA
e-mail: bhimsens@mail.ucf.edu

Shivamoggi, B.K.: *Plasma Relaxation in Hall Magnetohydrodynamics*.
Astrophys Space Sci Proc. **33**, 77–82 (2012)
DOI 10.1007/978-3-642-30442-2_9, © Springer-Verlag Berlin Heidelberg 2012

- Frequency lies between ion-cyclotron and electron-cyclotron frequencies ω_{c_i} and ω_{c_e}, respectively,
- Phase velocity exceeds that of Alfvén waves for wavelengths parallel to the applied magnetic fields less than d_i.

Further, the decoupling of ions and electrons in a narrow region around the magnetic neutral point (where the ions become unmagnetized while the electrons remain magnetized) allows for rapid electron flows in the ion-dissipation region and hence a faster magnetic reconnection process in the Hall MHD regime (Mandt et al. [9]).

The purpose of this paper is to extend Parker's [5–7] considerations to Hall MHD.

2 Beltrami States in Hall MHD

The Hall MHD equations (which were formulated by Lighthill [10] following his far-sighted recognition of the importance of the Hall term in the generalized Ohm's law) are (in usual notations),

$$\frac{\partial \boldsymbol{\Omega}_i}{\partial t} = \nabla \times (\mathbf{v}_i \times \boldsymbol{\Omega}_i) \tag{1}$$

$$\frac{\partial \mathbf{A}}{\partial t} = \frac{1}{c}\mathbf{v}_i \times \mathbf{B} - \frac{1}{nec}\mathbf{J} \times \mathbf{B} \tag{2}$$

where n is the number density of ions (or electrons) and $\boldsymbol{\Omega}_i$ is the generalized vorticity,

$$\boldsymbol{\Omega}_i \equiv \boldsymbol{\omega}_i + \boldsymbol{\omega}_{c_i},\ \boldsymbol{\omega}_i \equiv \nabla \times \mathbf{v}_i,\ \boldsymbol{\omega}_{c_i} \equiv \frac{e\mathbf{B}}{m_i c}. \tag{3}$$

Here, we have considered an incompressible, two-fluid, quasi-neutral plasma and have neglected the electron inertia.

A significant class of exact solutions of the Hall MHD Eqs. (1) and (2) emerges as the end result of the isotopological energy-lowering Beltramization process. The Hall MHD Beltrami state is characterized by (Turner [11], Shivamoggi [12]),

$$\frac{1}{c}(\mathbf{J} - ne\mathbf{v}_i) = \lambda_{(1)}\mathbf{B} \tag{4}$$

and

$$m_i n \mathbf{v}_i = \lambda_{(2)}\boldsymbol{\Omega}_i. \tag{5}$$

Combining (4) and (5), we obtain

$$\frac{m_i}{e}\nabla \times \mathbf{B} - \left(\lambda_{(1)}\frac{m_i}{e} + \frac{e}{m_i c}\lambda_{(2)}\right)\mathbf{B} = \lambda_{(2)}\boldsymbol{\omega}_i. \tag{6}$$

3 Plasma Relaxation in an Applied Uniform Magnetic Field

Consider now, following Parker [5–7], a plasma in an applied uniform magnetic field $\mathbf{B}_0 = B_0\hat{\mathbf{i}}_z$ and confined between two infinite parallel planes $z = 0$ and L, which relaxes[1] isotopologically toward the lowest available energy state described by Eq. (6) written in the form

$$\nabla \times \mathbf{B} = \alpha \mathbf{B} + \beta \boldsymbol{\omega}_i . \tag{7}$$

The MHD Lagrange multiplier α may be interpreted as the torsion coefficient while β is the Hall MHD Lagrange multiplier.

Suppose this process exhibits slow variations in the z-direction, characterized by the slow spatial scale,

$$\xi \equiv \epsilon z, \epsilon \ll 1. \tag{8}$$

Let the magnetic field involved in this process be given by

$$\mathbf{B} = \langle \epsilon B_0 b_x,\ \epsilon B_0 b_y,\ B_0 \left(1 + \epsilon b_z\right) \rangle \tag{9}$$

and the Lagrange multipliers α and β be given by

$$\alpha = \epsilon a,\ \beta = \epsilon b. \tag{10}$$

Using (8)–(10), Eq. (5) may be written as

$$v_x = \sigma \left(c_1 \epsilon b_x + \omega_x\right) \tag{11a}$$

$$v_y = \sigma \left(c_1 \epsilon b_y + \omega_y\right) \tag{11b}$$

$$v_z = \sigma \left[c_1 \left(1 + \epsilon b_z\right) + \epsilon \omega_z\right]. \tag{11c}$$

The out-of-plane (or *toroidal*) ion flow ($v_z \neq 0$) is peculiar to Hall MHD. Here, σ and c_1 are appropriate constants. Equation 7 leads to

$$\frac{\partial b_z}{\partial y} - \epsilon \frac{\partial b_y}{\partial \xi} = \epsilon a b_x + \epsilon b \omega_x \tag{12a}$$

$$\epsilon \frac{\partial b_x}{\partial \xi} - \frac{\partial b_z}{\partial x} = \epsilon a b_y + \epsilon b \omega_y \tag{12b}$$

$$\frac{\partial b_y}{\partial x} - \frac{\partial b_x}{\partial y} = a \left(1 + \epsilon b_z\right) + \epsilon b \omega_z \tag{12c}$$

[1] In this process, the magnetic field lines extending between the planes $z = 0$ and L are wrapped around and intermixed by the motion of their foot points on these planes (Parker [5–7]).

and the divergence-free condition on **B** leads to

$$\frac{\partial b_x}{\partial x} + \frac{\partial b_y}{\partial y} + \epsilon \frac{\partial b_z}{\partial \xi} = 0. \tag{13}$$

On the other hand, taking the divergence of Eq. (7), we obtain

$$\mathbf{B} \cdot \nabla \alpha + \boldsymbol{\omega}_i \cdot \nabla \beta = 0 \tag{14}$$

which, on using (8)–(10), leads to

$$b_x \frac{\partial a}{\partial x} + b_y \frac{\partial a}{\partial y} + (1 + \epsilon b_z) \frac{\partial a}{\partial \xi} + \omega_x \frac{\partial b}{\partial x} + \omega_y \frac{\partial b}{\partial y} + \epsilon \omega_z \frac{\partial b}{\partial \xi} = 0. \tag{15}$$

Equations 12a and 12b imply,

$$b_z \sim O(\epsilon). \tag{16}$$

Using (16), Eq. (13) leads to, to $O(1)$,

$$b_x = \frac{\partial \psi}{\partial y}, \; b_y = -\frac{\partial \psi}{\partial x} \tag{17}$$

for some magnetic flux function $\psi = \psi(x, y)$.

Using (17), we obtain from (11), to $O(\epsilon)$,

$$\frac{\partial v_x}{\partial y} = \sigma \left(c_1 \epsilon \frac{\partial^2 \psi}{\partial y^2} + \epsilon \frac{\partial^2 v_z}{\partial y^2} \right) \tag{18a}$$

$$\frac{\partial v_y}{\partial x} = \sigma \left(-c_1 \epsilon \frac{\partial^2 \psi}{\partial x^2} - \epsilon \frac{\partial^2 v_z}{\partial x^2} \right) \tag{18b}$$

and hence,

$$\omega_z \equiv \frac{\partial v_y}{\partial x} - \frac{\partial v_x}{\partial y} = -\sigma \epsilon \left(c_1 \nabla^2 \psi + \nabla^2 v_z \right) \tag{19}$$

where,

$$\nabla^2 \equiv \frac{\partial^2}{\partial x^2} + \frac{\partial^2}{\partial y^2}.$$

Next, using (17), Eq. (12c) leads to, to $O(1)$,

$$a = -\nabla^2 \psi. \tag{20}$$

Using (19), and putting

$$\omega_z \equiv \epsilon\sigma c_1 \omega \tag{21}$$

Eq. (20) leads to

$$a = q \equiv \omega + \frac{1}{c_1}\nabla^2 v_z \tag{22}$$

implying that the torsion coefficient α is proportional to the "*potential vorticity*" q in Hall MHD.

On the other hand, using (11) and (22), Eq. (15) leads to, to $O(\epsilon)$,

$$\epsilon\sigma c_1 \frac{\partial q}{\partial \xi} + v_x \frac{\partial q}{\partial x} + v_y \frac{\partial q}{\partial y} + \sigma\epsilon\left[(q - c_1 b), v_z\right] = 0 \tag{23}$$

where,

$$[f, g] \equiv \frac{\partial f}{\partial x}\frac{\partial g}{\partial y} - \frac{\partial f}{\partial y}\frac{\partial g}{\partial x}.$$

If we take the other Lagrange multiplier b also to be proportional to the "*potential vorticity*" q, i.e.,

$$b = \frac{1}{c_1} q \tag{24}$$

Eq. (23) becomes the "*potential vorticity*" conservation equation in 2D hydrodynamics (on identifying ξ with t),

$$\epsilon\sigma c_1 \frac{\partial q}{\partial \xi} + v_x \frac{\partial q}{\partial x} + v_y \frac{\partial q}{\partial y} = 0. \tag{25}$$

Thus, the Beltrami condition (7) in Hall MHD becomes equivalent to the "*potential vorticity*" conservation equation in 2D hydrodynamics if the Hall MHD Lagrange multiplier β is taken to be proportional to the "*potential vorticity*" q as well.[2] Equation 22 then implies that the winding pattern of the magnetic field lines in Hall MHD evolves in the same way as "*potential vorticity*" lines in 2D hydrodynamics.

4 Discussion

In this paper, we have extended Parker's [5–7] formulation of isotopological plasma relaxation process in MHD to Hall MHD. The torsion coefficient α in the Hall MHD Beltrami condition turns out now to be proportional to the "*potential vorticity*."

[2] Equation 24 is *sufficient* but not necessary to obtain Eq. (25).

The Hall MHD Beltrami condition becomes equivalent to the "*potential vorticity*" conservation equation in 2D hydrodynamics if the Hall MHD Lagrange multiplier β is taken to be proportional to the "*potential vorticity*" as well. The winding pattern of the magnetic field lines in Hall MHD then appears to evolve in the same way as "*potential vorticity*" lines in 2D hydrodynamics. The analogy between a smooth, continuous magnetic field in Hall MHD and 2D hydrodynamics as in ordinary MHD (Parker [7]) implies that the current sheets seem to have the same role in the development of Hall MHD equilibria as they do in the MHD case.

Acknowledgements This work was a result of my participation at the International Astrophysics Forum, Alpbach, 2011. I am thankful to Professor Eugene Parker for helpful suggestions and giving me access to Ref. [7] prior to publication and Professors Manfred Leubner and Zoltán Vörös for their hospitality.

References

1. S. Lundquist: *Arkiv. Fysik* **2**, 361, (1950).
2. R. Lust and A. Schluter: Z. Astrophys. **34**, 263, (1954).
3. E. R. Priest and T. Forbes: *Magnetic Reconnection*, Cambridge Univ. Press, (2000).
4. K. Schindler: *Physics of Space Plasma Activity*, Cambridge Univ. Press, (2007).
5. E. N. Parker: *Geophys. Astrophys. Fluid Dyn.* **34**, 243, (1986).
6. E. N. Parker: *Conversations on Electric and Magnetic Fields in the Cosmos*, Princeton Univ. Press, Ch. 10, (2007).
7. E. N. Parker: Field line topology and rapid reconnection, in *International Astrophysics Forum, Alpbach*, (2011).
8. B. U. O. Sonnerup: in *Solar System Plasma Physics*, Ed. L. J. Lanzerotti, C. F. Kennel and E. N. Parker, North Holland, p. 45, (1979).
9. M. E. Mandt, R. E. Denton and J. F. Drake: *Geophys. Res. Lett.* **21**, 73, (1994).
10. M. J. Lighthill: *Phil. Trans. Roy. Soc.* (London) **A 252**, 397, (1960).
11. L. Turner: *IEEE Trans. Plasma Sci.* **PS-14**, B49, (1986).
12. B. K. Shivamoggi: *Euro. Phys. J. D* **64**, 404, (2011).

Alfvén Waves in Dusty Proto-Stellar Accretion Disks

Aline de Almeida Vidotto and Vera Jatenco-Pereira

Abstract The magneto-rotational instability (MRI) is believed to be the mechanism responsible for a magneto-hydrodynamic (MHD) turbulence that could lead to the accretion observed in proto-stellar accretion disks. A minimum amount of ionization in this medium is necessary for the MRI to take place. In this work we study the role of MHD waves as an additional source of heating in disks. As dust is present in this medium, we suggest that the Alfvén waves are damped by the dust-cyclotron mechanism of damping. We present a disk model with two heating mechanisms: the "anomalous" viscosity considered in terms of the α-parameterization and the damping of Alfvén waves. We show that the waves can increase the temperature of the disk and can reduce the quiescent region.

1 Introduction

The magneto-rotational instability (MRI, [1]) is probably the mechanism responsible for a magneto-hydrodynamic (MHD) turbulence that leads to disk accretion: it provides a necessary torque for the disk's particles to lose angular momentum and to move towards the central object. Gammie [4] proposed the concept of a quiescent layer (called *dead zone*), not enough ionized, making difficult the operation of the MRI in an accretion disk.

A. de Almeida Vidotto (✉)
SUPA, School of Physics and Astronomy, University of St. Andrews, North Haugh, St. Andrews KY169SS, UK
e-mail: Aline.Vidotto@st-andrews.ac.uk

V. Jatenco-Pereira
Institute of Astronomy, Geophysics and Atmosferic Sciences, University of São Paulo, Rua do Matão 1226, São Paulo, SP 05508-090, Brazil
e-mail: jatenco@astro.iag.usp.br

de Almeida Vidotto, A. and Jatenco-Pereira, V.: *Alfvén Waves in Dusty Proto-Stellar Accretion Disks*. Astrophys Space Sci Proc. **33**, 83–87 (2012)
DOI 10.1007/978-3-642-30442-2_10, © Springer-Verlag Berlin Heidelberg 2012

In this work we propose a new mechanism of ionization: the damping of Alfvén waves as an additional heating mechanism in the disk. Although this non-thermal heating mechanism was already suggested by Vasconcelos et al. [13], it was not considered in the context of the presence of a dusty plasma.

In this work we concentrate at an early phase of disk formation. We assume grains and gas well mixed and disk in stationary state. In Sect. 2, we describe the α disk model used to make the initial set up of the disk structure and the α disk model with Alfvén waves. We also describe the mechanism responsible for the wave damping. In Sect. 3 we present our results and the conclusion of this work.

2 Model

In a magnetized and turbulent media as found in star formation sites it is feasible that MHD modes can arise. Several works study the propagation of Alfvén waves in astrophysical media (e.g. [3, 5, 7]). Here, we analyze the damping mechanism caused by the interaction of the waves with charged grains.

2.1 α Disk Model

To make the initial set up of the disk structure we adopt the Shakura and Sunyaev's model [10] with appropriate changes for a cold ambient: we neglect the radiation pressure term in the equation of state and we also admit that the opacity is suitable for this medium. The disk model assumptions are vertically isothermal, geometrically thin, optically thick, axisymmetric and in Keplerian rotation.

The α-prescription [10] suggests that the viscosity is set by the interaction of turbulent eddies: the maximum size of a turbulent cell cannot exceed the disk scale height (H) and its velocity is less than the sound speed (c_s). Hence the maximum kinematic viscosity is then $\nu_{\max} = Hc_s$. Using the α parameterization, we have $\nu = \alpha H c_s$, where $\alpha \leq 1$.

Following [13], the viscous dissipation provides an energy flux of

$$\mathscr{F}_v(H) = \frac{3\Omega_K^2 \dot{M}}{8\pi}\left[1 - \left(\frac{R_i}{r}\right)^{1/2}\right], \tag{1}$$

where $\Omega_K^2 = GM_\star/R_\star^3$ is the Keplerian rotation velocity, $M_\star$ and $R_\star$, the stellar mass and radius, $\dot{M}$, the mass accretion rate, R_i, the internal disk radius and r the radial coordinate of the disk.

If we consider a disk irradiating like a black-body, we obtain its effective temperature by setting the equilibrium between the energy flux liberated by the viscous dissipation ($\mathscr{F}_v$) and the black-body energy flux (σT_{eff}^4)

$$\sigma T_{\rm eff}^4 = \frac{3\Omega_K^2 \dot{M}}{8\pi}\left[1 - \left(\frac{R_i}{r}\right)^{1/2}\right]. \tag{2}$$

2.2 α Disk Model with Alfvén Waves

Considering an additional source of energy for the disk the equilibrium between energy gained and energy dissipated (blackbody) is not given anymore by Eq. (2). Instead, we should use

$$\mathscr{F}_v(H) + \mathscr{F}_A(H) = \sigma T_{\rm eff}^4, \tag{3}$$

where $\mathscr{F}_A(H)$ is the energy flux dissipated by the Alfvén waves and it is given by

$$\mathscr{F}_A(H) = \int_0^H \frac{\Phi_A}{L} dz. \tag{4}$$

Here $\Phi_A = \epsilon v_A$ is the wave energy flux that is damped along the vertical direction z with a damping length L, ϵ is the volumetric wave energy and v_A the Alfvén velocity.

As the wave energy flux Φ_A is an unknown quantity, we parameterize it in terms of ϵ. Considering $\epsilon = \langle \delta B^2 \rangle/(4\pi)$, where δB is the amplitude of the magnetic field perturbation, we write $\sqrt{\langle \delta B^2 \rangle} = fB$, that means that the perturbation is a fraction f of the magnetic field intensity. This is a free parameter of the model. Hence, we have

$$\Phi_A = \epsilon v_A = f^2 B^2 v_A/(4\pi) = f^2 v_A^3 \rho. \tag{5}$$

To evaluate the damping length, L, in Eq. (4) we considered the dust-cyclotron damping mechanism.

The presence of grains in disks is doubtless as shown by many observations (e.g. [9]). The Alfvén waves can have their properties modified in a dusty medium [8, 11, 14]. Especially, charged grains will acquire a circulation motion around the field lines that is defined by the cyclotron frequency. The dust cyclotron resonance occurs in low frequencies and it can be an important damping mechanism for the Alfvén waves. When the waves and the grains experience the same frequency, a resonance that leads to the damping of the waves occurs. If a distribution of grain sizes is considered, then we obtain a band of resonance frequencies going through the minimum $\omega_{\rm min}$ to the maximum dust-cyclotron frequency $\omega_{\rm max}$. We considered a distribution of grain size given by Mathis et al. [6] for the interestellar medium.

The dispersion relation of the Alfvén waves, with frequencies smaller than the ion cyclotron frequency, considering constant charged dust particles in a neutral and cold dusty plasma, is given by Cramer et al. [2]

$$k_z^2 = u_1 \pm u_2, \tag{6}$$

where u_1 and u_2 are function of size grain distribution, the angular wave frequency, ω, the ion cyclotron frequency, Ω_i, the maximum dust cyclotron frequency (i.e., for the smallest dust grain with mass $m_{\min}$ and charge $q_{\min}$), $\omega_{\max} = q_{\min} B/(m_{\min} c)$, the Alfvén speeds of the ions v_{Ai} and dust, v_{Ad}, respectively, and the speed of light.

Following [14], the right-hand polarized wave (positive sign in Eq. 6) is the mode damped by the dust resonance. In the case of $\omega_{\min} < \omega < \omega_{\max}$, the integral in the particles radii has singularities, whose residues give the complex part of the wave number ($k_z \equiv k_{\mathscr{R}} + i\, k_{\mathscr{C}}$) and that leads to the dust-cyclotron damping of the waves, with damping length $L \equiv L(\omega) = \frac{2\pi}{k_{\mathscr{C}}(\omega)}$.

Writing $\Phi^0_{A\omega}$ as the initial wave energy flux per frequency range, we have

$$\Phi^0_A = \int_{\omega_{\min}}^{\omega_{\max}} \Phi^0_{A\omega} d\omega \,, \tag{7}$$

where $\omega_{\min}$ and $\omega_{\max}$ set the limit of the spectral range. We also adopt a power-law for the wave spectrum $\Phi^0_{A\omega} = \Phi^0_{A\omega_0} \left(\frac{\omega}{\omega_0}\right)^{-\beta}$, where we set $\beta = 0.6$ [12].

As $\Phi^0_A \equiv \rho_0 v^3_{A_0} f$ depends on the local conditions of the disk, we have to evaluate it for each position r. For a given f (assumed constant for the entire disk), there is a frequency-integrated energy flux Φ^0_A associated. This total energy flux is spread over the frequencies accordingly to Eq. (7). However, the spectral range will depend on the dust-cyclotron frequencies $\omega_{\min}$ and $\omega_{\max}$ that depend linearly on the magnetic field. As the magnetic field intensity is a function of r, at each position, the total energy flux will be spread in a different spectral region, although the ratio $\omega_{\max}/\omega_{\min}$ is always the same for the entire disk. Also, it is important to note that the total initial flux $\Phi^0_A \propto \rho_0 v^3_{A_0}$ decreases with the distance r.

3 Results and Conclusion

Here we describe the results obtained for a protostar characterized by $M_\star = 0.7\ M_\odot$, $R_\star = 2.5\ R_\odot$, and $\dot{M} = 10^{-7}\ M_\odot\ \mathrm{yr}^{-1}$, and its disks whose mean molecular weight is $\mu = 2.33$ and internal radius $R_i = 2\ R_\star$ using the α prescription $= 10^{-2}$. Our models stop running at the position where the disk becomes optically thin where our assumptions are no longer valid. For the model with Alfvén waves (M-2–M-4 in Table 1) we assume that the gas and dust are always mixed. We fixed the minimum and maximum grain size in $a_{\min} = 0.001$ μm and $a_{\max} = 0.25$ μm, respectively. In Table 1 we present the results for the effective temperature T_{eff} (K) for three different locations of the disk ($[r_1 = 0.1(AU)]$, $[r_2 = 1(AU)]$ and $[r_3(AU)]$ the final distance of models's validity) as a function of the parametrized initial flux of Alfvén waves f.

As can be seen in Table 1, the increase in the initial wave energy flux causes the temperature rise in the regions farther from the central star. It is interesting to note that due to this temperature raising, the model breaks shift to higher r as f increase.

Table 1 Results for the effective temperature $T_{eff}\ (K)$ for three different locations in the disk as a function of the parametrized initial flux of Alfvén waves $[\Phi_A = f^2 v_A^3 \rho]$

Model	f	$T_{eff}\ (K)$	$[r_1(AU)]$	$T_{eff}\ (K)$	$[r_2(AU)]$	$T_{eff}\ (K)$	$[r_3(AU)]$
M-1	–	660	[0.1]	130	[1]	11	[31]
M-2	0.05	690	[0.1]	150	[1]	12	[35]
M-3	0.10	750	[0.1]	170	[1]	14	[39]
M-4	0.20	900	[0.1]	210	[1]	18	[42]

We present a model that suggests that Alfvén waves, present in the quiescent region in proto-stellar accretion disks, can transfer energy to the disk while they propagate and are damped by the interaction with charged dust. We show that the increase in the initial wave energy flux causes a higher temperature in the entire disk due to the wave dissipation, reducing the size of the dead zone.

Acknowledgements The authors would like to thank the Brazilian agencies FAPESP (under grant 04/13846-6) and CNPq (under grant 304184/2010-1) for financial support.

References

1. Balbus, S. A., & Hawley, J. F. 1991, ApJ, 376, 214
2. Cramer, N., Verheest, F., & Vladimirov, S. 2002, Phys. Plasmas, 9, 4845
3. Falceta-Gonçalves, D., Vidotto, A. A., & Jatenco-Pereira, V. 2006, MNRAS, 368, 1145
4. Gammie, C. F. 1996, ApJ, 457, 355
5. Leprovost, N., & Kim, E.-J. 2007, ApJ, 654, 1166
6. Mathis, J., Rumpl, W., & Nordsiek, K. 1977, ApJ, 217, 425
7. Pelletier, G., Lemoine, M., & Marcowith, A. 2006, A&A, 453, 181
8. Pillip, W., Morfill, G., Hartquist, T., & Havnes, O. 1987, ApJ, 314, 341
9. Sicilia-Aguilar, A., Hartmann, L. W., Fürész, G., Henning, T., Dullemond, C., & Brandner, W. 2006, AJ, 132, 2135
10. Shakura, N. I., & Sunyaev, R. A. 1973, A&A, 24, 337
11. Shukla, P. 1992, Phys. Scr., 45, 504
12. Tu, C.-Y., Marsch, E., & Thieme, K. M. 1989, JGR, 94, 11739
13. Vasconcelos, M. J., Jatenco-Pereira, V., & Opher, R. 2000, ApJ, 534, 967
14. Vidotto, A. A., & Jatenco-Pereira, V. 2006, ApJ, 639, 416

Part III
Statistical Physics and Entropy Approaches

Turbulent Equilibrium and Nonextensive Entropy

Peter H. Yoon

Abstract The Boltzmann-Gibbs (BG) entropy has been used in a wide variety of problems for almost 130 years. It is well known that BG entropy is extensive. However, for systems dictated by long-range forces, such as plasmas, the entropy must be non-extensive. Over the years, attempts were made to generalize BG entropy to non-extensive systems. Of these, Tsallis entropy characterized by the q parameter ($q = 1$ being the BG limit) has gained popularity. However, unless q is determined from microscopic dynamics, the model remains a phenomenological tool. To this date very few examples have emerged in which q can be computed from first principles. The present paper demonstrates that for electrons in dynamic equilibrium with steady-state Langmuir turbulence, the q parameter may be computed on the basis of plasma equations. It will also be shown that the steady-state electrons are characterized by a kappa-like velocity distribution, which resembles the most probable state in the Tsallis thermostatics. This strongly suggests that the quasi-equilibrium between Langmuir turbulence and electrons may be characterized by non-extensive entropy concept.

1 Introduction

The celebrated Boltzmann-Gibbs (BG) definition for the entropy $S = -k \sum_{i=1}^{W} p_i \ln p_i$, where p_i is the probability of the system being in a particular microstate, labeled i, has long been used by scientists in a variety of problems for almost 130 years. Here, W represents the combinatorial number of all possible miscrostates

P.H. Yoon (✉)
Institute for Physical Science and Technology, University of Maryland, College Park, MD 20742, USA

School of Space Research, Kyung Hee University, Yongin-Si, Gyeonggi-Do, 446–701, Korea
e-mail: yoonp@umd.edu

Yoon, P.H.: *Turbulent Equilibrium and Nonextensive Entropy*.
Astrophys Space Sci Proc. **33**, 91–96 (2012)
DOI 10.1007/978-3-642-30442-2_11, © Springer-Verlag Berlin Heidelberg 2012

of a system, be it classical or quantum mechanical. The constant k is taken as the Boltzmann constant k_B for thermostatistics, and unity for information system, in which case, it is known as the Shannon entropy. However, it is not too well-known that this definition is not universal. That is, while the definition is eminently suitable for an ideal gas and systems dictated by short-range interactions, for systems interacting through long-range forces, such as the plasma, the applicability of BG entropy has been doubted by a number of scientists, including Boltzmann himself, Einstein, Fermi, and others.

One of the characteristics of BG entropy is that it is additive, i.e., the entropy of the total system is equal to the sum of entropies of subsystems. If A and B represent two subsystems and $A + B$ the total system, then $S(A + B) = S(A) + S(B)$. Over the past many years a number of attempts were made to generalize BG entropy to a non-extensive situation, but the 1988 paper by Tsallis [1] seems to have triggered a recent interest in the non-extensive thermostatics. Tsallis put forth a model entropy of the form $S_q = -k(1-q)^{-1}\left(1 - \sum_{i=1}^{W} p_i^q\right)$ as a generalization to BG entropy. It can be shown that $S_q(A + B) = S_q(A) + S_q(B) + (1-q)\, S_q(A)\, S_q(B)/k$. Here, the parameter q is a measure of how far the system deviates from the BG statistics (for which $q = 1$). It should be noted, however, that Tsallis was not the first to suggest this particular functional form. As Tsallis acknowledges in his recent book [2], a number of scientists already entertained such a functional form for the generalized entropy [3]. The crucial issue is that unless q can be determined from microscopic dynamics, Tsallis' model is at best, a phenomenological tool. To this date, very few examples have emerged that lend themselves to a self-consistent determination of q based on microscopic dynamics [4]. In the present paper, we shall demonstrate that the q parameter in the case of space plasmas may be calculated from microscopic physics.

2 Nonextensive Versus Turbulent Equilibria

Since the 1960s when in situ spacecraft measurements of the charged particle distributions were first made, it was realized that the space plasma did not behave according to the Maxwell-Boltzmann statistics, but instead, the measured distributions typically featured energetic, or superthermal, component [5]. Vasyliunas [6] introduced the phenomenological kappa distribution, $f(v) \sim (1 + v^2/\kappa v_T^2)^{-(\kappa+1)}$ to model the observation, where $v_T = (2k_B T/m)^{1/2}$ is the thermal speed, T and m being the temperature and mass of the charged particles, respectively, and κ is a free fitting parameter. When $\kappa \to \infty$ the model reduces to the Maxwellian-Boltzmann (MB) distribution, $f(v) \sim \exp(-v^2/v_T^2)$.

The kappa model had no justification except that it worked, but later it was realized that it corresponds to the most probable state in Tsallis nonextensive thermostatistics [7]. For a continuous system such as in plasmas, BG entropy can be written as $S = -k_B \int d\mathbf{x} \int d\mathbf{v}\ f(\mathbf{v})\ \ln f(\mathbf{v})$. Upon minimizing the Helmholtz free

energy, $F = U - TS$, where $U = \int d\mathbf{x} \int d\mathbf{v}\ (mv^2/2)\ f(\mathbf{v})$ is the total energy, we find that the Maxwell-Boltzmann distribution naturally emerges as the most probable state. In contrast, upon making use of the continuous version of the Tsallis entropy, to wit,

$$S = -\frac{k_B}{1-q} \int d\mathbf{x} \int d\mathbf{v}\ \{f(\mathbf{v}) - [f(\mathbf{v})]^q\}, \tag{1}$$

the solution

$$f(\mathbf{v}) \sim \left[1 + (1-q)\, v^2/v_T^2\right]^{-1/(1-q)} \tag{2}$$

emerges as the most probable state. Upon defining $\kappa = 1/(1-q)$, it is straightforward to see that this solution is almost the kappa distribution, except that the asymptotic velocity power-law index $\kappa + 1$ is replaced by κ. (Note that in the modified Tsallis thermostatics defined in terms of the so-called "escort" entropy, the most probable state is the true kappa distribution with the velocity power-law index $\kappa + 1$.)

In this paper, we shall present a theory in which the κ (or q) parameter can be calculated from microscopic dynamics. We put forth a theory in which quasi-stationary Langmuir turbulence and superthermal electrons are treated in a self-consistent manner as a turbulent quasi-equilibrium. The set of steady-state Langmuir turbulence-electron system is given by Yoon [8]

$$\frac{\partial f_e}{\partial t} = 0 = \frac{\partial}{\partial v_i}\left(A_i\ f_e + D_{ij}\ \frac{\partial f_e}{\partial v_j}\right),$$

$$A_i = \frac{e^2}{4\pi m_e} \int d\mathbf{k}\ \frac{k_i}{k^2} \sum_{\sigma=\pm 1} (\sigma\omega_{\mathbf{k}})\ \delta(\sigma\omega_{\mathbf{k}} - \mathbf{k}\cdot\mathbf{v}),$$

$$D_{ij} = \frac{\pi e^2}{m_e^2} \int d\mathbf{k}\ \frac{k_i k_j}{k^2} \sum_{\sigma=\pm 1} \delta(\sigma\omega_{\mathbf{k}} - \mathbf{k}\cdot\mathbf{v})\ I_{\mathbf{k}},$$

$$\begin{aligned}\frac{\partial I_{\mathbf{k}}}{\partial t} = 0 = {} & \frac{\pi\omega_{pe}^2}{k^2} \int d\mathbf{v}\ \delta(\omega_{\mathbf{k}} - \mathbf{k}\cdot\mathbf{v}) \left(\frac{ne^2}{\pi}\ f_e + \omega_{\mathbf{k}}\ I_{\mathbf{k}}\, \mathbf{k}\cdot\frac{\partial f_e}{\partial \mathbf{v}}\right) \\ & - \left(\frac{\kappa - 3/2}{\kappa'}\right)^2 \frac{\omega_{\mathbf{k}}^L}{4\pi n\, T_i} \sum_{+,-} \int d\mathbf{k}' \int d\mathbf{v}\ \frac{(\mathbf{k}\cdot\mathbf{k}')^2}{k^2 k'^2} \\ & \times \delta[\omega_{\mathbf{k}} \mp \omega_{\mathbf{k}'} - (\mathbf{k} - \mathbf{k}')\cdot\mathbf{v}] \\ & \times \left[\frac{T_i}{4\pi^2}\left(\pm\omega_{\mathbf{k}'}\ I_{\mathbf{k}} - \omega_{\mathbf{k}}\ I_{\mathbf{k}'}\right) + I_{\mathbf{k}'}\ I_{\mathbf{k}}\,(\omega_{\mathbf{k}} \mp \omega_{\mathbf{k}'})\right] f_i,\end{aligned} \tag{3}$$

where f_e is the electron distribution function (normalized to unity, $\int d\mathbf{v}\ f_e = 1$), e and m_e are unit charge and electron mass, respectively, $I_{\mathbf{k}} = \langle |E_{\mathbf{k}}|^2 \rangle$, represents the Langmuir turbulence spectral intensity, $\mathbf{E}_{\mathbf{k}}$ being the electrostatic field vector

associated with the Langmuir wave, whose dispersion relation is given by $\omega_{\mathbf{k}} \approx \omega_{pe}$, (where $\omega_{pe} = (4\pi n e^2/m_e)^{1/2}$ is the plasma frequency, n being the ambient density), and $\mathbf{k}$ and $\mathbf{v}$ are the wave vector and electron velocity, respectively.

The particle kinetic equation is given by the Fokker-Planck form with the drag (A_i) and velocity space diffusion (D_{ij}) terms, while the wave kinetic equation for the Langmuir turbulence intensity is given in terms of the linear wave-particle resonance term dictated by the delta function $\delta(\omega_{\mathbf{k}} - \mathbf{k}\cdot\mathbf{v})$ and nonlinear wave-particle resonance term with the delta function condition $\delta[\omega_{\mathbf{k}} \mp \omega_{\mathbf{k}'} - (\mathbf{k}-\mathbf{k}')\cdot\mathbf{v}]$.

In a recent pair of works [8], the present author showed that the formal solution for the electron distribution function is given in terms of the reduced distribution, $F_e = 2\pi \int_0^\infty d v_\perp \, v_\perp \, f_e$, where $v_\perp$ and $v_\parallel$ are velocity components perpendicular and parallel to the implicit ambient magnetic field, respectively, by

$$F_e = C \, \exp\left(- \int d v_\parallel \, \frac{m_e v_\parallel}{4\pi^2} \frac{1}{\left[\mathscr{I}(k_\parallel^2) \right]_{k_\parallel^2 = \omega_{pe}^2/v_\parallel^2}} \right), \tag{4}$$

where $C = $ const. In the above we have defined the reduced turbulence intensity $\mathscr{I}(k_\parallel^2)$, where

$$\mathscr{H}(k_\parallel^2) = 2\pi \int_0^\infty \frac{k_\perp \, d k_\perp}{k^2}, \qquad \mathscr{H}(k_\parallel^2) \, \mathscr{I}(k_\parallel^2) = 2\pi \int_0^\infty \frac{k_\perp I(k^2) \, d k_\perp}{k^2}. \tag{5}$$

Here, $k_\perp$ and $k_\parallel$ are wave vector components perpendicular and parallel to the implicit $\mathbf{B}$ field. Reference [8] also shows that the formal steady-state turbulence intensity can be constructed on the basis of the requirement that the spontaneous and induced emissions (linear wave-particle resonance) as well as spontaneous and induced scattering processes (nonlinear wave-particle resonance) individually balance each other,

$$\begin{aligned} 0 &= \int d\mathbf{v} \, \delta(\omega_{\mathbf{k}} - \mathbf{k}\cdot\mathbf{v}) \left(\frac{n e^2}{\pi} \, f_e + \omega_{\mathbf{k}} \, I_{\mathbf{k}} \, \mathbf{k} \cdot \frac{\partial f_e}{\partial \mathbf{v}} \right), \\ 0 &= \sum_{+,-} \int d\mathbf{k}' \int d\mathbf{v} \, \frac{(\mathbf{k}\cdot\mathbf{k}')^2}{k^2 k'^2} \, \delta[\omega_{\mathbf{k}} \mp \omega_{\mathbf{k}'} - (\mathbf{k}-\mathbf{k}')\cdot\mathbf{v}] \\ &\quad \times \left[\frac{T_i}{4\pi^2} \left(\pm\omega_{\mathbf{k}'} \, I_{\mathbf{k}} - \omega_{\mathbf{k}} \, I_{\mathbf{k}'} \right) + I_{\mathbf{k}'} \, I_{\mathbf{k}} \left(\omega_{\mathbf{k}} \mp \omega_{\mathbf{k}'} \right) \right] f_i . \end{aligned} \tag{6}$$

After a number of steps that involve certain approximations, Ref. [8] demonstrates that the following set of velocity distribution function f_e and Langmuir turbulence intensity emerge as the self-consistent steady-state solution (i.e., turbulence equilibrium):

$$f_e(v) = \frac{1}{\pi^{3/2}\, v_{Te}^3}\, \frac{\Gamma(\kappa')}{\kappa'^{3/2}\, \Gamma(\kappa - 3/2)}\, \frac{1}{(1 + v^2/\kappa'\, v_{Te}^2)^{\kappa}},$$

$$I_{\mathbf{k}} = \frac{T_i}{4\pi^2}\, \frac{k_\parallel^2}{k^2}\, \ln\left(1 + \frac{k_0^2}{k_\parallel^2}\right)\left(1 + \frac{2\omega_{pe}^2}{\kappa'\, k^2 v_{Te}^2}\right), \tag{7}$$

provided

$$\kappa = \frac{13}{4} = 3.25, \qquad \kappa' = \frac{T_i}{T_e}\,(\kappa - 1). \tag{8}$$

The mathematical proof is quite involved, but interested readers may refer to Ref. [8].

The important point to emphasize is that the above solution not only shows that the electron distribution corresponds to a kappa-like state, but also that the values of κ (as well as the associated κ') are specifically determined. Consequently, if one may view the turbulent equilibrium between the superthermal electrons and Langmuir waves as representing a nonextensive quasi-equilibrium, then one may argue that the Tsallis q parameter is known.

3 Conclusion and Discussion

To conclude and summarize the essential findings, we have demonstrated through an example involving superthermal electrons and Langmuir turbulence that nonextensive parameter q can be determined on the basis of the plasma turbulence theory. Even though we did not invoke the concept of nonextensive entropy in obtaining the turbulent equilibrium solution, we may argue on the basis of similarity between the kappa-like electron distribution and the most probable state associated with the Tsallis thermostatics, that the turbulent equilibrium may indeed correspond to the nonextensive thermostatistical state. We also note that the plasma with its long-range interaction must, by definition, be nonextensive in nature. On these basis, we have henceforth argued for the equivalence between turbulent and nonextensive equilibria.

We note that there have been previous attempts to provide physical justification for a power-law or kappa-like velocity distribution functions. Most notable work is Ref. [9] in which it was shown a kappa distribution may result from enhanced diffusion due to photon-induced Coulomb-field fluctuations. However, such works do not solve for self-consistent wave kinetic equation, but instead model fluctuation is simply assumed.

In the present discussion the κ or q parameter has a specific value. Observations in space plasmas, however, indicate that a range of the kappa values may be realized depending on the solar-terrestrial activity level (see, e.g., Fig. 1 in Ref. [10]). It may be that the varying κ values in nature may simply be an indication that the space plasmas are not in strict turbulent equilibrium, but for true turbulent equilibrium

condition, the present prediction may be close to the observed value. As a matter of fact, it was brought to the author's attention that the quiet-time solar electrons near 1 AU possess a power-law tail known as the superhalo, with v^{-5} to v^{-8} dependence with a mean value of $v^{-6.9}$. This is close to the present prediction of asymptotic distribution $f \sim v^{-2\kappa} = v^{-6.5}$ for $\kappa = 3.25$ (R.P. Lin, private communications).

Finally, the present discussion focuses on the electron velocity distribution and the Langmuir turbulence. We believe that a similar consideration for ions may give a similar kappa distribution as well. However, in order to prove this, one needs a self-consistent kinetic theory of low-frequency (Alfvénic) turbulence, which at present does not exist.

Acknowledgements PHY acknowledges NSF grants ATM0837878, AGS0940985 and NASA grant NNX09AJ81G to the University of Maryland. PHY also acknowledgee WCU grant No. R31-10016 to Kyung Hee University from the Korean Ministry of Education, Science and Technology.

References

1. Tsallis, C. (1988), J. Stat. Phys. **52**, 479.
2. Tsallis, C., *Introduction to Nonextensive Statistical Mechanics* (Springer, New York, 2009).
3. See the entry 107 in the Bibliography section of Tsallis, C., *Introduction to Nonextensive Statistical Mechanics* (Springer, New York, 2009), p. 347 for a full reference of early works.
4. See Chapter 7 of Tsallis, C., *Introduction to Nonextensive Statistical Mechanics* (Springer, New York, 2009), where the author lists applications for the non-extensive thermostatistics. These include high-energy physics, turbulence, granular matter, geophysics and astrophysics, quantum chaos, etc. In most applications cited by the author the q parameter is given by phenomenological fits.
5. Feldman, W. C., et al. (1975), J. Geophys. Res. **80**, 4181; Gosling, J. T., et al. (1981), J. Geophys. Res. **86**, 547; Armstrong, T. P., et al. (1983), J. Geophys. Res. **88**, 8893, to cite a few early observations.
6. Vasyliunas, V. M. (1968), J. Geophys. Res. **73**, 2839 .
7. See for instance, Leubner, M. P. (2004), Phys. Plasmas **11**, 1308; Livadiotis, G., & McComas, D. J. (2009), J. Geophys. Res. **114**, A11105, doi:10.1029/2009JA014352, and references therein.
8. Yoon, P. H. (2011), Phys. Plasmas **18**, 122303, doi: 10.1063/1.3662105; Yoon, P. H. (2012), Phys. Plasmas **19**, **19**, 012304, doi: 10.1063/1.3676159.
9. Hasegawa, A., Mima, K., and Duong-van (1985), M., Phys. Rev. Lett. **54**, 2608.
10. Lui, A. T. Y. & Krimigis, S. M. (1983), Geophys. Res. Lett. **10**, 13.

Modeling Space Plasma Dynamics with Anisotropic Kappa Distributions

M. Lazar, V. Pierrard, S. Poedts, and R. Schlickeiser

Abstract Space plasmas are collisionpoor and kinetic effects prevail leading to wave fluctuations, which transfer the energy to small scales: wave-particle interactions replace collisions and enhance dispersive effects heating particles and producing suprathermal populations observed at any heliospheric distance in the solar wind. At large distances collisions are not efficient, and the selfgenerated instabilities constrain the solar wind anisotropy including the thermal core and the suprathermal components. The generalized power-laws of Kappa-type are the best fitting model for the observed distributions of particles, and a convenient mathematical tool for modeling their dynamics. But the anisotropic Kappa models are not correlated with the observations leading, in general, to inconsistent effects. This review work aims to reconcile some of the existing Kappa models with the observations.

1 Introduction

Direct in-situ measurements in the solar wind and terrestrial magnetosphere indicate that the velocity distribution functions (VDF) of space plasma particles are quasi-Maxwellian up to the mean thermal velocities (the core component), while they

M. Lazar (✉) · R. Schlickeiser
Institut für Theoretische Physik, Lehrstuhl IV: Weltraum- und Astrophysik, Ruhr-Universität Bochum, D-44780, Bochum, Germany
e-mail: mlazar@tp4.rub.de; rsch@tp4.rub.de

V. Pierrard
Belgian Institute for Space Aeronomy, Space Physics, av. circulaire 3, 1180, Brussels, Belgium
e-mail: viviane.pierrard@oma.be

S. Poedts
Centre for Plasma Astrophysics, Celestijnenlaan 200B, 3001, Leuven, Belgium
e-mail: Stefaan.Poedts@wis.kuleuven.be

Lazar, M. et al.: *Modeling Space Plasma Dynamics with Anisotropic Kappa Distributions*. Astrophys Space Sci Proc. **33**, 97–107 (2012)
DOI 10.1007/978-3-642-30442-2_12, © Springer-Verlag Berlin Heidelberg 2012

exhibit non-Maxwellian suprathermal tails (the halo component) at higher energies (see recent reviews of Marsch [1] and Pierrard and Lazar [2], and references therein). Processes by which the suprathermal particles are produced and accelerated [3–8] are of increasing interest for applications in astrophysics and laboratory or fusion plasma devices where they are known as the *runaway* particles decoupled from the thermal state of motion. The solar wind generally appears to involve an abundance of suprathermal electrons and ions observed to occur in the interplanetary medium, and their analysis provides valuable information about their source, whether it is in the Sun or outer heliosphere.

Accelerated particles (including electrons, protons and minor ions) are detected at any heliospheric distance in the quiet wind as well as in the solar energetic particle (SEP) events associated to flares and coronal mass ejections (CMEs) during solar maximum (see reviews by Lin [9] and Pierrard and Lazar [2]). A steady-state suprathermal ion population is observed throughout the inner heliosphere with a VDF close to $\sim v^{-5}$ [10], and, on the largest scales, the relativistic cosmic-ray gas also plays such a dynamical role through the galaxy and its halo [11].

2 Wave Instability Constraints of the Suprathermal Anisotropy

Nonthermal features and kinetic anisotropies like temperature anisotropies, heat fluxes or particle streams are also a characteristic of the solar wind and near the Earth's magnetosphere [1]. At low altitudes in the solar wind, velocity distributions of plasma particles regularly show an excess of kinetic energy transverse to the local mean magnetic field ($T_\perp > T_\parallel$, where $\perp$, and $\parallel$ denote directions with respect to the magnetic field) most probably due to the compression exerted by the strong guiding magnetic field near the Sun. At larger heliospheric distances, the anisotropy is controlled by the Chew-Goldberger-Low mechanism: the adiabatic expansion of the poorcollision plasma increases the pressure and temperature along the magnetic field leading to $T_\parallel > T_\perp$ (Fig. 1). In more violent interplanetary shocks resulting after solar flares and coronal mass ejections (CME), injection of particle beams into the ionized interplanetary medium creates additional anisotropy [1, 9].

The high rate of occurrence of an excess of perpendicular temperature ($T_\perp > T_\parallel$) in measurements at large distances [13, 14] is a proof that other mechanisms of acceleration, namely, the wave-particle interaction, must be at work there dominating the adiabatic expansion. Indeed, large deviations from isotropy quickly relax by the resulting wave instabilities, which act either to scatter particles back to isotropy, or to accelerate lower energetic particles (Landau or cyclotron heating) and maintain a suprathermal abundance because thermalization is not efficient at these scales [1].

None of these processes is well understood, mostly because these plasmas are low-collisional and require progress in modeling the wave turbulence, going beyond

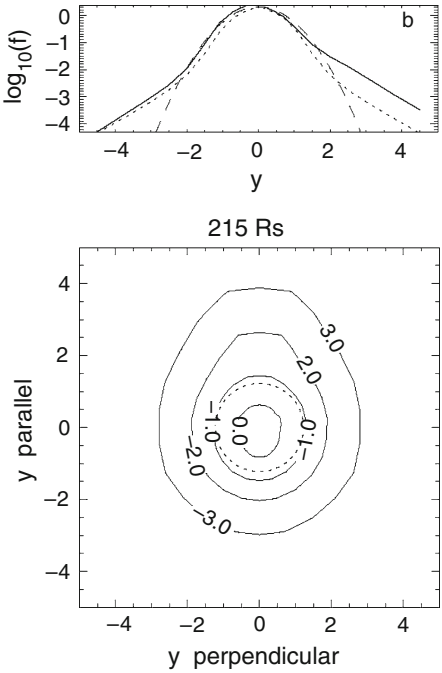

Fig. 1 Electron velocity distributions observed by *Wind* mission at 1 AU, as energy spectra (*top*) parallel (*solid*) and perpendicular (*dashed*) to magnetic field; and velocity space contours (*bottom*) in a high-speed solar wind. Note the anisotropic isodensity contours, less for the core and more pronounced for the halo and the strahl in fast solar wind (After Pierrard et al. [12])

MHD models to use a kinetic and selfconsistent description. In such plasmas transport of matter and energy is governed by the selfcorrelation between particles and electromagnetic fields, which can, for instance, convect charged particles in phase space but are themselves created by these particles. Thus, the suprathermal populations involve selfconsistently in both processes of wave turbulence generation and particle energization, and the resulting Kappa functions that elegantly describes distributions measured in the solar wind [2], represent therefore not only a convenient mathematical tool, but a natural and quite general state of the plasma [15].

While the thermal core in the solar wind is less anisotropic, the superthermal halo has in general a pronounced temperature anisotropy ($T_\perp \neq T_\parallel$) with respect to the local magnetic field [1, 2]. Deformations of the VDFs observed in the solar wind are not as strong as one would expect from a free motion of particles [14, 24, 25]. Because collisions are not effective, any increase of kinetic anisotropy is limited by converting the excess of free energy into electromagnetic fluctuations, and pitch-angle diffusion [26]. Modeling the VDF with a bi-Maxwellian, the instability thresholds shape precisely the core (Fig. 2, left) but show regularly an important departure from to the halo limits (Fig. 2, right). While the whistler instability limits the perpendicular temperature to grow ($T_\perp > T_\parallel$), the firehose instability constrains any excess of parallel temperature ($T_\perp < T_\parallel$). Suprathermal particles cannot fit into a Maxwellian approach ($\kappa \to \infty$), but must be modeled with an appropriate Kappa function. A bi-Kappa (or bi-Lorentzian) function has extensively been used to model gyrotropic distributions and their dispersion/stability properties [16, 17]

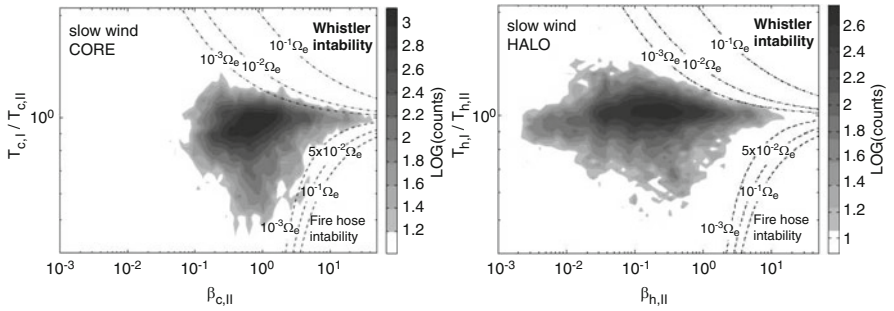

Fig. 2 Solar wind electron temperature anisotropy ($T_\perp/T_\parallel$) versus $\beta_\parallel$: the instability thresholds from a bi-Maxwellian model do not constrain the suprathermal halo (After Stverak et al. [14])

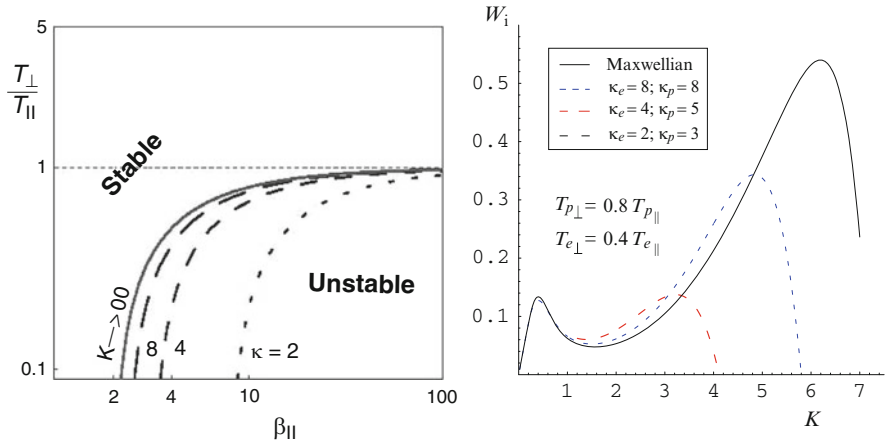

Fig. 3 Firehose instability: thresholds (*left*) and growth rates (*right*) from a bi-Kappa model

$$F_1(v_\parallel, v_\perp) = \frac{1}{\pi^{3/2} w_\perp^2 w_\parallel} \frac{\Gamma[\kappa+1]}{\kappa^{3/2}\Gamma[\kappa-1/2]} \left(1 + \frac{v_\parallel^2}{\kappa w_\parallel^2} + \frac{v_\perp^2}{\kappa w_\perp^2}\right)^{-\kappa-1}. \quad (1)$$

However, this model does not provide the expected better fits to the observations. For instance, both instabilities of interest for the electron populations, the whistler and the firehose, are inhibited and threshold constraints do not approach but rather depart from the measured limits of the halo [18, 19, 21, 22]. Marginal conditions of the firehose instability are illustrated in Fig. 3 (left) showing the need for a larger temperature anisotropy and a larger plasma $\beta_\parallel \equiv 8\pi n k_B T_\parallel / B_0^2$ to produce the instability in Kappa distributed plasmas (low values of $\kappa \to 3/2$). By comparison to a bi-Maxwellian ($\kappa \to \infty$), the growth rates are in general reduced and restrained to small wavenumbers (Fig. 3, right) [19, 22]. The same tendency is observed in the evolution of the whistler instability (Fig. 4): by comparison to a bi-Maxwellian

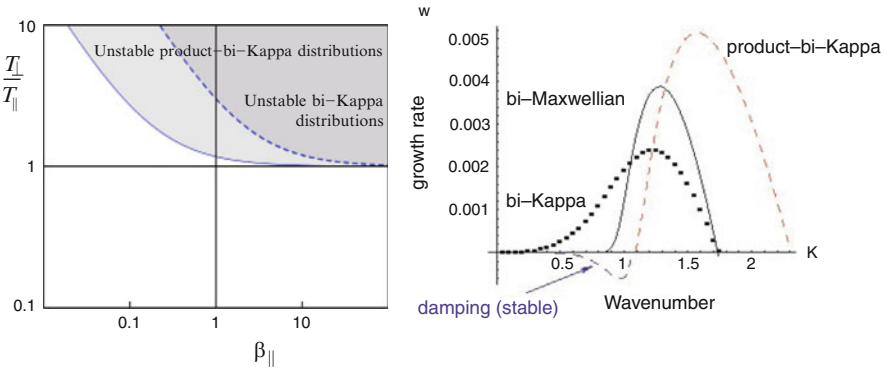

Fig. 4 Whistler instability: thresholds (*left*) and growth rates (*right*) from three different models: the bi-Kappa, the product-bi-Kappa and the bi-Maxwellian (After Lazar et al. [21])

thresholds do not depart much, but the growth rates decrease significantly for lower values of the index κ (Fig. 4, right) [18, 21].

3 Product-bi-Kappa Model

It is evident that a novel Kappa function is needed to model kinetic anisotropies and to incorporate the excess of free energy expected to exist in suprathermal anisotropic plasmas providing better fit to the observations. Recently a new approach has been proposed [20, 21, 23] based on the anisotropic product-bi-Kappa function [16]

$$F_2(v_\parallel, v_\perp) = \frac{w_\perp^{-2}}{\pi^{3/2} w_\parallel} \frac{\Gamma[\kappa_\parallel + 1]}{\kappa_\parallel^{1/2} \Gamma[\kappa_\parallel + \frac{1}{2}]} \left(1 + \frac{v_\parallel^2}{\kappa_\parallel w_\parallel^2}\right)^{-\kappa_\parallel - 1} \left(1 + \frac{v_\perp^2}{\kappa_\perp w_\perp^2}\right)^{-\kappa_\perp - 1}. \quad (2)$$

By contrast to the bi-Kappa function (1), which seems to be less realistic because the two degrees of freedom are coupled and controlled by the same power index κ, the new product-bi-Kappa function shows an advanced flexibility in modeling gyrotropic VDFs with two distinct temperatures $T_{\parallel,\perp}$ and two distinct power indices $\kappa_{\parallel,\perp}$. Thus, a new concept for the particle anisotropy can be introduced by including both anisotropies of the temperatures $T_\parallel \neq T_\perp$ and the Kappa indices $\kappa_\parallel \neq \kappa_\perp$. The analysis becomes therefore more relevant but complicated and this is probably the reason this model was only occasionally invoked (after Summers and Thorne [16] proposed it), merely in a simplified Maxwellian-Kappa form [17]

$$F_3(v_\parallel, v_\perp) = \frac{w_\perp^{-2}}{\pi^{3/2} w_\parallel} \frac{\Gamma[\kappa + 1]}{\kappa^{1/2} \Gamma[\kappa + 1/2]} \left(1 + \frac{v_\parallel^2}{\kappa w_\parallel^2}\right)^{-\kappa - 1} \exp\left(-\frac{v_\perp^2}{w_\perp^2}\right). \quad (3)$$

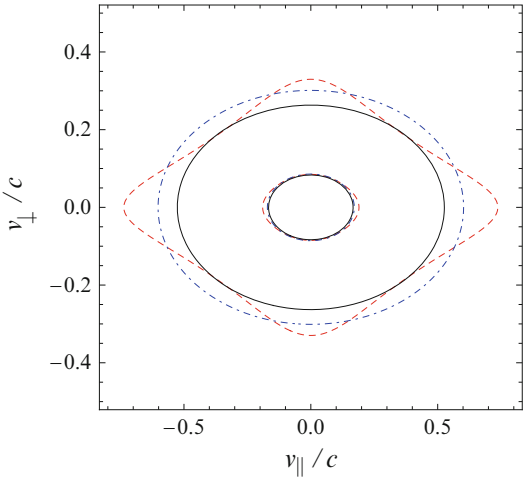

Fig. 5 Two sets of contours, one close to maximum and one close to the minimum base: the bi-Maxwellians ($\kappa_\parallel = \kappa_\perp \to \infty$) with *solid lines*, product-bi-Kappas with *red dashed lines*, and bi-Kappas with *blue dotted-dashed lines* (for the same $v_{T,\parallel}/c = 2v_{T,\perp}/c = 0.2$, and $\kappa_\parallel = \kappa_\perp = 3$)

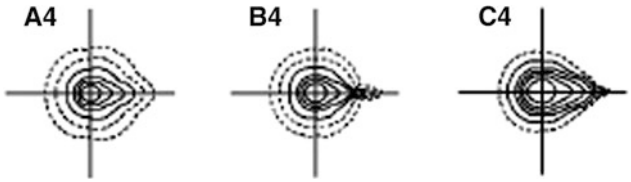

Fig. 6 The electron VDF with a strahl component in the high speed solar wind at a distance (in AU) $R = 0.98$ (*left*), $0.64 \leq R \leq 0.70$ (*middle*) and $0.29 \leq R \leq 0.34$ (*right*) (After Pilipp et al. [27])

The distribution function (2) reduces to distribution function (3) in the limit of very large values of $\kappa_\perp \to \infty$. Thus both forms of the new model represented by the general distribution function (2) or by the particular form (3) reduce to the same bi-Maxwellian in the limit of very large power indices ($\kappa_{\parallel,\perp} \to \infty$).

Contour plots in velocity plane are illustrated in Fig. 5 showing no visible excess of asymmetry of the bi-Kappa (dotted-dashed lines) by comparison to the bi-Maxwellian (solid lines), but a prominent asymmetry and anisotropy of the new product-bi-Kappa distribution function (dashed lines) by comparison to both the bi-Maxwellian and bi-Kappa distribution functions, even for the same temperatures $T_\parallel = T_\perp$, and the same $\kappa_\parallel = \kappa_\perp = \kappa$ [20, 21]. However, the new distribution model and its dispersion properties and stability must directly be confronted to the observations in the solar wind and terrestrial magnetosphere.

Thus, contours of the electron distribution functions measured at different heliospheric distances in a high speed solar wind (see Figs. 6 and 7) show such

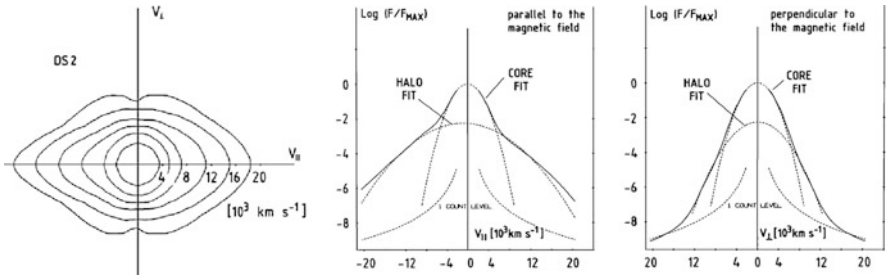

Fig. 7 Contours and one-dimensional cuts of unusual double-strahl distribution function observed by Helios (After Pilipp et al. [28])

skewed, highly anisotropic tails along the magnetic field direction [27, 28], which look quite similar to the product-bi-Kappa contours in Fig. 5. In Fig. 6, skews of the electron distributions are asymmetric being produced by the magnetic field aligned strahl population, which is highly energetic (suprathermal) and antisunward moving [27]. The presumable origin of the strahl electrons is in the energetic ejecta from the coronal holes, and radial evolution show a decreasing with distance from the Sun in the favor of the halo population, which is enhancing [29]. The strahl component is the main driver of the (electron) heat flux, and the main contributor to the anisotropy of suprathermals, apparently a manifestation of the adiabatic focusing.

The quite-time distribution in the fast solar wind (Fig. 6) is modeled by the product-bi-Kappa function only on one side, namely, the outward direction ($v_\parallel > 0$), while semicontours in the backward direction are similar to a bi-Kappa (low anisotropic) model. Analytically one can combine the Eqs. (2) and (3) to form

$$F_4(v_\parallel, v_\perp) = H[-v_\parallel]\, C_L \left(1 + \frac{v_\parallel^2}{\kappa_L w_{L,\parallel}^2} + \frac{v_\perp^2}{\kappa_L w_{L,\perp}^2}\right)^{-\kappa_L - 1} + H[v_\parallel]\, C_R \left(1 + \frac{v_\parallel^2}{\kappa_R w_{R,\parallel}^2}\right)^{-\kappa_R - 1} \exp\left(-\frac{v_\perp^2}{w_{R,\perp}^2}\right), \qquad (4)$$

where $H[x]$ is the Heaviside function, and $C_{L,R}$ are normalization constants. Contour plots are similar to the one-sided strahl observations in Fig. 6. Hence the immediate effect would be a corresponding asymmetric spectrum of the selfgenerated wave fluctuations, which are expected to dominate the outward direction. The future work should explore the stability of this new model and correlate with the observations.

Electron distribution functions (see Fig. 7) with an unusual double strahl have been observed on rare occasions in the solar wind by Helios probes [28]. Contours plots of these distribution function are illustrated in Fig. 7 (left) and show a strong symmetric bidirectional anisotropy very similar to the product-bi-Kappa model

in Fig. 5. Double-strahl distributions would be observed if the spacecraft was fortuitously near the outer end of a magnetic loop connected to the Sun, and electrons coming from both foot points have traveled roughly the same distance and thus may form a symmetric distribution with a counterstreaming strahl aspect. A similar distribution is expected in the observations if the spacecraft was at the outer end of a disconnected large scale loop [28].

Another important confirmation should come from the resulting electromagnetic fluctuations which constrain particle velocity anisotropy to grow [14, 24]. Some preliminary analysis have indeed shown that the whistler instability growth rates (see Fig. 4, right) calculated for the general product-bi-Kappa model are enhanced (dashed line) by comparison to those obtained for a bi-Maxwellian (solid line) or a bi-Kappa model (dotted line), and the instability thresholds illustrated in Fig. 4 (left) tend to approach better the limits of the electron halo in Fig. 2 (right) [21]. Unlike the bi-Maxwellian or bi-Kappa distributions, the product-bi-Kappa anisotropy can be stable against the excitation of the low-wavenumber whistler waves, the critical wavenumber $k_c \simeq \Omega/(\theta_\parallel \sqrt{\kappa_\parallel A})$ is vanishing only for $\kappa_\parallel \to \infty$ (Maxwellian plasma). Moreover, it was shown the instability of an asymmetric Maxwellian-Kappa distribution without an effective temperature anisotropy ($T_\perp = T_\parallel$) against the excitation of the whistler waves propagating obliquely to the magnetic field [30], most probably due to the same asymmetry of contours in velocity space (Fig. 5). Thus, the new product-bi-Kappa model seems to incorporate the excess of free energy expected to exist in anisotropic suprathermal plasmas. For the opposite case ($T_\parallel > T_\perp$), the firehose instability is currently under active investigations, and, according to the preceding discussion, we expect that a product-bi-Kappa model will enhance the growth rates and provide better agreement of the marginal stability with the observed limits of the halo (Fig. 2, right).

Generation of such asymmetric distribution profiles is also supported by the anisotropic turbulence of the solar wind, where the acceleration is expected to occur either perpendicular (cyclotron damping) [5] or in direction (Landau damping) [6] of the interplanetary magnetic field. The nonlinear wave-wave and wave-particle couplings involving intense low-frequency Alfvén waves or electrostatic Langmuir and ion sound (weak) turbulence driven by the beam-plasma instabilities can also be responsible for the acceleration in the corona, solar wind and magnetosphere [4, 7]. However, these models do not provide much guidance on a full 3D evolution of the distribution function and its nonthermal features, like suprathermal tails and kinetic anisotropies, in the acceleration process. This task is still complicated, but will, hopefully, make the object of the next investigations.

4 Conclusions and Perspectives

A large variety of nonthermal features like temperature anisotropies, heat fluxes or particle streams are permanently observed in the solar wind and near the Earth's magnetosphere [1,2]. These do not grow indefinitely, but tend to regulate themselves

since they contain sufficient free energy to drive plasma instabilities and micro-turbulence [25]. Plasma wave turbulence provides the main dissipation mechanisms maintaining a fluid-like behavior of the plasma in spite of the fact that collisional free paths become comparable to the large scales of the heliosphere. Bi-Maxwellian models have extensively been used to describe particle distributions and their dynamics in the solar wind, but the observations clearly indicate the relevance of Kappa distribution functions which incorporate both the quasithermal core and the suprathermal halo. Because the anisotropic Kappa functions are not correlated, in general, with the observations, here we have reviewed these models, and established their direct or indirect confirmations by the observations.

The nondrifting distribution functions used to describe the temperature anisotropy of the different plasma components (with respect to the magnetic field), are the bi-Kappa and product-bi-Kappa functions. The bi-Kappa function seems less realistic because the two degrees of freedom parallel and perpendicular to the magnetic field are coupled and controlled by the same power index k. Instead, the new product-bi-Kappa function shows more flexibility in modeling the gyrotropic VDFs with two distinct temperatures $T_{\parallel,\perp}$ and two distinct power indices $\kappa_{\parallel,\perp}$. A simple comparison of the contours plots show indeed a significant excess of anisotropy of the product-bi-Kappa by comparison to both the bi-Kappa and bi-Maxwellian models.

A further comparison with the contours plots of the measured distributions indicates two important results of our analysis. First, the bi-Kappa model is appropriate to describe particle distributions in the quiet and slow solar wind with a minimum strahl influence and, in general, small deformations of the halo. Secondly, the product-bi-Kappa (including the Maxwellian-Kappa) function seems to be adequate for modeling particle distributions in the fast solar wind with a prominent strahl component in the direction of magnetic field. Moreover, a double-strahl distribution looking just like the product-bi-Kappa contours can be observed near the magnetic large scale loops with electrons counterstreaming from both foot points.

The selfgenerated wave spectra originating from the Kappa models exhibit different properties. Thus, the wave instabilities constrains calculated for a bi-Kappa model do not fit with the halo limits in a slow solar wind as was expected, but those resulting from a product-bi-Kappa model seem to shape the halo electrons for any slow or fast solar wind. This suggests that the new product-bi-Kappa model incorporates in a proper way the excess of free energy expected to exist in anisotropic suprathermal plasmas. Assuming that the same wave fluctuations are the most plausible mechanism of acceleration and formation of suprathermal populations, we conclude pointing out the relevance of our study by the fact that an appropriate Kappa model enables a powerful selfconsistent analysis as it should be itself a product of particle acceleration by the selfexcited fluctuations.

Acknowledgements The authors acknowledge financial support from the Research Foundation Flanders (project G.0729.11), the KU Leuven (project GOA/2009-009, grant F/07/061), ESA Prodex 10 (project C 90205) and by the Deutsche Forschungsgemeinschaft (DFG), grant Schl

201/21-1. Financial support by the European Commission through the SOLAIRE Network (MTRN-CT-2006-035484), and the Seventh Framework Program (FP7/2007-2013) the grant agreement SWIFF (project nr. 2633430, www.swiff.eu) is gratefully acknowledged.

References

1. Marsch E. (2006). Kinetic physics of the solar corona and solar wind, *Living Rev. Solar Phys.* 3
2. Pierrard V. & Lazar M. (2010). Kappa distributions: theory and applications in space plasmas, *Sol. Phys.* 267, 153.
3. Hasegawa A., Mima K. & Duong-van N. (1985). Plasma distribution function in a superthermal radiation field, *Phys. Rev. Lett.* 54, 2608.
4. Miller J.A. & Roberts D.A. (1995). Stochastic proton acceleration by cascading Alfvén waves in impulsive solar flares, *Astrophys. J.* 452, 912.
5. Ma C. & Summers D. (1999). Correction to "Formation of Power-law Energy Spectra in Space Plasmas by Stochastic Acceleration due to Whistler-Mode Waves", *Geophys. Res. Lett.* 26, 1121.
6. Leubner M.P. (2000). Wave induced suprathermal tail generation of electron velocity space distributions, *Planet. Space Sci.* 48, 133.
7. Yoon P.H., T. Rhee & C.-M. Ryu (2006). Self-consistent formation of electron κ distribution: 1. Theory, *J. Geophys. Res.* 111, A09106.
8. Jokipii J.R. & M.A. Lee (2010). Compression acceleration in astrophysical plasmas and the production of $f(v) \sim v^{-5}$ spectra in the heliosphere, *Astrophys. J.* 713, 475.
9. Lin R.P. (1998). Wind observations of suprathermal electrons in interplanetary medium, *Space Sci. Rev.* 86, 61.
10. Fisk L.A. & Gloeckler, G. (2006). The common spectrum for accelerated ions in the quiet-time solar wind, *Astrophys. J.* 640, L79.
11. Schlickeiser R. (2002). *Cosmic Ray Astrophysics*, Springer, Heidelberg.
12. Pierrard V., Maksimovic M. & Lemaire J.F. (1999). Electron velocity distribution functions from the solar wind to corona, *J. Geophys. Res.* 104, 17021.
13. Hellinger, P.; Travnicek, P.; Kasper, J. C. & A. J. Lazarus (2006). Solar wind proton temperature anisotropy: Linear theory and WIND/SWE observations, *Geophys. Res. Lett.*, 33, L09101.
14. Stverak, S.; Travnicek, P.; Maksimovic, M. et al. (2008). Electron temperature anisotropy constraints in the solar wind, *J. Geophys. Res.*, 113, A03103.
15. Leubner M.P. (2002). A nonextensive entropy approach to kappa-distributions, *Astrophys. Space Sci.* 282, 573.
16. Summers D. & R.M. Thorne, 1991. The modified plasma dispersion function, Phys. Fluids B 3, 1835.
17. Hellberg M.A., R.L. Mace & T. Cattaert, 2005. Effects of superthermal particles on waves in magnetized space plasmas, Space Sci. Rev. 121, 127.
18. Lazar M., Schlickeiser R., Poedts S. & Tautz R. (2008). Counterstreaming magnetized plasmas with kappa distributions - I. Parallel wave propagation, *Mon. Not. R. Astron. Soc.*, 390, 168.
19. Lazar. M. & Poedts (2009). Firehose instability in space plasmas with bi-kappa distributions, *Astron. Astrophys.*, 494, 311.
20. Lazar. M., Schlickeiser, R., & Podts S. (2010). Is the Weibel instability enhanced by the suprathermal populations or not?, *Phys. Plasmas*, 17, 062112.
21. Lazar. M., Poedts, S. & Schlickeiser, R. (2011a). Instability of the parallel electromagnetic modes in Kappa distributed plasmas - I. Electron whistler-cyclotron modes, *Mon. Not. R. Astron. Soc.*, 410, 663.
22. Lazar. M., Poedts, S. & Schlickeiser, R. (2011b). Proton firehose instability in bi-Kappa distributed plasmas, *Astron. Astrophys.*, 534, A116.

23. Basu B. (2009). Hydromagnetic waves and instabilities in kappa distribution plasma, *Phys. Plasmas* 16, 052106.
24. Kasper, J. C.; Lazarus, A. J. & Gary S. P. (2002). Wind/SWE observations of firehose constraint on solar wind proton temperature anisotropy, *Geophys. Res. Lett.*, 29, 1839.
25. Bale S.D., Kasper J.C, Howes G.G. et al. (2009). Magnetic fluctuation power near proton temperature anisotropy instability thresholds in the solar wind, *Phys. Rev. Lett.* 103, 211101.
26. Pierrard V., Maksimovic M. & Lemaire J.F. (2001). Self-consistent model of solar wind electrons, *J. Geophys. Res.* 106, 29305.
27. Pilipp W.G., Miggenrieder H., Montgomery M.D., et al. (1987a). Variations of electron distribution functions in the solar wind, *J. Geophys. Res.* 92, 1103;
28. Pilipp W.G., Miggenrieder H., Montgomery M.D., et al. (1987b). Unusual electron distribution functions in the solar wind derived from the Helios plasma experiment: double-strahl distributions and distributions with an extremely anisotropic core, *J. Geophys. Res.* 92, 1093;
29. Maksimovic M., Zouganelis I., J.-Y. Chaufray, et al. (2005). Radial evolution of the electron distribution functions in the fast solar wind between 0.3 and 1.5 AU, *J. Geophys. Res.* 110, A09104.
30. Cattaert, T., Hellberg, M.A., Mace, R.L. (2007). Oblique propagation of electromagnetic waves in a kappa-Maxwellian plasma, *Phys. Plasmas* 14, 082111.

Part IV
Waves, Shocks and Turbulence

Magnetohydrodynamic Waves in Partially Ionized Prominence Plasmas

Roberto Soler and Jose Luis Ballester

Abstract Prominences or filaments are cool clouds of partially ionized plasma living in the solar corona. Ground- and space-based observations have confirmed the presence of oscillatory motions in prominences and they have been interpreted in terms of magnetohydrodynamic (MHD) waves. Existing observational evidence points out that these oscillatory motions are damped in short spatial and temporal scales by some still not well known physical mechanism(s). Since prominences are partially ionized plasmas, a potential mechanism able to damp these oscillations could be ion-neutral collisions. Here, we will review the work done on the effects of partial ionization on MHD waves in prominence plasmas.

1 Introduction

Quiescent solar filaments are clouds of cool and dense plasma suspended against gravity by forces thought to be of magnetic origin. High-resolution H_α observations ([1, 2]) have revealed that the fine structure of filaments is apparently composed by many horizontal and thin dark threads (see [3], for a review). The measured average width of resolved thin threads is about 0.3 arcsec (∼210 km) while their length is between 5 and 40 arcsec (∼3,500–28,000 km). The fine threads of solar filaments seem to be partially filled with cold plasma [1], typically two orders of magnitude denser and cooler than the surrounding corona, and it is generally assumed that they outline their magnetic flux tubes [1, 4–8]. This idea is strongly supported by

R. Soler (✉)
Centre for Plasma Astrophysics, Department of Mathematics, Katholieke Universiteit Leuven, Leuven, Belgium
e-mail: roberto.soler@wis.kuleuven.be

J.L. Ballester
Departament de Física, Universitat de les Illes Balears, Palma, Spain
e-mail: joseluis.ballester@uib.es

Soler, R. and Ballester, J.L.: *Magnetohydrodynamic Waves in Partially Ionized Prominence Plasmas*. Astrophys Space Sci Proc. **33**, 111–121 (2012)
DOI 10.1007/978-3-642-30442-2_13, © Springer-Verlag Berlin Heidelberg 2012

observations which suggest that they are inclined with respect to the filament long axis in a similar way to what has been found for the magnetic field ([9–11]).

Small amplitude oscillations in prominences and filaments are a commonly observed phenomenon. The detected peak velocity ranges from the noise level (down to $0.1\,\mathrm{km\,s^{-1}}$ in some cases) to $2–3\,\mathrm{km\,s^{-1}}$. The observed periodic signals are mainly detected from Doppler velocity measurements and can therefore be associated to the transverse displacement of the fine structures [12]. Two-dimensional observations of filaments [13, 14] revealed that individual threads or groups of threads may oscillate independently with their own periods, which range between 3 and 20 min. Furthermore, [15] have shown evidence about traveling waves along a number of filament threads with an average phase velocity of $12\,\mathrm{km\,s^{-1}}$, a wavelength of $4''$ ($\sim$2,800 km), and oscillatory periods of the individual threads that vary from 3 to 9 min.

Observational evidence for the damping of small amplitude oscillations in prominences can be found in [16]. Observational studies have allowed to obtain some characteristic spatial and time scales. Reliable values for the damping time have been derived, from different Doppler velocity time series by Terradas et al. [17], in prominences, and by Lin [5] in filaments. The values thus obtained are usually between 1 and 4 times the corresponding period, and large regions of prominences/filaments display similar damping times.

Finally, small amplitude oscillations in quiescent filaments have been interpreted in terms of magnetohydrodynamic (MHD) waves [18] and, in many cases, theoretical works studying the damping of prominence oscillations have studied first the effect of a given damping mechanism on MHD waves in a simple, uniform, and unbounded media before to introduce structuring and non-uniformity. This is the approach that we will follow in this paper.

2 MHD Waves in Unbounded Partially Ionized Prominence Plasmas

Since the temperature of prominences is typically of the order of $10^4\,\mathrm{K}$, the prominence plasma is only partially ionized. The exact ionization degree of prominences is unknown and the reported ratio of electron density to neutral hydrogen density [19] covers about two orders of magnitude (0.1–10). Partial ionization brings the presence of neutrals in addition to electrons and ions, thus collisions between the different species are possible. Because of the occurrence of collisions between electrons with neutral atoms and ions, and more importantly between ions and neutrals, Joule dissipation is enhanced when compared with the fully ionized case. A partially ionized plasma can be represented as a single-fluid in the strong coupling approximation, which is valid when the ion density in the plasma is low and the collision time between neutrals and ions is short compared with other time-scales of the problem. Using this approximation it is possible to describe the very low frequency and large-scale fluid-like behaviour of plasmas [20].

Partial ionization affects the induction equation, which contains additional terms due to the presence of neutrals and a non-zero resistivity [21]. These additional terms account for the processes of ohmic diffusion, ambipolar diffusion, and Hall's magnetic diffusion. Ohmic diffusion is mainly due to electron-ion collisions and produces magnetic diffusion parallel to the magnetic field lines; ambipolar diffusion is mostly caused by ion-neutral collisions and Hall's effect is enhanced by ion-neutral collisions since they tend to decouple ions from the magnetic field while electrons remain able to drift with the magnetic field [22]. Due to the presence of neutrals, perpendicular magnetic diffusion is much more efficient than longitudinal magnetic diffusion in a partially ionized plasma. It is important to note that this is so even for a small relative density of neutrals.

2.1 Homogeneous and Unbounded Prominence Medium

Several studies have considered the damping of MHD waves in partially ionized plasmas of the solar atmosphere [23–26]. In the context of solar prominences, [21] derived the full set of MHD equations for a partially ionized, one-fluid hydrogen plasma and applied them to the study of the time damping of linear, adiabatic fast and slow magnetoacoustic waves in an unbounded prominence medium. This study was later extended to the non-adiabatic case, including thermal conduction by neutrals and electrons and radiative losses [27]. Forteza et al. [21] considered a uniform and unbounded prominence plasma and found that ion-neutral collisions are more important for fast waves, for which the ratio of the damping time to the period is in the range 1–10^5, than for slow waves, for which values between 10^4 and 10^8 are obtained. Fast waves are efficiently damped for moderate values of the ionization fraction, while in a nearly fully ionized plasma, the small amount of neutrals is insufficient to damp the perturbations.

In the above studies, a hydrogen plasma was considered, although 90% of the prominence chemical composition is hydrogen while the remaining 10% is helium. The effect of including helium in the model of [27, 28] was assessed by De Pontieu et al. [23]. The species present in the medium are electrons, protons, neutral hydrogen, neutral helium (He I) and singly ionized helium (He II), while the presence of He III is neglected [29].

The hydrogen ionization degree is characterized by $\tilde{\mu}_{\mathrm{H}}$ which is equivalent to the mean atomic weight of a pure hydrogen plasma and ranges between 0.5 for fully ionized hydrogen and 1 for fully neutral hydrogen. The helium ionization degree is characterized by $\delta_{\mathrm{He}} = \frac{\xi_{\mathrm{HeII}}}{\xi_{\mathrm{HeI}}}$, where ξ_{HeII} and ξ_{HeI} denote the relative densities of single ionized and neutral helium, respectively. Figure 1a–c displays τ_D/P as a function of the wavenumber, k, for the Alfvén, fast and slow waves. In this Figure, the results corresponding to several helium abundances are compared for hydrogen and helium ionization degrees of $\tilde{\mu}_{\mathrm{H}} = 0.8$ and $\delta_{\mathrm{He}} = 0.1$, respectively, and it can be observed that the presence of helium has a minor effect on the results.

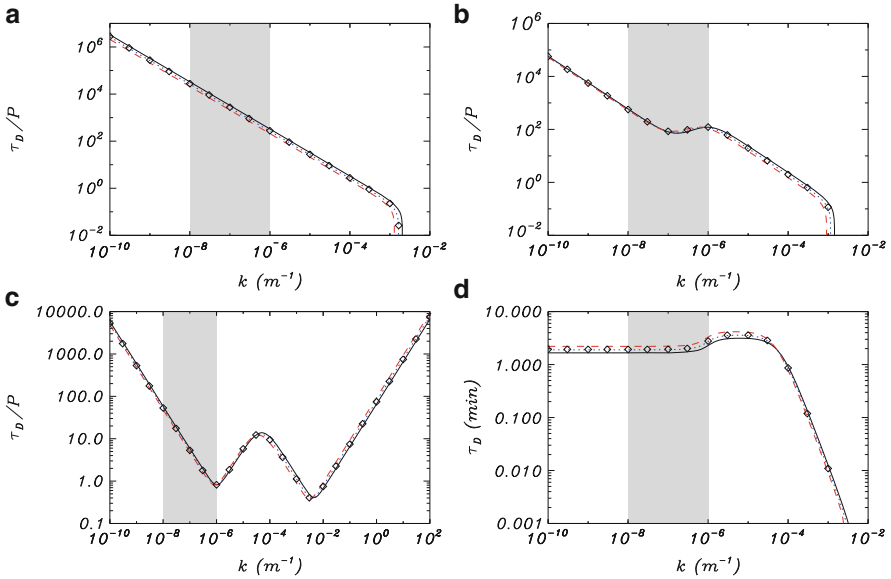

Fig. 1 Wave damping by ion-neutral effects in a uniform medium. (**a**)–(**c**) Ratio of the damping time to the period, τ_D/P, versus the wavenumber, k, corresponding to the Alfvén wave, fast wave and slow wave, respectively. (**d**) Damping time, τ_D, of the thermal wave versus the wavenumber, k. The different linestyles represent the following abundances: $\xi_{\mathrm{HeI}} = 0\%$ (*solid line*), $\xi_{\mathrm{HeII}} = 10\%$ (*dotted line*) and $\xi_{\mathrm{HeI}} = 20\%$ (*dashed line*). In all computations, $\tilde{\mu}_{\mathrm{H}} = 0.8$ and $\delta_{\mathrm{He}} = 0.1$. The results for $\xi_{\mathrm{HeI}} = 10\%$ and $\delta_{\mathrm{He}} = 0.5$ are plotted by means of symbols for comparison. The *shaded* regions correspond to the range of typically observed wavelengths of prominence oscillations. In all the figures shown, the angle, θ, between the wavevector and the magnetic field is $\pi/4$ (From De Pontieu et al. [23])

The thermal mode is a purely damped, non-propagating disturbance ($\omega_r = 0$), so only the damping time, τ_D, is plotted (Fig. 1d). We observe that the effect of helium is different in two ranges of k. For $k > 10^{-4}\,\mathrm{m}^{-1}$, thermal conduction is the dominant damping mechanism, so the larger the amount of helium, the shorter τ_D because of the enhanced thermal conduction by neutral helium atoms. On the other hand, radiative losses are more relevant for $k < 10^{-4}\,\mathrm{m}^{-1}$. In this region, the thermal mode damping time grows as the helium abundance increases. Since these variations in the damping time are very small, we again conclude that the damping time obtained in the absence of helium does not significantly change when helium is taken into account. Therefore, the inclusion of neutral or single ionized helium in partially ionized prominence plasmas does not modify the behaviour of linear, adiabatic or non-adiabatic MHD waves already found by Forteza et al. [21] and [27]. On the other hand, in Fig. 1c we can observe that in the case of slow waves, and within most of the interval of observed wavelengths in prominence oscillations, the ratio between the damping time and the period agrees with the observational determinations, which is due to the joint effect of ion-neutral collisions and non-adiabatic effects ([23, 27, 28]).

3 Magnetohydrodynamic Waves in Prominence Threads

In this Section, we summarize the results of papers which investigate the damping of MHD waves in partially ionized prominence thread models. For simplicity, early investigations neglected the variation of density along the thread and took into account the variation of density in the transverse direction only. Subsequent works incorporated longitudinal inhomogeneity in addition to transverse inhomogeneity.

3.1 Longitudinally Homogeneous Thread Models

The first papers that studied partial ionization effects on wave propagation in a longitudinally homogeneous prominence thread model were [30–32]. These authors investigated linear MHD waves superimposed on a straight magnetic cylinder of radius R, representing the thread itself, and embedded in a fully ionized and uniform coronal plasma. Gravity was neglected and the magnetic field was taken constant along the axis of the cylinder. Soler et al. [30] considered an abrupt jump of density in the transverse direction from the internal (prominence), $\rho_{\rm p}$, to the external (coronal), $\rho_{\rm c}$, densities at the thread boundary, while [31, 32] replaced the discontinuity in density by a continuous variation of density in a region of thickness l. For $l = 0$ the equilibrium of [31, 32] reverts to that of [30]. Hence the ratio l/R indicates the inhomogeneity length-scale in the transverse direction. In both papers the prominence plasma was assumed partially ionized with an arbitrary ionization degree, while the external coronal medium was fully ionized. The single-fluid approximation was adopted and Ohm's, Hall's, and Cowling's terms were included in the induction equation. Thus, the equilibrium configuration is similar to the classical straight flux tube model investigated by, e.g., [33, 34], with the addition of partial ionization. A sketch of the model is displayed in Fig. 2.

In this model the observed transverse oscillations of prominence threads can be interpreted in terms of transverse (Alfvénic) kink modes. Because of their observational relevance, here we discuss the results for transverse (Alfvénic) kink waves only. The interested reader is refereed to the original papers [30–32] where the results of other waves are explained in detail. It is well known that for $l \neq 0$ the kink mode is resonantly coupled to Alfvén continuum modes in the region of transversely non-uniform density. As a consequence the kink mode is damped by resonant absorption. In addition, the kink mode is also damped by magnetic diffusion effects due to partial ionization. In the fully ionized case, the ideal resonant damping of the kink mode in prominence threads was investigated by Engvold [6], Arregui et al. [35] and Soler et al. [36], while partial ionization does not affect the mechanism of resonant absorption, which is an ideal process independent of dissipation by ion-neutral collisions. This has been shown by Soler et al. [37] using multifluid theory.

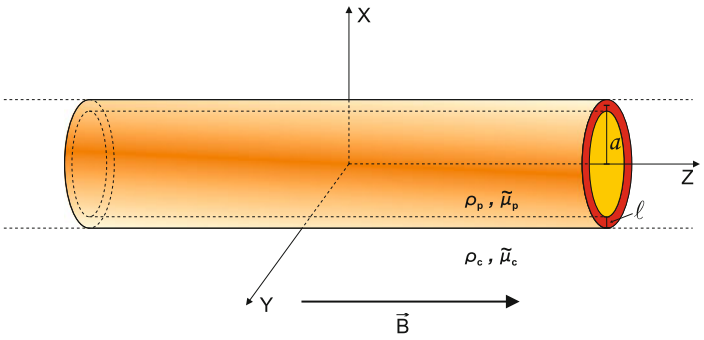

Fig. 2 Sketch of the longitudinally homogeneous prominence thread model used in [30] with $l = 0$ and in [31, 32] with $l \neq 0$. In this Figure a denotes the radius of the cylinder while in the text we use R (Adapted from Soler et al. [32])

Soler et al. [30, 31] studied temporal damping of standing waves. By neglecting the effects of Ohm's and Hall's diffusion in comparison to that of Cowling's diffusion, approximate expressions for the period, P, and for the ratio of the damping time, τ_D, to the period of the kink mode can be obtained in the long-wavelength limit, i.e., $\lambda/R \gg 1$, where λ is the wavelength. The long-wavelength limit is a reasonable approximation since wavelengths typically observed in prominences are roughly between 10^3 and 10^5 km (see [18]) while the observed widths of the threads are between 100 and 600 km (see [3]). The expressions for P and τ_D/P are

$$P = \frac{\lambda}{v_A}\sqrt{\frac{\zeta+1}{2\zeta}}, \tag{1}$$

$$\frac{\tau_D}{P} = \frac{2}{\pi}\left(\frac{l}{R}\frac{\zeta-1}{\zeta+1} + \frac{2\xi_n^2}{1-\xi_n}\frac{\omega_k}{\nu_{in}}\right)^{-1}, \tag{2}$$

where v_A is the prominence Alfvén velocity, $\zeta = \rho_p/\rho_c$ is the density contrast, $\omega_k = 2\pi/P$ is the kink mode frequency (with P given by Eq. (1)), ξ_n is the fraction of neutrals, and ν_{in} the ion-neutral collision frequency. $\xi_n = 0$ for a fully ionized plasma and $\xi_n = 1$ for a neutral medium. To perform a check, we take $\lambda = 10^4$ km, $v_A = 50\,\mathrm{km}^{-1}$, and $\zeta = 200$. Equation 1 gives $P \approx 2.4$ min, which is consistent with the observed periods.

Regarding damping, the first term within the parenthesis of Eq. (2) is due to resonant absorption and the second term is due to Cowling's diffusion. Note that the original expression of τ_D/P given in [31] involves Cowling's diffusivity, η_C. In the present discussion we have replaced η_C by its expression in terms of ξ_n and ν_{in} (see the expression of η_C in, e.g., [30]). Our purpose is to show that the term related to Cowling's diffusion is proportional to the ratio ω_k/ν_{in}. To perform a simple order-of-magnitude estimation of the importance of Cowling's diffusion, let us take a period of 3 min and compute ν_{in} using $\xi_n = 0.5$, a prominence density of $5 \times 10^{-11}\,\mathrm{kg\,m^{-3}}$, and a prominence temperature of 8,000 K (see the expression of

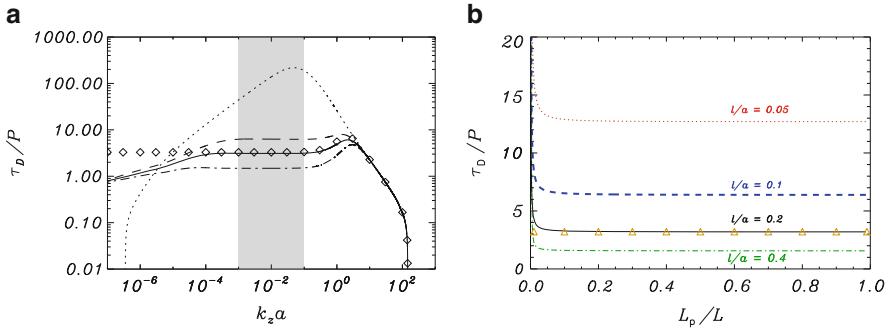

Fig. 3 (**a**) τ_D/P vs. $k_z a$ for the kink mode in a longitudinally homogeneous thread with $l/a = 0$ (*dotted*), $l/a = 0.1$ (*dashed*), $l/a = 0.2$ (*solid*), and $l/a = 0.4$ (*dash-dotted*). The shaded zone denotes realistic wavelengths (Adapted from Soler et al. [31]). (**b**) τ_D/P vs. L_p/L for the kink mode in a longitudinally inhomogeneous thread with $l/a = 0.05$ (*dotted*), $l/a = 0.1$ (*dashed*), $l/a = 0.2$ (*solid*), and $l/a = 0.4$ (*dash-dotted*). Symbols are the result from Eq. (2) with $l/a = 0.2$. In this Figure a denotes the radius of the cylinder while in the text we use R (Adapted from Soler et al. [38])

ν_{in} in [30]). The result is $\omega_k/\nu_{in} \approx 2.38 \times 10^{-4}$. This estimation indicates that the effect of Cowling's diffusion is negligible unless the prominence is almost neutral, i.e., $\xi_n \approx 1$, which is an unrealistic limit. Therefore, resonant absorption dominates the kink mode damping and the second term within the parenthesis of Eq. (2) can be dropped. Hence, for $\zeta = 200$ and $l/R = 0.2$ we obtain $\tau_D/P \approx 3.22$, which again is consistent with the observations.

Soler et al. [31] also obtained results beyond the long-wavelength approximation by means of full numerical solutions. They included Ohm's and Hall's terms along with Cowling's diffusion. Soler et al. [31] computed the kink mode τ_D/P as a function of the parameter $k_z R$, where $k_z = 2\pi/\lambda$ (see Fig. 3a). They concluded that Hall's term is always negligible in prominence conditions, Ohm's diffusion is only important for extremely long wavelengths (very small values of $k_z R$), and Cowling's diffusion is only relevant for short wavelengths (large $k_z R$). For realistic wavelengths, i.e., $10^{-3} < k_z R < 10^{-1}$, resonant absorption determines the damping rate of the kink mode and the analytical formula given in Eq. (2) is very accurate.

Subsequently, [32] used the same model as [31] to study spatial damping of kink waves. The results of [32] are qualitatively equivalent to those of [31], i.e., resonant damping dominates for realistic frequencies whereas Cowling's diffusion is efficient for high frequencies only.

3.2 *Longitudinally Inhomogeneous Thread Models*

A longitudinally homogeneous cylinder is a crude representation of a prominence fine structure. High-resolution observations of prominences (see [3]) suggest that the cool and dense material of the threads only occupies a small part of longer magnetic

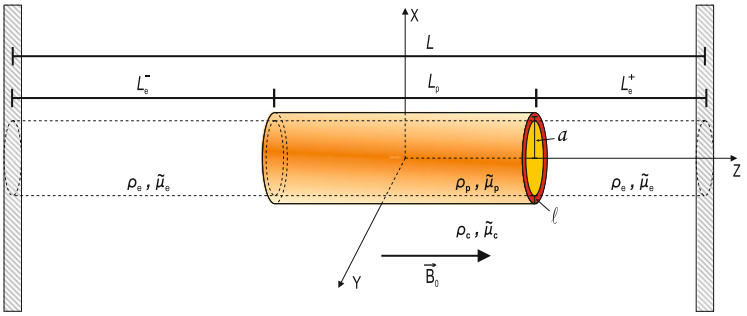

Fig. 4 Sketch of the longitudinally inhomogeneous prominence thread model used in [38]. In this Figure a denotes the radius of the cylinder while in the text we use R (Adapted from Soler et al. [38])

flux tubes, with the rest of the magnetic tube probably filled with hot coronal plasma. The observed length of the threads is believed to be only a small percentage of the total length of the magnetic tube, whose feet are rooted in the solar photosphere [39, 40]. This observational evidence may be omitted to study propagating waves in the dense part of the magnetic tube if the wavelengths are much shorter than the length of the threads. For this case the longitudinally homogeneous models discussed in Sect. 3.1 may be appropriate. However, in the case of standing modes, the associated wavelengths are of the order of the total length of magnetic field lines. Therefore the longitudinal structuring of the prominence magnetic tube cannot be neglected when standing modes are investigated.

This observational evidence has been taken into account in some works which studied ideal, undamped kink modes in the fully ionized case (see, e.g., [25, 41–43]). The first paper that incorporated the effects of damping by Cowling's diffusion and resonant absorption on standing kink modes in longitudinally inhomogeneous threads was [38]. These authors used the model displayed in Fig. 4. It is composed of a straight magnetic cylinder of length L and radius R whose ends are fixed at two rigid walls representing the solar photosphere. The magnetic field is constant. The cylinder is composed of a region of length L_p and density ρ_p, representing the prominence thread, surrounded by two regions of density ρ_e representing the evacuated part of the tube. The external coronal density is ρ_c and for simplicity it is set $\rho_\mathrm{e} = \rho_\mathrm{c}$. The prominence thread is transversely inhomogeneous in a region of thickness l where the density continuously varies from ρ_p to ρ_c. The prominence plasma is partially ionized while the coronal and evacuated plasmas are fully ionized.

To investigate standing kink modes analytically, [38] used the thin tube approximation, i.e., $R/L \ll 1$ and $R/L_\mathrm{p} \ll 1$. To check this approximation we take the values of R and L_p typically reported from the observations (see [3]) and assume $L \sim 10^5$ km, so that R/L_p and R/L are in the ranges $2 \times 10^{-3} < R/L_\mathrm{p} < 0.1$ and $5 \times 10^{-4} < R/L < 3 \times 10^{-3}$, meaning that the use of the TT approximation is justified. Arregui et al. [44] have shown that the results of [38] remain valid beyond

the thin tube approximation. Soler et al. [38] derived approximate expressions for P and the ratio τ_D/P. The expression for P is

$$P = \frac{\pi}{v_A}\sqrt{\frac{\zeta+1}{2\zeta}}\sqrt{(L-L_p)\,L_p}, \tag{3}$$

where here v_A is the Alfvén velocity of the dense, prominence plasma only, and $\zeta = \rho_p/\rho_c$ is the density constrast as before. In Eq. (3) it is assumed that the prominence thread is located at the center of the magnetic tube (a general expression is given in [38]). A direct comparison of Eq. (1) and (3) shows that the effect of the longitudinal structuring of the tube is to select a particular value of the wavelength, λ, which depends of the relation between L and L_p. Regarding the damping rate, the expression for τ_D/P is not explicitly given here because it is exactly the same as that in Eq. (2), where now $\omega_k = 2\pi/P$ has to be computed using the period from Eq. (3). Thus, as happens for kink modes in longitudinally homogeneous threads, the effect of Cowling's diffusion is negligible for realistic values of the period when compared to that of resonant absorption.

Figure 3b shows the ratio τ_D/P numerically computed by Soler et al. [38] as a function of L_p/L. Remarkably, the damping ratio is independent of the length of the thread and only depends on the transverse non-uniformity length scale l/R. These means that the expression of τ_D/P for longitudinally homogeneous (Eq. (2)) tubes also applies when longitudinal structuring is included.

Acknowledgements RS acknowledges support from a Marie Curie Intra-European Fellowship within the European Commission 7th Framework Program (PIEF-GA-2010-274716). RS and JLB acknowledge financial support from MICINN and FEDER funds through grant AYA2011-22486.

References

1. Y. Lin, O. Engvold, L. Rouppe van der Voort, J. Wiik, T. Berger, Solar Phys. **226**, 239 (2005). DOI 10.1007/s11207-005-6876-3
2. P. Heinzel, U. Anzer, Astrophys. J. Lett. **643**, L65 (2006). DOI 10.1086/504980
3. Y. Lin, Space Sci. Rev. (2011). DOI 10.1007/s11214-010-9672-9
4. O. Engvold, in *New Perspectives on Solar Prominences*, *ASP Conference Series*, vol. 150, ed. by D. Webb, B. Schmieder, D. Rust (Astronomical Society of the Pacific, San Francisco, 1998), *ASP Conference Series*, vol. 150, pp. 23–31
5. Y. Lin. Magnetic field topology inferred from studies of fine threads in solar filaments (2005)
6. O. Engvold, in *Waves & Oscillations in the Solar Atmosphere: Heating and Magneto-Seismology*, *IAU Symposia*, vol. 247, ed. by R. Erdélyi, C. Mendoza-Briceño (Cambridge University Press, Cambridge; New York, 2008), *IAU Symposia*, vol. 247, pp. 152–157. DOI 10.1017/S1743921308014816
7. S. Martin, Y. Lin, O. Engvold, Solar Phys. **250**, 31 (2008). DOI 10.1007/s11207-008-9194-8
8. Y. Lin, S. Martin, O. Engvold, in *Subsurface and Atmospheric Influences on Solar Activity*, *ASP Conference Series*, vol. 383, ed. by R. Howe, R. Komm, K. Balasubramaniam, G. Petrie (Astronomical Society of the Pacific, San Francisco, 2008), *ASP Conference Series*, vol. 383, pp. 235–242

9. J. Leroy, in *Proceedings of the Japan-France Seminar on Solar Physics*, ed. by F. Moriyama, J. Henoux (Nihon Gakujutsu Shinkokai and CNRS, Tokyo, 1980), p. 155
10. V. Bommier, E. Landi Degl'Innocenti, J.L. Leroy, S. Sahal-Bréchot, Solar Phys. **154**, 231 (1994)
11. V. Bommier, J. Leroy, in *New Perspectives on Solar Prominences*, *ASP Conference Series*, vol. 150, ed. by D. Webb, B. Schmieder, D. Rust (Astronomical Society of the Pacific, San Francisco, 1998), *ASP Conference Series*, vol. 150, pp. 434–438
12. Y. Lin, R. Soler, O. Engvold, J. Ballester, Ø. Langangen, R. Oliver, L. Rouppe van der Voort, Astrophys. J. **704**, 870 (2009). DOI 10.1088/0004-637X/704/1/870
13. Z. Yi, O. Engvold, Solar Phys. **134**, 275 (1991)
14. Z. Yi, O. Engvold, S. Keil, Solar Phys. **132**, 63 (1991)
15. Y. Lin, O. Engvold, L. Rouppe van der Voort, M. van Noort, Solar Phys. **246**, 65 (2007). DOI 10.1007/s11207-007-0402-8
16. I. Arregui, J.L. Ballester, Space Sci. Rev.**158**, 169 (2011). DOI 10.1007/s11214-010-9648-9
17. J. Terradas, R. Molowny-Horas, E. Wiehr, H. Balthasar, R. Oliver, J. Ballester, Astron. Astrophys. **393**, 637 (2002). DOI 10.1051/0004-6361:20020967
18. R. Oliver, J. Ballester, Solar Phys. **206**, 45 (2002). DOI 10.1023/A:1014915428440
19. S. Patsourakos, J.C. Vial, Solar Phys. **208**, 253 (2002)
20. M. Goossens, *An Introduction to Plasma Astrophysics and Magnetohydrodynamics*, *Astrophysics and Space Science Library*, vol. 294 (Kluwer, Dordrecht; Norwell, MA, 2003)
21. P. Forteza, R. Oliver, J. Ballester, M. Khodachenko, Astron. Astrophys. **461**, 731 (2007). DOI 10.1051/0004-6361:20065900
22. B. Pandey, M. Wardle, Mon. Not. R. Astron. Soc. **385**, 2269 (2008). DOI 10.1111/j.1365-2966.2008.12998.x
23. B. De Pontieu, P. Martens, H. Hudson, Astrophys. J. **558**, 859 (2001). DOI 10.1086/322408
24. S. James, R. Erdélyi, B. De Pontieu, Astron. Astrophys. **406**, 715 (2003). DOI 10.1051/0004-6361:20030685
25. M. Khodachenko, T. Arber, H. Rucker, A. Hanslmeier, Astron. Astrophys. **422**, 1073 (2004). DOI 10.1051/0004-6361:20034207
26. J. Leake, T. Arber, M. Khodachenko, Astron. Astrophys. **442**, 1091 (2005). DOI 10.1051/0004-6361:20053427
27. P. Forteza, R. Oliver, J. Ballester, Astron. Astrophys. **492**, 223 (2008). DOI 10.1051/0004-6361:200810370
28. R. Soler, R. Oliver, J. Ballester, Astron. Astrophys. **512**, A28 (2010). DOI 10.1051/0004-6361/200913478
29. P. Gouttebroze, N. Labrosse, Astron. Astrophys. **503**, 663 (2009). DOI 10.1051/0004-6361/200811483
30. R. Soler, R. Oliver, J. Ballester, Astrophys. J. **699**, 1553 (2009). DOI 10.1088/0004-637X/699/2/1553
31. R. Soler, R. Oliver, J. Ballester, Astrophys. J. **707**, 662 (2009). DOI 10.1088/0004-637X/707/1/662
32. R. Soler, R. Oliver, J. Ballester, Astrophys. J. **726** (2011). DOI 10.1088/0004-637X/726/2/102
33. P. Edwin, B. Roberts, Solar Phys. **88**, 179 (1983). DOI 10.1007/BF00196186
34. M. Goossens, J. Terradas, J. Andries, I. Arregui, J. Ballester, Astron. Astrophys. **503**, 213 (2009). DOI 10.1051/0004-6361/200912399
35. I. Arregui, J. Terradas, R. Oliver, J. Ballester, Astrophys. J. Lett. **682**, L141 (2008). DOI 10.1086/591081
36. R. Soler, R. Oliver, J. Ballester, M. Goossens, Astrophys. J. Lett. **695**, L166 (2009). DOI 10.1088/0004-637X/695/2/L166
37. R. Soler, J. Andries, M. Goossens, Astron.Astrophys. **537**, A84 (2012)
38. R. Soler, I. Arregui, R. Oliver, J. Ballester, Astrophys. J. **722**, 1778 (2010). DOI 10.1088/0004-637X/722/2/1778
39. J. Ballester, E. Priest, Astron. Astrophys. **225**, 213 (1989)
40. M. Rempel, D. Schmitt, W. Glatzel, Astron. Astrophys. **343**, 615 (1999)

41. A. Díaz, R. Oliver, J. Ballester, Astrophys. J. **580**, 550 (2002). DOI 10.1086/343039
42. J. Terradas, I. Arregui, R. Oliver, J. Ballester, Astrophys. J. Lett. **678**, L153 (2008). DOI 10.1086/588728
43. R. Soler, M. Goossens, Astron. Astrophys. **531** (2011). DOI 10.1051/0004-6361/201116536
44. I. Arregui, R. Soler, J.L. Ballester, A.N. Wright, Astron. Astrophys.**533**, A60 (2011). DOI 10.1051/0004-6361/201117477

Alfvén Amplifier in the Solar Atmosphere

Youra Taroyan

Abstract Since their discovery, Alfvén waves have been studied in relation to the formation of spicules, the acceleration of the solar wind and the heating of the solar atmospehre. It is shown that under certain conditions magnetic flux tubes become amplifiers of Alfvénic disturbances that are generated at their footpoints through random convective motions. The amplification mechanism can be explained in terms of over-reflection of incompressible Alfvénic disturbances in compressible plasma flows. The process does not require flow shear or super-Alfvénic speeds. The implications of these results will be discussed in the context of recently observed large nonthermal velocities and associated blue-shifts.

1 Introduction

Magnetohydrodynamic (MHD) instabilities play a key role in a number of processes occurring in the Sun and in the solar-terrestrial environment: small perturbations become exponentially amplified leading to large scale changes in the system. Well-known examples include the Rayleigh-Taylor and the Kelvin-Helmholtz instabilities.

Since their discovery in the 1940s Alfvén waves have been studied in relation to the heating of laboratory plasmas and the solar atmosphere, the formation of spicules, and the acceleration of the solar wind. Recently, an MHD instability associated with the amplification of incompressible Alfvénic disturbances in compressible plasma flows has been found [1]. We elaborate on the implications of this new instability in the context of nonthermal velocities and outflows observed in the solar atmosphere (e.g. [2–4]).

Y. Taroyan (✉)
IMAPS, Aberystwyth University, Aberystwyth SY23 3BZ, Wales, UK
e-mail: yot@aber.ac.uk

Taroyan, Y.: *Alfvén Amplifier in the Solar Atmosphere*.
Astrophys Space Sci Proc. **33**, 123–127 (2012)
DOI 10.1007/978-3-642-30442-2_14, © Springer-Verlag Berlin Heidelberg 2012

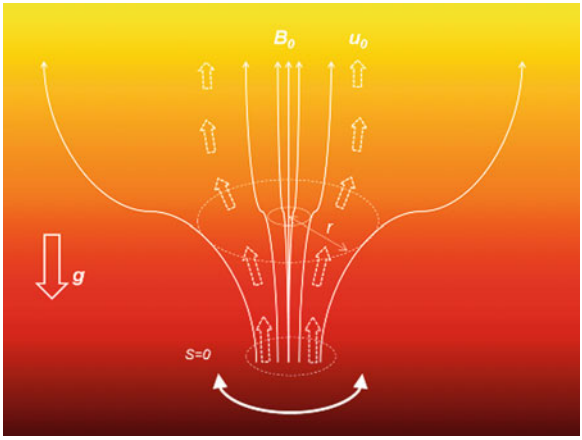

Fig. 1 A cartoon of an expanding flux tube. The tube is gravitationally stratified and permeated by a field-aligned smooth mass flow u_0. The $s = 0$ level represents the photospheric footpoint shaken by convective motions

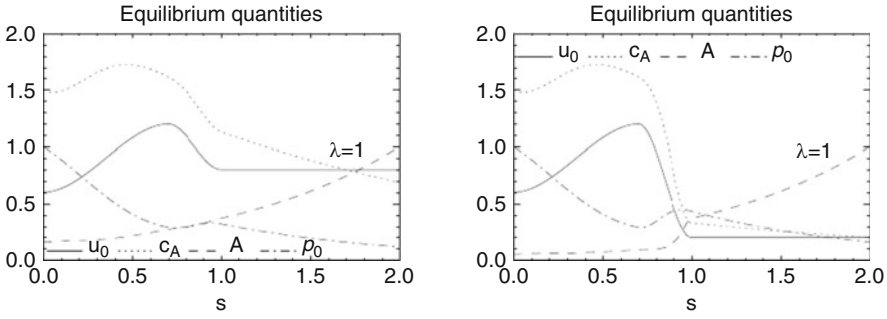

Fig. 2 Equilibrium quantities along the flux tube. The tube is semi-infinite ($0 < s < \infty$), however, only a finite segment between $s = 0$ and $s = 2$ is shown. In the *left panel*, $u_0(L) = 0.8$, and in the *right panel*, $u_0(L) = 0.2$

2 Unstable Flux Tubes

We analyse the stability of an axis-symmetric magnetic flux tube in a steady state (Fig. 1). The flux tube is gravitationally stratified and permeated by a field-aligned isothermal mass flow u_0. The flow may accelerate or decelerate upwards in different sections of the tube. Small-amplitude perturbations are launched from the footpoint by a photospheric driver representing random convective motions. The evolution of torsional perturbations is analysed. In the following analysis we identify solutions that grow exponentially in time, for a range of smooth flow profiles. The details of the treatment and numerical setup are presented in [5]. Figure 2 shows various equilibrium profiles. The flux tube is divided into uniform and nonuniform parts.

In the nonuniform part ($0 < s < L$), the flow remains sub-Alfvénic but can be either subsonic or supersonic. In the uniform part ($L < s < \infty$), the flow is constant. The decrease in the Alfvén speed is due to the presence of gravity. Length and speed are normalised with respect to the length of the nonuniform layer, L, and the sound speed, respectively. The solid, dotted, dashed and dot-dashed curves represent the flow speed, u_0, the Alfvén speed, c_A, the cross-sectional area of the tube, A, and density, ρ_0. The difference between the left and right panels is the flow speed in the uniform layer ($u_0 = 0.8$ and $u_0 = 0.2$). In both panels, the scale height, $\lambda = 1$. The variation of the eigenmode frequencies with the flow speed in the uniform part is plotted in Fig. 2. Both the real and imaginary parts are shown for the first four eigenmodes. Positive and negative values of the imaginary frequency correspond to growth and decay. The mode indicated with a dotted curve is amplified for relatively low values of $u_0(L)$. The modes become damped when $u_0(L)$ increases.

3 The Mechanism Behind the Alfvén Instability

In the case of the Kelvin-Helmholtz instability of incompressible plasmas, compressibility may either stabilise or destabilise the steady state depending on the density jump and the velocity shear. A magnetic field aligned with the flow introduces a threshold flow speed below which the instability is suppressed. In contrast to the Kelvin-Helmholtz instability, the Alfvén instability presented here only arises in the presence of a compressible flow and a magnetic field. As an example we have considered an expanding flux tube permeated by a moderate sub-Alfvénic flow. No high speed flows or shear are required.

The Alfvénic perturbations travelling from the footpoint are over-reflected back and transmitted forward as the decelerating plasma flow reduces their propagation speed. Over-reflection represents reflection with a coefficient greater than one. From Fig. 2 it is clear that the deceleration of flow corresponds to more rapid expansion of the tube. According to Fig. 3, the instability requires deceleration of the flow. Thus the region of rapid expansion acts as an amplifier for the perturbations, where the flow provides the required energy. Figure 4 compares stable and unstable tubes with accelerating and decelerating flows.

4 Implications

Observations of bright network regions suggest that two types of magnetic structures coexist: small closed loops in the chromosphere and funnels that are connected to the corona. The second type is usually associated with blue-shifts representing outflows and enhanced line-widths [2]. These enhanced line-widths are best interpreted as nonlinear Alfvén waves passing through the funnel. A number of recent observational studies of chromospheric and transition region lines have found evidence for

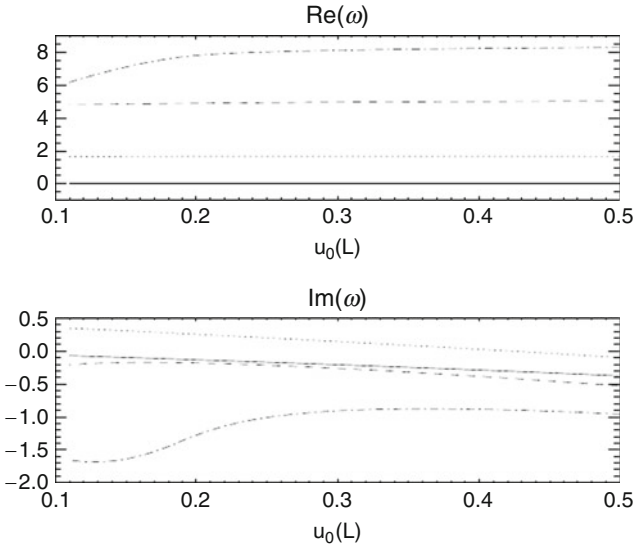

Fig. 3 The real and imaginary parts of the eigenmode frequencies are plotted in the *top* and *bottom panels*, respectively. Different modes are indicated by different linestyles

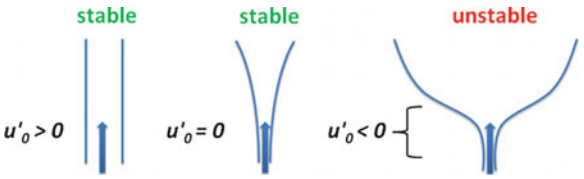

Fig. 4 Comparison of three tubes. The first two remain stable. The third tube is unstable due to rapid expansion in a marked section. The derivative of the flow velocity with respect to the coordinate along the background field is denoted by u_0

the presence of Alfvén waves or non-periodic nonthermal velocities (e.g., [3]) *and* outflows in magnetic structures of the solar atmosphere (e.g. [3,4]). Estimates of the energy flux carried by these waves indicate that they could accelerate the solar wind and heat the corona.

According to our results (Fig. 4), a funnel shaped flux tube permeated by outflowing plasma may be unstable. The funnel acts as an amplifier of Alfvénic disturbances which could then be seen as periodic or non-periodic line-width enhancements. As the amplitudes increase the energy of the disturbances will eventually be converted into heating or acceleration through some dissipative process, e.g., shock heating due to non-linear mode conversion.

5 Conclusions

Expanding isothermal flux tubes with smooth flow profiles can be unstable with respect to linear torsional perturbations. This is a new ideal MHD instability: a funnel shaped fraction of the tube becomes an amplifier of Alfvénic disturbances. The obtained results could explain the non-thermal broadenings associated with outflows in magnetic regions of the lower solar atmosphere. However, further work is required to establish the dynamic and energetic implications of the Alfvén instability in the solar atmosphere.

References

1. Taroyan, Y: Physical Review Letters, **101**, 5001 (2008)
2. Peter, H: Astronomy & Astrophysics, **374**, 1108 (2001)
3. Jess, D. B., Mathioudakis, Mihalis, Erdélyi, R., Crockett, P. J., Keenan, F. P., Christian, D.: Science, **323**, 1582 (2009)
4. McIntosh, S. W., de Pontieu, B., Carlsson, M., Hansteen, V., Boerner, P., Goossens, M.: Nature, **475**, 477 (2009)
5. Taroyan, Y.: Astronomy & Astrophysics, **533**, A68 (2011)

Alfvénic Solitary and Shock Waves in Plasmas

Padma Kant Shukla, Bengt Eliasson, and Lennart Stenflo

Abstract We present a review of nonlinear Alfvénic solitary and shock waves in a magnetized electron-ion plasma. The dynamics of these nonlinear dispersive Alfvén waves is governed by the two-fluid equations, coupled with Faraday's and Ampère's laws. First, we demonstrate the existence of large amplitude compressional Alfvénic solitary and shock waves propagating across the external magnetic field in a warm electron-ion magnetoplasma. It is found that these nonlinear structures can exist in well defined speed ranges above the Alfvén speed, and their widths are several times larger than the electron skin depths. Second, we study the formation of nonlinear slow magnetosonic solitary (SMS) waves propagating almost perpendicular to the external magnetic field direction. The propagation speed of the SMS waves is below the Alfvén speed and their width is a few ion skin depths in a collisionless magnetoplasma. The nonlinear dispersive Alfvén waves, as discussed here, can be associated with localized electromagnetic field excitations in magnetized laboratory and space plasmas that are composed of magnetized electrons and ions.

P.K. Shukla (✉)
International Centre for Advanced Studies in Physical Sciences and Institute for Theoretical Physics, Faculty of Physics and Astronomy, Ruhr University Bochum, D-44780, Bochum, Germany, EU

Department of Mechanical and Aerospace Engineering and Center for Energy Research, University of California San Diego, CA 92093, La Jolla, USA
e-mail: profshukla@yahoo.de

B. Eliasson
International Centre for Advanced Studies in Physical Sciences and Institute for Theoretical Physics, Faculty of Physics and Astronomy, Ruhr University Bochum, D-44780, Bochum, Germany
e-mail: beliass@yahoo.se

L. Stenflo
Department of Physics, Linköping University, SE-581 83, Linköping, Sweden
e-mail: lennart.stenflo@physics.umu.se

Shukla, P.K. et al.: *Alfvénic Solitary and Shock Waves in Plasmas*.
Astrophys Space Sci Proc. **33**, 129–141 (2012)
DOI 10.1007/978-3-642-30442-2_15, © Springer-Verlag Berlin Heidelberg 2012

1 Introduction

The Alfvén wave [1] is the most fundamental normal mode of a magnetized plasma. The restoring force for the wave comes from the magnetic field tension and pressure, and the ion mass provides the inertia to sustain the non-dispersive Alfvén wave [2]. In their classic paper, Adlam and Allen [3] presented a theoretical study of large amplitude nonlinear dispersive Alfvén waves [4] that propagate across the external magnetic field direction in a cold collisionless electron-ion plasma. They used the two fluid equations for the electrons and ions together with Ampère's and Faraday's laws for the Alfvén wave fields to predict the existence of large amplitude compressional Alfvénic solitary (CAS) pulses. The latter arise due to a balance between the Alfvén wave dispersion and the nonlinearities associated with the harmonic generation [5]. By using the reductive perturbation method and stretched variables for space and time, Nairn et al. [6] derived a Korteweg-de Vries (KdV) equation [7–9] that governs the dynamics of small amplitude nonlinear CDA waves in a cold magnetoplasma. The KdV equation admits stationary solutions in the form of solitary and periodic wave trains that move with super-Alfvénic speeds. Finite temperature and collisions have been included in the model for a study of small amplitude compressional Alfvén shock waves by Shukla et al. [10]. Furthermore, large amplitude CDA solitary and CDA shock waves [11] propagate with supersonic Alfvén speed, and their widths are several times the electron skin depth (=the ratio between the speed of light c in vacuum and the electron plasma frequency ω_{pe}).

Besides the CDA waves propagating across the external magnetic field direction, there are obliquely propagating coupled inertial Alfvén waves, the slow and fast Alfvén waves [12, 13], the electromagnetic ion-cyclotron Alfvén wave and the kinetic Alfvén wave [14–16] in a uniform magnetoplasma. About a decade ago, McKenzie and Doyle [17] analytically solved the nonlinear governing equations for non-MHD Alfvén waves [16] in a warm magnetoplasma, and predicted the existence of sub-and super-magnetosonic solitary pulses associated with the fast and slow magnetosonic waves. Stasiewicz et al. [18] reported the first observations of slow magnetosonic solitary (SMS) pulses that are detected by the fleet of four Cluster space crafts at the magnetopause boundary layer. The SMS pulses are composed of an extremely large amplitude inverted bell-shaped magnetic field cavity that traps a considerably enhanced density hump distribution. The observed width of the SMS pulses is several times the ion skin depth, and they move with the speed below the Alfvén speed. Thus, the features of the SMS pulses are different than those of the CDA solitary pulses.

In this paper, we review the underlying physics of linear and nonlinear CDA and SMS pulses in a uniform electron-ion magnetoplasma. We focus special attention on the finite amplitude theories for nonlinear CDA and SMS waves that are propagating across and obliquely to the ambient magnetic field direction, respectively. The relevance of our investigation to localized dispersive Alfvén waves in magnetized space and laboratory plasmas is pointed out.

2 Governing Nonlinear Equations

Let us consider a uniform, warm electron-ion magnetoplasma in the presence of the low-frequency (in comparison with the electron gyrofrequency) nonlinear dispersive electromagnetic (DEM) waves. The external magnetic field is ($\hat{\mathbf{z}}B_0$), where $\hat{\mathbf{z}}$ is the unit vector along the z-axis in a Cartesian coordinate system, and B_0 is the strength of the magnetic field. The dynamics of the DEM waves is governed by the continuity equation

$$\frac{d\mathbf{u}_j}{dt} + n_j \nabla \cdot \mathbf{u}_j = 0, \tag{1}$$

the momentum equation

$$n_j m_j \frac{d\mathbf{u}_j}{dt} = n_j q_j \left[\mathbf{E} + \frac{1}{c}(\mathbf{u}_j \times \mathbf{B})\right] - \nabla p_j + \mathbf{R}_j, \tag{2}$$

Faraday's law

$$\frac{\partial \mathbf{B}}{\partial t} = -c\nabla \times \mathbf{E}, \tag{3}$$

Ampère's law

$$\nabla \times \mathbf{B} = \frac{4\pi e}{c}(n_i \mathbf{u} - n_e \mathbf{u}_e), \tag{4}$$

Poisson's equation

$$\nabla \cdot \mathbf{E} = 4\pi e(n_i - n_e), \tag{5}$$

together with $\nabla \cdot \mathbf{B} = 0$. Here $d/dt = (\partial/\partial t) + \mathbf{u}_j \cdot \nabla$, n_j and $\mathbf{u}_j$ are the number density and the fluid velocity of the particle species j (j equals e for the electrons, and i for the ions), m_j the mass, q_j the charge ($q_e = -e$ and $q_i = e$, with e being the magnitude of the electron charge), $\mathbf{E}$ and $\mathbf{B}$ the electric and magnetic fields, respectively, p_j the scalar pressure, and $\mathbf{R}_j = \sum_\alpha \mathbf{R}_{j\alpha}$ represents the momentum gained by the jth species through collisions with the αth species. We note that the displacement current has been neglected in Eq. (4) by assuming that the phase speed of the DEM waves is much smaller than c.

3 Large-Amplitude CDA Solitary and Shock Waves

In this section, we present a theory for large amplitude CDA solitons [11] that are propagating in a warm electron-ion plasma across a uniform magnetic field $\hat{\mathbf{z}}B_0$. The restoring forces on the CDA waves comes from the magnetic pressure, whereas

the ion mass provides the inertia to sustain the CDA waves [19]. The CDA wave dispersion is due to the electron polarization drift (or the electron inertial effect) in the wave electric field $\mathbf{E}_\perp = \hat{\mathbf{x}}E_x + \hat{\mathbf{y}}E_y$, where $\hat{\mathbf{x}}$ and $\hat{\mathbf{y}}$ are the unit vectors along the y and y axes, respectively. The CDA wave magnetic field B_z is aligned along the z-axis. In a quasi-neutral plasma with $n_e = n_i \equiv n$, the x components of the electron and ion fluid velocities are equal (viz. $u_{ex} = u_{ix} \equiv u$), whereas the x and y components of the electron fluid velocities differ owing to the electron polarization drift. The electrons carry currents only along the y-direction. The CDA waves compress the magnetic field-lines without bending them, and are accompanied by density perturbations.

The nonlinear propagation of one-dimensional CDA waves along the x-axis in our quasi-neutral magnetoplasma is thus governed by the ion continuity equation

$$\frac{dn}{dt} + n\frac{\partial u}{\partial x} = 0, \tag{6}$$

and the x-components of the electron and ion momentum equations, which are, respectively,

$$m_e\frac{du}{dt} = -eE_x - \frac{e}{c}u_{ey}B - \frac{k_BT_e}{nn_0^2}\frac{\partial n^3}{\partial x}, \tag{7}$$

and

$$m_i\frac{du}{dt} = eE_x + \frac{e}{c}u_{iy}B - \frac{k_BT_i}{nn_0^2}\frac{\partial n^3}{\partial x}, \tag{8}$$

where $d/dt = \partial/\partial t + u\partial/\partial x$, u_{ey} (u_{iy}) is the y-component of the electron (ion) fluid velocity, B the sum of the ambient and compressional wave magnetic fields, k_B the Boltzmann constant, T_e (T_i) the electron (ion) temperature, m_e (m_i) the electron (ion) mass, and n_0 the equilibrium plasma number density. In Eqs. (7) and (8), we have adopted the adiabatic pressure laws [viz. $p_j = p_{j0}(n/n_0)^3$, where $p_{j0} = n_0k_BT_j$].

Eliminating E_x from (8) by using (7) we obtain

$$\frac{du}{dt} = \frac{e}{m_ic}u_yB - \frac{C_s^2}{nn_0^2}\frac{\partial n^3}{\partial x}, \tag{9}$$

where $u_y = u_{iy} - u_{ey}$ is the relative speed between the electrons and ions, and $C_s = [k_B(T_e + T_i)/m_i]^{1/2}$ the effective ion-acoustic speed. From the y-component of Eq. (4) we have

$$\frac{\partial B}{\partial x} = -\frac{4\pi en}{c}u_y, \tag{10}$$

which can be used to eliminate u_y from Eq. (9), obtaining [11]

$$\frac{du}{dt} + \frac{B}{4\pi nm_i}\frac{\partial B}{\partial x} + \frac{C_s^2}{nn_0^2}\frac{\partial n^3}{\partial x} = 0. \tag{11}$$

From the z-component of Eq. (3) we have

$$\frac{\partial B}{\partial t} = -c\frac{\partial E_y}{\partial x}, \tag{12}$$

where E_y is determined from the y-component of the electron momentum equation

$$E_y = \frac{uB}{c} - \frac{m_e}{e}\frac{du_{ey}}{dt} - \frac{m_e}{e}\nu_{ei}u_y, \tag{13}$$

where ν_{ei} is the constant electron-ion collision frequency. The third term in the right-hand side of Eq. (13) represents the momentum exchange between the electrons and ions due to collisions. Equation 13 reveals that the electron Lorentz force, the linear and nonlinear electron inertial forces along the y-axis, and the electron-ion momentum exchange due to collisions are the key players in maintaining the CAW electric field along the y-axis.

Eliminating E_y from Eq. (12) by using Eqs. (13) and (10), we obtain [11]

$$\frac{\partial B}{\partial t} + \frac{\partial (uB)}{\partial x} - \frac{m_e c^2}{4\pi e^2}\frac{\partial}{\partial x}\left[\frac{d}{dt}\left(\frac{1}{n}\frac{\partial B}{\partial x}\right)\right] - \frac{m_e c^2 \nu_{ei}}{4\pi e^2}\frac{\partial}{\partial x}\left(\frac{1}{n}\frac{\partial B}{\partial x}\right) = 0, \tag{14}$$

where we have used $m_i du_{iy}/dt = eE_y - euB/c$, the contribution of which is smaller by a factor $m_e/m_e \ll 1$, and therefore neglected in Eq. (14).

Equations 6, 11 and 14 are the governing equations for the nonlinear CDA waves [11] in a warm collisional magnetoplasma.

3.1 Linear Waves

Letting $n = n_0 + n_1$ and $B = B_0 + B_1$, where $n_1 \ll n_0$ and $B_1 \ll B_0$, in Eqs. (6), (11) and (14) we linearize them and combine the resultant equations to obtain the wave equation

$$\left(1 - \lambda_e^2\frac{\partial^2}{\partial x^2}\right)\left(\frac{\partial^2}{\partial t^2} - C_s^2\frac{\partial^2}{\partial x^2}\right)B_1 - C_A^2\frac{\partial^2}{\partial x^2} - \nu_{ei}\lambda_e^2\frac{\partial^3 B_1}{\partial t\partial x^2} = 0, \tag{15}$$

which can be Fourier transformed by supposing that B_1 is proportional to $\exp(-i\omega t + ikx)$, where the frequency ω and the wavenumber k are related by Shukla et al. [11]

$$\omega = -i\frac{\Gamma}{2} \pm \frac{1}{2}(4\Omega^2 - \Gamma^2)^{1/2}, \tag{16}$$

where $\Gamma = \nu_{ei}k^2\lambda_e^2/(1 + k^2\lambda_e^2)$ and $\Omega = (3k^2C_s^2 + \Omega_A^2)^{1/2}$, with $\Omega_A = kC_A/(1 + k^2\lambda_e^2)^{1/2}$. Here $\lambda_e = c/\omega_{pe}$ is the electron skin depth, $\omega_{pe} = (4\pi n_0 e^2/m_e)^{1/2}$ the electron plasma frequency, and $C_A = B_0/\sqrt{4\pi n_0 m_i}$ the Alfvén speed.

Equation 16 reveals that the CDA waves are damped due to collisions in a magnetized electron-ion plasma. In the absence of collisions (viz. $\nu_{ei} = 0$), we have from (16), $\omega = \Omega$, which in a cold magnetoplasma gives [19] $\omega = \Omega_A$. Furthermore, in the limit $\nu_{ei} = 0$ and $k^2\lambda_e^2 \gg 1$, Eq. (16) depicts the frequency of the propagating lower-hybrid wave, viz. $\omega = \left(\omega_{LH}^2 + 3k^2C_s^2\right)^{1/2}$, where $\omega_{LH} = (\omega_{ce}\omega_{ci})^{1/2}$ is the lower hybrid resonance frequency and $\omega_{ce} = eB_0/m_ec$ ($\omega_{ci} = eB_0/m_ic$) the electron (ion) gyrofrequency.

3.2 Nonlinear Stationary Waves

Let us next normalize n by n_0, B by B_0, u by C_A, t by ω_{LH} and x by $\lambda_e \equiv C_A/\omega_{LH}$ in Eqs. (6), (11) and (14), to obtain

$$\frac{dn}{dt} + n\frac{\partial u}{\partial x} = 0, \tag{17}$$

$$\frac{du}{dt} + \frac{1}{2n}\frac{\partial B^2}{\partial x} + \frac{\beta}{n}\frac{\partial n^3}{\partial x} = 0, \tag{18}$$

and

$$\frac{\partial B}{\partial t} + \frac{\partial (uB)}{\partial x} - \frac{\partial}{\partial x}\left[\frac{d}{dt}\left(\frac{1}{n}\frac{\partial B}{\partial x}\right)\right] - \alpha\frac{\partial}{\partial x}\left(\frac{1}{n}\frac{\partial B}{\partial x}\right) = 0, \tag{19}$$

where $\beta = 4\pi n_0 k_B T/B_0^2$ and $\alpha = \nu_{ei}/\omega_{LH}$.

We now seek stationary nonlinear solutions of Eqs. (17)–(19) in the moving frame $\xi = x - Mt$, where $M = U/C_A$ is the Mach number and U the constant propagation speed of the nonlinear structures (e.g. solitary pulses and shock waves). Assuming that n, u and B are functions of ξ only, we have $u = M(n-1)/n$, and

$$M^2\left(\frac{1}{n} - 1\right) + \frac{1}{2}(B^2 - 1) + \beta(n^3 - 1) = 0, \tag{20}$$

and

$$\frac{\partial}{\partial \xi}\left(\frac{1}{n}\frac{\partial B}{\partial \xi}\right) - \frac{\alpha}{M}\frac{\partial B}{\partial \xi} - B + n = 0, \tag{21}$$

where we have imposed the boundary conditions $u = 0$, $n = 1$, $B = 1$ and $\partial B/\partial \xi = 0$, supposing that the plasma is unperturbed at $|\xi| \to \infty$. In the unperturbed state far away from the solitary pulse and shock waves, we have $\partial/\partial\xi = \partial^2/\partial\xi^2 = 0$ in Eq. (21) so that $B = N$. Inserting the latter into Eq. (20) we obtain

$$M^2\left(\frac{1}{B} - 1\right) + \frac{1}{2}(B^2 - 1) + \beta(B^3 - 1) = 0, \tag{22}$$

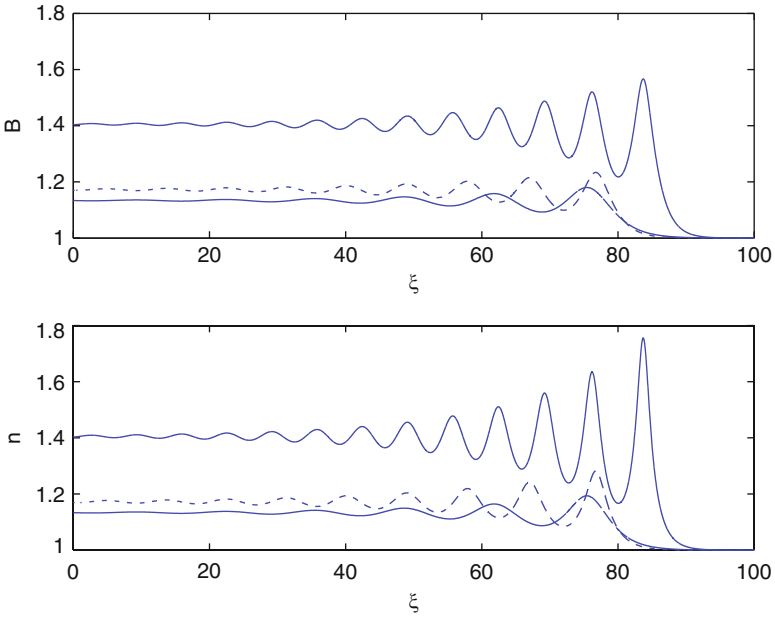

Fig. 1 The spatial profiles of the magnetic field and plasma density for $\alpha = 0.1$, exhibiting oscillatory shock structures for $M = 1.3$ and $\beta = 0$ (*solid curves*), $M = 1.1$ and $\beta = 0$ (*dashed curves*), and $M = 1.3$ and $\beta = 0.1$ (*dash-dotted curves*) (After Ref. [11])

which exhibits the existence diagram for M versus B for given values of β. At $\xi = \infty$ we have $B = n = 1$, while for $\xi = -\infty$, we have from (22), which by eliminating a common factor $(B - 1)$ can be expressed as

$$\frac{M^2}{B} - \frac{1}{2}(B + 1) - \beta(B^2 + B + 1) = 0. \tag{23}$$

The solution of Eq. (23) gives the amplitude of B at $\xi = -\infty$. For a cold magnetoplasma, viz. $\beta = 0$, Eq. (23) yields $M^2 = B/2(1 + B)$, which reveals that the nonlinear structures have super Alfvénic speed for $B > 1$.

Equations 20 and 21 have been numerically solved, and the spatial profiles of the magnetic field and the plasma number density for different values of M, β and α are displayed in Figs. 1–3. In Fig. 1, we used $\alpha = 0.1$, which leads to oscillatory shock structures. The amplitudes of the structures increase with increasing values of M, while they decrease significantly even for small values of β. On the other hand, for a larger value of $\alpha = 1.5$, we see in Fig. 2 that the shock structures are more or less monotonic, while their amplitudes depend on M and β in the same manner as in Fig. 1. For vanishing α, the shock structure will dissolve into a train of solitary CDA waves, as seen in Fig. 3. The amplitudes of the solitary waves increase with increasing M, while they decrease with increasing values of β.

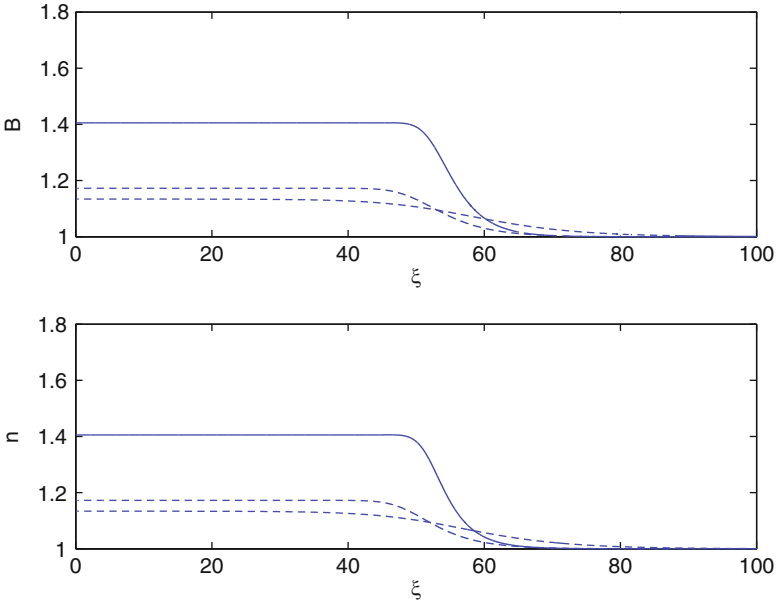

Fig. 2 The spatial profiles of the magnetic field and plasma density for $\alpha = 1.5$, exhibiting monotonic shock structures for $M = 1.3$ and $\beta = 0$ (*solid curves*), $M = 1.1$ and $\beta = 0$ (*dashed curves*), and $M = 1.3$ and $\beta = 0.1$ (*dash-dotted curves*) (After Ref. [11])

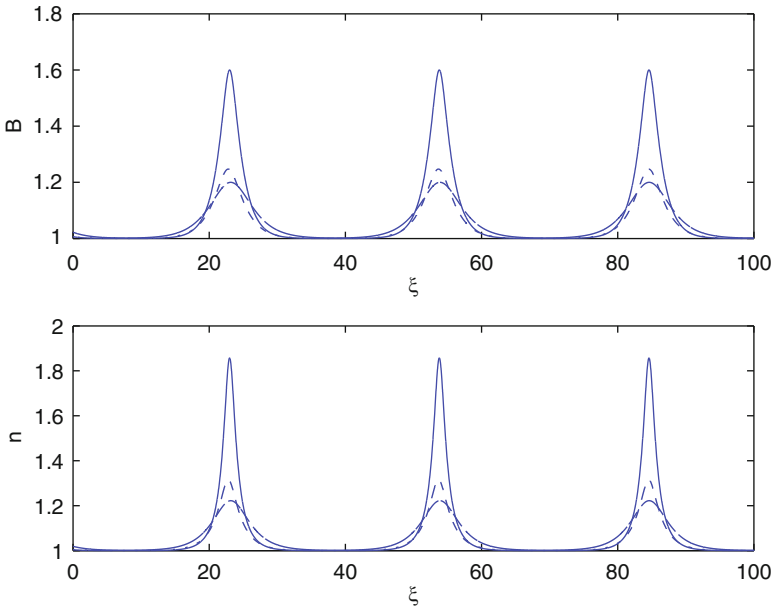

Fig. 3 The spatial profiles of the magnetic field and plasma density for $\alpha = 0$, exhibiting trains of solitary waves for $M = 1.3$ and $\beta = 0$ (*solid curves*), $M = 1.1$ and $\beta = 0$ (*dashed curves*), and $M = 1.3$ and $\beta = 0.1$ (*dash-dotted curves*) (After Ref. [11])

4 Slow Magnetosonic Solitary (SMS) Pulses

Next, we turn our attention to large amplitude SMS pulses that propagate obliquely to the external magnetic field direction in an electron-ion plasma. In our quasi-neutral ($n_e = n_i$) magnetoplasma, the dynamics of the SMS pulses is governed by the Hall-MHD equations composed of the ion continuity and ion momentum equations, respectively,

$$\frac{Dn_i}{Dt} + n_i \nabla \cdot \mathbf{u}_i = 0, \tag{24}$$

$$m_i n_i \frac{D\mathbf{u}_i}{Dt} = -k_B T_e \nabla n_i - \frac{k_B T_i}{n_0^2} \nabla n_i^3 - \frac{(\nabla \times \mathbf{B}) \times \mathbf{B}}{4\pi}, \tag{25}$$

and Faraday's law

$$\frac{\partial \mathbf{B}}{\partial t} = \nabla \times \left[\left(\mathbf{u}_i - \frac{c \nabla \times \mathbf{B}}{4\pi e n_i} \right) \times \mathbf{B} \right] - n_0 \lambda_e^2 \nabla \times \left[D_{te} \left(\frac{\nabla \times \mathbf{B}}{n_i} - \frac{4\pi e \mathbf{u_i}}{c} \right) \right] + \eta \nabla^2 \mathbf{B}, \tag{26}$$

where $D_{te} = D/Dt - (c/4\pi e n_i)[(\nabla \times \mathbf{B}) \cdot \nabla]$, $D/Dt = (\partial/\partial t) + \mathbf{u}_i \cdot \nabla$, and $\eta = \nu_{ei} \lambda_e^2$ the plasma resistivity. In deducing (25) and (26), we have used the electron momentum equation and Ampère's law. Furthermore, we also used the isotropic pressure law for the electron and ion fluids.

4.1 Linear Waves

Letting $n = n_0 + n_1$ and $\mathbf{B} = \hat{\mathbf{z}} B_0 + \mathbf{B}_1$, where $n_1 \ll n_0$ and $|\mathbf{B}_1| \ll B_0$, we first linearize the system of Eqs. (24)–(26), Fourier transform them by supposing that n_1 and $\mathbf{B}$ are proportional to $\exp(-i\omega t + i\mathbf{k} \cdot \mathbf{r})$, where $\mathbf{k}$ is the wave vector, and combine the resultant equations to obtain the dispersion relation for obliquely propagating DEM waves in a collisionless ($\eta = 0$) magnetoplasma [13]

$$(\Omega^2 - k_z^2 C_A^2)[\Omega^2(\omega^2 - k^2 V_s^2) - k^2 C_A^2(\omega^2 - k_z^2 V_s^2)] = \frac{\omega^2}{\omega_{ci}^2} k_z^2 k^2 C_A^4 (\omega^2 - k^2 V_s^2), \tag{27}$$

where $\Omega^2 = \omega^2(1 + k^2 \lambda_e^2)$, $V_s^2 = (T_e + 3T_i)/m_i$, and k_z ($k_\perp$) is the component of $\mathbf{k}$ along and across $\hat{\mathbf{z}}$. The right-hand side of (28) represents the Hall current or finite-ω/ω_{ci} effects. It emerges that the latter provides a linear coupling between the magnetic field aligned inertial Alfvén wave, the modified (by the electron skin depth effect) fast and slow magnetosonic waves, the kinetic Alfvén wave and the electromagnetic ion-cyclotron Alfvén waves. For $k^2 \lambda_e^2 \ll 1$, one can neglect the electron inertial effects, and Eq. (27) reduces to that given in Ref. [16].

4.2 The SMS Pulses

Let us now discuss the features of the SMS pulses in a warm collisionless magnetoplasma, by neglecting the electron inertial and collisional effects. For this purpose, we chose the external magnetic field as $\mathbf{B}_0 = (B_{x0}, 0, B_{z0})$, and normalize n_i by n_0, the wave electric field $\mathbf{E}$ and the wave magnetic field $\mathbf{B}$ $(=\hat{\mathbf{y}}B_y + \hat{\mathbf{z}}B_z)$ by B_{z0}, $\mathbf{u}_i$ by C_A, and the time and space variables by ω_{ci}^{-1} and $\lambda_i = C_A/\omega_{ci}$, and rewrite Eqs. (24)–(26) as [22]

$$\frac{Dn_i}{Dt} + n_i \nabla \cdot \mathbf{u}_i = 0, \tag{28}$$

$$\frac{Du_i}{Dt} - \frac{1}{n_i}(\mathbf{B} \cdot \nabla)\mathbf{B} + \frac{1}{2n_i}\nabla B^2 + \frac{\beta_e}{n_i}\nabla n_i + \frac{\beta_i}{n_i}\nabla n_i^3 = 0, \tag{29}$$

and

$$\frac{\partial \mathbf{B}}{\partial t} - \nabla \times (\mathbf{u}_{iH} \times \mathbf{B}) = 0, \tag{30}$$

where $\beta_e = 4\pi n_0 T_e/B_0^2$, $\beta_i = 3(T_i/T_e)\beta_e$, $\mathbf{u}_{iH} = \mathbf{v}_i - \mathbf{v}_H$, and $\mathbf{v}_H = \nabla \times \mathbf{B}$ is the normalized Hall-velocity associated with the Hall current. In deducing Eqs. (29) and (30), we have used the normalized electric field

$$\mathbf{E} = -\frac{C_A}{c}\left(\mathbf{u}_{iH} \times \mathbf{B} + \frac{\beta_e}{n_i}\nabla n_i\right), \tag{31}$$

which comes from the inertialess electron momentum equation, Ampère's law, and $n_e = n_i$.

The nonlinear solutions of the governing equations for one-dimensional non-dispersive magnetohydrodynamic waves(without the Hall current) have been presented by Stenflo et al. [20] in the cold-plasma limit (viz. $\beta = 0$), and by Shukla et al. [21] in the warm plasma limit (viz. $\beta \neq 0$).

In the following, following McKenzie and Doyle [17], we outline solutions of Eqs. (28)–(30) in the form of the localized SMS pulses (of the form $F(x - Mt)$) propagating along the x-axis, in an oblique magnetic field $(B_{x0}, 0, B_{z0})$, where $M = U_0/C_A$ is the Mach number and U_0 the constant speed of the solitary pulse. The wave magnetic field is $(0, B_y, B_z)$. In the stationary frame, we have from Eqs. (28)–(30), the relations $u = M(1 - 1/n_i)$, together with

$$Mu \equiv M^2\left(1 - \frac{1}{n_i}\right) = \frac{1}{2}(B_y^2 + B_z^2) - \frac{1}{2} - \beta_e(n_i - 1) - \beta_i(n_i^3 - 1), \tag{32}$$

where the wave magnetic fields are determined from

$$\frac{\partial^2 B_z}{\partial x^2} + M_A^2(B_z - 1) + M_A^2(1 + B_z)\left(1 - \frac{1}{n_i}\right) = 0, \tag{33}$$

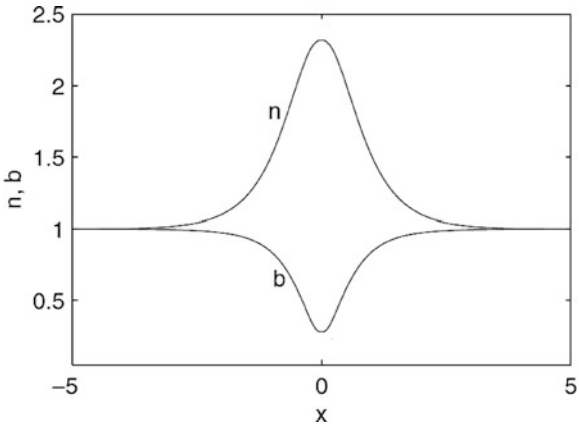

Fig. 4 The spatial profiles of the normalized plasma number density $n = n_i/n_0$ and normalized magnetic field $b = |\mathbf{B}|/B_0$ for $\beta_e \approx 0.25$, $T_i/T_e = 0.1$, $M = 0.1$, and $\cos(\alpha) = 0.13$ (After Stasiewicz et al. [18])

and

$$\frac{\partial B_y}{\partial x} - B_y \frac{\partial}{\partial x}\left(\frac{1}{n_i}\right) + M_A(B_z - 1) = 0. \tag{34}$$

Here $M_A = M^2/\cos^2\alpha$ and $\cos\alpha = B_{x0}/B_{z0}$. Furthermore, in deducing (32)–(34) we have imposed the appropriate boundary conditions for localized SMS pulses (viz. $n_i = 1$, $B_z = 1$, and $\partial B_z/\partial x = 0$) in the unperturbed region $|x| \to \infty$. Equations 32–34 have to be numerically solved to obtain the profiles of the SMS pulses.

In Fig. 4, we display the profiles of the SMS pulses for $M = 0.1$ and $\beta \approx 0.25$. It is seen that the SMS pulse profile is composed of an extremely large amplitude wave magnetic field hole which traps enhanced electron density perturbations. The propagation speed of such a SMS pulse is one tenth of the Alfvén speed and the SMS pulse width is a few times the ion skin depth. The features of the SMS pulses are consistent with the Cluster observations of localized SMS pulses that were reported by Stasiewicz et al. [18] at the magnetopause boundary layer in the Earth's magnetosphere.

5 Summary and Conclusions

In this paper, we have presented a review of linear and nonlinear theories for CDA solitary and shock waves, which propagate perpendicular to the magnetic field direction in collisionless and collisional magnetoplasmas, respectively, as well as for obliquely propagating SMS pulses in a collisionless magnetoplasma. The CDA solitary and shock waves move with super-Alfvén speed and their widths are several times larger than the electron skin depths. Thus, the electron inertial effect plays an important role in the formation of CDA solitary waves. On the other hand, the SMS pulses move with sub-Alfvénic speed and their width is several times

the ion skin depth. Here, the Hall current plays an important role. Physically, the formation of the CDA solitary waves and SMS pulses is attributed to the balance between the harmonic generation nonlinearities and the wave dispersion arising for the electron inertial effect appearing in the CDA wave dynamics and the Hall current appearing in the SMS wave dynamics. Furthermore, the formation of the CDA shock waves is due to the balance between the harmonic generation nonlinearities and dissipation arising from either electron-ion collisions or collisions caused by turbulent electrostatic fields in a uniform magnetoplasma. The CDA shock wave pressures might be responsible for the cross-field proton acceleration/energization over the electron skin depth in a collisional magnetoplasma. The physics of collisionless shocks in collisionless plasmas in terms of wave-particle interactions has been discussed by Moiseev and Sagdeev [23]. Furthermore, the theory for large amplitude obliquely propagating SMS waves in a collisionless magnetoplasma reveals that the SMS pulses are composed of an inverted bell shaped extremely large amplitude magnetic hole/cavity and a bell shaped finite amplitude density perturbations that move with the sub-Alfvénic speed.

The results presented in this review paper should be useful for understanding the salient features of solitary and shock-like compressional magnetic field structures encountered in observational data from very low-β magnetoplasmas in laboratory and space plasmas [24, 25]. Furthermore, we stress that the SMS pulses have been observed [18] by the fleet of the Cluster spacecrafts at the magnetopause boundary layer in the Earth' magnetosphere. In conclusion, we must also explore new aspects of nonlinear Alfvén waves and their role with regard to electron and ion acceleration in magnetic confinement fusion devices and in small-scale laboratory plasma discharges [26] that have been build for studying the nonlinear physics of dispersive Alfvén waves in a controlled fashion.

Acknowledgements This research was supported by the Deutsche Forschungsgemeinschaft through the project SH21/3-2 of the Research Unit 1048.

References

1. H. Alfvén, Nature (London) **150**, 405 (1942).
2. P. K. Shukla and J. M. Dawson, Astrophys. J. Lett. **276**, L49 (1984).
3. J. H. Adlam and J. E. Allen, Phil. Mag. **3**, 448 (1958).
4. D. A. Tidman and N. A. Krall, *Shock Waves in Collisionless Plasmas* (Wiley, New York, 1971), and references therein.
5. R. Z. Sagdeev, Rev. Mod. Phys. **51**, 1 (1979).
6. C. M. C. Nairn, R. Bingham, and J. E. Allen, J. Plasma Phys. **71**, 631 (2005).
7. G. B. Whitham, *Linear and Nonlinear Waves* (John Wiley & Sons, New York, 1974).
8. V. I. Karpman, *Nonlinear Waves in Dispersive Media* (Pergamon Press, 1975), pp. 101–104.
9. V. I. Petviashvili and O. A. Pokhotelov, *Solitary Waves in Plasmas and in the Atmosphere* (Gordon Breach, London, 1992).
10. P. K. Shukla, B. Eliasson, and L. Stenflo, Phys. Lett. A **375**, 2371 (2011).
11. P. K. Shukla, B. Eliasson, and L. Stenflo, Eur. Phys. Lett. **95**, 45001 (2011).

12. N. F. Kramer, *Physics of Alfvén Wave* (Wiley, Berlin, 2001).
13. P. A. Damiano, A. N. Wright, and J. F. McKenzie, Phys. Plasmas **16**, 062901 (2009).
14. R. J. Stefant, Phys. Fluids **13**, 440 (1971).
15. A. Hasegawa and C. Uberoi, *The Alfvén wave*, DOE/TIC No. 11197 (Technical Center, US Department of Energy, Washington, DC, 1982).
16. P. K. Shukla and L. Stenflo, in *Nonlinear MHD Waves and Turbulence*, Eds. T. Passot and P. L. Sulem (Springer, Berlin, 1999), pp. 1–30.
17. J. F. McKenzie and T. B. Doyle, Phys. Plasmas **9**, 55 (2002).
18. K. Stasiewicz, P. K. Shukla, G. Gustafsson *et al.*, Phys. Rev. Lett. **90**, 085002 (2003).
19. B. B. Kadomtsev, "Cooperative Effects in Plasmas", in *Reviews of Plasma Physics*, Edited by V. D. Shafranov (Kluwer Academic/Plenum Publishers, New York, 2001), pp. 189–192.
20. L. Stenflo, A. B. Shvartsburg, and J. Weiland, Phys. Lett. A **225**, 113 (1997).
21. P. K. Shukla, B. Eliasson, M. Marklund, and R. Bingham, Phys. Plasmas **11**, 2311 (2004).
22. D. Shaikh and P. K. Shukla, Phys. Rev. Lett. **102**, 045004 (2009).
23. S. S. Moiseev and R. Z. Sagdeev, J. Nucl. Energy: Plasma Phys. **5**, 43 (1963).
24. O. A. Pokhotelov, M. A. Balikhin, R. Z. Sagdeev, and R. A. Treumann, Phys. Rev. Lett. **95**, 129501 (2005).
25. M. G. G. T. Taylor, C. P. Escoubet, H. Laasko, A. Masson, and M. L. Goldstein, The Cluster Mission: Space Plasma in Three Dimensions, in The Cluster Active Archive, Astrophys. Space Sc. Proceedings, Part 4, 309–330 (2010).
26. W. Gekelman, S. Vincena, B. Van Commernolle *et al.*, Phys. Plasmas **18**, 055501 (2011).

Recent Progress in the Theory of Electron Injection in Collisionless Shocks

Takanobu Amano and Masahiro Hoshino

Abstract The injection problem in diffusive shock acceleration theory is discussed with particular focus on electrons. The following issues are addressed: Why it has been considered to be so difficult, what is the required condition, and how it can be resolved. It is argued that there exists a critical Mach number above which the electron injection is achieved. Above the threshold, back-streaming electrons reflected back upstream by the shock front can self-generate high-frequency whistler waves, which can scatter themselves as required for subsequent acceleration. The theoretical estimate is found to be well consistent with in-situ measurements, indicating this could provide a possible solution to the long standing problem in the diffusive shock acceleration theory.

1 Introduction

The acceleration of charged particles at collisionless shocks has been a subject of great interest in connection with the early conjecture that cosmic rays are produced in association with Galactic supernovae. A more concrete theoretical background was given by the theory of diffusive shock acceleration (DSA) proposed in the late 1970s by several independent research groups (see [1] for review). It is actually the most successful theory in that it naturally predicts a power-law type energy spectrum, which is close to the source spectrum inferred from cosmic-ray

T. Amano (✉)
Department of Physics, Nagoya University, Nagoya, Japan

Max-Planck-Institut für Kernphysik, Heidelberg, Germany
e-mail: amanot@stelab.nagoya-u.ac.jp

M. Hoshino
Department of Earth and Planetary Science, University of Tokyo, Tokyo, Japan
e-mail: hoshino@eps.s.u-tokyo.ac.jp

Amano, T. and Hoshino, M.: *Recent Progress in the Theory of Electron Injection in Collisionless Shocks*. Astrophys Space Sci Proc. **33**, 143–152 (2012)
DOI 10.1007/978-3-642-30442-2_16, © Springer-Verlag Berlin Heidelberg 2012

measurements on the earth. Indeed, there is direct observational evidence for the presence of relativistic electrons in young supernova remnants (SNRs) as observed by radio and X-ray synchrotron emission. These cosmic-ray electrons can therefore be used as an important probe to investigate the properties of the particle acceleration sites. It is, on the other hand, also known that the shock acceleration of electrons is rarely observed in the heliosphere [2, 3]. These shocks are generally weaker than astrophysical shocks which are radiating strong synchrotron emission. Protons or other heavier nuclei seem to be accelerated rather efficiently even by such relatively weak shocks, although there are many events showing no evidence for the ion acceleration as well. Identification of the astrophysical proton acceleration sites is of significant importance, because it is this component that constitutes a large fraction of cosmic rays. It is, however, still difficult even with present-day observation facilities due to their intrinsic low radiation efficiency.

The difficulty for the detection of the proton component is to some extent related to a theoretical flaw. The DSA theory can predict the spectral index of accelerated particles, but does not tell anything about the fraction of accelerated particles (or the normalization factor),—the issue known as the injection problem. The injection fraction seems to depend on particle species and parameters of the shock as implied by observations. This actually makes it difficult to identify cosmic-ray protons, because the expected radiative signature of protons in the γ-ray spectrum is contaminated by electron contributions with unknown amount. It is important to give a theoretical constraint for the number of accelerated electrons and protons independently, to reduce this ambiguity as much as possible. To do so, we must address the injection problem, in particular, for electrons. Because in contrast to relatively well understood ion injection, the electron injection is known to be much more difficult [4, 5]. In this review, we outline the basic concept of the injection problem, and describe the difficulty of the electron injection. We then introduce our recent idea in which the electron injection is achieved by exploiting high-frequency whistler waves. A future perspective on the theory of electron injection is also discussed.

2 The Injection Problem

The DSA theory, as its name suggests, is based on the assumption that the transport of energetic particles around the shock is described by the diffusion process. Since the medium is a highly ionized collisionless plasma, the particles have to be scattered by waves so that they diffuse in space otherwise their transport would be ballistic. Assuming the isotropy of the distribution function as a result of strong scatterings, energetic particles will diffuse in the local fluid rest frame. The diffusive transport makes it possible for them to propagate against the downstream flow and cross the shock front. This means that the energetic particles are essentially confined in the vicinity of the shock before being advected far away by the downstream flow (escape toward upstream can be ignored under this assumption.) Across the

shock, there exists a compression of the flow, indicating converging motion of scattering centers. This converging motion brings the particle energy gain during their confinement around the shock, just like a fluid adiabatically heated by the compression. As is evident from the above consideration, the scattering by waves is crucial for the confinement and acceleration of particles. The required conditions for the injection are therefore summarized that the energetic particles (1) should have velocities large enough to travel for a long distance to repeatedly cross the shock front, and (2) need to be scattered by waves so that the transport becomes diffusive. Below, we discuss these conditions in more detail.

2.1 Shock Internal Structure

Since one must consider the dynamics of thermal and/or suprathermal particles to understand the injection, the internal structure of the shock determined primarily by low-energy particles needs to be taken into account. Nevertheless, we will not go into details of rich variety of collective phenomena associated with collisionless shocks, and look for the simplest possible explanation essential for understanding the injection.

Consider upstream particles penetrating into a thin shock transition layer whose scale length comparable to the ion inertial length. Because of the inertial difference between ions and electrons, electrons are easily decelerated at the leading edge of the shock front, while ions are not. As a result, an electrostatic potential is produced, which has to be large enough to decelerate upstream ions otherwise the shock would not form. Although the actual value of the potential is difficult to determine, it is estimated to be 10−20% of the upstream bulk ion energy by in-situ measurements of the bow shock [6], which is more or less consistent with kinetic numerical simulations. The structure of the shock depends strongly on upstream parameters, in particular, Alfvén Mach number $M_A = V_1/v_A$ (V_1 and v_A are the shock and Alfvén speeds), and the shock angle θ_{Bn} defined as the angle between the shock normal and the upstream magnetic field. It is known that, whenever the Alfvén Mach number exceeds a few, a fraction of ions are reflected by the shock front and then dominate the shock structure. Conventionally, shocks with $\theta_{Bn} \lesssim 45$ and $\theta_{Bn} \gtrsim 45$ are respectively called quasi-parallel and quasi-perpendicular shocks, and have different characteristics.

2.2 Escape Condition: Thermal Leakage

Since particles have to cross the shock front many times to be accelerated significantly, the lower limit for the threshold energy is obviously characterized by the condition that particles can traverse the shock almost freely. Here, we consider the condition that downstream thermal particles can escape toward upstream.

A particle in the downstream region whose velocity parallel to the magnetic field line denoted by $v_\parallel$ can travel toward the shock when $v_\parallel \geq \frac{V_1}{r}\sqrt{1+r^2\tan^2\theta_{Bn}}$, where r is the shock compression ratio. Assuming Maxwellian distributions and strong shocks, the downstream particle velocity is characterized by the thermal velocity determined by Rankine-Hugoniot relations (or roughly $\sim V_1$). Then, it is easy to confirm that the downstream thermal particles can escape toward upstream when $\theta_{Bn} \lesssim 30$, while the threshold energy becomes higher as increasing the shock angle. Although this simple argument gives a rather good estimate for the escape condition of ions, one must take into account the effect of the electrostatic potential for electrons. Since the potential develops so as to decelerate the upstream ions, it actually prevents the downstream electrons from escaping upstream. If the downstream temperature is determined solely by the conversion of the bulk energy into the thermal energy and there is no energy transfer between ions and electrons, the thermal velocities of electrons and ions would be the same. In this case, the downstream electron kinetic energy $\sim m_e V_1^2/2$ is not enough to overcome the potential of the order of $\sim \eta m_i V_1^2/2$, where $\eta = 0.1{-}0.2$ is the normalized electrostatic potential, and m_j is the mass of particle species j. In reality, the energy conversion from ions to electrons is known to occur, although the efficiency, especially the dependence on upstream parameters, is not known very well. Nevertheless, in-situ measurements have shown that the temperatures of downstream electrons are mostly less than several tens of percent of the ion temperature, i.e., of the order of the electrostatic potential energy. This indicates that the escape condition of electrons is more or less similar to that of ions. One thus finds that the thermal leakage is possible for both electrons and ions at quasi-parallel shocks, while it is not in quasi-perpendicular shocks unless the downstream distribution develops into one which possesses a high energy tail. Note that, as mentioned earlier, there exist ions that are directly reflected by the shock in the upstream, which can also be considered as a seed population. Qualitatively, however, the condition for ion injection is not so much different, while the processes become much more complicated.

2.3 Resonance Condition

Suppose there exist back-streaming particles in the upstream region. In the absence of upstream waves, these particles would just stream away freely and never get back to the shock. For a self-consistent description of the injection process, one has to consider waves generated by these back-streaming particles themselves through beam instabilities. Since they are streaming along the ambient field line, the condition for instability may qualitatively be analyzed by considering the cyclotron resonance $\omega = kV_b - \Omega_j$ (V_b is the beam velocity and Ω_j is the cyclotron frequency of particle species j) with a normal mode (ω, k) of a magnetized plasma.

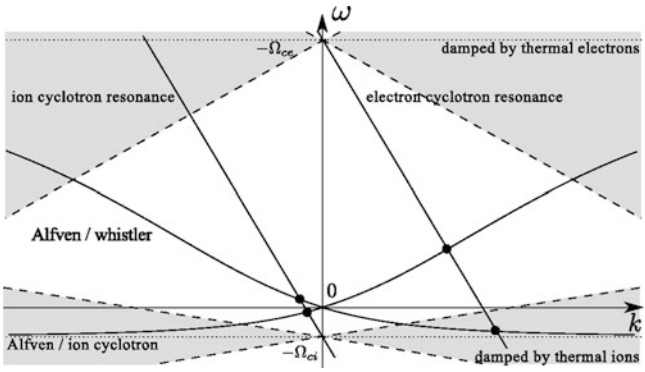

Fig. 1 Schematic dispersion diagram of circularly polarized electromagnetic waves propagating parallel to the ambient magnetic field. Positive and negative frequencies correspond to the *right-hand* (R-mode) and *left-hand* (L-mode) circular polarization. The negative velocity for the cyclotron resonance condition indicates a particle propagating away from the shock

Figure 1 shows schematic dispersion relations of circularly polarized electromagnetic waves propagating parallel to the ambient magnetic field. The solid straight lines in the figure showing the cyclotron resonance condition of electrons and ions intersect with the normal modes. There are actually two intersection points for each species, while only one of them becomes unstable. This can be easily understood by invoking the momentum conservation law. Through the excitation of an instability, the momentum of back-streaming particles are partially transferred into the wave. Therefore, the generated wave should propagate in the direction of the beam, i.e., away from the shock ($\omega/k < 0$ in Fig. 1). Consequently, the ion (electron) beam will be unstable against the excitation of a wave on the R-mode Alfvén/whistler (L-mode Alfvén/ion cyclotron) branch.

In reality, one must also consider the effect of cyclotron damping by thermal particles. Waves with which thermal particles can satisfy the cyclotron resonance condition are actually strongly damped, and thus cannot be recognized as the normal modes of the plasma. Since high frequency waves are more strongly damped, the velocity of back-streaming particles needs to be large enough so that the interaction occurs at sufficiently low frequencies. More specifically, the cyclotron resonance condition defined by using the thermal velocity $\omega = \pm k v_j - \Omega_j$ (where v_j denotes the thermal velocity) may be used to estimate the strongly damped regions (shaded regions in Fig. 1).

First, let us consider the case of back-streaming ions that are leaked from the downstream. Since they have upstream directed velocities in the shock frame, their streaming velocities in the upstream rest frame is larger than the Alfvén speed at least by a factor of M_A. For M_A greater than a few, the interaction will occur well within the magnetohydrodynamics (MHD) regime, so that the ion cyclotron damping is virtually negligible. The back-streaming ions can thus easily excite Alfvén waves. The excitation of low-frequency Alfvén waves in the upstream region

(the foreshock) and associated pitch-angle scattering of ions have been confirmed both by numerical simulations and in-situ observations.

On the other hand, the situation for electrons is completely different. The backstreaming electrons would typically interact with the ion-cyclotron wave in high frequency regime ($\omega \sim \Omega_i$) where the ion cyclotron damping is significant unless the electron velocity is extremely large. More specifically, the required condition that the electrons interact with low-frequency MHD waves ($kv_A/\Omega_i \lesssim 1$) may be written as

$$\left|\frac{V_b}{v_A}\right| \gtrsim \left|\frac{\Omega_e}{\Omega_i}\right|. \tag{1}$$

In the typical interstellar or interplanetary media, the electron velocity should be of the order of the speed of light $V_b \sim c$ to satisfy the above condition. This is the reason why the electron injection has been believed to be so difficult. For instance, the electron temperatures downstream of young SNR shocks are estimated to be $\sim$1 keV, which are far too small for the injection. These shocks, on the other hand, are radiating radio and X-ray photons by synchrotron emission from ultra-relativistic electrons. This apparent contradiction has not yet been resolved so far.

In order to achieve the electron injection, one must have a pre-acceleration mechanism that energizes thermal electrons to mildly relativistic energies. Several possible mechanisms have been proposed so far that could accelerate to the required energies involving microinstabilities in the shock transition region [7–13]. Or, alternatively, there must be a mechanism that produces high-frequency whistler waves that can scatter low-energy electrons [14]. In any case, there has been no general consensus about what would be the most probable mechanism for the electron injection. In the following section, we discuss our recent work on the electron injection problem, which is found to be consistent with existing observations.

3 Electron Injection Mechanism: Recent Progress

3.1 Shock Drift Acceleration

We have seen that the thermal leakage does not provide sufficient energies for the electron injection. It is known that electrons can also be directly reflected by the shock front, as in the case of ions, and thus be energized more efficiently. Shock drift acceleration (SDA), or a fast Fermi process, is known as an adiabatic magnetic mirror reflection process in the Hoffmann-Teller frame (HTF) [15,16]. The HTF can be defined as the frame where the motional electric field vanishes. Because of the absence of electric fields, the particle energy measured in this frame is a conserved quantity. An upstream electron traveling toward the shock will be reflected by the shock acting as a magnetic mirror if the particle pitch-angle defined in the HTF is large enough (Fig. 2). Notice that, however, a finite electrostatic potential at the

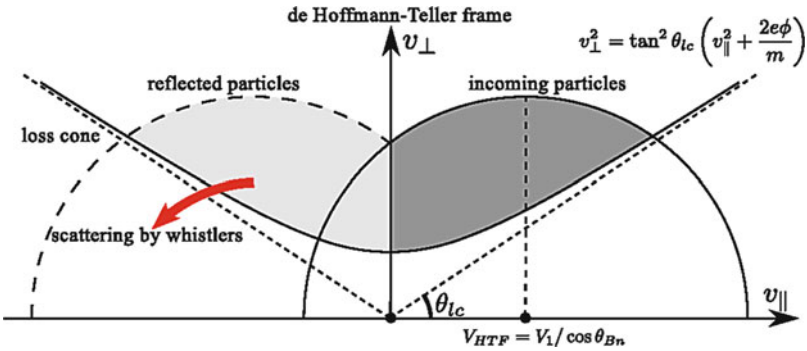

Fig. 2 Schematic particle distribution function in the Hoffmann-Teller frame (HTF). Incoming particles (positive $v_\parallel$) above the *solid curve* are reflected by the shock acting as a magnetic mirror. The electrostatic potential ϕ measured in the HTF enlarges the loss cone at low energies

shock enlarges the loss cone angle at low energies, while it has little effects on sufficiently high-energy particles.

When the particle energy is measured in the upstream rest frame, it will actually increase as a result of the reflection. The average velocity of the reflected beam in the upstream frame is given by $V_b \simeq 2V_1/\cos\theta_{Bn}$ (see [15, 16] for detail), which is larger than that of a thermal leakage population by a factor of $\sim 2/\cos\theta_{Bn}$ (strictly speaking, this holds only for low-energy electrons having gyroradii much smaller than the shock thickness). Therefore, this effect alone can to some extent help the situation in quasi-perpendicular shocks. The condition that the reflected electron beam resonates with low-frequency Alfvén waves at $kv_A/\Omega_i \lesssim 1$ may be written as

$$M_A \gtrsim \frac{\cos\theta_{Bn}}{2}\frac{m_i}{m_e}. \tag{2}$$

This condition may be satisfied, for instance, at the very beginning of supernova evolution with moderate shock angles. However, typical SNR shocks with a speed of a few 1,000 km/s require a rather severe condition $\cos\theta_{Bn} \ll 1$.

3.2 Generation of Whistler Wave

The electron beam generated by the SDA process provides another source of free energy because the distribution is expected to possess a loss cone in velocity space. This is an inevitable consequence of a mirror reflection process, and is actually frequently observed in the upstream region of the bow shock. It is known that a loss-cone type velocity distribution tends to be unstable against the excitation of whistler waves, unlike the case of a Maxwellian beam in which an instability on this branch is prohibited. The reason why the loss-cone type distribution can generate whistler waves is that electrons will be scattered by waves so as to fill the loss

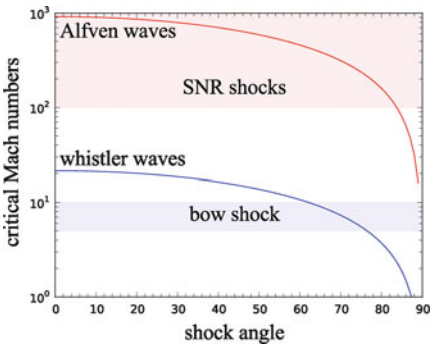

Fig. 3 Critical Mach number as a function of the shock angle. *Upper* and *lower solid lines* indicate Eqs. (2) and (3) ($\beta_e = 1$), respectively. Typical Mach numbers of SNR shocks and the bow shock are also indicated

cone (because of a positive slope of the distribution function along the diffusion curve). Therefore, the momentum of electrons decreases (notice for the sign) on average as a result of scattering. Consequently, a whistler wave propagating toward the shock (having positive momentum) can be excited. It is noted that electrostatic waves possibly excited by the electron beam will scatter the electrons primarily in the parallel direction, but not fill the loss cone. Thereby the result will qualitatively be the same even taking into account the effect of electrostatic instabilities.

Again, the instability must overcome the electron cyclotron damping. It is easy to confirm that the beam instability even in the presence of a loss cone has the maximum growth rate around the point where the cyclotron resonance condition $\omega = kV_b - \Omega_e$ is satisfied. One can thus avoid significant electron cyclotron damping when the beam velocity is larger than the electron thermal velocity $V_b \gtrsim v_e$, which leads

$$M_A \gtrsim \frac{\cos\theta_{Bn}}{2}\sqrt{\frac{m_i}{m_e}\beta_e}, \tag{3}$$

where β_e is the electron thermal pressure to magnetic pressure ratio. Notice for the different dependence on the mass ratio between Eqs. (2) and (3) (see also Fig. 3). One can see that the required condition is now much less stringent. In particular, the bow shock can be super-critical in the quasi-perpendicular regime. This actually gives a firm theoretical background for a statistical analysis of bow shock measurements done by Oka et al. [17], who found an almost the same dependence. According to them, the spectral index of energetic electrons in the shock transition region becomes systematically harder when an approximately (within a factor of ∼2) the same condition to Eq. (3) is satisfied. (More specifically, they claimed the dependence on the so-called whistler critical Mach number [18], which happens to have a similar form. However, since it has a different theoretical background, the authors of [17] could not find any reasonable explanations.) Based on the observational fact, we believe that it is actually this condition that determines the electron acceleration efficiency in the bow shock. This also explains naturally the reason why strong SNR shocks are efficient electron accelerators as opposed to weaker heliospheric shocks. A more detailed numerical investigation of the instability given in [19] basically confirmed this argument.

3.3 Non-adiabatic Effects

We have discussed the process by which the electron injection is achieved. However, we still do not know the fraction of electrons being injected into the acceleration cycle. Answering this question probably needs understanding of nonlinear collective plasma phenomena occurring around the collisionless shocks. This is because the adiabatic theory is not necessarily a good description for the dynamics of suprathermal electrons being considered. This does not mean that the adiabatic description is totally wrong; rather, we think that non-adiabatic corrections to SDA need to be taken into account for quantitative discussion. Furthermore, the situation will increasingly become complicated with increasing the Mach number of the shock.

As seen in Fig. 2, the SDA operates only for electrons having sufficiently large initial pitch angles because otherwise they would be just transmitted to the downstream. The required threshold particle velocity (defined in the upstream rest frame) is roughly proportional to $V_1/\cos\theta_{Bn}$. The condition for the injection Eq. (3), on the other hand, can be rewritten as $V_1/\cos\theta_{Bn} \gtrsim v_e$ (apart from a factor of order unity). Taking this literally, the reflection of thermal particles will hardly occur for strong shocks well above the critical Mach number such as SNR shocks. This implies the need for taking into account non-adiabatic effects that could lead to a non-negligible electron injection rate.

Indeed there have been a lot of discussion on plasma instabilities in the vicinity of the shock. In the regime $V_1/\cos\theta_{Bn} \gg v_e$, one can actually expect stronger instabilities in the shock transition region driven by the reflected ion beam [7, 20]. These plasma waves can play a role for the acceleration of thermal electrons above the threshold energy so that the electron injection rate is dramatically increased even in a highly super-critical regime. We have actually demonstrated by using particle-in-cell (PIC) simulations that such can actually occur in high Mach number quasi-perpendicular shocks [12], although there is still much work to be done to understand quantitatively the complicated electron injection process dominated by nonlinear plasma phenomena, particularly dependence on the Mach number and multidimensional effects. Large scale kinetic numerical simulations of high Mach number shocks will further improve our understanding in the future.

4 Discussion

We have presented a possible mechanism for the electron injection, which is proven to be consistent with in-situ measurements of the bow shock. We believe this resolves, at least qualitatively, the observational discrepancy found between shocks associated with high-energy astrophysical objects and those directly measured in the heliosphere. One might have concern about the possibility of back-streaming electron scattering toward the shock because the instability is fed by the scattering of electrons away from the shock. In the steady state, however, we anticipate that the

pitch-angle distribution of electrons will become closer to isotropic. This indicates there will also be back scattering of electrons as well, so that the diffusion approximation is justified. This needs to be clarified in relation to issues discussed below.

Our discussion has been restricted to the linear stability analysis, which indicates that the growth rate of the instability is so large that the acceleration of electrons can occur within the thin shock layer. This idea is consistent with the fact that the observed energetic electrons associated with quasi-perpendicular shocks are typically confined within the shock [17, 21]. Nevertheless, the acceleration process will probably be modified by the inhomogeneity, affecting the propagation of whistler waves (through refraction and mode conversion), and the transport of electrons by the lowest order mirror force.

It is particularly important to mention that the electron injection will be influenced by the ion injection when the latter is so efficient that the upstream medium is strongly disturbed. Although the local electron injection rate is likely to be determined only by local shock parameters, the total number of injected population will be affected by the global modification of the shock. Comprehensive understanding of the whole process is needed for elucidation of cosmic-ray acceleration in astrophysical shocks.

Acknowledgements T. A. is supported by the Global COE program of Nagoya University (QFPU) and KAKENHI 22740118 from JSPS and MEXT of Japan. This manuscript was written while one of the authors (T. A.) was visiting Max-Planck-Institut für Kernphysik at Heidelberg, Germany.

References

1. R. Blandford, D. Eichler, Phys. Rep. **154**(1), 1 (1987)
2. N. Shimada, et al., Astrophys. Space Sci. (1), 481 (1999)
3. M. Oka, et al., Earth Planets Space **61**, 603 (2009)
4. M.A. Malkov, H.J. Voelk, Astron. Astrophys. (1995)
5. J.G. Kirk, R.O. Dendy, J. Phys. G: Nucl. Partic. **27**(7), 1589 (2001)
6. S.J. Schwartz, et al., J. Geophys. Res. **93**(A11), 12923 (1988)
7. K. Papadopoulos, Astrophys. Space Sci. **144**, 535 (1988)
8. P.J. Cargill, K. Papadopoulos, Astrophys. J. **329**, L29 (1988)
9. K.G. McClements, et al., Mon. Not. R. Astron. Soc. **291**(2), 241 (1997)
10. K.G. McClements, et al., Phys. Rev. Lett. **87**(25) (2001)
11. M. Hoshino, N. Shimada, Astrophys. J. **572**(2), 880 (2002)
12. T. Amano, M. Hoshino, Astrophys. J. **661**(1), 190 (2007)
13. T. Amano, M. Hoshino, Astrophys. J. **690**(1), 244 (2009)
14. A. Levinson, Astrophys. J. **401**, 73 (1992)
15. C.S. Wu, J. Geophys. Res. **89**, 8857 (1984)
16. M.M. Leroy, A. Mangeney, Ann. Geophys. **2**, 449 (1984)
17. M. Oka, et al., Geophys. Res. Lett. **33**(24) (2006)
18. V.V. Krasnoselskikh, et al., Phys. Plasmas **9**(4), 1192 (2002)
19. T. Amano, M. Hoshino, Phys. Rev. Lett. **104**(18), 181102 (2010)
20. C.S. Wu, et al., Space Sci. Rev. **37**(1-2), 63 (1984)
21. J.T. Gosling, et al., J. Geophys. Res. **94**(A8), 10011 (1989)

Superdiffusive Transport at Shocks in Space Plasmas

Gaetano Zimbardo and Silvia Perri

Abstract Superdiffusion is characterized by a nonlinear growth of the mean square deviation with time. Superdiffusive transport can be interpreted in terms of a Lévy random walk, a stochastic process where a power-law distribution of free path lengths is allowed. Considering particles accelerated at interplanetary shocks, it is found that their intensity profile is a power-law in time in the case of superdiffusion, while it is an exponential decay for normal diffusion. Analysis of energetic particle fluxes from the Ulysses spacecraft at about 5 AU and from the Voyager 2 spacecraft at the solar wind termination shock shows that superdiffusive transport is found.

1 Introduction

The propagation of energetic particle in space plasmas is an important problem, which is relevant for the heat transport in solar coronal loops, for the propagation of solar energetic particles in the heliosphere, and for the propagation of particles accelerated at corotating interaction regions to high heliographic latitudes [4,11,13]. The transport properties and the value of the diffusion coefficient are also important for understanding particle acceleration at shocks by diffusive shock acceleration [1–3, 17]. In either weakly collisional or collisionless plasmas, the transport is influenced by wave particle interactions, which cause pitch angle scattering and transverse particle drifts, and by low frequency magnetic fluctuations, which cause a field line random walk [4]. However, the strength of these effects varies with the particle species and energy and with the properties of turbulence, so that a large

G. Zimbardo (✉) · S. Perri
Università della Calabria, Ponte P. Bucci, Cubo 31C, I-87036 Arcavacata di Rende, Italy
e-mail: gaetano.zimbardo@fis.unical.it; silvia.perri@fis.unical.it

Zimbardo, G. and Perri, S.: *Superdiffusive Transport at Shocks in Space Plasmas*. Astrophys Space Sci Proc. **33**, 153–158 (2012)
DOI 10.1007/978-3-642-30442-2_17, © Springer-Verlag Berlin Heidelberg 2012

number of different transport regimes can be obtained, as shown by independent numerical simulations [12, 15, 18]. We can divide these regimes in normal diffusion regimes, for which the mean square deviation grows as $\langle \Delta x^2 \rangle = 2Dt$, i.e., linearly with time, and anomalous diffusion regimes, for which $\langle \Delta x^2 \rangle \propto t^\alpha$, with $\alpha \neq 1$. In this chapter we give some basic ideas on superdiffusive transport, i.e., when $\alpha > 1$, and we indicate how superdiffusive transport regimes can be deduced from data analysis.

2 Main Properties of Superdiffusion

In the case of normal diffusion, for times much longer than the collision time, the mean square displacement can be written as

$$\langle \Delta x^2 \rangle = 2Dt \tag{1}$$

where D is the diffusion coefficient. Let us follow the particles which are subject to the random walk: for a particle moving with velocity v_x we have $\Delta x(t) = \int_0^t v_x(t')dt'$; for a statistically homogeneous and stationary system, we can obtain the so-called Green-Taylor-Kubo formula for the running diffusion coefficient [14]:

$$D(t) = \int_0^t \langle v_x(0)v_x(t') \rangle dt' \tag{2}$$

where the angle brackets denote the ensemble average. The integrand represents the Lagrangian velocity autocorrelation function; if this goes to zero sufficiently fast, as in the case of an exponential decay, a correlation time τ can be defined such that $\langle v_x(0)v_x(t) \rangle$ is negligible for $t \gg \tau$. In such a case the upper integration limit can be extended to infinity, and at the same time the integral can be estimated as

$$D = \int_0^\infty \langle v_x(0)v_x(t) \rangle dt \approx v_x^2 \tau. \tag{3}$$

Considering that the mean free path $\lambda = v\tau$ is given by the mean collision (or correlation) time τ times the velocity $v = (v_x^2 + v_y^2 + v_z^2)^{1/2}$, we can estimate the diffusion coefficient as $D \simeq \frac{1}{3}v^2\tau = \frac{1}{3}\lambda v$.

On the other hand, if the Lagrangian velocity autocorrelation function does not go to zero fast, as for instance in the case that it has power-law tails like $\langle v_x(0)v_x(t) \rangle \sim t^{-\beta}$ with $\beta < 1$, the above integral is diverging, so that no time asymptotic diffusion coefficient and no mean free path can be defined. This divergence is related to long range correlations in the velocity, i.e., to a non Markovian, non local process. If $D(t)$ grows indefinitely with time, the mean square deviation in Eq. (1) will exhibit a superdiffusive growth. Also, the divergence of D implies that λ is diverging, too, since the particle velocity is finite.

The divergence of D and of λ requires a new, non Gaussian approach to transport: one such approach is based on a probabilistic description involving a Lévy random walk, which is a random walk characterized by a power law distribution of the free path, or jump, lengths. In one dimension, the probability ψ of a random walker making a free path of length ℓ (forward or backward) in a time t is given as [5]

$$\psi(\ell, t) = A\,|\ell|^{-\mu}\,\delta(\ell - vt), \qquad |\ell| > \ell_0 \tag{4}$$

where it is essential to have a coupling between jump length and jump duration, as expressed by the delta function, in order to ensure the conservation of energy. It is readily verified that for $\mu < 3$ the mean square value of ℓ, and hence the mean free path λ, is diverging,

$$\langle \ell^2 \rangle = \int \ell^2\,\psi(\ell, t)\,d\ell dt \to \infty \qquad \mu < 3 \tag{5}$$

which means that the central limit theorem, which leads to normal diffusion, is not applicable. Therefore, the jump probability distribution in Eq. (4) for $\mu < 3$ opens the gate to anomalous transport. This can be described by introducing the probability density $P(x, t)$ of being at position x at time t—the propagator. It can be shown that the transport regime depends on the index μ of the jump probability distribution, and that superdiffusion with $\alpha = 4 - \mu$ is obtained for $2 < \mu < 3$ [5]. In addition, the solution for the propagator $\hat{P}(k, s)$ in Fourier-Laplace space can also be obtained from the Montroll-Weiss equation [19]; the analytical inversion of $\hat{P}(k, s)$ is not known in general, but it can be obtained in limiting cases. One such case is that of short distances x compared to the typical width of the bell-shaped part of $P(x, t)$, which is given by $\Delta x = (k_\mu t^{2/(\mu-1)})^{1/2}$ [19], where k_μ is a scale parameter with dimensions of a length squared over a time to the power $2/(\mu - 1)$. In such a limit $x \ll (k_\mu t^{2/(\mu-1)})^{1/2}$ the Fourier-Laplace inversion of $\hat{P}(k, s)$ yields [19]

$$P(x, t) = \frac{A_0}{t^{1/(\mu-1)}} \exp\left(-\frac{x^2}{k_\mu t^{2/(\mu-1)}}\right). \tag{6}$$

In the opposite limit of the distance x much larger than the typical width of $P(x, t)$, i.e., for $x \gg (k_\mu t^{2/(\mu-1)})^{1/2}$, the following expression is obtained [19]

$$P(x, t) = A_1\,\frac{t}{x^\mu}, \qquad x < vt, \tag{7}$$

with the propagator being zero for $x > vt$ because of the causality relation imposed by the δ function in Eq. (4). Above, A, A_0 and A_1 are normalization constants. As can be seen, the long distance propagator has a power-law form, sharply different from the normal Gaussian propagator.

3 Superdiffusion from Energetic Particles Upstream of Shocks

How to detect anomalous transport from observations? An important example is that of particles accelerated at shock waves in the solar wind: the energetic particles reach energies of order of 1–10 MeV, and are clearly distinguishable from the background plasma. We notice that particles are accelerated continuously by the shock, that is, the injection is not pointlike, whence the omnidirectional distribution function of particles of energy E, $f(x, E, t)$, measured by a spacecraft at (x, t) can be expressed in integral form as

$$f(x, E, t) = \int P(x - x', t - t') q_{\rm sh}(x', E, t') dx' dt'. \tag{8}$$

In this expression we consider a one dimensional planar shock at (x', t'), therefore only the dependence on the x coordinate, which is normal to the shock, is retained, and $q_{\rm sh}(x', E, t')$ represents the source of particles of energy E emitted at the shock. For a moving shock, this can be modelled as [7, 8]

$$q_{\rm sh}(x', E, t') = q_0(E) \delta(x' - V_{\rm sh} t') \tag{9}$$

where $q_0(E)$ represents the number of particles emitted per unit time, and $V_{\rm sh}$ is the shock speed as seen from the observer at x. Assuming that the shock is coming from $x < 0$ and that the observer is at $x = 0$, and using the Gaussian propagator as appropriate for normal diffusion, the following time profile is obtained [8]

$$f(0, E, t) \propto q_0(E) \exp[-V_{\rm sh}(V_{sw} + V_{\rm sh}) t / D] \tag{10}$$

that is an exponential decay, which is in agreement with the well known result of [6]. On the other hand, in the case of superdiffusion the propagator has the power-law shape in Eq. (7), appropriate at some distance upstream of the shock,

$$P(x - x', t - t') = A_1 \frac{t - t'}{(x - x')^{\mu}} \tag{11}$$

Using this expression the double integration in Eq. (8) yields, for $x = 0$ and $t < 0$ (i.e., upstream of the shock) [7, 8]

$$f(0, E, t) \propto (-t)^{2-\mu} = (-t)^{-\gamma} \tag{12}$$

In other words, a power-law time profile for energetic particles upstream of the shock with slope $\gamma = \mu - 2 < 1$ is the signature of superdiffusion with anomalous diffusion exponent $\alpha = 4 - \mu = 2 - \gamma > 1$.

Using this technique as a diagnostic tool, [7–9] have shown that electron transport upstream of the shocks associated with corotating interaction regions (CIRs) detected by the Ulysses spacecraft in the solar wind at 4–5 AU is superdiffusive, with $\alpha \simeq 1.1$–1.7. Also, ion transport upstream of CIR shocks is found to be normal in most cases, although a slightly superdiffusive case with $\alpha = 1.13$ is found at a CIR shock detected by Voyager 2 at 6.9 AU. The more decidedly superdiffusive behaviour of electrons has been ascribed to the fact that electrons have smaller gyroradii then ions, and therefore the resonant interaction with turbulence happens at larger wavenumbers, where the wave power is less: this favours weak pitch angle scattering and hence superdiffusion [7, 8]. On the other hand, analyzing the Voyager 2 data of low energy particles, [10] have shown that ion transport upstream of the solar wind termination shock at 84 AU is superdiffusive, too, with $\alpha \simeq 1.3$. Perri and Zimbardo [10] have interpreted this result as due to the decrease of the turbulence level with the distance from the sun, so that weak turbulence corresponds to weak pitch angle scattering.

Nevertheless, recently [16], using ACE data and the approach outlined above, have found that proton transport upstream of a coronal mass ejection driven shock at 1 AU is superdiffusive, too, with $\alpha \simeq 1.3$. A careful selection of the events has been done by Sugiyama and Shiota [16] in order to be sure that the shock could be considered planar and with constant velocity. They also point out that the level of magnetic fluctuations is not so small for the considered event (at variance with what can be assumed for the termination shock at 84 AU), therefore pitch angle scattering should not be so weak. Sugiyama and Shiota [16] propose that superdiffusion is due to the fact that the wave particle interaction falls into a nonlinear regime, where the quasilinear pitch angle diffusion coefficient no longer applies (in other words, quasilinear theory overestimates the pitch angle diffusion rate). So we can see that the observation of superdiffusion gives information on the wave particle interactions in the nonlinear regime, too.

References

1. Dosch, A., Shalchi, A. Diffusive shock acceleration at interplanetary perpendicular shock waves: influence of the large scale structure of turbulence on the maximum particle energy. Adv. Space Res., 46, 1208–1217, 2010.
2. Fisk, L. A., Lee, M. A. Shock acceleration of energetic particles in corotating interaction regions in the solar wind. Astrophys. J., 237, 620–626, 1980.
3. Giacalone, J. Cosmic-ray transport and interaction with shocks. Space Sci. Rev., 10.1007/s11214-011-9763-2, 2011.
4. Jokipii, J. R. Cosmic-ray propagation. I. Charged particles in a random magnetic field. Astrophys. J., 146, 480–487, 1966.
5. Klafter, J., Blumen, A., Shlesinger, M. F. Stochastic pathway to anomalous diffusion. Phys. Rev. A, 35, 3081–3085, 1987.
6. Lee, M. A., Fisk, L. A. Shock acceleration of energetic particles in the heliosphere. Space Sci. Rev., 32, 205–228, 1982.

7. Perri, S., Zimbardo, G. Evidence of superdiffusive transport of electrons accelerated at interplanetary shocks. Astrophys. J. Lett., 671, 177–180, 2007.
8. Perri, S., Zimbardo, G. Superdiffusive transport of electrons accelerated at corotating interaction regions. J. Geophys. Res., 113, A03107, doi:10.1029/2007JA012695, 2008.
9. Perri, S., Zimbardo, G., Ion and electron superdiffusive transport in the interplanetary space. Adv. Space Res., 44, 465–470, 2009a.
10. Perri, S., Zimbardo, G., Ion superdiffusion at the solar wind termination shock, Astrophys. J. Lett., 693, L118–L121, 2009b.
11. Pommois, P., Veltri, P., Zimbardo, G. Field line diffusion in solar wind magnetic turbulence and energetic particle propagation across heliographic latitudes J. Geophys. Res., 106, 24965–24978, 2001.
12. Pommois, P., Zimbardo, G., Veltri, P. Anomalous, non-Gaussian transport of charged particles in anisotropic magnetic turbulence. Phys. Plasmas, 14, 012311-1–012311-11, 2007.
13. Reames, D. V. Particle acceleration at the Sun and in the heliosphere. Space Sci. Rev., 90, 413–491, 1999.
14. Shalchi, A. Applicability of the Taylor-Green-Kubo formula in particle diffusion theory. Phys. Rev. E, 83, 046402-1–046402-6, 2011.
15. Shalchi, A., Kourakis, I. A new theory for perpendicular transport of cosmic rays. Astron. Astrophys., 470, 405–409, 2007.
16. Sugiyama, T., and Shiota, D. Sign for super-diffusive transport of energetic ions associated with a coronal-mass-ejection-driven interplanetary shock. Astrophys. J., 731, L34–L37, 2011.
17. Zank, G. P., Li, G., Florinski, V., Hu, Q., Lario, D., Smith, C. W. Particle acceleration at perpendicular shock waves: Model and observations. J. Geophys. Res., 111, A06108, doi:10.1029/2005JA011524, 2006.
18. Zimbardo, G., Veltri, P., Pommois, P. Anomalous, quasilinear, and percolative regimes for magnetic-field-line transport in axially symmetric turbulence. Phys. Rev. E, 61, 1940–1948, 2000.
19. Zumofen,G., Klafter, J. Scale-invariant motion in intermittent chaotic systems. Phys. Rev. E, 47, 851–863, 1993.

Inversion of Physical Parameters in Solar Atmospheric Seismology

Iñigo Arregui

Abstract Magnetohydrodynamic (MHD) wave activity is ubiquitous in the solar atmosphere. MHD seismology aims to determine difficult to measure physical parameters in solar atmospheric magnetic and plasma structures by a combination of observed and theoretical properties of MHD waves and oscillations. This technique, similar to seismology or helio-seismology, demands the solution of two problems. The direct problem involves the computation of wave properties of given theoretical models. The inverse problem implies the calculation of unknown physical parameters, by means of a comparison of observed and theoretical wave properties. Solar atmospheric seismology has been successfully applied to different structures such as coronal loops, prominence plasmas, spicules, or jets. However, it is still in its infancy. Far more is there to come. We present an overview of recent results, with particular emphasis in the inversion procedure.

1 Introduction

The term solar atmospheric seismology refers to the study of the physical conditions in solar atmospheric magnetic and plasma structures by the study of the properties of waves in those structures. The aim is to increase our knowledge about the complicated structure and dynamics of the solar atmosphere. The reason why solar atmospheric structures can be probed from their oscillations is that the properties of these oscillations are entirely determined by the plasma and magnetic field properties. This remote diagnostics technique was first suggested by Uchida [27] and Roberts et al. [20], in the coronal context, and by Roberts et al. [21] and Tandberg-Hanssen [24] in the prominence context. Solar atmospheric seismology

I. Arregui (✉)
Departament de Física, Universitat de les Illes Balears, E-07122 Palma de Mallorca, Spain
e-mail: inigo.arregui@uib.es

Arregui, I.: *Inversion of Physical Parameters in Solar Atmospheric Seismology*. Astrophys Space Sci Proc. **33**, 159–169 (2012)
DOI 10.1007/978-3-642-30442-2_18, © Springer-Verlag Berlin Heidelberg 2012

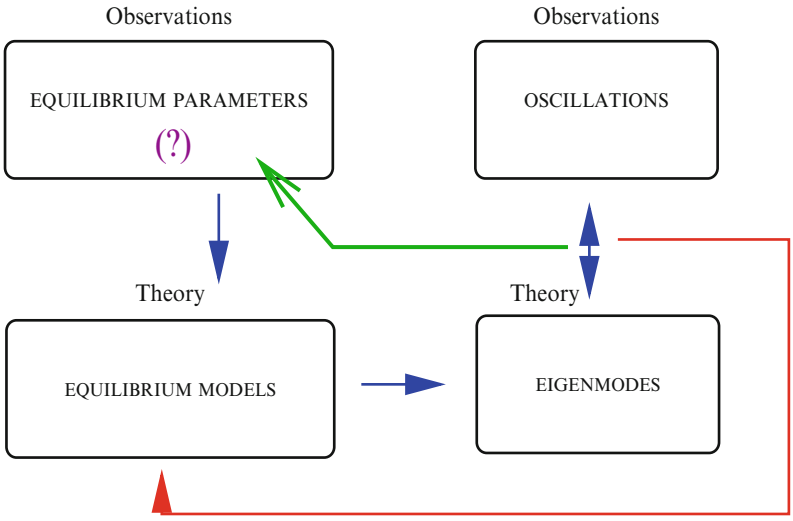

Fig. 1 The method of MHD seismology

has experienced a great advancement in the last decade, made possible by the increase in the quantity and quality of wave activity observations obtained from space-borne observatories (TRACE, Hinode, SDO), and the refinement of theoretical MHD wave models.

The method of MHD seismology is displayed in Fig. 1. Observations of solar coronal magnetic and plasma structures provide us with information that can be used to construct theoretical models. Observations also provide us with measurements of certain wave properties, such as periods, damping times, or additional parameters, such as mass flow speeds. By analyzing the wave properties of given theoretical models (direct problem) these can be compared to the observed wave properties, and difficult to measure physical quantities can be obtained (inverse problem).

This paper presents an overview of recent results obtained from the application of MHD seismology techniques to infer physical properties in solar atmospheric structures. Some representative examples are selected. Our emphasis will be on the different inversion techniques that have been used.

2 Seismology Using the Period of Oscillations

Quickly damped transverse coronal loop oscillations where first reported by Aschwanden et al. [7] and Nakariakov et al. [18]. They are interpreted as the fundamental MHD kink mode of a magnetic flux tube. Using this interpretation [17] performed the first modern seismology application, determining the magnetic field strength in a coronal loop. Their analysis was based on the observational

determination of the period (P) of the oscillation and length (L) of the loop, that lead to an estimate of the phase speed

$$\frac{\omega}{k} = \frac{2L}{P}, \tag{1}$$

with ω the frequency and k the longitudinal wavenumber. Theory for standing kink waves in the long wavelength approximation tells us that the phase speed can be approximated by the so-called kink speed, $c_{\rm k}$, which in terms of the physically relevant quantities reads

$$\frac{\omega}{k} \approx c_{\rm k} \equiv v_{\rm Ai}\left[\frac{2\zeta}{1+\zeta}\right]^{1/2}. \tag{2}$$

In this expression, $v_{\rm Ai}$ is the Alfvén speed in the loop and $\zeta = \rho_{\rm i}/\rho_{\rm e}$ the ratio of internal to external densities. Notice that both quantities are unknown, hence no unique solution can be obtained from the observed period alone. Further progress with algebraic relation (2) requires the consideration of the density contrast a parameter, to obtain the Alfvén speed. Then the magnetic field strength is determined as $B = (4\pi\rho_i)^{1/2}v_{\rm Ai}$. By considering loop number densities in the range $[1–6]\times10^9\,{\rm cm}^{-3}$, magnetic field strengths in between 4 and 30 G are obtained. The method outlined by Nakariakov and Ofman [17] for single mode seismology of coronal loops has been subsequently employed using better observations and more accurate data analysis techniques. Some relevant analyses can be found in [30, 36, 40].

Prominence fine structures also display transverse oscillations. A recent study by Lin et al. [16] follows the same inversion procedure as [17] applying it to propagating transverse thread oscillations. A fundamental difference with respect to the coronal loop case is that, in the limit of high density contrast typical of prominence plasmas, the ratio $\rho_{\rm i}/\rho_{\rm e}$ is very large and the ratio $c_{\rm k}^2/v_{\rm Ai}^2$ is almost independent from it. The kink speed can then be approximated by

$$c_{\rm k} \approx \sqrt{2}v_{\rm Ai}. \tag{3}$$

Reference [16] assumed that thread oscillations observed from the Hα sequences were the result of a propagating kink mode, which implies that the measured phase velocity, $c_{\rm p}$, is equal to the kink speed. Then, the prominence thread Alfvén speed ($v_{\rm Ap}$) can be computed from

$$v_{\rm Ap} \approx \frac{c_{\rm p}}{\sqrt{2}}. \tag{4}$$

The inferred values of $v_{\rm Ap}$ for ten selected threads show that the physical conditions in different threads were very different in spite of belonging to the same filament. Once the Alfvén speed in each thread was determined, the magnetic field strength could be computed when a value for the thread density was adopted. For the analyzed events, and considering a typical value for the prominence density, $\rho_{\rm i} = 5\times10^{-11}\,{\rm kg\,m}^{-3}$, magnetic field strengths in the range 0.9–3.5 G were obtained.

The widespread use of the concept of period ratios as a seismological tool (reviewed by Andries et al. [3]) has been remarkable in the context of coronal loop oscillations. The idea was first put forward by Andries et al. [1] and Goossens et al. [12] as a means to infer the coronal density scale height using multiple mode oscillations in coronal loops embedded in a vertically stratified atmosphere. In coronal loop seismology, the ratio of the fundamental mode period to twice that of its first overtone in the longitudinal direction ($P_1/2P_2$) mainly depends on the density structuring along magnetic field lines. It is equal to unity in longitudinally uniform tubes, but is smaller than one when density stratification is present (magnetic field stratification has the opposite effect as we discuss in Sect. 5). It can therefore be used as a diagnostic tool for the coronal density scale height, since there is a one-to-one relation between density stratification and period ratio. Using observational estimates for two simultaneous multiple mode observations by Verwichte et al. [39] and Andries et al. [1] find that both observations are consistent with an expected scale height of about 50 Mm. For the second case a reasonably confined estimate for the density scale height in between 20 and 99 Mm is calculated. For a different event and following the same method, [29] obtain a value of 109 Mm, which is about double the estimated hydrostatic value.

The period ratio approach has also been followed by Díaz et al. [9] to obtain information about the density structuring along prominence threads. These authors showed that the dimensionless oscillatory frequencies of the fundamental kink mode and the first overtone are almost independent of the ratio of the thread diameter to its length. Thus, the dependence on the length of the tube and the thread Alfvén speed can be removed by considering the period ratio,

$$\frac{P_1}{2P_2} = F(W/L, \rho_{\rm p}/\rho_{\rm c}). \tag{5}$$

Equation (5) can be used for diagnostic purposes, once reliable measurements of multiple mode periods are obtained. From an observational point of view, there seem to be hints of the presence of multiple mode oscillations in observations by Lin and Engvold [15], who reported on the presence of two periods, $P_1 = 16$ and $P_2 = 3.6$ min in their observations of a prominence region. Reference [9] used the period ratio from these observations to infer a value of $v_{\rm Ap} \sim 160$ km s^{-1} for the prominence Alfvén speed.

3 Seismology Using the Damping of Oscillations

Soon after transverse coronal loop oscillations were discovered a number of physical mechanisms were proposed to explain their quick time damping. We concentrate here on resonant absorption [13, 22]. Damping is another source of information for plasma diagnostics and seismology using resonant absorption enables us to infer information about the transverse density structuring in magnetic flux tubes. The

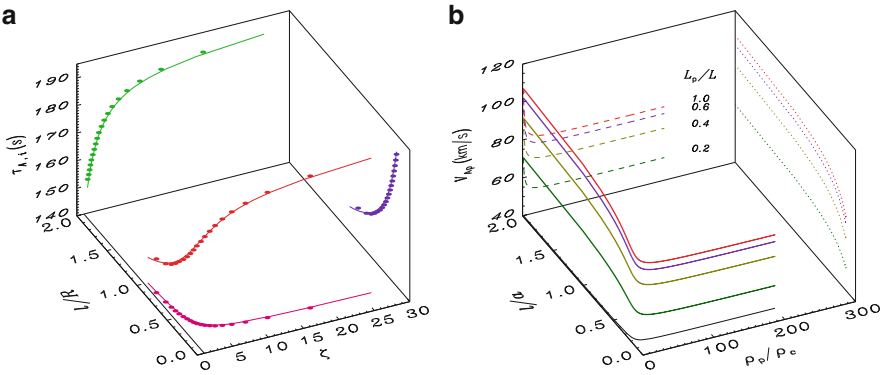

Fig. 2 (**a**) Inversion curve for a coronal loop oscillation with $P = 272$ s and $\tau_d = 849$ s in the parameter space of unknowns. (**b**) Application of the same inversion technique to a prominence thread using different lengths. The observed period and damping time are 20 and 60 min, respectively, and $L = 10^5$ km

period and damping ratio of kink oscillations in the thin tube and thin boundary limits can be expressed by the following analytic approximations

$$P = \tau_{Ai}\sqrt{2}\left(\frac{\zeta+1}{\zeta}\right)^{1/2} \quad \text{and} \quad \frac{\tau_d}{P} = \frac{2}{\pi}\frac{\zeta+1}{\zeta-1}\frac{1}{l/R}. \tag{6}$$

These equations express the period, P and the damping time, τ_d, which are observable quantities in terms of the internal Alfvén travel time, τ_{Ai}, the density contrast, $\zeta = \varrho_i/\varrho_e$, and the transverse inhomogeneity length scale, l/R, in units of the radius of the loop. By only considering the damping ratio, [22] estimated a transverse inhomogeneity of $l/R = 0.23$, for an event observed by Nakariakov et al. [18] after assuming a density contrast of 10. The determination of transverse density structuring in a set of observed coronal loop oscillations was performed by Goossens et al. [13] and values of the transverse inhomogeneity length-scale in between 0.15 and 0.5 were obtained. Eigenmode computations and comparison to observations for highly inhomogeneous loops were performed by Van Doorsselaere et al. [28] and Aschwanden et al. [8].

The first seismology inversions that used the observational information on both periods and damping times in the context of resonant damping in a consistent manner were performed by Arregui et al. [4] and Goossens et al. [14]. Their important finding is that when no further assumptions are made on any of the unknown parameters, the inversion gives rise to a one-dimensional solution curve in the three-dimensional parameter space (see Fig. 2a). Although there is an infinite number of solutions that equally well reproduce observations, the internal Alfvén travel time is constrained to a narrow range. Further information on coronal loop seismology using resonantly damped oscillations can be found in the review by Goossens [11].

Prominence thread oscillations also display damping [16] and damping by resonant absorption provides a plausible explanation [6]. The period and damping time of thread oscillations are seen to depend on the length of the thread (L_p/L) in units of the length of the magnetic tube [5, 23], but the damping ratio $P/\tau_{\rm d}$ is almost insensitive to this parameter. When applying the period and damping inversion technique to prominence threads, one inversion curve is obtained for each value of the length of the thread. The solutions obtained by Soler et al. [23] for a set of values for L_p are shown in Fig. 2b. Because of the insensitiveness of the damping ratio with density contrast ($\rho_{\rm p}/\rho_{\rm c}$), in prominence plasmas, the obtained solution curves display an asymptotic behavior for large values of density contrast that enables us to obtain precise estimates for the thread Alfvén speed and the transverse inhomogeneity length scale.

Seismology inversions using the damping of oscillations have also been performed by interpreting the damping of vertically polarized kink oscillations in coronal loops by wave leakage. Fast waves with frequencies above the external Alfvén frequency cannot be trapped and radiate energy away the structure. Reference [37] obtain, from the observed oscillation period, damping time and relative intensity amplitude, the values for the loop density contrast, the local slope of the Alfvén frequency, and the Alfvén speed at the loop axis self-consistently. A shortcoming of the curved slab model is that it predicts a wave leakage that is too strong to explain the observations.

4 Seismology in the Presence of Flows

The first seismological application of prominence seismology using Hinode observations of flowing and transversely oscillating threads was presented by Terradas et al. [25], using observations obtained in an active region filament by Okamoto et al. [19]. The observations show a number of threads that flow following a path parallel to the photosphere while they are oscillating in the vertical direction. Reference [25] interpret these oscillations in terms of the kink mode of a magnetic flux tube. First, by neglecting the effect of flows, [25] find that a one-to-one relation between the thread Alfvén speed and the coronal Alfvén speed can be established. For one of the observed threads, and considering a length of the total magnetic flux tube of $L = 100\,$Mm, an overall value for the thread Alfvén speed between 120 and 350 km s^{-1} is obtained. Next, mass flows are considered and [25] find that the flow velocities measured by Okamoto et al. [19] result in slightly shorter (3–5%) kink mode periods than the ones derived in the absence of flow. Hence, on this particular case, the detected flow speeds would produce only slightly different results in the seismology inversion.

More recently, [26] argue that the presence of siphon flows can cause an underestimation of magnetic field strength in coronal loops using the traditional method outlined in Sect. 2. In particular, the calculation of the kink speed and the estimation of magnetic field strength, assuming a static model, give values that are

considerably smaller than the ones obtained in the presence of flow. The reason is that, contrary to the static case, different positions along the tube oscillate with a different phase. The theory is applied to the linear phase shift reported along the post-flare coronal loop analyzed by Verwichte et al. [38], by assuming that its cause is a siphon flow. The inversion result shows that the flow would be in the fast flow regime ($\sim 10^3$ km s^{-1}). This is not completely unreasonable in the dynamic post-flare environment of coronal loops.

5 Seismology in the Spatial Domain

For longitudinally stratified loops, [2] noticed that the amplitude profiles for the perturbed variables along the magnetic field direction are directly affected by density stratification. Several studies make use of observations of the spatial distribution of equilibrium model parameters and wave properties for plasma diagnostic purposes. The first studies that make use of spatial information from observations, in combination with theoretical results of the effect of density stratification are by Erdélyi and Verth [10] and Verth et al. [35]. These authors show that density stratification causes the anti-nodes of the first harmonic of the standing kink mode in coronal loops to shift towards the loop foot-points. The anti-node shift corresponding to a density scale height of 50 Mm and a loop half length of 100 Mm is approximately 5.6 Mm. Shifts in the Mm range are measurable quantities, hence spatial seismology was proposed as a complementary method of probing the plasma stratification in the corona.

Magnetic field inhomogeneity also affects oscillation properties. A varying longitudinal magnetic field implies an equilibrium with flux tube expansion. This expansion is a measurable quantity. Reference [31] combine density and magnetic field structuring and, in the context of seismology using period ratios, find that even a relatively small coronal loop expansion can have a significant effect on the inferred density scale height. A detailed and step-by-step inversion is presented by Verth et al. [33]. The results indicate that using the observed ratio of the first overtone and fundamental mode to predict the plasma density scale height and not taking account of loop expansion will lead to an overestimation of scale heigh by a factor of 2. Similar physical models and inversion techniques have recently been applied to other wave types, e.g., Alfvén waves in stratified waveguides [32], and to different magnetic and plasma structures, such as spicules [34].

6 Bayesian Inference

Reference [5] have recently proposed an alternative statistical approach to the inversion problem, based on parameter inference in the bayesian framework. The method makes use of the Bayes' theorem. According to this rule, the state of

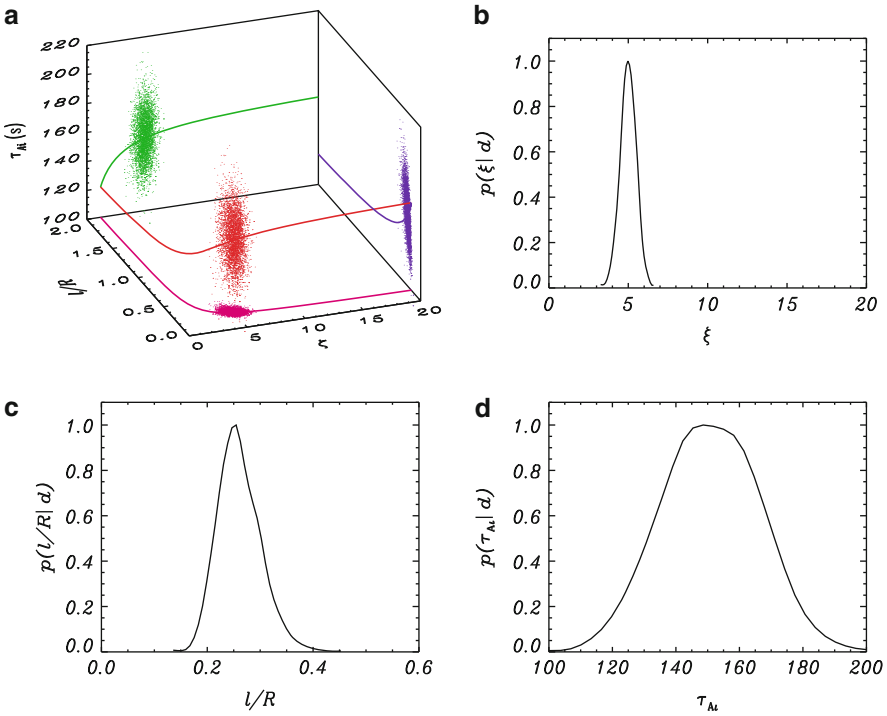

Fig. 3 (**a**) Bayesian inversion technique results in the form of converged Markov chain elements in the parameter space, together with analytic inversion result in *solid line*. (**b**)–(**c**) Marginal posteriors for density contrast, transverse inhomogeneity and Alfvén travel time. The observed period and damping time are 232 and 881 s, respectively

knowledge on a given set of parameters (the posterior distribution), is a function of what is known a priori, independently of the data, (the prior), and the likelihood of obtaining a data realization actually observed as a function of the parameter vector (the likelihood function). In an application to transverse coronal loop oscillations, posterior probability distribution functions were obtained by means of Markov Chain Monte Carlo simulations, incorporating observed uncertainties in a consistent manner. By using observational estimates for the density contrast by Aschwanden et al. [8] and Arregui et al. [5] find well-localized solutions in the posterior probability distribution functions for the three parameters of interest (see Fig. 3). From these probability distribution functions, numerical estimates for the unknown parameters can be obtained. The uncertainties on the inferred parameters are given by error bars correctly propagated from observed uncertainties.

7 Conclusion

The application of seismology techniques to better understand the physics of the solar atmosphere has produced fruitful results in the last years. Some relevant examples are mentioned in this paper. Nearly all the necessary steps for a proper seismology seem to have been followed, i.e., the observational evidence of oscillations and waves; the correct identification of observed with theoretical wave modes; the determination or restriction of physical parameters and their structuring. The challenge that is recurrently mentioned is the need for better observations and more realistic analytic/numerical models. Besides this, often the quantity of unknowns outnumbers that of measured wave properties and information is always incomplete and uncertain. In this respect, the use Bayesian parameter inference methods could be of high value for the future of solar atmospheric seismology, when the inversion of physical parameters will be based on the combination of large scale numerical parametric results and the analysis of data sets obtained from, e.g., SOLAR-C.

Acknowledgements The author acknowledges the financial support received from the Spanish MICINN and FEDER funds under Grant No. AYA2006-07637. The author is also grateful to the Solar Physics Group members at Universitat de les Illes Balears, for many years of fruitful work.

References

1. Andries, J., Arregui, I., Goossens, M.: Determination of the Coronal Density Stratification from the Observation of Harmonic Coronal Loop Oscillations. Astrophys. J. Lett. **624**, L57–L60 (2005)
2. Andries, J., Goossens, M., Hollweg, J. V., Arregui, I., Van Doorsselaere, T.: Coronal loop oscillations: Calculation of resonantly damped MHD quasi-mode kink oscillations of longitudinally stratified loops. Astron. Astrophys. **430**, 1109–1118 (2005)
3. Andries, J., van Doorsselaere, T., Roberts, B., Verth, G., Verwichte, E., Erdélyi, R.: Coronal Seismology by Means of Kink Oscillation Overtones. Space Sci. Rev. **149**, 3–29 (2009). DOI 10.1007/s11214-009-9561-2
4. Arregui, I., Andries, J., Van Doorsselaere, T., Goossens, M., Poedts, S.: MHD seismology of coronal loops using the period and damping of quasi-mode kink oscillations. Astron. Astrophys. **463**, 333–338 (2007). DOI 10.1051/0004-6361:20065863
5. Arregui, I., Soler, R., Ballester, J.L., Wright, A. N.: Magnetohydrodynamic kink waves in two-dimensional non-uniform prominence threads. Astron. Astrophys. **533**, A60 (2011). DOI 10.1051/0004-6361/201117477
6. Arregui, I., Terradas, J., Oliver, R., Ballester, J. L.: Damping of Fast Magnetohydrodynamic Oscillations in Quiescent Filament Threads. Astrophys. J. Lett. **682**, L141–L144 (2008). DOI 10.1086/591081
7. Aschwanden, M. J., Fletcher, L., Schrijver, C. J., Alexander, D.: Coronal Loop Oscillations Observed with the Transition Region and Coronal Explorer. Astrophys. J. **520**, 880 (1999)
8. Aschwanden, M. J., Nightingale, R. W., Andries, J., Goossens, M., Van Doorsselaere, T.: Observational Tests of Damping by Resonant Absorption in Coronal Loop Oscillations. Astrophys. J. **598**, 1375 (2003)
9. Díaz, A. J., Oliver, R., Ballester, J. L.: Prominence Thread Seismology Using the $P_1/2P_2$ Ratio. Astrophys. J. **725**, 1742–1748 (2010). DOI 10.1088/0004-637X/725/2/1742

10. Erdélyi, R., Verth, G.: The effect of density stratification on the amplitude profile of transversal coronal loop oscillations. Astron. Astrophys. **462**, 743–751 (2007). DOI 10.1051/0004-6361:20065693
11. Goossens, M.: Seismology of kink oscillations in coronal loops: Two decades of resonant damping. In: R. Erdélyi & C. A. Mendoza-Briceño (ed.) IAU Symposium, *IAU Symposium*, vol. 247, pp. 228–242 (2008). DOI 10.1017/S1743921308014920
12. Goossens, M., Andries, J., Arregui, I.: Damping of magnetohydrodynamic waves by resonant absorption in the solar atmosphere. Royal Society of London Philosophical Transactions Series A **364**, 433–446 (2006). DOI 10.1098/rsta.2005.1708
13. Goossens, M., Andries, J., Aschwanden, M. J.: Coronal loop oscillations. An interpretation in terms of resonant absorption of quasi-mode kink oscillations. Astron. Astrophys. **394**, L39 (2002)
14. Goossens, M., Arregui, I., Ballester, J. L., Wang, T. J.: Analytic approximate seismology of transversely oscillating coronal loops. Astron. Astrophys. **484**, 851–857 (2008). DOI 10.1051/0004-6361:200809728
15. Lin, Y., Engvold, O., Rouppe van der Voort, L. H. M., van Noort, M.: Evidence of Traveling Waves in Filament Threads. Solar Phys. **246**, 65–72 (2007). DOI 10.1007/s11207-007-0402-8
16. Lin, Y., Soler, R., Engvold, O., Ballester, J. L., Langangen, Ø., Oliver, R., Rouppe van der Voort, L. H. M.: Swaying Threads of a Solar Filament. Astrophys. J. **704**, 870–876 (2009). DOI 10.1088/0004-637X/704/1/870
17. Nakariakov, V. M., Ofman, L.: Determination of the coronal magnetic field by coronal loop oscillations. Astron. Astrophys. **372**, L53 (2001)
18. Nakariakov, V. M., Ofman, L., DeLuca, E. E., Roberts, B., Davila, J. M.: Trace observations of damped coronal loop oscillations: implications for coronal heating. Science **285**, 862 (1999)
19. Okamoto, T. J., Tsuneta, S., Berger, T. E., Ichimoto, K., Katsukawa, Y., Lites, B. W., Nagata, S., Shibata, K., Shimizu, T., Shine, R. A., Suematsu, Y., Tarbell, T. D., Title, A. M.: Coronal Transverse Magnetohydrodynamic Waves in a Solar Prominence. Science **318**, 1577– (2007). DOI 10.1126/science.1145447
20. Roberts, B., Edwin, P. M., Benz, A. O.: On coronal oscillations. Astrophys. J. **279**, 857 (1984)
21. Roberts, B., Joarder, P. S.: Oscillations in quiescent prominences. In: G. Belvedere, M. Rodono, & G. M. Simnett (ed.) Advances in Solar Physics, *Lecture Notes in Physics, Berlin Springer Verlag*, vol. 432, pp. 173–178 (1994)
22. Ruderman, M. S., Roberts, B.: The Damping of Coronal Loop Oscillations. Astrophys. J. **577**, 475–486 (2002). DOI 10.1086/342130
23. Soler, R., Arregui, I., Oliver, R., Ballester, J. L.: Seismology of Standing Kink Oscillations of Solar Prominence Fine Structures. Astrophys. J. **722**, 1778–1792 (2010). DOI 10.1088/0004-637X/722/2/1778
24. Tandberg-Hanssen, E.: The nature of solar prominences. Dordrecht ; Boston : Kluwer, c1995. (1995)
25. Terradas, J., Arregui, I., Oliver, R., Ballester, J. L.: Transverse Oscillations of Flowing Prominence Threads Observed with Hinode. Astrophys. J. Lett. **678**, L153–L156 (2008). DOI 10.1086/588728
26. Terradas, J., Arregui, I., Verth, G., Goossens, M.: Seismology of Transversely Oscillating Coronal Loops with Siphon Flows. Astrophys. J. Lett. **729**, L22 (2011). DOI 10.1088/2041-8205/729/2/L22
27. Uchida, Y.: Diagnosis of Coronal Magnetic Structure by Flare-Associated Hydromagnetic Disturbances. PASJ **22**, 341 (1970)
28. Van Doorsselaere, T., Andries, J., Poedts, S., Goossens, M.: Damping of Coronal Loop Oscillations: Calculation of Resonantly Damped Kink Oscillations of One-dimensional Nonuniform Loops. Astrophys. J. **606**, 1223 (2004)
29. Van Doorsselaere, T., Nakariakov, V. M., Verwichte, E.: Coronal loop seismology using multiple transverse loop oscillation harmonics. Astron. Astrophys. **473**, 959–966 (2007). DOI 10.1051/0004-6361:20077783

30. Van Doorsselaere, T., Nakariakov, V. M., Young, P. R., Verwichte, E.: Coronal magnetic field measurement using loop oscillations observed by Hinode/EIS. Astron. Astrophys. **487**, L17–L20 (2008). DOI 10.1051/0004-6361:200810186
31. Verth, G., Erdélyi, R.: Effect of longitudinal magnetic and density inhomogeneity on transversal coronal loop oscillations. Astron. Astrophys. **486**, 1015–1022 (2008). DOI 10.1051/0004-6361:200809626
32. Verth, G., Erdélyi, R., Goossens, M.: Magnetoseismology: Eigenmodes of Torsional Alfvén Waves in Stratified Solar Waveguides. Astrophys. J. **714**, 1637–1648 (2010). DOI 10.1088/0004-637X/714/2/1637
33. Verth, G., Erdélyi, R., Jess, D. B.: Refined Magnetoseismological Technique for the Solar Corona. Astrophys. J. Lett. **687**, L45–L48 (2008). DOI 10.1086/593184
34. Verth, G., Goossens, M., He, J. S.: Magnetoseismological Determination of Magnetic Field and Plasma Density Height Variation in a Solar Spicule. Astrophys. J. Lett. **733**, L15 (2011). DOI 10.1088/2041-8205/733/1/L15
35. Verth, G., Van Doorsselaere, T., Erdélyi, R., Goossens, M.: Spatial magneto-seismology: effect of density stratification on the first harmonic amplitude profile of transversal coronal loop oscillations. Astron. Astrophys. **475**, 341–348 (2007). DOI 10.1051/0004-6361:20078086
36. Verwichte, E., Aschwanden, M. J., Van Doorsselaere, T., Foullon, C., Nakariakov, V. M.: Seismology of a Large Solar Coronal Loop from EUVI/STEREO Observations of its Transverse Oscillation. Astrophys. J. **698**, 397–404 (2009). DOI 10.1088/0004-637X/698/1/397
37. Verwichte, E., Foullon, C., Nakariakov, V. M.: Seismology of curved coronal loops with vertically polarised transverse oscillations. Astron. Astrophys. **452**, 615–622 (2006)
38. Verwichte, E., Foullon, C., Van Doorsselaere, T.: Spatial Seismology of a Large Coronal Loop Arcade from TRACE and EIT Observations of its Transverse Oscillations. Astrophys. J. **717**, 458–467 (2010). DOI 10.1088/0004-637X/717/1/458
39. Verwichte, E., Nakariakov, V. M., Ofman, L., Deluca, E. E.: Characteristics of transverse oscillations in a coronal loop arcade. Solar Phys. **223**, 77–94 (2004). DOI 10.1007/s11207-004-0807-6
40. White, R.S., Verwichte, E.: Transverse coronal loop oscillations seen in unprecedented detail by AIA/SDO. Astron. Astrophys.**537**, A49 (2012). DOI 10.1051/0004-6361/201118093

Interaction of Wave Packets in MHD and EMHD Turbulence

Jungyeon Cho

Abstract In the presence of a strong magnetic field, disturbances travel along magnetic field lines. In most theories for strongly magnetized turbulence, collisions between opposite-traveling wave packets (or 'eddies') are essential for energy cascade. In those theories, it is generally assumed that only interactions between similar-size eddies are important. That is, most magnetohydrodynamic (MHD) turbulence models assume scale-locality of energy cascade. In this paper, we show that collisions between different size eddies, especially between outer scale eddies and smaller eddies, are also important and discuss how this non-locality affects energy spectrum. We also discuss dynamics of electron MHD (EMHD) wave packets (a.k.a. whistler wave packets). We show that EMHD wave packets moving in one direction can cascade energy through self-interactions and that they exhibit inverse energy cascade.

1 Introduction

Astrophysical plasmas are observed in a wide range of length-scales. On large scales, we can treat such plasmas as conducting fluids and therefore we can use magnetohydrodynamics (MHD). On small scales, especially scales near and below the proton gyro-scale, we can no longer use MHD. Electron magnetohydrodynamics (EMHD) is a simple fluid-like model of small-scale plasmas [10].

If a uniform external magnetic field ($\mathbf{B}_0$) is present in an incompressible fluid, any magnetic perturbation propagates *along* the magnetic field line. To the first order, the speed of propagation is constant. The speed is equal to the Alfvén speed

J. Cho (✉)
Chungnam National University, Daejeon, Korea
e-mail: jcho@cnu.ac.kr

Cho, J.: *Interaction of Wave Packets in MHD and EMHD Turbulence*.
Astrophys Space Sci Proc. **33**, 171–176 (2012)
DOI 10.1007/978-3-642-30442-2_19, © Springer-Verlag Berlin Heidelberg 2012

$V_A = B_0/\sqrt{4\pi\rho}$ in ordinary MHD and whistler wave speed kV_A in EMHD.[1] Since wave packets are moving along the magnetic field line, there are two possible directions for propagation. Interacting wave packets produce turbulence. Therefore, dynamics of wave packets is essential for the study of magnetized turbulence.

Then when do we have turbulence? In ordinary MHD, it is relatively simple. If all the Alfvénic wave packets are moving in one direction, then they are stable to nonlinear order [12] (see Fig. 1a). Therefore, wave packets moving in one direction do not create turbulence. In order to initiate turbulence, there must be opposite-traveling wave packets and energy cascade occurs only when they collide (Fig. 1b). Most MHD turbulence theories start from this observation. In general, those theories assume locality of interactions, which means interactions between similar size eddies are important in energy cascade. In this paper, we show that collisions between different size eddies (see Fig. 1c), especially between outer scale eddies and smaller eddies, are also important in MHD turbulence. There have been earlier discussions about non-locality in MHD turbulence threaded by a strong mean field (see, for example, [2]).

In EMHD, the situation is more complicated. EMHD perturbation moves along magnetic field at a speed proportional to kB_0, which implies that a perturbation with a larger k is faster than that with a smaller k. As a result, whistler waves are dispersive and whistler wave packets moving in one direction can self-interact and produce small-scale structures (see [11] for 2D EMHD), which means that collisions of whistler wave packets are not essential for generation of EMHD turbulence. Therefore understanding dynamics of EMHD wave packets is important for study of EMHD turbulence. Traveling EMHD wave packets can commonly occur in nature. Any local disturbances (e.g. reconnections) can create wave packets traveling along magnetic field lines. Therefore, propagation of whistler wave packets moving in one direction deserves a scrutiny.

In Sect. 2, we review models for MHD and EMHD turbulence based on locality. In Sect. 3, we show that non-locality is more pronounced in MHD turbulence compared with its hydrodynamic (HD) counterpart. In Sect. 4, we show that 3D EMHD wave packets moving in one direction can create turbulence and exhibit inverse energy cascade.

2 Locality and Scaling Relations in MHD and EMHD

In this section, we briefly review scaling models for MHD and EMHD turbulence. We assume the medium is threaded by a strong mean magnetic field. Under a strong magnetic field, we expect either a strong or a weak turbulence regime. In

[1] Here ρ is the density and k is the wavenumber. In this paper, we use the following convention: magnetic field $\mathbf{B}$ actually means $\mathbf{B}/\sqrt{4\pi\rho}$. Thus, the field $\mathbf{B}$ is in fact the Alfvénic velocity. For Alfvenic perturbations (in ordinary MHD), we have $v \sim b$, where $\mathbf{B} = \mathbf{B}_0 + \mathbf{b}$ and $\mathbf{b}$ is the fluctuating field. For whistler perturbations (in EMHD), we have $v \propto kb$.

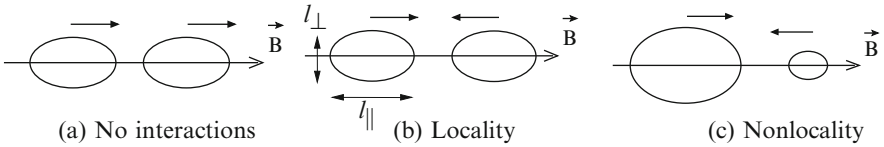

Fig. 1 Wave packets in a magnetized medium. (**a**) In MHD, packets moving in one direction are stable and do not produce turbulence. However, in EMHD, such packets are dispersive and can produce turbulence, which however is a slow process. (**b**) In MHD, collisions of opposite traveling packets are required for generation of turbulence. In EMHD, such collisions also produce turbulence, which is a fast process. (**c**) Non-locality (in MHD). We calculate interactions between the energy-injection scale eddies and smaller scale eddies. Therefore, the bigger eddies in this figure can be regarded as energy-injection scale eddies

this paper, we consider only a strong turbulence. For weak turbulence, readers may refer to [8].

For MHD, there is a popular model proposed by Goldreich and Sridhar [9] (hereinafter GS95 model). Suppose that a uniform external magnetic field ($\mathbf{B}_0$) is present. Note that a strong (local) mean field naturally makes MHD turbulence anisotropic, which implies that eddies are elongated along the (local) mean field direction. Therefore, in Fig. 1, we intentionally draw that the parallel size of eddies is larger than the perpendicular size. Here 'parallel' and 'perpendicular' refer to the directions with respect to the (local) mean magnetic field.

The GS95 model assumes locality of interactions: only collisions between similar-size eddies are important for energy cascade. When two opposite-traveling wave packets (of size $l_\perp$ and $l_\parallel$) collide, they lose the following amount of energy to smaller scales:

$$\Delta E \sim (db^2/dt)\Delta t \sim (b_l^3/l_\perp)(l_\parallel/B_0), \tag{1}$$

where Δt ($\sim l_\parallel/V_A = l_\parallel/B_0$) is the duration of collision and l denotes $l_\perp$. We obtained db^2/dt from the (ideal) induction equation.

GS95 argued that there is a regime of turbulence where

$$\Delta E/E \sim b_l l_\parallel/(B_0 l_\perp) \sim 1 \tag{2}$$

is maintained. This type of turbulence is called 'strong' turbulence. When we combine this condition and constancy of energy cascade rate, $b^2/t_{cas} \sim constant$, where $t_{cas} \sim l_\parallel/B_0 \sim l_\perp/b_l$ (see Eq. (2)), we get the GS95 scaling relations

$$E(k_\perp) \propto k_\perp^{-5/3} \quad \text{and} \quad k_\parallel \propto k_\perp^{2/3}. \tag{3}$$

Here we used $b_l^2 \sim k_\perp E(k_\perp)$. Numerical tests for GS95 model can be found in [6, 7].

For EMHD, Cho and Lazarian [5] proposed a model based on locality, which predicts

$$E(k_\perp) \propto k_\perp^{-7/3} \quad \text{and} \quad k_\parallel \propto k_\perp^{1/3}. \tag{4}$$

We can derive the scaling relations similarly, keeping in mind that whistler speed is proportional to kB_0 and $v_l \propto kb_l$.

3 Non-locality in MHD Turbulence

In this section, we directly calculate the strength of interactions between the energy-injection scale eddies and smaller-scale eddies (see Fig. 1c for explanations). Left panel in Fig. 2 shows that non-locality in MHD turbulence is stronger than that in HD turbulence. In the figure, we actually calculated strength of interactions between Fourier modes in the driving scale ($2 \le k < 4$) and those near the wavenumber k ($k/\sqrt{2} \le k < \sqrt{2}k$). We normalize it by the strength of interactions between Fourier modes in all scales ($1 \le k < k_{max}$) and those in the same range near k ($k/\sqrt{2} \le k < \sqrt{2}k$). The ratio for MHD (dotted line) is non-negligible and substantially larger than that for HD (solid line). Therefore, we can conclude that non-locality is indeed present in MHD turbulence.[2]

When shearing motions of the outer scale eddies influence energy transfer of inertial-range eddies, energy spectrum becomes flatter than the Kolmogorov one. Suppose that the shearing motions of the outer scale eddies completely dominate energy cascade. In this case, from $b_l^2/t_{cas} \sim b_l^2/(L/v_L) \propto b_l^2 = constant$, we can easily show that energy spectrum is $E(k) \propto k^{-1}$, where L the outer scale and v_L the rms velocity at the outer scale. If the shearing motions of the outer scale eddies do not completely dominate, we will have a spectrum between k^{-1} and $k^{-5/3}$. Therefore, non-locality may be a way to explain flattening of energy spectrum in MHD turbulence, which has been observed in earlier studies.

4 Inverse Energy Cascade in EMHD Turbulence

In this section, we consider dynamics of EMHD wave packets moving in one direction. Cho [4] numerically studied propagation of 3D EMHD wave packets moving in one direction. Unlike its MHD counterpart, an EMHD wave packet is dispersive. Because of this, EMHD wave packets traveling in one direction create

[2] We note that the ratio for MHD gradually decreases as k increases. Although it is not very clear at this moment whether it will continue to drop when we have a very long inertial range, it is likely that the ratio will continue to drop and the non-local effects of the outer scale will ultimately vanish on very small scales. If this is true, we will recover a Kolmogorov spectrum on very small scales (see a related work in [1]).

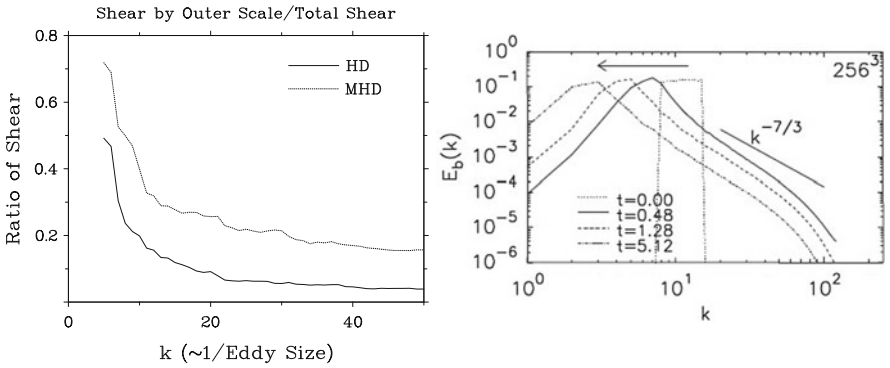

Fig. 2 (*left*) Non-locality in MHD and HD turbulence. Influence of outer-scale eddies are relatively stronger in MHD, which means non-locality is more pronounced in MHD. The mathematical definition of 'the ratio of shear' can be found in [3]. (*right*) Inverse cascade in EMHD. At $t = 0$, all wave packets move in the same direction. In Fourier space, modes between $k = 8$ and $k = 15$ are excited. The *dotted curve* shows the initial spectrum. We clearly observe inverse cascade of magnetic energy (From [4])

opposite traveling wave packets via self-interactions and cascade energy to smaller scales.

Cho [4] also showed that EMHD wave packets traveling in one direction clearly exhibit inverse energy cascade (see right panel in Fig. 2). Figure 2 shows magnetic energy spectrum as a function of time. The dotted curves in the figure show the initial spectrum. As time goes on, the initial energy cascades down to smaller scales and, as a result, a power-law-like spectrum forms for $k > 15$. At the same time the peak of the energy spectrum moves to larger scales, so that the wavenumber at which the spectrum peaks, k_p, gets smaller. We clearly observe inverse cascade of magnetic energy.

This inverse energy cascade is due to conservation of magnetic helicity. If we use the Coulomb gauge, the spectrum of magnetic helicity is $E(k)/k$. The magnetic helicity is a conserved quantity. Therefore, if magnetic energy goes down as a result of self-interactions, the peak of magnetic spectrum should move to the left (i.e. to smaller k values) to conserve helicity.

5 Summary

We have considered two issues related to wave packets in strongly magnetized media. In MHD turbulence, we have considered collisions of opposite-traveling packets and showed that non-locality can make the energy spectrum shallower. In EMHD turbulence, we have considered propagation of wave packets moving in one direction and found that, due to magnetic helicity conservation, inverse energy cascade occurs.

Acknowledgements This research was supported by National R&D Program through the National Research Foundation of Korea (NRF) funded by the Ministry of Education, Science and Technology (No. 2011-0018751).

References

1. Beresnyak, A. 2011, Phys. Rev. Lett., **106**, 075001 (arXiv:1109.4644)
2. Beresnyak, A., & Lazarian, A. 2010, Astrophys. J., **722**, 110
3. Cho, J. 2010, Astrophys. J., **725**, 1786
4. Cho, J. 2011, Physical Review Letters, **106**, 191104
5. Cho, J. & Lazarian, A. 2004, Astrophys. J. Lett., **615**, L41
6. Cho, J., & Vishniac, E. T. 2000, Astrophys. J., **539**, 273
7. Maron, J. & Goldreich, P. 2001, Astrophys. J., **554**, 1175
8. Galtier, S., Nazarenko, S. V., Newell, A. C., & Pouquet, A. 2000, Journal of Plasma Physics, **63**, 447
9. Goldreich P., Sridhar H. Astrophys. J. **438**, 763 (1995) (GS95)
10. Kingsep A. S., Chukbar K.V., & Yan'kov V.V., Reviews of Plasma Physics (Consultants Bureau, New York, 1990), Vol. 16.
11. Ng, C., Bhattacharjee, A., Germaschewski, K., & Galtier, S. 2003, Phys. Plasmas, **10**, 1954
12. Parker E. N. *Cosmical magnetic fields: Their origin and their activity* (Oxford University Press, New York, 1979)

Observations of Electromagnetic Fluctuations at Ion Kinetic Scales in the Solar Wind

John J. Podesta

Abstract Wavelet techniques enable reduced power spectra and cross-spectra to be analyzed as a function of the angle θ_{BV} formed by the scale dependent local mean magnetic field $\mathbf{B_0}$ and the flow direction of the solar wind. These techniques allow the data along a line oriented at any angle θ_{BV} to $\mathbf{B_0}$ to be isolated and studied independently thus providing new information about the properties of the fluctuations along directions parallel, perpendicular, and at arbitrary angles to the local mean magnetic field. Recent investigations of the normalized magnetic helicity spectrum σ_m using this technique have revealed the existence of two distinct populations of fluctuations near the proton inertial length scale, that is, at wavenumbers near $kc/\omega_{pp} = 1$. These observations and their physical interpretation are briefly reviewed.

1 Introduction

Solar wind plasma and magnetic field fluctuations at magnetohydrodynamic (MHD) scales, scales much greater than the proton inertial length c/ω_{pp} or the thermal proton gyro-radius $v_{\perp p}/\Omega_p$, have been studied extensively since the first in-situ spacecraft measurements became available in the 1960s [2, 9, 20, 27]. Fluctuations at proton kinetic scales, $kc/\omega_{pp} \sim 1$ and $kv_{\perp p}/\Omega_p \sim 1$, have been studied much less since they require relatively high time resolution measurements with sampling frequencies on the order of 10 or 20 Hz (the fluctuations of interest here are *frozen*

J.J. Podesta (✉)
Los Alamos National Laboratory, Los Alamos, NM 87545, USA
e-mail: jpodesta@solar.stanford.edu

Podesta, J.J.: *Observations of Electromagnetic Fluctuations at Ion Kinetic Scales in the Solar Wind*. Astrophys Space Sci Proc. **33**, 177–186 (2012)
DOI 10.1007/978-3-642-30442-2_20, © Springer-Verlag Berlin Heidelberg 2012

into the flow,[1] an assumption that is valid for many, but not necessarily all of the fluctuations that may occur at spacecraft-frame frequencies between 0.1 and 10 Hz at 1 AU). Detailed observational knowledge of the fluctuations at proton kinetic scales is crucial for understanding the microphysics of the solar wind, e.g., the kinetic processes which heat solar wind ions and regulate ion distribution functions during the solar wind expansion.

The goal of this paper is to review in-situ wave observations obtained in the last year using novel data analysis techniques. The observations reveal separate populations of parallel and obliquely propagating electromagnetic waves near $kc/\omega_{pp} = 1$. The waves occur at the *spectral break* in the magnetic field spectrum and have spacecraft-frame frequencies near 1 Hz. Measurements consist of high time resolution magnetic field data having sampling frequencies near 10 Hz. Unfortunately, simultaneous three-axis electric field, magnetic field, and plasma data with sampling frequencies of 10 or 20 Hz are not available for existing solar wind missions. This is a significant impediment for the scientific study of kinetic scale processes in the interplanetary medium. The kinds of wave studies described in this review are, perhaps, the best that can be done using magnetic field data alone.

2 Concept of the Local Mean Magnetic Field

At small scales, fluctuations are organized by the *local mean magnetic field* $\mathbf{B_0}$ (defined below), similar to the way the matter in the universe is organized by the local gravitational field. The term "small scales" refers to small inertial range scales[2] and ion kinetic scales of order $kc/\omega_{pp} = 1$ or $kv_{\perp p}/\Omega_p = 1$ which usually occur at or near the spectral break. Fluctuations are so organized because the dynamics of the fluctuations at a given scale are governed by the local mean field at that same scale, not by the local mean magnetic field at larger or smaller scales. Evidence that solar wind fluctuations are structured by the local mean magnetic field comes from in-situ observations described below as well as observations of distinctly different magnetic field spectra parallel and perpendicular to the local mean magnetic field. Even though spectral decomposition techniques using the local mean magnetic field have been criticized by some solar wind researchers, from a practical point of view they are an indispensable tool for analysis of the anisotropy of solar wind fluctuations at small scales as shown by many investigators [3–5, 7, 10–13, 18, 22, 25, 28, 29].

[1] The oscillation period is much greater than the time required for the fluctuations to be swept past the spacecraft by the super-Alfvénic solar wind or, more precisely, $\omega \ll |\mathbf{k} \cdot \mathbf{V}_{sw}|$.

[2] The inertial range covers the range of spacecraft-frame frequencies from the outer scale—often defined by the correlation time of the fluctuations—approximately equal to 1 h or 3×10^{-4} Hz at 1 AU, to the spectral break, approximately equal to 3×10^{-1} Hz at 1 AU.

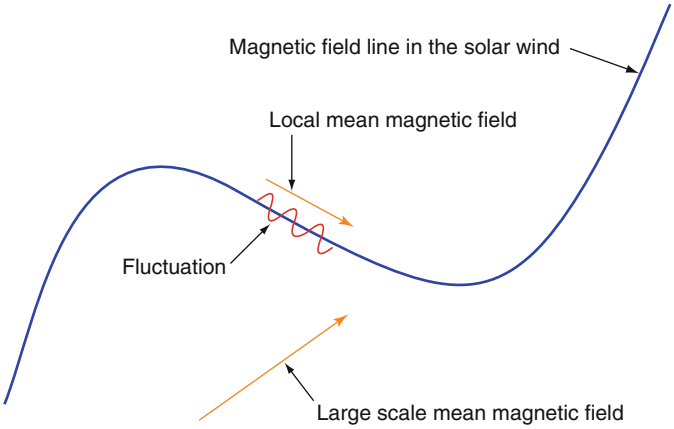

Fig. 1 Small scale Alfvénic fluctuations in the interplanetary medium propagate along the local mean magnetic field, not the large scale mean magnetic field. The local mean magnetic field at the point $(\mathbf{x}, t)$ for fluctuations with a characteristic scale length λ is defined by Eq. (1) as a spatial average in the neighborhood of the point $(\mathbf{x}, t)$

The notion of the local mean magnetic field is illustrated in Fig. 1. The local mean magnetic field is defined by a local volume average of the form

$$\mathbf{B_0}(\mathbf{x}, t; \lambda) = \iiint \mathbf{B}(\mathbf{x} - \mathbf{x}', t) w_\lambda(\mathbf{x} - \mathbf{x}')\, d\mathbf{x}', \tag{1}$$

where $w_\lambda(\mathbf{x})$ is a weight function such that $\iiint w_\lambda(\mathbf{x})\, d\mathbf{x} = 1$ and the integral is over all space. In Eq. (1), $\mathbf{B_0}(\mathbf{x}, t; \lambda)$ is the local mean magnetic field at the point $(\mathbf{x}, t)$ for fluctuations of lengthscale λ. A Gaussian weight function $w_\lambda(\mathbf{x}) \propto \exp(-|\mathbf{x}|^2/2\sigma^2)$ with $\sigma = \lambda$ is often used [11,22]. Because in-situ data from a single spacecraft take the form of a time series, the spatial average in Eq. (1) is replaced by a temporal average centered about the time t. It is important to note that the local mean magnetic field is a scale dependent quantity.

In the solar wind, the instantaneous magnetic field $\mathbf{B}(t)$ changes direction incessantly, changing by 10° every 10 s, on average. Similar behavior occurs for the local mean magnetic field $\mathbf{B_0}$ which, like $\mathbf{B}(t)$, sweeps out a wide range of angles over time. The angle formed by the local mean magnetic field and the average flow direction of the solar wind is denoted by θ_{BV}. For data restricted to a single magnetic sector, the distribution of angles θ_{BV} is usually peaked near the Parker spiral direction, but the distribution is quite broad so there are also times when $\mathbf{B_0}$ is nearly perpendicular to the flow, $\theta_{BV} = 90°$, or nearly parallel to the flow, $\theta_{BV} = 0$ for away sectors or $\theta_{BV} = 180°$ for toward sectors [22]. Provided the fluctuations are approximately frozen into the flow, one may use the data in different angle bins to analyze the properties of the fluctuations along lines oriented at different directions to $\mathbf{B_0}$. For example, by examining only those times when $\theta_{BV} \approx 90°$ one can study the properties of the fluctuations along a line perpendicular to $\mathbf{B_0}$.

This methodology was first used by Horbury et al. [11] and Podesta [22] to compute reduced magnetic power spectra along directions parallel and perpendicular to the local mean magnetic field. Because wavelets can be used to compute a frequency spectrum at each instant of time (a dynamic spectrum), it is possible to compute power spectra using only the data at those times when θ_{BV} falls within a particular range of angles, called an angle bin, and thereby obtain separate power spectra for each angle bin. The same technique may be used to analyze other solar wind spectra as functions of the angle θ_{BV}; for example, the spectrum of velocity fluctuations, the cross-helicity spectrum, the magnetic-helicity spectrum, etc.

3 Normalized Magnetic-Helicity Spectrum σ_m

The data analysis techniques described in the last section have been used to investigate the normalized magnetic helicity spectrum σ_m as a function of the angle θ_{BV} [10, 25]. These studies have opened a new window on the fluctuations at ion kinetic scales $kc/\omega_{pp} \sim 1$ and $kv_{\perp p}/\Omega_p \sim 1$ that is advancing scientific knowledge and understanding of the kinetic process at these scales. Before discussing this work, we recall the properties of the normalized magnetic helicity spectrum σ_m. Figure 2 shows an example of the magnetic field spectrum (trace spectrum) and the normalized magnetic helicity spectrum σ_m for a 4 day interval of high-speed solar wind observed by the *Stereo A* spacecraft far away from the influences of the earth's magnetosphere and bow shock. The spectra in Fig. 2 were obtained using traditional Fourier analysis techniques [25].

It is well known that the normalized magnetic helicity spectrum $\sigma_m(k)$, the solid red curve in Fig. 2, is approximately zero in the inertial range—often fluctuating above and below zero—indicating that inertial range fluctuations contain approximately equal amounts of left- and right-hand helicity [21]. At kinetic scales, however, the spectrum $\sigma_m(k)$ shows a significant peak that coincides with the spectral break. This peak, first observed by Goldstein et al. [8] and studied further by Leamon et al. [15] and others, indicates that the fluctuations at ion kinetic scales posses a net right-hand sense of polarization in the spacecraft frame.

To explain the peak in the σ_m spectrum, Goldstein et al. [8] hypothesized that in the inertial range there exists a turbulent cascade of parallel propagating ion-cyclotron and magnetosonic-whistler waves and that at $kc/\omega_{pp} \simeq 1$ cyclotron damping acts only on the ion-cyclotron waves. For incompressible MHD turbulence, the energy cascade in wavevector space occurs primarily in the $k_\perp$ direction and solar wind turbulence is believed to behave similarly. It is not known whether, in addition, a parallel cascade may exist in turbulent *collisionless* plasmas. As an alternative explanation, Howes and Quataert [14] have shown that if the fluctuations at ion kinetic scales consist predominantly of a spectrum of obliquely propagating kinetic Alfvén waves (KAWs), as various measurements suggest [1, 16, 26], and if the waves are predominantly propagating away from the sun so $\mathbf{k} \cdot \mathbf{B_0} > 0$ for

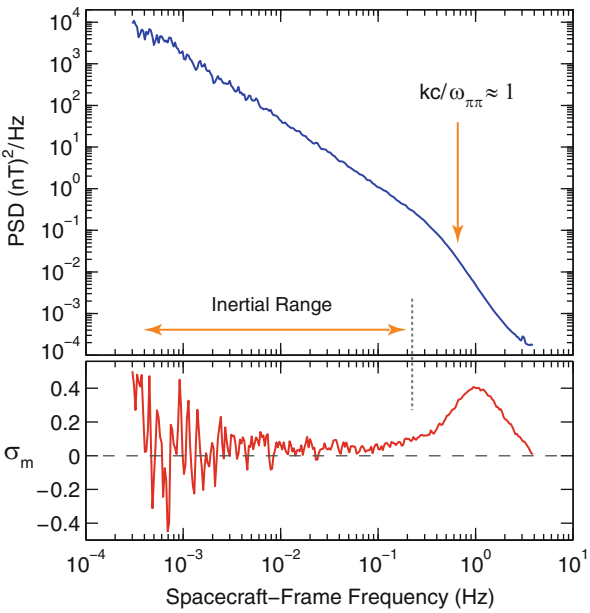

Fig. 2 Trace power spectral density (PSD) of the magnetic field (*blue*) and normalized magnetic helicity spectrum σ_m (*red*) for a 4 day interval of high speed wind observed by *Stereo A* from 13 Feb 2008 08:00 to 17 Feb 08:00. By Taylor's hypothesis, the abscissa is proportional to the wavenumber which is the physically relevant quantity. The heliospheric magnetic sector was directed away from the sun throughout this 4 day interval. The average wind speed, proton density, and proton temperature are 655 km/s, 2.2 cm^{-3} and 1.6×10^5 K, respectively. $\beta_p \approx 0.7$

an outward magnetic sector, then this KAW spectrum will produce a normalized magnetic helicity spectrum qualitatively and quantitatively similar to that observed. The physical interpretation of the observed peak in the spectrum is, therefore, a matter of debate.

4 Magnetic Helicity Spectrum σ_m as a Function of θ_{BV}

As first shown by He et al. [10] and then Podesta and Gary [25], further insight is obtained by using the techniques described in Sect. 2 to analyze the spectrum $\sigma_m(k)$ as a function of the angle θ_{BV}. Results of such an analysis are shown in Fig. 3. The quantity $\sigma_m(k, \theta_{BV})$ is plotted in color as a function of the angle θ_{BV} and of the timescale τ of the fluctuations in the spacecraft frame. From a physical point of view, it is more useful to plot the dimensionless wavenumber on the vertical axis. Therefore, the wavenumber at which $kc/\omega_{pp} \simeq 1$ is indicated by a dashed line.

Note that in the light green colored regions $\sigma_m \approx 0$, i.e., the net helicity of the fluctuations is zero in these regions. The inertial range, $\tau > 5$ s, also has $\sigma_m \approx 0$ (only partially shown). The data in Fig. 3 is restricted primarily to kinetic scales near the spectral break and shows two non-zero signals: (1) The dark blue colored region near $\theta_{BV} = 0$ and (2) the yellow and orange colored region centered about $\theta_{BV} = 90°$. Note from the colorbar that $\sigma_m < 0$ in the dark blue colored region indicating that those fluctuations have a net left-hand sense of polarization in the spacecraft frame. Similarly, $\sigma_m > 0$ in the yellow and orange colored region

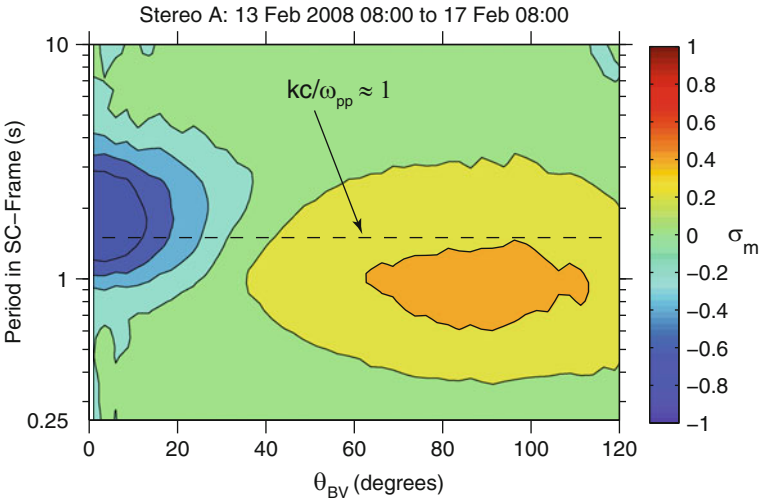

Fig. 3 Normalized magnetic helicity spectrum σ_m (*color coded*) as a function of θ_{BV} and the oscillation period in the spacecraft frame for the same 4 day interval of high speed wind in Fig. 2. By Taylor's hypothesis, the oscillation period in the spacecraft frame is inversely proportional to the wavenumber; the wavenumber $kc/\omega_{pp} \simeq 1$ is indicated by a *dashed line*. $\Delta\theta = 2.5°$

indicating that those fluctuations have a net right-hand sense of polarization in the spacecraft frame.

Assuming the waves are predominantly propagating away from the sun, He et al. [10] interpreted the dark blue colored region in Fig. 3 as evidence of parallel propagating ion cyclotron waves and the yellow and orange colored region as obliquely propagating KAWs or possibly whistler waves. Our current understanding of these observations may be summarized as follows.

The spectrum in Fig. 3 pertains only to electromagnetic fluctuations since electrostatic fluctuations have a vanishing magnetic field. A spectrum of KAWs is expected to exhibit a net right-hand sense of polarization in the spacecraft frame provided the waves are predominantly outward propagating in the plasma frame so that $\mathbf{k} \cdot \mathbf{B_0} > 0$ for an outward magnetic sector. Therefore, a spectrum of KAWs may cause the $\sigma_m > 0$ yellow and orange signal in Fig. 3. However, the wide angular width of this region also needs to be explained. Is this possibly a projection effect? Comparisons between theory and observation are needed to determine whether the yellow and orange signal may be generated by KAWs. Because angles near $\theta_{BV} = 0$ are observed to occur much less frequently in the solar wind than angles near $\theta_{BV} = 90°$ [22], the fluctuations in the yellow and orange region should dominate the traditional Fourier spectral calculation of σ_m near 1 Hz shown in Fig. 2 (bottom) even though the power of the fluctuations associated with the dark blue signal is often comparable to that of the yellow and orange signal [25]. This is confirmed by the fact that the peak value $\sigma_m \simeq 0.4$ in Fig. 2 matches the peak value $\sigma_m \simeq 0.4$ at $\theta_{BV} = 90°$ in Fig. 3.

The dark blue signal in Fig. 3 is somewhat easier to interpret. There are only two parallel propagating electromagnetic modes in collisionless plasmas such as the solar wind: The left circularly polarized ion-cyclotron wave and the right circularly polarized electron cyclotron (magnetosonic/whistler) wave. The dark blue color in Fig. 3 indicates $\sigma_m \approx -1$ which can only occur if a particular mode propagates nearly unidirectionally. If a given mode propagates both parallel and anti-parallel to $\mathbf{B_0}$ with nearly equal power in both directions, then $\sigma_m \approx 0$. The data in Fig. 3 can be generated by ion-cyclotron waves propagating predominantly away from the sun along $\mathbf{B_0}$ or by magnetosonic/whistler waves propagating predominantly toward the sun along $\mathbf{B_0}$ or both. To uniquely identify the wave mode(s) responsible for the observed spectra would require additional data; electric field data, for example, to compute the Poynting vector in the plasma frame. Electric field data at 10 Hz is relatively scarce and such an analysis has not yet been carried out.

Another noteworthy characteristic of the kinetic scale fluctuations seen in Fig. 3 is that they appear to be a persistent feature of high speed solar wind that are almost always present in the data. This has been investigated by analyzing successively shorter and shorter time intervals. While a 6 h interval of high speed wind at 1 AU is often sufficient to form a spectrum such as that shown in Fig. 3, intervals shorter than 6 h often do not provide adequate coverage for all angles θ_{BV} of interest. For example, a 1 h interval of data may only cover a small range of angles, such as $50° < \theta_{BV} < 70°$, which is inadequate to form a complete angular spectrum. However, if it happens that a particular 1 h interval covers the range $0 < \theta_{BV} < 20°$, then the dark blue signal in Fig. 3 is very often seen in the data. Likewise, when a 1 h interval of data covers the range of angles $75° < \theta_{BV} < 95°$, then the yellow and orange feature in Fig. 3 is almost always seen in that data. Therefore, the kinetic fluctuations seen in Fig. 3 are a ubiquitous feature of high speed wind near 1 AU and presumably throughout the inner heliosphere. More recent work, not yet published, suggests that the same spectral features are present in low speed wind.

5 Origin of the Parallel Propagating Waves

Parallel propagating ion-cyclotron and/or magnetosonic-whistler waves have tentatively been identified near $kc/\omega_{pp} = 1$ through data like that shown in Fig. 3. While these waves coexist with solar wind turbulence, they are not believed to be an integral part of the turbulent energy cascade which primarily transfers energy in the $\mathbf{k}_\perp$ direction. Instead, the parallel propagating waves are believed to be generated in-situ by kinetic plasma instabilities [24]. It is reasonably well established that instabilities, such as the electromagnetic ion-cyclotron (EMIC) instability and the proton parallel firehose instability, regulate proton pressure anisotropies in the expanding solar wind—see, for example, the references given in [24].

In textbook treatments of the EMIC instability driven by a proton temperature anisotropy with $T_{p\perp} > T_{p\parallel}$ or the firehose instability driven when $T_{p\parallel} > T_{p\perp}$, the unstable waves generated by these instabilities propagate with the same growth rate

both parallel and anti-parallel to the local mean magnetic field. However, in high speed wind, alpha particles usually flow faster than the protons in the direction parallel to the local mean magnetic field. Differential streaming of the alpha particles causes the growth rates of these instabilities to become asymmetric, that is, the growth rates for waves propagating parallel and antiparallel to $\mathbf{B_0}$ are not equal [24]. For a plasma characterized by drifting bi-Maxwell distributions, Podesta and Gary [24] have shown that the presence of alpha-proton differential streaming causes the EMIC instability to preferentially generate left circularly polarized EMIC waves propagating *away* from the sun along $\mathbf{B_0}$ and it causes the firehose instability to preferentially generate right circularly polarized magnetosonic/whistler waves propagating *toward* the sun along $\mathbf{B_0}$. Moreover, these preferred directions of propagation are independent of the polarity of the mean magnetic field and depend only on the direction of the differential alpha-proton flow velocity $\mathbf{V}_\alpha - \mathbf{V}_p$ which is usually directed away from the sun along $\mathbf{B_0}$.

The waves generated by these two instabilities have wavenumbers of order $kc/\omega_{pp} \sim 1$, frequencies $\omega_r/\Omega_p \sim 1$, and phase speeds on the order of the Alfvén speed V_A [24]. Because the solar wind flow speed is super-Alfvénic with $V_{\rm sw} \gg V_A$ and the fluctuations are essentially frozen into the flow, outward propagating EMIC waves and inward propagating magnetosonic/whistler waves both appear left-hand polarized in the spacecraft frame[3]. Therefore, either one of these modes can produce the dark blue spot observed in Fig. 3. Remarkably, the instability mechanisms generate waves with the observed magnetic helicity signature no matter whether $T_{p\perp} > T_{p\parallel}$ or $T_{p\parallel} > T_{p\perp}$. However, past studies of instabilities based on measured proton distribution functions in the solar wind suggest that the EMIC instability with $T_{p\perp} > T_{p\parallel}$ is more likely to operate in the fast wind near 1 AU [6, 17, 19].

The theoretical analysis of Podesta and Gary [24] has also shown that for both the EMIC and firehose instabilities there exist significant ranges of plasma parameters for which the waves generated by these instabilities propagate approximately unidirectionally, plasma parameters that are consistent with the parameters of the solar wind at 1 AU. Unidirectional propagation is necessary to explain observations in which σ_m assumes extreme values near $+1$ or -1. A parallel propagating mode must propagate nearly unidirectionally to have $|\sigma_m| \simeq 1$, as in the dark blue region in Fig. 3. Based on the preferred directions of propagation predicted by linear instability theory and the nearly unidirectional nature of propagation predicted over significant regions of parameter space, it is reasonable to conclude that the EMIC and firehose instabilities provide a natural explanation for the parallel propagating waves observed in Fig. 3. Further support for this idea comes from predictions, based on measured proton distribution functions, that the EMIC instability is often active in the fast solar wind [6, 17, 19].

[3]Ideally, wavelet measurements of the parallel propagating waves are performed when $\mathbf{B_0}$ is parallel to the solar wind flow direction

6 Conclusions

The concept of the local mean magnetic field is essential for quantifying the anisotropy of magnetic field fluctuations in the solar wind where the magnetic field direction is highly variable. Using this concept in conjunction with wavelet analysis techniques, it is possible to measure the magnetic field spectrum as a function of the angle θ_{BV} between the local mean magnetic field and the solar wind flow velocity [11, 12, 22, 23]. The same technique may be applied to other kinds of spectra and cross-spectra. Recent application to the study of the normalized magnetic helicity spectrum σ_m [10, 24, 25] has revealed important new information about the ubiquitous fluctuations at proton kinetic scales and the kinetic processes which operate at those scales. I have presented one example in detail and discussed the current physical interpretation of these novel wave observations.

Acknowledgements I am grateful to Manfred Leubner and Zoltán Vörös for the invitation to the International Astrophysics Forum Alpbach 2011 held in Alpbach, Tyrol, Austria in June 2011. And to S. Peter Gary for helpful discussions and comments on the manuscript. This research was supported by NASA's Solar and Heliophysics Program and the NSF Shine program.

References

1. Bale, S.D., Kellogg, P.J., Mozer, F.S., Horbury, T.S., Reme, H.: Measurement of the Electric Fluctuation Spectrum of Magnetohydrodynamic Turbulence. Phys. Rev. Lett. **94**, 215002 (2005). DOI 10.1103/PhysRevLett.94.215002
2. Bruno, R., Carbone, V.: The Solar Wind as a Turbulence Laboratory. Living Reviews in Solar Physics **2**, 4 (2005)
3. Chen, C.H.K., Horbury, T.S., Schekochihin, A.A., Wicks, R.T., Alexandrova, O., Mitchell, J.: Anisotropy of Solar Wind Turbulence between Ion and Electron Scales. Phys. Rev. Lett. **104**(25), 255002 (2010). DOI 10.1103/PhysRevLett.104.255002
4. Chen, C.H.K., Mallet, A., Schekochihin, A.A., Horbury, T.S., Wicks, R.T., Bale, S.D.: Three-Dimensional Structure of Solar Wind Turbulence. ArXiv e-prints:1109.2558 (2011)
5. Chen, C.H.K., Mallet, A., Yousef, T.A., Schekochihin, A.A., Horbury, T.S.: Anisotropy of alfvénic turbulence in the solar wind and numerical simulations. Mon. Not. R. Astron. Soc. **415**, 843 (2011). DOI 10.1111/j.1365-2966.2011.18933.x
6. Dum, C.T., Marsch, E., Pilipp, W.: Determination of wave growth from measured distribution functions and transport theory. Journal of Plasma Physics **23**, 91–113 (1980). DOI 10.1017/S0022377800022170
7. Forman, M.A., Wicks, R.T., Horbury, T.S.: Detailed Fit of "Critical Balance" Theory to Solar Wind Turbulence Measurements. Astrophys. J. **733**, 76 (2011). DOI 10.1088/0004-637X/733/2/76
8. Goldstein, M.L., Roberts, D.A., Fitch, C.A.: Properties of the fluctuating magnetic helicity in the inertial and dissipation ranges of solar wind turbulence. J. Geophys. Res. **99**, 11519–11538 (1994)
9. Goldstein, M.L., Roberts, D.A., Matthaeus, W.H.: Magnetohydrodynamic Turbulence In The Solar Wind. Annu. Rev. Astron. Astrophys. **33**, 283–326 (1995). DOI 10.1146/annurev.aa.33.090195.001435

10. He, J., Marsch, E., Tu, C., Yao, S., Tian, H.: Possible Evidence of Alfvén-cyclotron Waves in the Angle Distribution of Magnetic Helicity of Solar Wind Turbulence. Astrophys. J. **731**, 85 (2011). DOI 10.1088/0004-637X/731/2/85
11. Horbury, T.S., Forman, M., Oughton, S.: Anisotropic Scaling of Magnetohydrodynamic Turbulence. Phys. Rev. Lett. **101**(17), 175005 (2008). DOI 10.1103/PhysRevLett.101.175005
12. Horbury, T.S., Wicks, R.T., Chen, C.H.K.: Anisotropy in Space Plasma Turbulence: Solar Wind Observations. Space Sci. Rev. p. 293 (2011). DOI 10.1007/s11214-011-9821-9
13. Howes, G.G., Bale, S.D., Klein, K.G., Chen, C.H.K., Salem, C.S., TenBarge, J.M.: The slow-mode nature of compressible wave power in solar wind turbulence. ArXiv e-prints:1106.4327 (2011)
14. Howes, G.G., Quataert, E.: On the Interpretation of Magnetic Helicity Signatures in the Dissipation Range Of Solar Wind Turbulence. Astrophys. J. **709**, L49–L52 (2010). DOI 10.1088/2041-8205/709/1/L49
15. Leamon, R.J., Smith, C.W., Ness, N.F., Matthaeus, W.H., Wong, H.K.: Observational constraints on the dynamics of the interplanetary magnetic field dissipation range. J. Geophys. Res. **103**, 4775 (1998). DOI 10.1029/97JA03394
16. Leamon, R.J., Smith, C.W., Ness, N.F., Wong, H.K.: Dissipation range dynamics: Kinetic Alfvén waves and the importance of β_e. J. Geophys. Res. **104**, 22331–22344 (1999). DOI 10.1029/1999JA900158
17. Leubner, M.P., Viñas, A.F.: Stability analysis of double-peaked proton distribution functions in the solar wind. J. Geophys. Res. **91**, 13366–13372 (1986). DOI 10.1029/JA091iA12p13366
18. Luo, Q.Y., Wu, D.J.: Observations of Anisotropic Scaling of Solar Wind Turbulence. Astrophys. J. **714**, L138–L141 (2010). DOI 10.1088/2041-8205/714/1/L138
19. Marsch, E.: Kinetic Physics of the Solar Wind Plasma, pp. 45–133. Springer-Verlag Berlin. (1991)
20. Marsch, E.: MHD Turbulence in the Solar Wind, pp. 159–241. Springer-Verlag Berlin. (1991)
21. Matthaeus, W.H., Goldstein, M.L.: Measurement of the rugged invariants of magnetohydrodynamic turbulence in the solar wind. J. Geophys. Res. **87**, 6011–6028 (1982)
22. Podesta, J.J.: Dependence of solar-wind power spectra on the direction of the local mean magnetic field. Astrophys. J. **698**, 986–999 (2009). DOI 10.1088/0004-637X/698/2/986
23. Podesta, J.J.: Spectral anisotropy of solar wind turbulence in the inertial range and dissipation range. In: M. Maksimovic, K. Issautier, N. Meyer-Vernet, M. Moncuquet & F. Pantellini (ed.) Twelfth International Solar Wind Conference, *AIP Conference Series*, vol. 1216, pp. 128–131 (2010). DOI 10.1063/1.3395817
24. Podesta, J.J., Gary, S.P.: Effect of Differential Flow of Alpha Particles on Proton Pressure Anisotropy Instabilities in the Solar Wind. Astrophys. J. **742**, 41 (2011). DOI 10.1088/0004-637X/742/1/41
25. Podesta, J.J., Gary, S.P.: Magnetic Helicity Spectrum of Solar Wind Fluctuations as a Function of the Angle with Respect to the Local Mean Magnetic Field. Astrophys. J. **734**, 15 (2011). DOI 10.1088/0004-637X/734/1/15
26. Sahraoui, F., Goldstein, M.L., Belmont, G., Canu, P., Rezeau, L.: Three Dimensional Anisotropic k Spectra of Turbulence at Subproton Scales in the Solar Wind. Phys. Rev. Lett. **105**(23), 131101 (2010). DOI 10.1103/PhysRevLett.105.131101
27. Tu, C.Y., Marsch, E.: MHD structures, waves and turbulence in the solar wind: Observations and theories. Space Sci. Rev. **73**, 1–210 (1995). DOI 10.1007/BF00748891
28. Wicks, R.T., Horbury, T.S., Chen, C.H.K., Schekochihin, A.A.: Power and spectral index anisotropy of the entire inertial range of turbulence in the fast solar wind. Mon. Not. R. Astron. Soc. **407**, L31–L35 (2010). DOI 10.1111/j.1745-3933.2010.00898.x
29. Wicks, R.T., Horbury, T.S., Chen, C.H.K., Schekochihin, A.A.: Anisotropy of Imbalanced Alfvénic Turbulence in Fast Solar Wind. Phys. Rev. Lett. **106**, 045001 (2011). DOI 10.1103/PhysRevLett.106.045001

On the Passive Nature of Proton Temperature in Solar Wind Turbulence

Giuseppe Consolini

Abstract In the framework of space plasma physics the solar wind is commonly recognized as an example of turbulent medium. Although turbulence studies mainly focalize on the features of velocity field (and magnetic field for plasma media), another field of investigation deals with the properties of scalar quantities (such as the concentrations of tracers, the temperature, etc.) passively advected in turbulent media. In this brief work, we present a preliminary study of the scaling and intermittent features of the solar wind proton temperature, considered for its possible passive scalar nature, in a long-lasting period of slow solar wind as observed by the ULYSSES mission. In detail, the results on the scaling and intermittent features of the solar wind proton temperature are compared and discussed in terms of a turbulent advected passive scalar quantity.

1 Introduction

The solar wind is a supersonic and super-Alfvènic collisionless plasma flow showing turbulence [1]. Indeed, the solar wind evolves towards a state characterized by large-amplitude scale-invariant fluctuations whose spectral features resemble those observed in turbulent media in presence of a magnetic field. For this reason, the solar wind is an excellent natural laboratory to study magnetohydrodynamic (MHD) turbulence in space plasmas [1]. Furthermore, the understanding of the turbulent nature of the solar wind is also propaedeutic to other astrophysical frameworks from the understanding of transport processes in space plasmas to plasma heating, from solar wind generation to high-energy particle acceleration, and so on.

G. Consolini (✉)
INAF-Istituto di Astrofisica e Planetologia Spaziali, Via del Fosso del Cavaliere, 100, 00133 Roma, Italy
e-mail: giuseppe.consolini@inaf.it

Consolini, G.: *On the Passive Nature of Proton Temperature in Solar Wind Turbulence*. Astrophys Space Sci Proc. **33**, 187–193 (2012)
DOI 10.1007/978-3-642-30442-2_21, © Springer-Verlag Berlin Heidelberg 2012

Although the early studies on solar wind turbulence date back to the 1970s and 1980s [2], great advances have been reached using the in-situ observations of the ULYSSES mission in the last decade [1]. These observations provided a considerable improvement in the knowledge of the MHD turbulence features of the solar wind with the heliospheric latitude and its evolution with the radial distance. Furthermore, these studies greatly increased the understanding of the observed intermittency phenomenon. However, they focused primarily on magnetic and velocity field, while less attention was posed on the analysis of the scaling and turbulent features of other plasma parameters, such as the density, the temperature, etc., which could deserve a particular interest for their possible passive nature. Indeed, the advection of passive scalar quantities and the occurrence of passive scalar turbulence have both theoretical aspects and practical ones, which are particularly interesting in the field of turbulence [4, 5].

Given a fluid turbulent flow, a passive scalar quantity is a diffusive contaminant, substance or quantity, whose effects are negligible on the fluid motion. Examples of passive scalar quantities are heat, chemical substances, dye blobs, etc. In this framework, the turbulent fluid motions transport, stretch and disperse the passive scalar quantity, causing an amplification of local scalar concentration gradients that improve the rate mixing of scalar quantities, independently of molecular diffusivity [4, 5]. Thus, the study of passive scalar advection in turbulent flows has a great impact in several natural and engineering settings.

The dynamics of a passive scalar field $\theta(\mathbf{r}, t)$ is governed by the following convection-diffusion (CD) equation,

$$\frac{\partial \theta}{\partial t} + u_j \partial^j \theta = \kappa \partial_j \partial^j \theta + f \ , \tag{1}$$

where $\mathbf{u}(\mathbf{r}, t)$ is the local velocity field, κ is the diffusion coefficient and $f(\mathbf{r}, t)$ is a forcing term. In the CD-equation the diffusivity κ plays a central role in the development of the turbulent behavior. Indeed, a small amount of diffusivity greatly affects the evolution of the passive scalar leading to a behavior similar to that observed in the case of turbulence. Conversely, the passive scalar is only rigidly transported in the limit of zero diffusivity.

The application of Kolmogorov's theory of turbulence [3] to passive scalar behavior led Obukhov and Corrsin [6, 7] to predict the scaling of second order structure function $S_2(r)$,

$$S_2(r) = \langle \Delta_r \theta^2 \rangle \sim \epsilon_\theta \epsilon^{-1/3} r^{2/3} \ , \tag{2}$$

where ϵ_θ is dissipation rate of the scalar variance, ϵ is the energy dissipation rate for the turbulent velocity field and r is the scale at which the increment of the passive scalar is evaluated. The predictions of the Kolmogorov-Obukhov-Corrsin (KOC) theory imply a simple scaling for the scalar increment structure functions $S_p(r) = (S_2(r))^{p/2}$. However, deviations from this simple scaling are observed and they are generally interpreted as a consequence of intermittency effects.

The temperature, measured at a given point in a turbulent flow, is one of the most studied passive scalar quantities [8, 9]. It can be indeed considered a passive scalar when its effects on the velocity turbulent field are negligible. The studies of temperature scaling features in turbulent fluid flows (see e.g. [9]) evidenced the anomalous scaling of temperature increments and its more pronounced intermittent character with respect to velocity field one. This stronger intermittent character is discussed in terms of a double intermittency correction for kinetic energy and temperature fluctuations dissipation rates [9].

Here, the scaling features of solar wind proton temperature and its passive scalar nature are investigated, using the traditional structure function approach for a long-lasting period of slow solar wind condition observed by ULYSSES mission. Apart from the theoretical aspects we believe that the relevance of this study stands in its importance for heat transport and evolution toward a situation of thermal equilibrium.

2 Data Set and Analysis

Data used in this work are the solar wind parameters (velocity $\mathbf{v}$ and proton temperature T_p) measured by the SWOOPS experiment (P.I. D. McComas, Southwest Research Institute, USA) on board of ULYSSES satellite, and refer to a long-lasting period of slow solar wind condition from 01, October, 1997 to 31, March, 1998 at $\sim$5 AU on the heliospheric equatorial plane (HGI Lat $\in [-6°, 4°]$). This period is located during the beginning of the ascending phase of the 23rd solar activity cycle. Data come from NASA – CDAweb site (http://cdaweb.gsfc.nasa.gov) and the typical time resolution is about 4–8 min. The considered period, already studied in other works [10, 11], is peculiar for its solar wind conditions, being a very long time interval of nearly constant slow solar wind ($\langle v_R \rangle = [370 \pm 20]$ km/s), characterized by very small gradients.

The ULYSSES plasma experiment [12] provides two different estimates of the proton temperature, namely T_{Large} and T_{Small}, which can be considered as an overestimate and an underestimate of the true solar wind proton temperature, $T_{Small} \leq T_p \leq T_{Large}$. However, from a statistical point of view these two temperatures display the same behavior in the selected period. Thus, we consider the mean value between the two estimates $T_p = (T_{Small} + T_{Large})/2$.

The radial velocity v_R and the proton temperature T_p in the selected time interval are shown in Fig. 1. The average proton temperature is $T_p = [3 \pm 2]10^4$ K, and its variability (as estimated by the standard deviation) is very high ($\sim$67%) in comparison with that of the velocity field ($\sim$5%). We note how the observed average proton temperature agrees with previous observations by other satellites (see e.g. [14] and references therein).

Figure 2 reports both the power spectral density (PSD) S_T of the proton temperature in the selected period (left panel) and a comparison between the temperature power spectrum S_T and the velocity one S_v (right panel), computed in terms of the

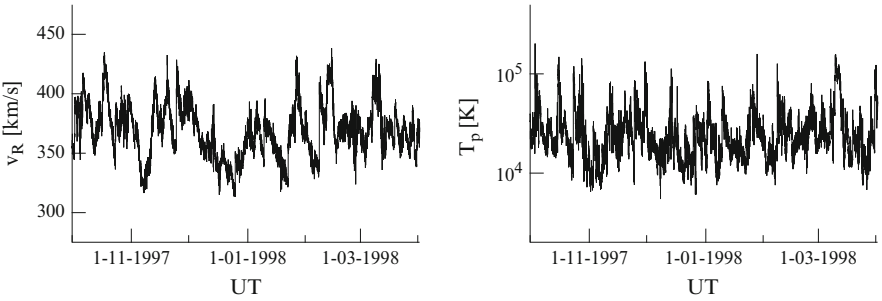

Fig. 1 The radial velocity and the proton temperature for the selected time interval

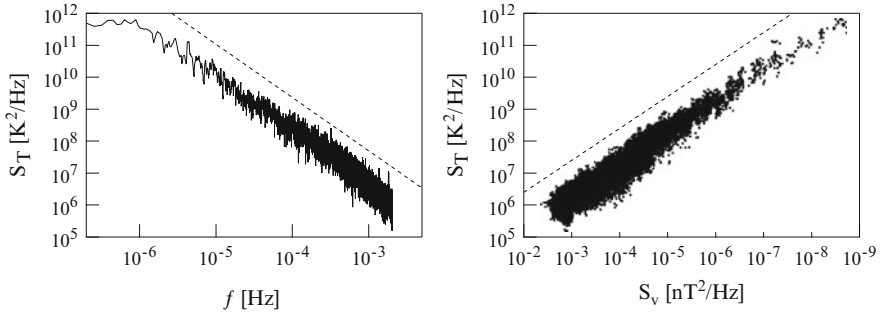

Fig. 2 The power spectral density (PSD) of the proton temperature (*left panel*) and the comparison between the temperature and velocity PSDs (*right panel*). The two *dashed lines* are the expected Kolmogorov's $5/3$ law (*left panel*) and a linear dependence (*right panel*), respectively

trace of the spectral density matrix ($S_v = \sum_i S_v^i$, where $i = R, T, N$). We remark that to evaluate the PSDs we interpolate missing data using a linear interpolation scheme. According to KOC-theory of passive scalar turbulence a $f^{-5/3}$ region is found at frequencies $\geq 10^{-6}$ Hz, suggesting that the proton temperature fluctuations are due to passive scalar turbulence. Furthermore, the passive nature of the proton temperature is also suggested by the linear dependence between the two power spectral densities ($S_T \sim S_v$).

To analysize the scaling features of the proton temperature we examine the scaling of the structure functions $S_p(\tau)$, defined according to Ref. [9, 13] as

$$S_p(\tau) = \langle \mid \theta(t+\tau) - \theta(t) \mid^p \rangle. \tag{3}$$

In particular, we evaluate the second order structure function $S_2(\tau)$, which is reported in the left panel of Fig. 3, where the $S_2(\tau)$ is shown in a log-log plot as a function of the time lag τ. A quite good power-law behavior is recovered in the whole time interval. The power-law dependence is the evidence of scaling

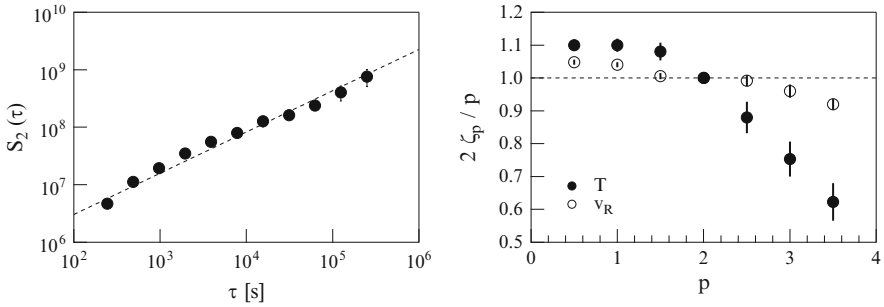

Fig. 3 The second order structure function $S_2(\tau)$ of the proton temperature (*left panel*) and the rescaled relative scaling exponents ζ_p of proton temperature and radial velocity (*right panel*). *Dashed lines* are a power law best fit (*left panel*) and the KOC-theory prediction (*right panel*), respectively

Table 1 Scaling exponents of velocity and temperature structure functions. The fourth column refers to observations in neutral fluid turbulence [9]

Moment order p	Velocity ξ_p [this work]	Temperature ξ_p [this work]	Temperature ξ_p Ruiz-Chavarria et al. [9]
1	0.37 ± 0.01	0.38 ± 0.01	0.370 ± 0.003
2	0.70 ± 0.02	0.63 ± 0.02	0.620 ± 0.005
3	0.98 ± 0.03	0.79 ± 0.05	0.800 ± 0.008

invariance properties of the proton temperature increments over more than three orders of magnitude. Based on Taylor's hypothesis, the observed scaling exponent ξ_2 is close to the one predicted by the KOC theory, being $\xi_2 = [0.63 \pm 0.02]$, even if a slight deviation is observed. Table 1 reports the scaling exponents ξ_p of velocity and temperature structure functions along with those of temperature, as a passive scalar, observed in the case of neutral fluid turbulence by Ruiz-Chavarria et al. [9]. The proton temperature scaling behavior shows relevant deviations from the KOC-theory prediction, $\xi_p = p/3$, already for lower order moments ($p = 3$). This behavior is quite common in the case of passive scalar turbulence. Furthermore, a good agreement exists between solar wind temperature scaling exponents ξ_p and those found by Ruiz-Chavarria et al. [9].

To better analyze the role of intermittency in proton temperature fluctuations, we investigate the relative scaling of the $p-$order structures function $S_p(\tau)$ as a function of the second-order one $S_2(\tau)$: i.e., $S_p(\tau) \sim S_2(\tau)^{\zeta_p}$. The right panel of Fig. 3 shows the relative scaling exponents ζ_p of the proton temperature T_p and the radial component v_R of the velocity, normalized using the values predicted by the KOC-theory. Deviations from the KOC-theory (dashed line) are observed in both cases, suggesting the occurrence of intermittency. However, the deviations are again more important for proton temperature than for the radial velocity, that is common in passive scalar turbulence [8, 9].

3 Summary and Conclusions

In this preliminary work we studied the scaling features of the proton temperature for a long-lasting period of slow solar wind condition at ∼5 AU on the heliospheric equatorial plane. Our results on proton temperature fluctuations can be summarized as follows: (1) the PSD displays a $f^{-5/3}$-domain; (2) the scaling features of the structure functions agree with those observed for passive scalar in fully developed turbulence; (3) the relative scaling of the $p-$order structure functions displays large departures form the KOC-theory prediction that are the signature of intermittency; (4) the temperature intermittency is more pronounced than the velocity one.

This last result, which is a distinctive feature of passive scalar turbulence is probably due to a double intermittency correction for the kinetic energy and temperature dissipation rates. In the classical passive scalar theory [6, 7] the statistical features of the passive scalar exclusively depend on molecular diffusivity κ, kinetic viscosity, kinetic energy dissipation rate ϵ and dissipation rate of the scalar variance ϵ_θ. For this reason the theoretical scaling of the p-order structure function is

$$S_p(r) \sim \epsilon_\theta^{p/2} \epsilon^{-p/6} r^{p/3}. \tag{4}$$

However, the observed scaling exponents are significantly different from theoretical predictions and this discrepancy is believed to be the results of intermittencies of ϵ and ϵ_θ. In fluid passive scalar turbulence the observed anomalous scaling is ascribed to the organization of the scalar field in structures, which are not a mere signature of an organized vorticity in the shear flow, but are principally due to mixing process [5]. Furthermore, numerical simulations [15] have clearly shown that intermittency is an intrinsic feature of passive scalars also in structureless, artificial gaussian velocity fields and is due to the formation of local patches of nearly constant scalar fields interrupted by intense gradients sheets. Thus, intermittency in an advected scalar field is to some extent decoupled from that of velocity field, as already found by Kraichnan [16], being expected also in the case of gaussian velocity fields. From the above points it is clear what is the origin of the more intermittent character of passive scalar field and the meaning of the previous sentence stating that the anomalous scaling is due to a cumulative effect of intermittency of ϵ and ϵ_θ.

We could imagine that a similar situation occurs in the case of solar wind. Even an initially nearly stochastic temperature field at the Sun surface could evolve towards the formation of patchy structures of temperature, which are responsible of the observed strong intermittency, being superimposed to the turbulent intermittent velocity field. By the way, at this moment this is still a speculation that will be better investigated and studied in a forthcoming work [17].

In conclusion, all the properties of the solar wind proton temperature, observed in this preliminary work, suggest that in slow solar wind the proton temperature resembles the typical behavior of passive scalar in a turbulent flow [4]. Clearly, further work is necessary to see if this feature extends also to fast solar wind conditions, and to better understand the origin of the observed properties within a general view on solar wind turbulence.

Acknowledgements We acknowledge the Ulysses PIs of SWOOPS D. Mc-Comas (Southwest Res. Inst., USA), M. Lancaster and C. Tranquille of the Ulysses Data System (ESA-ESTEC, NL), the NASACDAweb service staff (USA) for the data (available on web) used in this work. This work was made with the support of the International Space Science Institute of Bern (Switzerland) in the framework of the ISSI team 185 *Dispersive cascade and dissipation in collisionless space plasma turbulence: observations and simulations.*

References

1. Bruno, R., Carbone, V.: The solar wind as a turbulence laboratory. Living Rev. Sol. Phys. **2**, 4–354 (2005)
2. Tu, C.-Y., Marsch, E.: MHD structures, waves and turbulence in the solar wind: Observations and theories. Space Sci. Rev. **73**, 1–210 (1995)
3. Frisch, U.: Turbulence. The Legacy of A.N. Kolmogorov, Cambridge Univ. Press, Cambridge (1995)
4. Warhaft, Z.: Passive scalars in turbulent flows, Ann. Rev. Fluid Mech. **32**, 203 (2000)
5. Shraiman, B.I., Siggia, E.D.: Scalar turbulence, Nature, **405**, 639 (2000)
6. Obukhov, A.M.: Structure of the temperature field in turbulent flows, Izv. Akad. Nauk. SSSR, Geogr. Geo z., **13**, 58 (1949)
7. Corrsin, S.: On the spectrum of isotropic temperature fluctuations in isotropic turbulence, J. Appl. Phys., **22**, 469 (1951)
8. Antonia, R.A., Hopfinger, E.J., Gagne, Y., Anselmet, F.: Temperature structure functions in turbulent shear flows, Phys. Rev. A, **30**, 2704–2707 (1984).
9. Ruiz-Chavarria, G., Baudet, C., Ciliberto, S.: Scaling laws and dissipation scale of a passive scalar in fully developed turbulence, Physica D, **99**, 369–380 (1996).
10. Consolini, G., Bavassano, B., De Michelis, P.: A probabilistic approach to heterogeneity in space plasmas: the case of magnetic field intensity in solar wind, Nonlin. Processes Geophys., **16**, 265–273 (2009).
11. Consolini, G., De Michelis, P.: Relative ordering in the radial evolution of solar wind turbulence: the S-Theorem approach, Ann. Geophys., **29**, 2317–2326 (2011).
12. Bame, J. et al.: Astron. & Astrophys. Suppl. Ser., **92**, 237 (1992)
13. benzi, R., Biferale L., Parisi, G:: Intermittency correction to Obukhov-Corrsin theory of a passive scalar, Europhys. Lett., **18**, 213–217 (1992)
14. Richardson, J.D., Smith, C.W.: The radial temperature profile of the solar wind, Geophys. Res. Lett., **30**, 1206, doi:10.1029/2002GL016551 (2003)
15. Chen, S., Kraichnan, R.H.: Simulations of a randomly advected passive scalar field, Phys. Fluids, **68**, 2867–2884 (1998)
16. Kraichnan, R.H.: Anomalous scaling of a randomly advected passive scalar, Phys. Rev. Lett., **72**, 1016–1019 (1994)
17. Consolini, G.: Intermittency and scaling features of solar wind proton temperature, in preparation (2012)

Part V
Heliogeophysics and Planetary Physics

Fine Particles and Nonlinear Processes in Plasma Heliogeophysics

Sergey I. Popel

Abstract Plasma heliogeophysics is a relatively new and important field of research which deals with problems stemming from processes taking place in cosmic space and described in terms of electrodynamics and plasma physics. It is relevant to diverse topics such as the physics of the Sun, solar wind, heliosphere, terrestrial magnetosphere and ionosphere, solar-terrestrial relations, the dusty (complex) plasma, the fundamental concepts of plasma physics, etc. Recently it has been shown that fine nano- and micro-meter sized electrically charged particulates from the interplanetary space and from the Earth's environments can affect the local properties as well as the diagnostics of the interplanetary, magnetospheric, ionospheric, and terrestrial complex plasmas. In this paper the sources of the charged dust particulates and some nonlinear dusty plasma effects in cosmic space and Earth environments are examined.

1 Introduction

Plasma heliogeophysics deals with problems stemming from processes taking place in cosmic space and described in terms of electrodynamics and plasma physics. These include the physics of the Sun, solar wind, heliosphere, terrestrial magnetosphere and ionosphere, solar-terrestrial relations, the dusty (complex) plasma, the fundamental concepts of plasma physics, etc. [1]. Thus, the study of the problems of plasma heliogeophysics usually starts at the Sun, which is the main source of radiation and energetic particles entering, in particular, the Earth's magnetosphere and atmosphere. Thus the Earth's environment is directly affected by the solar activity. Sophisticated magnetohydrodynamic models have been developed

S.I. Popel (✉)
Institute for Dynamics of Geospheres RAS, Leninsky pr. 38, bldg. 1, 119334 Moscow, Russia
e-mail: s_i_popel@mtu-net.ru

Popel, S.I.: *Fine Particles and Nonlinear Processes in Plasma Heliogeophysics*.
Astrophys Space Sci Proc. **33**, 197–208 (2012)
DOI 10.1007/978-3-642-30442-2_22, © Springer-Verlag Berlin Heidelberg 2012

for simulating the solar corona as well as the interaction of the solar wind and the Earth's magnetosphere. Different models are also combined in order to obtain a more complete description of the entire heliogeophysics system, from the Sun to the Earth's upper atmosphere [2–5].

It is well known that the interplanetary, magnetospheric, ionospheric, as well as terrestrial plasmas contain charged dust particulates, which are in fact ubiquitous in the entire solar system and beyond, except perhaps in the interior of the Sun and stars [6]. In this review we shall be concerned with the effect of charged dust particulates and nonlinear processes related to plasma heliogeophysics system.

2 Dust Particulates

The behavior of nanometer and micrometer sized particulates in a dust containing plasma has been extensively studied in recent years [7–15]. The particulates can easily acquire a negative charge because of the high mobility of the electrons. For the same reason nanometer sized dust particulates are less charged than the micrometer ones. When they are confined, say in an external electric or magnetic field, they can self-organize into various lattice structures, with the background plasma remaining gaseous. At higher temperatures, melting of the structure occurs and the dusts become liquid-like. Often regions void of dusts can also appear. Laboratory observations suggest that the voids are quite robust, and the structure is independent of their formation.

Besides the electrostatic force, other forces that can act on the dust particulates include thermophoretic, ion and neutral particle drag, etc. However, it is often difficult to pinpoint the interaction mechanism between two dust particulates in any specific process because of the complexity of the dust-containing plasmas, often referred to as complex plasmas. In a thermal dusty plasma, a charged dust particulate is always Debye screened, so that its electrostatic potential has a range of the order of the plasma Debye length, which is much shorter than that of the Coulomb potential. Moreover, in many situations the dust particulates can still be at different stages of formation that are separated by different chemical processes and physical time scales. It is thus difficult to formulate a complete self-consistent theory. Several novel models, including that of combinations of shielded and unshielded, as well as repulsive and attractive, potentials, can be found in the literature [16–24]. Of special interest is the possibility of (effective) attractive interaction force between like-charged particulates. Since the force between two particulates is a collective effect involving not only the background plasma but also the nearby dust particulates, the exact nature and source of the effective attractive force remains unclear. For example, Tsytovich et al. [16, 20, 22] showed that the shielding and scattering of impacting plasma ions by neighboring particulates can result in an attractive force between the latter. Chen et al. [23] showed that an effective attractive force can appear if one assumes that particulates have a limited sphere (determined by complete charge neutralization within it) of influence.

Wang [24] found that if neighboring particulates have the same surface potential, a shielded attractive part can appear in the interaction potential. For convenience, usually the Debye-screened repulsive Coulomb (or Yukawa) potential is used in the theoretical considerations [16].

3 Particulates in Space

Of particular relevance to plasma heliogeophysics are the intense solar flares and coronal mass ejections. For example, brightness observations of the F-corona made during total solar eclipses and from coronagraphs on satellites have indicated the possibility that the innermost dust cloud is at distances not exceeding 0.3 astronomical units (AU) from the Sun [25–30]. These dust particulates can originate from the interplanetary space as well as from asteroids and comets. The dust particulates in the solar system are traditionally considered to be in a quasistationary state, with interplanetary dust particulates drifting towards the Sun under the Poynting-Robertson effect [31]. The particulates near the Sun experience a variety of local forces and other effects that are considerably less significant in the more distant parts of the zodiacal cloud. These include radiation and corpuscular pressure forces, time-dependent magnetic fields, erosion, heating and sublimation, etc. The charge of a dust particulates is due to capture of electrons and ions from the local plasma, electron emission from impacts of energetic ions or electrons, release of photoelectrons from the particulates by UV radiation, etc. The radius of a dust particulate in the solar corona plasma is typically $a \sim 0.1$–$20\,\mu\mathrm{m}$. The charge of the larger, i.e., micron-sized, dust particulates can reach $10^6 e$, where $-e$ is the electron charge. The dust density is inversely proportional to the distance from the Sun, and the distance of the dust cloud from the Sun is typically $10R_\odot$, where $R_\odot$ is the solar radius. The enhancement factor of the dust number density in a typical dust zone of width $0.2R_\odot$ near the Sun is 1–4. The dust density increases with the particulates size for the porous particulates and decreases for the more solid ones. For dust particulates in orbits close to the ecliptic plane, those larger than $10\,\mu\mathrm{m}$ tend to remain in a disk with a typical thickness of 10°, and particulates of several $\mu\mathrm{m}$ can be in a larger disk-like volume, which has a moderate (but time depending) tilt with respect to the ecliptic plane and that can vary slightly depending on the solar activity. The less charged nano, or submicron, particulates form a nearly spherical halo with a radius of more than $10R_\odot$ around the Sun. Micron-sized and even larger particulates, originating from their parent bodies such as long-period comets, can exist at higher ecliptic latitudes. This scenario is consistent with the fact that a significant amount of such larger particles have been observed at high ecliptic latitudes. It also supports the suggestion that the long-period comets are an essential source of the dust particulates in the inner solar system. Sublimation and the resulting reduction of the dust size can lead to the production of micrometeoroids near the Sun, and the dust particulates that are expelled from the Sun can interact with the Earth's magnetosphere and atmosphere. The characteristic size of the

micrometeoroids is 0.1 – several μm and they have been found in situ measurements [32–34]. Even smaller nano dust particulates can also exist, but they are difficult to detect because of their size and low charge.

Emission from the Sun forms the low-density low-energy plasma of the solar wind, which also contains non-thermal high and low energy charged particles, including nano- and micro-meter sized charged particulates. The plasma and magnetic field of the solar wind then interacts with that of the Earth, forming the magnetosphere. The boundary of this region is referred to as the magnetopause, which is usually at about ten Earth radii (R_E) in the sunward direction, although this distance is highly variable, say between 5 and $15R_E$, because of changes in the dynamic pressure of the solar wind.

The solar wind can interact with comets having relatively dense and extended atmosphere. The latter is due to evaporation of the volatile substances in the comet's nucleus by solar radiation and tend to expand rapidly as the comet moves through the low pressure interplanetary plasma. Other nano- and micro-meter sized charged particulates and fragments from the comet's nucleus can also enter its atmosphere, forming the dust component. Remote sensing observations of comets inform us on the dust/gas ratio, or the ratio of the production rates of refractory and volatile masses in the coma. The size distribution of coma grains is such that the total area is dominated by the smallest grains present, and the 1P/Halley in-situ results showed that this continued to hold, down to the radius $a \sim 0.01\,\mu\text{m}$ [35, 36]. From the viewpoint of light scattering efficiency, this implies that the observed cometary-comae continuum brightness is dominated by that from particles of radius $a \sim 10\,\mu\text{m}$ [37].

Due to photo-ionization by solar radiation, the atmosphere of a comet at the distances exceeding several kilometers from the its nucleus can become ionized [38]. Interaction between the ions and charged dust particulates in the cometary coma and the solar wind protons can lead to the formation of dust ion acoustic bow shocks [14].

The number of nano- and micro-meter sized charged particulates in the cometary coma can be significant. In fact, the observed dust/gas ratio is in the range 0.1–1 [39–41]. Under the action of the solar light volatile components of the comet nucleus evaporate and vapor stream entrains dust particles. Assuming a 10% dust content in the comet nucleus and a bulk comet density of $1\,\text{g/cm}^3$, one finds that the number density of micron-sized particulates is of the order of $10^{11}\,\text{cm}^{-3}$ [42]. We emphasize that such high density is common to laboratory reactive plasma processing [43]. For a typical comet nucleus of size 1 km having a relatively dense dusty coma ($n_d > 10^6\,\text{cm}^{-3}$), the bow shock from the interaction of solar wind with the coma should be due to the anomalous dissipation arising from the charging of the nano- and micro-meter sized particulates [14].

Interaction of the solar wind with the interplanetary dust particulates is clearly exhibited through the zodiacal light, which can be attributed to the scattering, absorption, and thermal emission of light by the dust particulates. Other sources of the interplanetary dust particulates include collisional fragmentation of the comet debris, micrometeoroids, man-made pollution, etc. The dust size is usually

$a \sim 2$–$10\,\mu$m and the dust number density $n_d \sim 10^{-10}$–$10^{-9}\,\mathrm{cm}^{-3}$. The zodiacal light observations by the Helios 1 and 2 space probes from 1 to 0.3 AU in the ecliptic plane shows that the radial increase in the number density is $n_d \propto r^{-1.3}$ [29,44]. The charge of the nano- and micro-meter sized particulates can reach $10^4 e$. Observations also show that the main composition of the interplanetary and cometary dusts is 60% chondritic (Fe, Mg, Si, C, S), 30% iron–sulphur–nickel, and 10% silicates (olivine).

4 Particulates in the Magnetosphere and Ionosphere

The source of dust particulates in the Earth's magnetosphere include terrestrial aerosols (man-made pollution), micrometeoroids, etc. The composition of the terrestrial aerosols is 90% Al_2O_3. The other parameters are $a \sim 0.1$–$10\,\mu$m and $n_d \sim 10^{-10}$–$10^{-6}\,\mathrm{cm}^{-3}$. The parameters for the micrometeoroids are $a \sim 5$–$10\,\mu$m and $n_d \sim 10^{-10}$–$10^{-9}\,\mathrm{cm}^{-3}$. A micron-sized particulate can be charged up to $10^4 e$. Interaction of the solar wind with the magnetosphere, such as during storms and substorms, can result in strong variations in the dust charge. Theoretical and laboratory investigations of complex plasmas show that even for small dust mass density, the dusts can affect the formation and propagation of perturbations, as well as other phenomena in space and the laboratory [21,23,45–54].

Most magnetospheric activities are also manifested by easily observable changes in the ionosphere and thermosphere, since the magnetospheric activities usually involve large electrical currents, frictional heating, ionization, scintillation, auroral emission, etc. that are important elements of plasma heliogeophysics. In particular, magnetospheric processes can influence the structure of the dusty mesosphere – a layer of the polar summer mesosphere at altitudes of approximately 80–95 km, where the conditions for local nucleation and synthesis of dust particulates are fulfilled. The dusty mesosphere contains layered structures, manifested spectacularly as noctilucent clouds (NLC) and polar mesosphere summer echoes (PMSE). Such structures can be attributed to an ample presence of nano- and micro-meter sized charged dusts and/or aerosols in the upper atmosphere [55,56]. There is much interest in these structures because they could be closely associated with global warming. Investigation of the condensation process of water vapor at altitudes of 80–85 km shows that for the parameters (namely, gas density $\rho_0 \approx 1.2{\cdot}10^{-8}\,\mathrm{g/cm}^{-3}$, temperature $T = 141\,\mathrm{K}$, water vapor pressure $P_{\mathrm{H_2O}} \sim 6.3 \cdot 10^{-5}\,\mathrm{g/s^2cm}$ [57]) of the polar summer mesosphere at these altitudes critical nuclei are formed. Their size is 2.57 nm. Later the condensation of water vapor on the critical nuclei continues until the water vapor pressure equals the saturated vapor pressure. If the number density of the critical nuclei and the number density of the dusts in the mesospheric structures is $n_d = 100\,\mathrm{cm}^{-3}$, one finds that the size of the condensed particulates is $a = 61\,\mathrm{nm}$. This is consistent with that of the observed dust particulates in the NLCs. For $n_d = 1,000\,\mathrm{cm}^{-3}$ we obtain $a = 28\,\mathrm{nm}$, which is consistent with that of the subvisional dust particulates associated with the PMSE. The theoretical results

are in good agreement with the observations (see, e.g., Ref. [55]). The charge of the dust particulates in the ionosphere can reach $100e$.

To describe the ionization properties of the dusty mesosphere, a self-consistent model has been proposed [58]. The model takes into account nucleation of particulates, growth of dust particulates size from nanometers to micrometers, charging of the dust particulates, ionization, recombination, solar radiation, photoelectric effect, sedimentation, as well as self-consistent electric fields. The spectra of the solar radiation at the altitudes corresponding to the dusty mesosphere have been calculated [59] and the dust structures have been analyzed. The model can explain most of the ionization-related effects observed in the polar summer mesosphere, in particular, electron and ion depletion and the formation of the ionization layers. It is shown that these effects are closely associated with the charged dust particulates. For example, reaction of the dusty mesospheric plasma on the external perturbations can lead to nonlinear wave propagation in the NLC and PMSE regions [50, 51]. Results from analysis of the nonlinear structures can be used to diagnose the properties of the NLC and PMSE regions and can thus provide information on the space weather around the Earth's environment.

PMSE phenomena occur most frequently during the polar summer times at altitudes between 80 and 90 km, and are characterized by unusually strong radar backscattering. One of the distinct features of VHF radars is that the backscattered signal is highly directional (the so-called high aspect sensitivity), i.e., the strong backscatter was observed only when the radar beam was launched in almost the vertical direction [60]. This indicates that the backscatter was due to specular reflection by vertically layered small-scale structures of the dusty plasma at scale-lengths comparable to the VHF radar wavelength (several meters) [61]. The small scale structures (irregularities) have been attributed to perturbations in the plasma density [62] and localized nonlinear structures, such as dust-acoustic solitons, etc. [50]. An alternative model has recently been presented. It is based on the evolution of the plasma in the presence of dust particulates flowing downward at the terminal velocity, and the dust location is also determined by a balance between the gravitational and frictional forces [51]. The model took into account the effects of ionization and recombination, as well as charge neutrality among the electrons, ions, and ice particulates in the mesosphere. It is shown that there can exist a steady-state layered structure in the moving dust background, in which the electron and ion density drop dramatically while the electric field increases appreciably. It is found that the characteristic scalelength of the electron density distribution is about 9 m, which is close to that of the observed irregularities [63].

5 Nonlinear Processes

Nonlinear processes play an important role in dusty plasma heliogeophysics. In Sect. 3 we have mentioned the bow shock formation from the interaction of solar wind with the cometary coma. This is a nonlinear process consistent with the

formation of the shocks observed in Refs. [45, 46] and predicted theoretically in Refs. [64, 65].

Redistribution of dust particles in the ionosphere occurs as a result of nonlinear vortex motions [66]. The dust particles are captured by acoustic-gravitational (AG) vortices, that leads to the formation of dust vortices as a result of involving a great number of dust particles into vortex motions. Layers of dust particles in the ionosphere with a thickness of about 1 km, which are formed at the altitudes less than 120 km, distribute within the region of the existence of AG-vortex structures. As a result, at the altitudes of 110–120 km, dust vortices can appear, and transportation of particles up to the altitudes of 130 km becomes possible. Another way of transportation of dust particles in the ionosphere is shown to be vertical fluxes (streamers) [67], which are generated by dust vortices due to the development of parametric instability.

From the viewpoint of the plasma heliogeophysics, the following manifestations of the nonlinear processes in dusty ionospheric plasmas at 80–120 km altitude during high-speed meteor showers are representative: ground-based observations of low-frequency ionospheric radio noise with the frequencies lower than 50 Hz [68], ground-based observations of infrasonic waves, and amplification of the intensity of the green radiation at 557.7 nm from a layer of the lower ionosphere at 110–120 km. All of them are related to the nonlinear excitation of dust acoustic waves [69]. The physical processes governing these manifestations are the following [70]. During intensive high-speed meteor showers, the meteors are ablated at the altitudes of 80–120 km. The ablation produces supersaturated vapors of metals such as sodium, calcium, magnesium, etc., which then condense into nanometer-to-micrometer sized secondary (dust) grains of cosmic origin. The grains acquire electric charge because of unbalanced electron and ion currents flowing into them as well as photoemission due to solar radiation. As an electromagnetic wave propagates in the dusty plasma in the Earth's upper atmosphere, nonlinear modulational interaction [71] excites low-frequency electrostatic perturbations at characteristic frequencies close to that of the dust acoustic waves, so that the electromagnetic waves can become modulated. It is the low-frequency component of the modulated wave against the ionospheric noise background that is recorded at the Earth's surface. Interaction of the modulationally excited dust acoustic perturbations with the neutrals leads to excitation of rather intense infrasonic waves that can be detected on the Earth's surface. The growth of the infrasonic waves from the convective instability at the altitude 110–120 km can result in the appearance of localized nonlinear vortex structures or Rayleigh-Taylor instabilities [72], which in turn leads to convective overturn of oxygen in the vertical direction and increase in the atomic oxygen density at 110–120 km. The increase in the atomic oxygen density is accompanied by amplification of the intensity of the green radiation at 557.7 nm from this layer of the upper atmosphere.

Finally, we note the behavior of nonlinear localized dust acoustic structures which can exist in the mesosphere at altitudes of 80–95 km [50]. Their properties are determined mainly by the sign of the local dust charge which is related to the material constituting the dust grain. Dust acoustic structures containing positive grains appear as electron-density humps and ion-density dips, and

those with negative grains appear as electron-density dips and ion-density humps. In general, knowledge of the nonlinear structures is useful for understanding the origin, behavior and effect of the NLCs on the mesosphere and its relation with the other regions of the Earth's atmosphere.

6 New Vistas

The examples we have given make clear the importance of dusty plasma effects in some situations in cosmic space and Earth environments. However, in reality, many other situations exist where a comprehensive analysis of dusty plasma processes should be used. Here we outline some problems which can be important for applications to space dusty plasmas and Earth sciences.

6.1 Dusty Plasma Processes in the System Earth-Moon

Research on dusty plasma processes in the system Earth-Moon is helpful for the future missions to the Moon (Luna-Resource, Luna-Glob). The lunar landers Luna-Resource and Luna-Glob will study polar regions of the Moon and carry, in particular, the equipment designed to detect dust particles [73]. The research assumes the description of lunar dust interaction with the solar wind and Earth's magnetospheric plasmas, dust grain charging, theoretical investigation and modelling of wave and collective phenomena in the dusty plasma system Earth-Moon, determination of mechanisms of energy exchange between dust and solar wind particles, dust particle acceleration by the solar wind particles, etc.

The consideration of the dusty plasmas in the system Earth-Moon has to take into account the surface electric field of the Moon. In the electric field, positive ions are accelerated, acquiring at least the Bohm speed, which is the same as the ion-acoustic speed. Thus, wake-field effects associated with the ion flow are to be expected. The wake-fields provide the possibility of attraction of the dust particles of the similar polarity. It then turns out that in dusty plasmas in the vicinity of the Moon, we have long range (in comparison with the dusty plasma Debye radius) attractive forces besides the short range Debye-Hückel-Yukawa repulsive force. This effect can result in the formation of dust clouds over the lunar surface. Furthermore, as it has been shown in the laboratory experiments [74], the dust particle transport in the presence of near-surface electric fields can be important for explanation of the origin of the lunar horizon glow.

6.2 Dusty Plasma Processes in the Vicinity of Titan

Titan, the largest moon of Saturn, has atmosphere and ionosphere which are largely composed of nitrogen, minor components lead to the formation of methane and

ethane clouds and nitrogen-rich organic smog. With its robust nitrogen atmosphere and ionosphere, Titan is viewed as analogous to the early Earth, although at a much lower temperature. The process of dust formation in chemical reactions is inherent in Titan's environment. In particular, dusts in the form of harbor organic aerosols (tholins) are formed from simple molecules, such as methane and nitrogen (CH_4 and N_2) in Titan's atmosphere and ionosphere [75]. Other sources of dust in Titan's atmosphere and ionosphere are evaporated meteor matter and cryovolcanos. As a result, the role of the dust in Titan's ionosphere is even more significant than in the Earth's one. This points out the importance of research of dusty ionospheric plasma of Titan.

6.3 Influence of Dusty Plasma Processes on Primary Earth's Crust, Hydrosphere, and Atmosphere

Theory and the data of comparative planetology as well as the Earth sciences (consistent with each other) enable us to state that the formation of the terrestrial planets occurred during 30–100 million years beginning from an appearance of the first condensate approximately 4.6×10^9 years ago [76]. During the Earth growth the main energy source was related to impacts of cosmic bodies falling to the growing planet. The mass spectrum of the cosmic bodies is considered to be proportional to m^{-q} where $q \approx 1.8 \pm 0.2$. The main mass is concentrated in the bodies with diameters of 100 km and larger. Craters formed as a result of the impact of such large bodies with Earth's surface are estimated to have depths of the order of the Earth's diameter. The matter of the impact generated vapor plume has the mass of the order of the cosmic body (impacting the Earth) while its temperature reaches several electron-Volts. All this matter expands (lifts) with subsequent ionization, cooling, condensation, formation of nano- and microscale dust particles, and their charging. Thus the dusty plasma is formed. The important problem is to determine the characteristic sizes of the dust particles and estimate their mass spectrum because these will allow us to determine behavior of the dust grains: whether they work to the primary Earth's surface or they evolve in the primary atmosphere. This study will allow us to update the scenario of the formation of the primary Earth's crust, hydrosphere, and atmosphere and possibly to modify the scenario of the origin of terrestrial planets.

7 Summary

Important topic of the plasma heliogeophysics research is the nonlinear processes in space and near-Earth dusty (complex) plasmas. Dust particulates are present in space plasmas and in Earth's environments. They strongly affect (by their large

and variable charges) the structuring and transport in dusty (complex) plasmas and result in new qualitative phenomena in nature. Even at relatively small mass density, the dust particulates can be crucial in determining the characteristics of space plasmas and Earth's environments. Future theoretical and laboratory investigations of dust particulates in dusty (complex) plasmas, combined with in situ and remote sensing of the mesosphere, ionosphere, magnetosphere, as well as the solar wind and solar atmosphere, should lead to better understanding of the phenomena studied by the plasma heliogeophysics. New vistas in dusty plasma research important for applications to space and Earth sciences are dusty plasma processes in the system Earth-Moon, in the vicinity of Titan, the largest moon of Saturn, as well as the influence of dusty plasma processes on the origin of the primary Earth's crust, hydrosphere, and atmosphere.

Acknowledgements This work is supported by the Presidium of the Russian Academy of Sciences (the basic research program No. 22 "Fundamental problems of research and exploration of the solar system"), the Division of Earth Sciences of the Russian Academy of Sciences (the basic research program "Nanoscale particles: conditions of formation, methods of analysis and recovery from mineral raw"), the Russian Foundation for Basic Research (grant No. 12-02-00270-a), and the Dynasty Foundation.

References

1. L.M. Zelenyi, I.S. Veselovskii (eds.), *Plasma Heliogeophysics*, vols. 1 & 2 (Nauka, Moscow, 2008) [in Russian]
2. W.K. Tobiska, T. Woods, F. Eparvier, R. Viereck, L. Floyd, D. Bouwer, G. Rottman, O.R. White, J. Atm. Solar Terr. Phys. **62**, 1233 (2000)
3. I.A. Daglis (ed.), *Space Storms and Space Weather Hazards*, NATO Science Series (Kluwer, Dordrecht, 2001)
4. R. Qahwaji, T. Colak, Solar Phys. **241**, 195 (2007)
5. I. Klotz, Space Weather **8**, S05003 (2010)
6. F. Verheest, *Waves in Dusty Space Plasmas* (Kluwer, Dordrecht, 2000)
7. P.K. Shukla, A.A. Mamun, *Introduction to Dusty Plasmas Physics* (Institute of Physics Publishing, Bristol/Philadelphia, 2002)
8. S.V. Vladimirov, K. Ostrikov, A.A. Samarian, *Physics and Applications of Complex Plasmas* (Imperial College Press, London, 2005)
9. V.N. Tsytovich, G.E. Morfill, S.V. Vladimirov, H. Thomas, *Elementary Physics of Complex Plasmas* (Springer, Berlin/Heidelberg, 2008)
10. V.E. Fortov, A.G. Khrapak, S.A. Khrapak, V.I. Molotkov, O.F. Petrov, Phys. Usp. **47**, 447 (2004)
11. V.E. Fortov, A.V. Ivlev, S.A. Khrapak, A.G. Khrapak, G.E. Morfill, Phys. Rep. **421**, 1 (2005)
12. K. Ostrikov, Rev. Mod. Phys. **77**, 489 (2005)
13. A.M. Ignatov, Plasma Phys. Rep. **31**, 46 (2005)
14. S.I. Popel, A.A. Gisko, Nonlinear Proc. Geophys. **13**, 223 (2006)
15. S.I. Popel, S.I. Kopnin, M.Y. Yu, J.X. Ma, Feng Huang, J. Phys. D: Appl. Phys. **44**, 174036 (2011)
16. V.N. Tsytovich, N.G. Gousein-zade, G.E. Morfill, Phys. Plasmas **13**, 033503 (2006)
17. Z.Y. Chen, M.H. Kong, M.Y. Milošević, Y.C. Wu, Phys. Scr. **67**, 439 (2003)
18. Z.Y. Chen, M.Y. Yu, H.Q. Luo, Phys. Scr. **64**, 476 (2001)

19. A.G. Bashkirov, Phys. Rev. E **69**, 046410 (2004)
20. V.N. Tsytovich, G.E. Morfill, Plasma Phys. Rep. **28**, 171 (2002)
21. B. Liu, J. Goree, Phys. Rev. Lett. **94**, 185002 (2005)
22. V.N. Tsytovich, Y.K. Khodatev, R. Bingham, Comments Plasma Phys. Controlled Fusion **17**, 249 (1996)
23. Y.P. Chen, H.Q. Luo, M.F. Ye, M.Y. Yu, Phys. Plasmas **6**, 699 (1999)
24. L. Wang, Comments Plasma Phys. Controlled Fusion **1**, 117 (1999)
25. M.J.S. Belton, Science **151** (3706), 35 (1966)
26. A.W. Peterson, Astrophys. J. **148**, L37 (1967)
27. R.M. MacQueen, Astrophys. J. **154**, 1059 (1968)
28. A.W. Peterson, Astrophys. J. **155**, 1009 (1969)
29. C. Leinert, I. Richter, E. Pitz, B. Planck, Astron. Astrophys. **103**, 177 (1981)
30. I. Mann, A. Krivov, H. Kimura, Icarus **146**, 568 (2000)
31. J.A. Burns, P.L. Lamy, S. Soter, Icarus **40**, 1 (1979)
32. H.A. Zook, O.E. Berg, Planet. Space Sci. **23**, 183 (1975)
33. E. Grün, M. Baguhl, H. Divine, H. Fechtig, D.P. Hamilton, M.S. Hanner, J. Kissel, B.-A. Lindblad, D. Linkert, G. Linkert, I. Mann, J.A.M. McDonnell, G.E. Morfill, C. Polanskey, R. Riemann, G. Schwehm, N. Siddique, P. Staubach, H.A. Zook, Planet. Space Sci. **43**, 953 (1995)
34. A. Wehry, I. Mann, Astron. Astrophys. **341**, 296 (1999)
35. O.L. Vaisberg, V. Smirnov, A. Omelchenko, L. Gorn, M. Iovlev, Astron. Astrophys. **187**, 753 (1987)
36. E.P. Mazets, R.Z. Sagdeev, R.L. Aptekar, S.V. Golenetskii, Y.A. Guryan, A.V. Dyatchkov, V.N. Ilyinskii, V.N. Panov, G.G. Petrov, A.V. Savvin, I.A. Sokolov, D.D. Frederiks, N.G. Khavenson, V.D. Shapiro, V.I. Shevchenko, Astron. Astrophys. **187**, 699 (1987)
37. H. Rickman, in *Solar System Ices* (Kluwer, Dordrecht, 1998), p. 395
38. M. Marconi, D. Mendis, Astrophys. J. **260**, 386 (1981)
39. R.L. Newburn Jr., H. Spinard, Astron. J. **97**, 552 (1989)
40. P.D. Singh, A.A. de Almeida, W.F. Huebner, Astron. J. **104**, 848 (1992)
41. A.D. Storrs, A.L. Cochran, E.S. Barker, Icarus **98**, 163 (1992)
42. T.V. Losseva, A.P. Golub', I.B. Kosarev, S.I. Popel, I.V. Nemtchinov, in *Proc. Conf. Asteroids, Comets, Meteors – ACM2002* (European Space Agency, Noordwijk, 2002), p. 873
43. I.B. Denysenko, K. Ostrikov, S. Xu, M.Y. Yu, C.H. Diong, J. Applied Phys. **94**, 6097 (2003)
44. H. Link, C. Leinert, E. Pitz, N. Salm, in *Interplanetary Dust and Zodiacal Light* (Springer, Berlin, 1976), p. 113
45. Y. Nakamura, H. Bailung, P.K. Shukla, Phys. Rev. Lett. **83**, 1602 (1999)
46. Q.-Z. Luo, N. D'Angelo, R.L. Merlino, Phys. Plasmas **6**, 3455 (1999)
47. M.Y. Yu, H. Luo, Phys. Plasmas **2**, 591 (1995)
48. J.X. Ma, M.Y. Yu, X.P. Liang, J. Zheng, W.D. Liu, C.X. Yu, Phys. Plasmas **9**, 1584 (2002)
49. T.V. Losseva, S.I. Popel, M.Y. Yu, J.X. Ma, Phys. Rev. E **75**, 046403 (2007)
50. S.I. Kopnin, I.N. Kosarev, S.I. Popel, M.Y. Yu, Planet. Space Sci. **52**, 1187 (2004)
51. W.-G. Zhang, J.X. Ma, Y.-R. Li, Y.-B. Zheng, Y.-H. Chen, Planet. Space Sci. **58**, 801 (2010)
52. K. Ostrikov, I.B. Denysenko, S.V. Vladimirov, S. Xu, H. Sugai, M.Y. Yu, Phys. Rev. E **67**, 56408 (2003)
53. I. Denysenko, M.Y. Yu, K. Ostrikov, N.A. Azarenkov, L. Stenflo, Phys. Plasmas **11**, 4959 (2004)
54. K.N. Ostrikov, S.V. Vladimirov, M.Y. Yu, J. Geophys. Res. **104**, 593 (1999)
55. O. Havnes, T. Aslaksen, A. Brattli, Phys. Scr. **T89**, 133 (2001)
56. O. Havnes, in *Dusty Plasmas in the New Millennium* (AIP, Melville, 2002), p. 13
57. V.V. Adushkin, V.P. Kudriavtsev, A.B. Khrustalev, in *Physical Processes in Geospheres: their Manifestations and Interaction* (IDG, Moscow, 1999), p. 217 [in Russian]
58. B.A. Klumov, G.E. Morfill, S.I. Popel, JETP **100**, 152 (2005)
59. B.A. Klumov, S.I. Popel, R. Bingham, JETP Lett. **72**, 364 (2000)
60. P. Czechowsky, I.M. Reid, R. Rüster, Geophys. Res. Lett. **28**, 1475 (1988)

61. O. Havnes, L.I. Nasheim, T.W. Hartquist, G.E. Morfill, F. Melandso, B. Schleiher, J. Troim, T. Blix, E. Thrane, Planet. Space Sci. **44**, 1191 (1996)
62. M. Rapp, F.-J. Lübken, J. Geophys. Res. **108**, 8437 (2003)
63. T.A. Blix, M. Rapp, F.-J. Lübken, J. Geophys. Res. **108**, 8450 (2003)
64. S.I. Popel, M.Y. Yu, V.N. Tsytovich, Phys. Plasmas **3**, 4313 (1996)
65. S.I. Popel, A.A. Gisko, A.P. Golub', T.V. Losseva, R. Bingham, P.K. Shukla, Phys. Plasmas **7**, 2410 (2000)
66. Yu.N. Besedina, S.I. Popel, P.K. Shukla, Doklady Earth Sci. **429**, 1407 (2009)
67. S. Benkadda, D.N. Klochkov, S.I. Popel, Yu.N. Izvekova, Phys. Plasmas **18**, 052306 (2011)
68. S.I. Musatenko, Yu.S. Musatenko, E.V. Kurochka, A.V. Lastochkin, V.Ya. Cholij, O.I. Maksimenko, A.S. Slipchenko, Geomagn. Aeron. **46**, 173 (2006)
69. N.N. Rao, P.K. Shukla, M.Y. Yu, Planet. Space Sci. **38**, 543 (1990)
70. S.I. Kopnin, S.I. Popel, M.Y. Yu, Phys. Plasmas **16**, 063705 (2009)
71. S.V. Vladimirov, V.N. Tsytovich, S.I. Popel, F.Kh. Khakimov, *Modulational Interactions in Plasmas* (Kluwer, Dordrecht, 1995)
72. J.X. Ma, Y. Chen, B. Gan, M.Y. Yu, Planet. Space Sci. **54**, 719 (2006)
73. A.P. Golub', G.G. Dol'nikov, A.V. Zakharov, L.M. Zelenyi, Yu.N. Izvekova, S.I. Kopnin, S.I. Popel, Pis'ma v ZhETF **95**, 198 (2012)
74. X. Wang, M. Horanyi, S. Robertson, J. Geophys. Res. **114**, A05103 (2009)
75. J.H. Waite Jr., D.T. Young, T.E. Cravens, A.J. Coates, F.J. Crary, B. Magee, J. Westlake, Science **316**, 870 (2007)
76. A.V. Vitjazev, G.V. Pechernikova, V.S. Safronov, *Terrestrial Planets: Origin and Early Evolution* (Nauka, Moscow, 1990)(in Russian)

Magnetospheres of the Mercury, Earth, Jupiter, and Saturn

Igor I. Alexeev, Elena S. Belenkaya, and M.S. Grigoryan

Abstract Physical phenomena in the magnetospheres of the solar system planets that have intrinsic magnetic fields: Mercury, Earth, Jupiter, and Saturn, are discussed. As demonstrated by the evaluation of the Mercury, Earth, Jupiter, and Saturn magnetopauses, all these surfaces can be well approached by a paraboloids of revolution with different subsolar distances and flaring angles (Alexeev and Belenkaya, Ann Geophys 23:809–826, 2005; Alexeev et al., Geophys Res Lett 33:L08101, 2006; Joy et al., J Geophys Res 107(A10):1309,2002; Kanani et al., J Geophys Res 115:A06207, 2010). Based on this fact a universal model of the planetary magnetosphere is constructed. We choose the planets in the inner magnetospheres of which the magnetic field vectors have been measured by spacecraft magnetometers. Modifications of general model that are applied to the individual planets are considered. The proposed models describe the basic physical processes which are responsible for the structure and dynamics of the magnetospheres. Additionally to the inner planetary field the different magnetospheric sources of magnetic field are included in the model.

1 Introduction

Magnetopause is a boundary formed between the planetary magnetic field and the shocked solar wind, separating the solar wind plasma from the planetary plasma. The shape and location of a planetary magnetopause can be determined by balancing the solar wind dynamic pressure with the magnetic and thermal pressures found inside the boundary. In this paper we discuss the works on the planetary

I.I. Alexeev (✉) · E.S. Belenkaya · M.S. Grigoryan
Scobeltsyn Institute of Nuclear Physics, Lomonosov Moscow State University, Leninskie Gory, 119991, Moscow, Russia
e-mail: alexeev@dec1.sinp.msu.ru; elena@dec1.sinp.msu.ru; grg@dec1.sinp.msu.ru

Alexeev, I.I. et al.: *Magnetospheres of the Mercury, Earth, Jupiter, and Saturn*.
Astrophys Space Sci Proc. **33**, 209–216 (2012)
DOI 10.1007/978-3-642-30442-2_23, © Springer-Verlag Berlin Heidelberg 2012

magnetopause shapes [4,6,11,15,16,18,19] and use the universal model of planetary magnetopause.

Using a Newtonian form of the pressure balance equation, the stand-off distance is estimated as a size-pressure dependence described by a power law $D_P^{\alpha_m}$. This exponent is consistent with that one derived from the numerical magnetohydrodynamic simulations. The power low index α is estimated as $\alpha_E = -1/6.6$ for Earth [18], $\alpha_J = -1/4$ for Jupiter [5, 14], and $\alpha_S = -1/5$ for Saturn [16]. The similar function for Mercury is not determined till now. Many spacecraft launched over the past 55 years measured directly magnetic fields of the solar system planets. It was found that Venus and Mars do not have magnetic fields, while Mercury, Jupiter, Saturn, Uranus, and Neptune – have their intrinsic magnetic fields like the Earth. The magnetic field deflects the incident supersonic plasma flow of the solar wind and forms the magnetosphere, a region which is free (or almost free) from the solar wind plasma. Voyager two was the only spacecraft which flyby Uranus and Neptune, and we have no enough data so far to check models on the observed structures of their magnetospheres [13]. So, further we shall confine ourselves to the magnetized planets Mercury, Earth, Jupiter, and Saturn. It is natural that the Earth's magnetosphere has been studied using numerous spacecraft in much more detail in the past years than the magnetospheres of distant planets.

2 Magnetospheres of the Earth, Jupiter, and Saturn

Magnetospheric magnetic field paraboloid model originally constructed by Alexeev et al. ([1] and references therein) for the Earth's magnetosphere, was later developed for Mercury [4], Jupiter [5, 7], and Saturn [2]. The primary purpose of this paper is to modify the existing paraboloid model of the Earth's magnetospheric magnetic field incorporating the differing magnetopause flaring [8] for Mercury, Jupiter, and Saturn [6]. The planetary magnetosphere, as well as the terrestrial one, undergoes expansion and compression, particularly, due to a change in the solar wind dynamic pressure. The concept of the dependence of the Earth's magnetopause location on the dynamic pressure of the solar wind was first introduced by Chapman and Ferraro [9].

The dependence of the Jupiter's magnetospheric boundary location (in particular, the distance of the jovian subsolar magnetopause, R_{ss}) on the solar wind dynamic pressure, p_{sw}, was investigated in [14, 17]. In good agreement with results of [19], it occurred that R_{ss} depends on p_{sw} in the power -0.22 ± 0.04. Results presented in [14] were summarized by the empirical formula [10]

$$R_{ss} = 35.5 R_J / {p_{sw}}^{0.22} (\text{nPa}) . \tag{1}$$

According to [5] the Jupiter's magnetospheric size is proportional to $p_{sw}^{-0.23}$. All these expressions show more strong dependence than for the dipole magnetosphere, when R_{ss} is proportional to $p_{sw}^{-1/6}$ (as in the case of the Earth). Huddleston et al. [14] noted that in the jovian magnetosphere, the hot internal plasma gives

significant contribution to the pressure balance which determines the location of the magnetopause. In addition, the activity of the volcanoes of Io is episodic, so this process can also influence on the jovian magnetospheric size. According to observations by spacecraft, in the jovian environment, R_{ss} changed from 45 R_J to 110 R_J. However, for each value of R_{ss}, different distances from the planetary center to the magnetopause in the direction perpendicular to Jupiter–Sun line (X axis) could exist.

The paraboloid model of the Earth's magnetosphere has a modular structure. The scaling relations allow to adapt the magnetopause and the tail current systems developed for the Earth's magnetosphere to the case of Mercury, Jupiter, and Saturn. However, for the currents caused by the rapid planetary rotation (magnetodisc for Jupiter and Saturn) there is no analogy in the terrestrial magnetosphere. Magnetodisc is the main source of the Jupiter's magnetospheric magnetic field. Its effective magnetic moment prevails the Jupiter's dipole magnetic moment (in ∼2.6 times [5, 7]).

Here we investigate various flaring of the planetary magnetopause and generalize the geodipole screening current field for the case of Mercury, Jupiter, and Saturn. From the known boundary conditions, a solution of Laplace equation for the scalar potential of the magnetopause current magnetic field will be obtained.

Based on the knowledge of the Earth's magnetosphere where flaring changes significantly with variations in the solar wind parameters and interplanetary magnetic field, we can suggest that other planetary magnetospheres will show the same behavior (till now there are not enough measurements to make a definite conclusion about changes in the magnetopause flaring angle). In the Earth's magnetosphere such behavior is caused by the dependence of the current sources inside the magnetosphere on the solar wind density, velocity, and magnetic field. Moreover, own magnetospheric dynamics may also play an essential role. In the Jupiter's case the inner magnetospheric sources are more intense in comparison with the Earth's ones. Thus, the changes in the currents inside the magnetosphere should result in significant changes in the magnetopause flaring.

The result of calculations for different flaring angles for the planetary magnetospheres which include the dipole field and the field of the magnetopause currents screening it, is shown in Fig. 1.

The magnetic field in the model is calculated using the separation of variables in paraboloid coordinates while solving the Laplace equation [6, 7]. The most simple way to take into account possible changes in the magnetopause flaring in the paraboloid model is to make changes in the coordinate system [12]:

$$x = \frac{R_1}{2}\left(\beta^2 - \alpha^2 + \gamma^2\right), \quad y = R_1\alpha\beta\sin\varphi, \quad z = R_1\alpha\beta\cos\varphi, \tag{2}$$

here the X axis is directed toward the Sun, the XZ surface contains the planetary dipole, φ is the azimuth angle around the X axis, γ is a dimensionless constant that is a measure of the magnetopause expansion, and R_1 is the radius of the magnetopause curvature in the subsolar point. The dimension scale $R_1 = \frac{2R_{ss}}{\gamma^2+1}$ is determined by

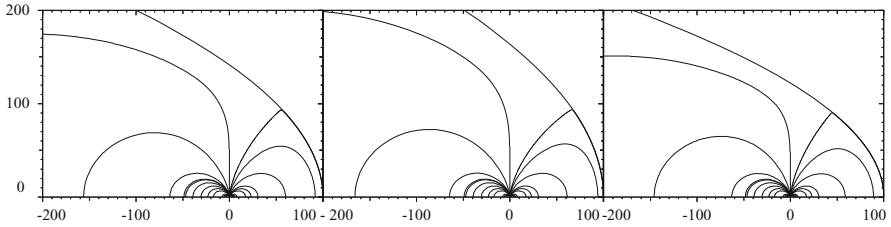

Fig. 1 The planetary dipole magnetic field screened by the magnetopause currents for different values of the magnetopause flaring. From *left* to *right*: Earth case $\gamma = 1$, the axis tips scale is 0.1 R_E; Saturn case $\gamma = 0.67$, the axis tips scale is 0.22 R_S; and Jupiter case $\gamma = 1.25$, the axis tips scale is 1 R_J

R_{ss} and a flaring parameter γ:

$$\gamma = \sqrt{\frac{4R_{ss}^2}{{R_T}^2} - 1}\ , \quad R_{ss} = 0.5\ R_1\ (1+\gamma^2), \text{ and } \quad \frac{R_T}{R_{ss}} = \frac{2}{\sqrt{1+\gamma^2}}, \quad (3)$$

which represents the dimensionless flaring of the paraboloid of revolution considered as the magnetopause when $\beta = 1$. The coordinates α, β, φ are the parabolic coordinates connected with the solar-magnetospheric coordinates x, y, z by expressions (2). The flaring parameter γ is determined by $R_T = y|_{x=0}$ which is the distance from the planet's center to the magnetopause at $x = 0$ in the dawn–dusk direction. For $\gamma = 1$ we have an ordinary (with average flaring) terrestrial magnetosphere in the paraboloid model. For this case the dimension scale R_1 is equal to R_{ss}, and $R_T = \sqrt{2}R_{ss}$. For $\gamma > 1$ ($\gamma < 1$) the flaring angle is smaller (higher). The equation of the magnetopause (the surface $\beta = 1$) is given by the paraboloid of revolution in the Cartesian coordinate system:

$$\frac{x_{mp}}{R_{ss}} + \frac{y_{mp}^2 + z_{mp}^2}{R_T^2} = 1. \quad (4)$$

The paraboloid model of the magnetosphere is based on the assumption that a magnetospheric field can be described by a planetary dipole supplemented by two current systems. One of them corresponds to the magnetopause currents that shield the dipole field and the magnetic field component normal to the magnetopause becomes equal to zero. Another current system corresponds to the tail currents. These create a magnetic field tangential to the magnetopause and form two bundles of field lines coming from opposite directions. The current layer in the magnetospheric tail separates the northern and southern tail parts, in which opposite bundle of magnetic field lines are almost parallel to each other. The tail currents form a theta shaped current in the nightside sector of the magnetosphere. The described model of the magnetosphere received the name *paraboloid* due to the

Table 1 Planetary magnetosphere parameters

Parameters (units)	Equation	Mercury	Earth	Jupiter	Saturn
Heliocentric distance (AU)	r_0	0.38	1	5.2	9.5
Equatorial radius ($R_E = 6,371\,km$)	R_p	0.38	1	11.2	9.45
Magnetic moment ($T \cdot km^3$)	$B_0 \cdot R_P^3$	$2.8\,10^{-6}$	0.008	150.	4.6
Dipole tilt angle (degrees)	ψ	0°	10.5°	10°	0°
Equatorial magnetic field (μT)	B_0	0.196	30.	420.	20.
Dipole hemisphere magnetic flux (GWb)	$2\pi B_0 R_p^2$	0.0072	7.7	13, 450	456.
Open field line magnetic flux (GWb)	$\pi B_0 R_p^2 \frac{R_p}{R_{ss}}$	0.0024	0.42	450	11.4
Polar oval radius (degrees)	$\sin\theta = \sqrt{\frac{R_p}{R_{ss}}}$	55°	20°	15°	13°
Average IMF magnitude (nT)	$\frac{5\sqrt{1+r_0^2}}{\sqrt{2}\cdot r_0^2}$	10.2	5	1	0.5
Nominal Parker spiral angle ϕ	$\tan\phi = \frac{1}{r_0}$	20.8°	45°	80°	85°
Solar wind ram pressure (nPa)	$\frac{1.7}{r_0^2}$	11.8	1.7	0.07	0.015
Subsolar magnetic field magnitude (nT)	$B_{ss} = \frac{74.5}{r_0}$	196	74.5	14.3	7.8
Subsolar magnetopause distance (R_P)	R_{ss}	1.4 R_M	10 R_E	70 R_J	22 R_S
Magnetopause flaring parameter	$\gamma = \frac{\sqrt{4R_{ss}^2 - R_T^2}}{R_T}$	1.	1.	1.25	0.66
Nose magnetopause curvature radius (R_P)	$\frac{2R_{ss}}{1+\gamma^2}$	1.4 R_M	10 R_E	55 R_J	31 R_S
Terminator magnetopause radius (R_p)	R_T	2. R_M	14 R_E	112 R_J	37 R_S

shape of the surface, a paraboloid of revolution, approximating the magnetopause [1]. The dimensions of planetary magnetospheres may vary by a factor of several thousand (see Table 1), but different planets have similarly shaped magnetopauses. The front part of the magnetosphere coincides with the paraboloid of revolution, which has a symmetry axis that is a line joining the planet and the Sun. The magnetic field at the subsolar point can be determined from the balance of the solar wind plasma dynamic pressure and the pressure of the magnetic field inside the magnetosphere. This field does not depend on the value of the planetary dipole and is determined unambiguously by the solar wind dynamic presssure. The planetary

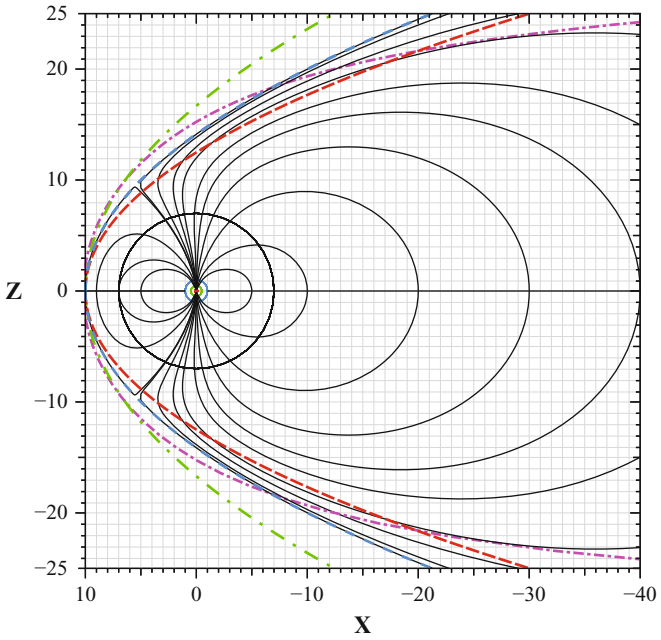

Fig. 2 The Mercury and Earth magnetospheric *field lines* are shown for the dipole and screening magnetopause currents in the noon – midnight plane for general magnetospheric model. All planetary magnetopauses are scaled to R_{ss} and one tip on *horizontal axis* is 0.1 R_{ss} ($R_{ss} = 10.$). *Biggest circle* shows the Mercury with radius, $R_M = R_{ss}/1.4 = 7.$. The Earth's surface with radius $R_E = R_{ss}/10 = 1.$, the Saturn's surface with radius $R_S = R_{ss}/22 = 0.45$, and Jupiter with radius $10./70. = 0.14$ are shown. The flaring parameters γ are equal to 1.25 and 0.66 for Jupiter and Saturn, correspondingly

dipole determines the size of the magnetosphere, R_{ss}. For Jupiter's and Saturn's magnetospheres the equatorial magnetodiscs are formed by the rotational uploading of the satellite's plasma. As a result, R_{ss} is determined not by the planetary dipole only, but by some "effective" dipole which is bigger than the planetary one.

The Mercury and Earth magnetic field lines for the dipole and screening magnetopause currents without the tail current field are shown in Fig. 2 in the noon – midnight plane for the general magnetospheric model. All planetary magnetopauses are scaled to R_{ss}. Circles in Fig. 2 show the Mercury (light black circle), the Earth (blue circle), the Saturn (green circle), and Jupiter (red circle). Because the paraboloids of the revolution in the chosen coordinate system are the same for both Mercury and Earth planets (blue dashed curve), the magnetic field lines (black curves) are coincided. The yellow curves are marked by the magnetic fild lins which go to the cusp (the neutral points). The magnetopause of Jupiter (dashed red curve) is more compressed to the $X-$ axis comparable to the Earth's magnetopause. The magnetopause of Saturn (dot-and-dashed green curve) is more

expanded comparable to the Earth's case. The best fit magnetopause obtained by Shue et al. [18] is shown in Fig. 2 by the dashed purple curve.

The strength of the currents at the magnetopause and those in the tail depends on the magnetic moment of the "effective" planetary dipole and on the character size of the magnetosphere. The comparison of the results obtained in the model with the observational data for Mercury shows that the two abovementioned current systems suffice to describe their magnetospheric field. For Earth, Jupiter, and Saturn, the ring current in the inner magnetosphere is significant. Different planets have ring currents of different natures. Near Earth, the ring current is formed by the trapped particles; ring current enhancement mostly determines the depression of the equatorial field during geomagnetic storms. In the case of Jupiter, this current is included into a plasma disc that is formed by the ionized eruptions from Io's volcanoes. The fast rotation of Jupiter drives and accelerates cool plasma, which is thrown into the outer magnetosphere. As the magnetic moment of the plasma disc is more than twice exceeds the magnetic moment of Jupiter, the size of the Jovian magnetosphere is almost two times bigger than the size of the magnetosphere formed around the planetary dipole only. The pressure of the magnetospheric jovian plasma is equal to the magnetic field pressure near the noon magnetopause. Saturn and Jupiter rotate at similar angular rates. The sizes of both planets are also close to each other. The planetary magnetic field of Saturn, however, is almost 20 times weaker than that of Jupiter. Therefore, the 'dipole enhancement effect' is considerably weaker for Saturn than for Jupiter, and the plasma disc of Saturn enhances its effective magnetic moment by a factor of 1.2–1.5.

3 Conclusions

In the present paper the general paraboloid magnetospheric model was constructed on the base of the terrestrial one [1]. We took into account changes of the magnetopause shape, introducing a new parameter γ, characterizing a flaring. This model was specified for the Mercury, Jupiter, and Saturn magnetospheres. The model results demonstrated good agreements with in situ magnetometer data by – MESSENGER [3,4], Ullyses [5], and Cassini [2] flybys by the planets.

The high solar wind plasma conductivity prevents the penetration of the magnetic field caused by the internal magnetospheric sources into the magnetosheath. We have demonstrated the method to calculate more accurately the planetary dipole screening magnetopause current field, which allows us to use the presented model more efficiently.

Acknowledgements Work was supported by the RFBR Grants No 11-05-00894. The authors are thankful to the European FP7 project IMPEx (No.262863) for partial support. I.I. Alexeev and E.S. Belenkaya acknowledge the subdivisions of the European research infrastructure EUROPLANET-RI, – the JRA3/EMDAF (European Modelling and Data Analysis Facility; http://europlanet-jra3.

oeaw.ac.at) and Science Networking NA2 (working groups WG4 and WG5; https://europlanet-scinet.fi) for support of their scientific communication and collaboration exchange visits.

References

1. Alexeev, I. I., The penetration of interplanetary magnetic and electric fields into the magnetosphere. *J. Geomag. Geoelectr.*, **38**, 1199–1221, 1986.
2. Alexeev, I. I., et al., A global magnetic model of Saturn's magnetosphere, and a comparison with Cassini SOI data. *Geophys. Res. Lett.*, **33**, L08101, doi:10.1029/2006GL025896, 2006.
3. Alexeev, I. I., E. S. Belenkaya, et al., Mercury's magnetospheric magnetic field after the first two MESSENGER flybys, *Icarus*, **209**, 23–39, doi: 10.1016/j.icarus.2010.01.024, 2010.
4. Alexeev, I. I., et al., Paraboloid model of Mercury's magnetosphere, *J. Geophys. Res.,* **113**, A12210, doi:10.1029/2008JA013368, 2008.
5. Alexeev, I. I., and E. S. Belenkaya, Modeling of the jovian magnetosphere. *Ann. Geophys.*, **23**, 809–826, 2005.
6. Arridge, C. S., et al., Modeling the size and shape of Saturn's magnetopause with variable dynamic pressure, *J. Geophys. Res.,* **111**, A11227, doi:10.1029/2005JA011574, 2006.
7. Belenkaya, E. S., The jovian magnetospheric magnetic and electric fields: effects of the interplanetary magnetic field, *Planet. Space Sci.,* **52**, 499–511, 2004.
8. Belenkaya, E. S., et al., A model of Jupiter's magnetospheric magnetic field with variable magnetopause flaring, *Planet. Space Sci.,* **53**, 863–872, 2005.
9. Chapman, S., and V.C.A. Ferraro, A new theory of magnetic storm, *J. Geophys. Res.,* **36**, 77, 1931.
10. Cowley, S.W.H., and E. J. Bunce, Modulation of Jupiter's main auroral oval emissions by solar wind induced expansions and compressions of the magnetosphere, *Planet. Space Sci.,* **51**,57–79, 2003.
11. Fairfield, D. H., Average and unusual locations of the Earth's magnetopause and bow shock, *J. Geophys. Res.,* **76**, 6700, 1971.
12. Greene, J. M., and R. L. Miller, The field of a screened magnetic dipole, *Planet. Space Sci.,* **42**, 895–900, 1994.
13. Herbert, F., Aurora and magnetic field of Uranus, *J. Geophys. Res.,* **114**, A11206, doi: 10.1029/2009JA014394, 2009.
14. Huddleston, D. E., et al., Location and shape of the jovian magnetopause and bow shock, *J. Geophys. Res.,* **103**, No E9, 20075–20082, 1998.
15. Joy, S. P., et al., Probabilistic models of the jovian magnetopause and bow shock locations, *J. Geophys. Res.,* **107**, No A10, 1309, doi:10.1029/2001JA009146, 2002.
16. Kanani, S. J., et al., A new form of Saturn's magnetopause using a dynamic pressure balance model, based on in situ, multi-instrument Cassini measurements, *J. Geophys. Res.,* **115**, A06207, doi: 10.1029/2009JA014262, 2010.
17. Kivelson, M. G., and D. J. Southwood, First evidence of IMF control of Jovian magnetospheric boundary locations: Cassini and Galileo magnetic field measurements compared, *Planet. Space Sci.,* **51**, 891–898, 2003.
18. Shue, J.-H., et al.,Magnetopause location under extreme solar wind conditions, *J. Geophys. Res.,* **103**, No A8, 17961–17700, 1998.
19. Slavin, J. A., et al., Solar wind flow about the outer planets: Gas dynamic modeling of the Jupiter and Saturn bow shocks, *J. Geophys. Res.,* **90**, 6275–6283, 1985.

Location of the Inner Edges of Astrophysical Discs Related to the Central Object

Elena S. Belenkaya, Igor I. Alexeev, and Maxim L. Khodachenko

Abstract The accreting ionized gas surrounding a neutron star or white dwarf creates an accretion disc. Radius R_A (the Alfven radius), where the magnetic energy density is equal to the kinetic energy density is an inner boundary of a disc. Accretion disc in a binary system and around a black hole is disrupted at a radius R_A. The heliospheric current sheet's inner edge is also located at the solar Alfven radius. The inner edges of Jupiter and Saturn discs are located close to their Alfven radii determined by the plasma azimuthal velocities. Due to the star-exoplanet interaction, a magnetosphere with a magnetodisc arises around the magnetized extrasolar planet placed in close orbit about the host star ("Hot Jupiter"). The distance to disc's inner edge from the center of the host star is a key parameter of the exoplanet magnetospheric model. It determines the disc's magnetic moment, and as a consequence, the total magnetospheric magnetic field and the character size of the magnetosphere. Here we discuss the exoplanet's disc inner edge location at R_A in a context of other astrophysical discs and emphasize that for definite parameters (existence of a strong magnetic field, for example) a lot of them also have location of their inner edges at the Alfven radii independent of nature of their origin, of the disc's material, and of the motion direction in the disc, which means that a large class of discs is well described by the MHD theory.

E.S. Belenkaya (✉) · I.I. Alexeev
Institute of Nuclear Physics, Moscow State University, Leninskie Gory, 119991, Moscow, Russia
e-mail: elena@dec1.sinp.msu.ru; alexeev@dec1.sinp.msu.ru

M.L. Khodachenko
Space Research Institute, Austrian Academy of Sciences, A-8042, Graz, Austria
e-mail: maxim.khodachenko@oeaw.ac.at

Belenkaya, E.S. et al.: *Location of the Inner Edges of Astrophysical Discs Related to the Central Object*. Astrophys Space Sci Proc. **33**, 217–226 (2012)
DOI 10.1007/978-3-642-30442-2_24, © Springer-Verlag Berlin Heidelberg 2012

1 Introduction

Magnetospheric magnetic field paraboloid model originally constructed by I. Alexeev [2] for the Earth's magnetosphere, was later developed for Mercury [5], Jupiter [3,9], Saturn [4,10,11], and "Hot Jupiters" – the tidally locked close-in giant exoplanets [27]. In [27] the exoplanet's magnetospheric equatorial disc surrounding the planet was introduced. This disc significantly enlarges the magnetospheric size and magnetic field. The magnetodisc-dominated magnetospheres in most cases appear to be large enough to protect exoplanets against of destructive action of the stellar wind plasma flows.

Location of the inner edge of magnetodisc around a magnetized exoplanet is very important, in particular, it determines the substellar magnetopause distance from the exoplanet's center which is a scale of the magnetosphere, and magnetodisc's magnetic field which can give significant contribution to the total magnetospheric field [27]. It was proposed that magnetodisc's inner edge coincides with the Alfven radius, R_A, in the equatorial exoplanet magnetosphere, while its outer edge is close to the magnetopause substellar distance. Alfven radius is the characteristic radius at which the magnetic energy density is equal to the kinetic energy density.

In this paper we consider several kinds of discs surrounding different celestial bodies and note that many of them for definite parameters, in the presence of magnetic field, have the inner edges at the Alfven radii independent of the nature of their origin, of the motion direction inside the disc, of the sort of material in the disc, and of plasma behavior outside the disc. The other types of discs for which the inner edges do not coincide with the Alfven radii also exist (for example, discs around stars, white dwarfs, or neutron stars with weak or without magnetic fields, the cold matter which was initially at rest without magnetic field undergoing free radial equatorial infall to the non-rotating black hole, etc.), but here we pay the main attention to a large group of discs possessing this feature. We emphasize that location of the inner disc's boundary at the Alfven radius occurs in numerous forms in the universe. Below we shortly consider a large class of astrophysical objects possessing discs.

2 Discs Around Neutron Stars, Pulsars and White Dwarfs

Neutron stars arise as a result of gravitational collapse (usually during a supernova explosion) of cores of normal stars with masses 1.4–3 M_{Sun} after exhaustion of all thermonuclear energy sources ($M_{Sun} = 2{\cdot}10^{30}$ kg is a solar mass). Pulsar is a rapidly rotating (the speed period 0.1–5 s) small (its radius is 10–20 km), extremely dense ($\sim 10^{17}$ kg m^{-3}) neutron star that emits brief, sharp pulses of energy. Pulsar has very strong magnetic field (10^{11}–10^{15} G) and beams of radiation are emitted along its magnetic axis which does not coincide with the spin axis. Radio-pulsars is the mostly numerous class of pulsars. Most of radio pulsars are single neutron stars [12]. There are a group of pulsars called millisecond pulsars with spin period

1–10 ms and magnetic field 10^8–10^9 G; about half of millisecond pulsars are in binaries – binary star systems containing two stars that orbit around their common center of mass (observations and theory of binary star systems are described e.g. in [17–19]. If in a binary system one star is a neutron star, a period of pulsar is a spin period of accreting neutron star.

Following a supernova explosion, some part of the ejected matter may remain bound to the remnant and fall back forming a disc surrounding the remnant star. Some of neutron stars possess accretion discs, while the others are accreting directly from a stellar wind. A disc can form if its specific angular momentum l exceeds the Keplerian value at the surface of a newly formed neutron star, $l_K = (GM_* R_*)^{1/2}$, where M_* is the mass of the star and R_* is its radius, G is Newton's gravitational constant ($G = 6.673 \cdot 10^{-11} \cdot \mathrm{m}^3 \cdot \mathrm{kg}^{-1} \cdot \mathrm{s}^{-2}$).

The behavior at the inner edge of the accretion disc depends on the neutron star's magnetic field. In the case of a neutron star without magnetic field, the disc extends to its surface. Ghosh and Lamb [24, 25] described the interaction of a dipolar stellar magnetic field penetrating a surrounding disc. They found that the inner edge of the disc is located where the integrated magnetic stress acting on the disc becomes comparable to the integrated material stress associated with plasma inward radial drift and orbital motion (at Alfven radius). Later Cheng et al. [16] stated that in the neutron star-accretion disc system the inner edge of the disc is of the order of R_A.

Accretion to a rotating neutron star whose magnetic field dipole axis does not coincide with the axis of rotation can lead to the phenomenon of an X-ray pulsar [31]. Zhang and Dai [36] noted that disc around magnetars (neutron stars with magnetic field $> 10^{15} - 10^{16}\,G$) is viscously stable outside the Alfven radius. They showed that the thermally-driven outflow wind can also exist in the magnetized discs beyond the Alfven radius, where the matter pressure dominates over the magnetic pressure. A strong magnetic field inside the Alfven radius causes the accretion flow to co-rotate with the stellar field. Bednarek [7] studied magnetar and a massive companion star of the O, B type inside close binary system. It was assumed that mass from the stellar wind is captured by the magnetar in the propeller phase. The distance at which the magnetic field starts to dominate the dynamics of the in-falling matter was estimated as the Alfven radius. The matter in this region is very turbulent and strongly magnetized providing acceleration of electrons up to TeV energies which leads to production of gamma-ray emission. Plasma accelerated to very high velocities, brakes dawn near the neutron star surface wich leads to increasing of plasma temperature up to $\mathrm{T} \geq 10^7 - 10^8$ K [26]. As a result, emission not only in γ, but also in the UV, and mainly X-ray diapasons arises.

If the magnetic field of a neutron star is weak or absent, material from the inner parts of disc reaches the neutron star equatorial region, forming at its surface a hot boundary layer where thermo-nuclear reactions may occur. It could lead to short powerful irregular X-ray flashes (an X-ray burster of first type). Quickly rotating magnetized neutron star without accretion could act as a radio pulsar emitting short periodic impulses due to transformation in a strong magnetic field of rotation energy into the energy of radio emission. In models for disc accretion onto magnetized objects, the inner radius R_0 of the Keplerian disc is conventionally expressed in the

form $R_0 = \xi R_A$ (R_A is for spherical accretion) and the parameter ξ (depending on the fraction of the star's magnetic flux threading the disc) is usually taken to be 0.5 (e.g., [23]). Application of the beat frequency model to binary X-ray pulsars showing quasi-periodic oscillations suggests strongly that for these objects the stellar dipole field essentially fully threads the disc and $\xi \cong 1$ [34] and plasma velocity in the inner part of accretion disc could be close to the light velocity (c). Eksi and Alpar [21] found that the position of the inner radius of a thin disc around radio pulsar can be estimated by comparing the electromagnetic energy density generated by the neutron star as a rotating magnetic dipole in vacuum with the kinetic energy density of the disc. In the inner zone, inside the light cylinder, the electromagnetic field is essentially the dipole magnetic field, and the disc inner radius is the conventional Alfven radius, which is a stable equilibrium point.

Bednarek and Pabich [8] studied high-energy processes in the intermediate polar cataclysmic variables. These objects have been recently established by the INTEGRAL (observatory at the near-Earth orbit) as a class of the hard X-ray sources with evidences of non-thermal components. Rather often cataclysmic variables (CVs) are white dwarfs within compact binary systems which accrete matter from companion normal stars. Stars with $M_* < 1.4 M_{Sun}$ become white dwarfs after they have exhausted their nuclear fuel. In intermediate polar systems, the accretion disc is disrupted by the magnetic field of its white dwarf star. The accretion process can occur in different modes depending on the strength of the surface magnetic field of the white dwarfs, the accretion rate and the angular momentum of matter. Specific modes correspond to different types of accreting white dwarf systems such as polars (direct accretion on to a magnetic pole), intermediate polars (accretion on to a magnetic pole from the accretion disc) and nonmagnetic white dwarfs (the accretion disc extends to the surface of the white dwarf). The physical processes in CVs are expected to be similar to those observed in the X-ray binaries containing accreting neutron stars [8]. Bednarek and Pabich [8] also used the equation $R_0 = \xi R_A$ and at R_0 they assume $\xi = 1$ for the chosen parameters in their model. Thus, the inner edges of the discs around magnetized neutron stars, the X-ray pulsars, radio pulsars, and white dwarfs with intrinsic magnetic field are located near Alfven radii.

Stars with mass $> 3 M_{Sun}$ after they have exhausted their nuclear fuel are transferred to black holes. Ginzburg [26] noted that quasar (quasi-stellar radio source) or galactic nuclear also could evolve to black hole under certain conditions. The structure of magnetic fields in discs around magnetized white dwarfs, neutron stars or magnetars are very different from their black hole counterparts [36], because the intrinsic magnetic field of black hole is absent beyond the horizon of events.

3 Discs Around Black Holes and in the Close Binary Systems

Gravitational field of the black hole is so large that all radiation and matter is limited inside the horizon of events. The radius of the event horizon of a non-rotating uncharged (Schwarzchild) black hole is equal to gravitation or Schwarzchild radius

$R_G = 2GM_*/c^2$. For rotating black hole the event horizon radius is less than R_G. Methods and results of searching for stellar mass black holes in binary systems and supermassive black holes in galactic nuclei of different types are described by Cherepashchuk [20]. Bochkarev and Gaskell [14] also analysed methods for estimation of supermassive black hole masses. Beyond R_G gravitational field of black hole exists and gas falling on a black hole generates a rapidly spinning disc. Gas in the disc has a very high temperature which could lead to strong X-ray generation. Under certain conditions gas near black hole may become turbulent, magnetic field in it growths, and the particle acceleration and synchrotron emission could arise [26].

The black hole has no intrinsic magnetic field out of its horizon, but magnetic field can be generated by plasma which surrounds the black hole and forms the accretion disc. Interaction of disc's rotation with electromagnetic fields can give rise to appearance of sub-light narrow and very long jets starting from the black hole poles. The last stable circular orbit for the pseudo-Newtonian potential is located at $3R_G$. Shakura and Sunayev [31] considered that for the Schwarzschild black holes the inner edge of the disc is at $3R_G$, as near the black hole at $R < 3R_G$, stable circular orbits are not possible and the material motion acquires a radial character without transport of angular momentum and without any external observable effects. However, Tomsick et al. [33] have studied the stellar mass black holes at high luminosities, including GX 339–4, and reported that R_0 less than the radius of the innermost stable circular orbit for a non-rotating black hole have been measured.

In a close binary system including visible star and black hole, the outflow of matter from the surface of the visible star and its accretion by the black hole should lead to the appreciable observational effect: the gas can release a large amount of energy. If the matter undergoes free radial infall (if it was initially at rest and there was no magnetic field), the cold matter accretes to the black hole without any energy release or observational effects [35]. However, in a binary system, in which the matter flowing out from the normal star falls on the black hole with considerable angular momentum the situation is different. If the companion star fills its Roche equipotential lobe, a narrow stream of gas escapes the star through the inner Lagrangian (L1) point. The outward transfer of the angular momentum of the accreting matter leads to formation of a thin disc around the black hole. In the disc the gas moves in Keplerian orbits, however, viscous dissipation slowly taps energy from the bulk orbital motion, and viscosity transports angular momentum outward. As a result, the gas gets hotter as it moves deeper into the gravitational field of the black hole. Near the black hole the disc terminates. Due to the energy release of the system there, the black holes could be found among the optical objects and X-ray sources [31]. In the presence of strong magnetic field (supported, for example, by currents in external gas) and in the case of a rapidly rotating black hole, the spin/electromagnetic effects not only drive relativistic jets, but also may modify the spectrum of the inner accretion disc. The power of a relativistic jet is taken from the magnetic field of an accretion disc and from the rotating black hole. Observations indicate that accretion disc instabilities may be related to jet ejection.

The observed speed of more than $0.9\,c$ can be achieved in general by magneto-hydrodynamic acceleration [22]. As a consequence, the acceleration takes place predominantly across the Alfven point as expected from MHD theory. Kuperus [28] considering a binary system in which accretion disc originates when mass overflow occurs from the primary star onto the compact star, noted that when the compact star is a neutron star or a black hole the inner parts of the thin disc extend to the R_A respectively a few times the Schwarzchild radius. The inner edge of the stellar mass black hole disc moves sharply outward as the luminosity decreases [33]. This fact allowing for the possibility that the inner disc is replaced by magnetically dominated accretion flows, for example, also supports this paradigm.

4 Galactic Discs

Galactic disc containing gas, dust, and stars and orbiting the galaxy's centre is the major element of spiral, lenticular, and some irregular galaxies. The thickness of the disc is small in relation to its diameter. The formation of a star occurs in a star-forming region located mainly in the disc. Alfven proposed that a protogalaxy behaves like a protostar, transferring away angular momentum. A galactic circuit, in which galaxy field-aligned current should be $10^{17} - 10^{19} A$ and the closure currents flow on the plane of the galaxy and out along the axis of rotation was proposed [6].

Most galaxies with active nuclei (AGNs) host supermassive black holes with masses $\sim 10^6 - 10^{10}$ solar masses (quasars) at their centers. Very active quasar could emit more energy than its galaxy. For explanation of this phenomenon the non-spherical accretion to the supermassive black hole was suggested. Emitted by the AGN energy could be taken from the black hole rotation and from the accreting material [12]. The center of our Galaxy (Milky Way) is located in the direction of the constellation Sagittarius. As the dust becomes thicker to the center of the Galaxy, this region is usually studied in radio waves and in infrared light. Observation of 22 GHz H_2O maser in Sgr A West located near the inner edge of the circumnuclear disc within 2 pc of the center of our Galaxy was reported [29]. Water maser emission at 22 GHz has been detected from more than hundred extragalactic AGNs.

Seyfert galaxies (spiral or barred-spiral galaxies with a bright compact nucleus) exhibit a strong continuum from IR through X-ray regions of the spectrum. In some Seyfert galaxies the very asymmetric profile of the iron Kα line suggests that the emission arises in the innermost region of a relativistic accretion disc. Velocity near the inner edge of accretion disc is close to c. The iron lines provide a measurement of R_0 because they are Doppler broadened due to relativistic motion of the accretion disc material and gravitationally redshifted due to the black hole's gravitational field. Broad iron lines have been seen from both stellar mass and supermassive black holes. Tomsick et al. [33] studied the location of the inner edge of the accretion disc using iron emission lines that arise due to fluorescence of iron in the disc, and these indicate that the inner edge of the accretion disc is occurred to be close to the black hole at high and moderate luminosities, while

for low luminosity it significantly increases. Variations of geometrical and physical characteristics of innermost regions of AGN were analyzed in [13]. Camenzind [15] noted that discs in quasars extend most probably down to the marginally stable orbit, while in intermediate luminosity objects, like radio galaxies and normal Seyfert 1 galaxies, the disc most likely exists at distances of a few tens to a few hundreds of Schwarzschild radii.

Beskin [12] noted that usually it is suggested that accretion to the central black hole has a disc form, which determines the character direction: disc axis, along which the powerful jets are formed. Often the matter in jets preserves the relativistic velocity very far from the galactic nuclear. The main physical processes leading to generation of jets in AGNs, microquasars, radio pulsars, and young stars are explained by the work of a unipolar inductor (in the frame of MHD-theory) creating strong field-aligned currents at the place where rigid-corotation is broken [12].

Suzuki [32] considered the accretion disc wind generated when the magnetic energy starts to dominate the gas energy (at R_A) and found that the result is qualitatively similar to what was received in the MHD simulation of the solar and stellar winds. Livio [30] noted that most of the astrophysical objects which exhibit jets contain accreting central bodies. He considered, particularly, young stellar objects, X-ray binaries, black hole transients, AGNs and showed that these objects possess discs which could generate jets. He obtained that all energy of accretion matter could be transferred to the energy of jets, if R is of the order of $2R_A$. According to Camenzind [15], the ergosphere of the black hole is typically a region smaller than $3R_G$ and the Alfven surface is located within the ergosphere, while the currents across the rotating black hole magnetosphere and forming disc arise near R_A. Thus, it follows that for bright AGNs connected with the powerful jets R_0 could be located at R_A.

5 Discs Around Sun, Giant Planets in the Solar System, and in the Exoplanet Magnetospheres

In the heliosphere, there is the global heliospheric current sheet serving as a magnetic equatorial plane between sectors of opposite polarity. Alfven considered the heliospheric current sheet (with current $3 \cdot 10^9$ A) to be part of a heliospheric current system in which Sun acts as a unipolar inductor producing a current (e.g., [6]). This equatorial current is closed by the field-aligned currents going to the Sun polar regions and later to the Sun's atmosphere. In the solar wind the rigid corotation with the Sun, in zero-order approximation, occurs as far as the Alfven radius. For typical models of the magnetized solar wind, R_A is 0.11 AU. Inside the Alfven radius, the solar magnetic field force plasma to corotate, while outside the Alfven radius, the magnetic field is passively convected by the solar wind plasma. Although there is no strict definition of the inner boundary of the heliosphere, it is generally assumed to be a surface that separates the super-Alfven solar wind from

the sub-Alfvenic coronal expansion [37]. So, it means that the heliospheric current sheet's inner edge is located at the highest radial Alfven critical point, where the radial solar wind velocity equals to the Alfven velocity (at 14 solar radii near solar minimum phase).

The main motion in the inner part of discs around Jupiter and Saturn is directed along the azimuthal direction, thus the azimuthal velocity is dominated and determines their Alfven radii. Using of the Alfven radius for determination of the disc's inner edge position in the paraboloid magnetospheric magnetic field models for Jupiter and Saturn (18.4 and 6.5 planetary radii, respectively) allowed us to receive results which describe observations with a good accuracy [3, 4, 9, 11].

At the present time hundreds of extrasolar exoplanets have been observed. Many of them are located at distances less than 10 parent stellar radii and have masses of the order of Jupiter's (the so called, "Hot Jupiters"). Khodachenko et al. [27] considered formation of disc in the exoplanet's magnetosphere. As the gas/plasma surrounding the rotating magnetized object moves outwards along the magnetic field lines, its angular velocity is approximately constant until speed V_ϕ reaches a value of Alfven speed V_A, when magnetic tension balances the centrifugal force per unit mass. There, at Alfven radius, the field lines are distorted by the inertia of the gas. Finally, the disc is generated with the inner edge near the Alfven radius.

6 Conclusions

The theory and observations of discs develops very fast due to the progress in astronomical equipment, data base and theoretical treatment. One of the main tasks is the study of discs structure and location. Here we considered different types of astrophysical discs: discs around Sun, planets, exoplanets, and compact objects. We also shortly reviewed discs around supermassive black holes in AGNs and discs in binary systems. Abubekerov and Lipunov [1] stated that the size of the magnetosphere of the accreting star is close to the Alfven radius. Magnetized objects surrounded by accreting disc beyond the magnetosphere boundary are found among X-ray pulsars, X-ray-bursters, cataclismic variables (polars, intermediate polars), and T Tauri stars. The mentioned above accretor's properties are independent of the nature of the central object.

In the other systems, at the Alfven radius the matter can be rotationally ejected. The ejected matter carries away angular momentum and brakes the central rotation magnetized object. As we showed in this paper, the Sun, Jupiter, Saturn, and magnetized exoplanets are surrounded by discs with outflowing plasma, the inner edges of which coincide with their Alfven radii.

Discs occur in a wide range of astrophysical contexts, differing in size, in the nature of origin, in material and direction of its motion inside them. However, the dynamical laws in each type of disc are relatively similar. One specific feature

common for a large group of discs in a sufficiently strong magnetic field is considered in the present paper: we show that in spite of different nature of origin, a lot of astrophysical discs have their inner edges near the Alfven radii.

Acknowledgements Work at the Institute of Nuclear Physics, Moscow State University was supported by the RFBR Grants No 11-05-00894 and 09-05-00798. The authors are thankful to EU FP7 projects EUROPLANET/JRA3 and IMPEX for support of their collaboration. This work was partially supported by the Austrian Science Fund (FWF) within the project P21197-N16.

References

1. M.K. Abubekerov, and V.M. Lipunov: The lower temperature limit of accretors. Astron. Rep. **4**7(8), 681–686 (2003)
2. I.I. Alexeev: The penetration of interplanetary magnetic and electric fields into the magnetosphere. J. Geomag. Geoelectr. **38**, 1199–1221 (1986)
3. I.I Alexeev, and E.S. Belenkaya: Modeling of the jovian magnetosphere. Ann. Geophys. **23**, 809–826 (2005)
4. I.I. Alexeev, V.V. Kalegaev, E.S. Belenkaya, S.Y. Bobrovnikov, E.J. Bunce, S.W.H. Cowley, J.D. Nichols: A global magnetic model of Saturn's magnetosphere, and a comparison with Cassini SOI data. Geophys. Res. Lett. **33**, L08101 (2006). doi:10.1029/2006GL025896
5. I.I. Alexeev, E.S. Belenkaya, S.Yu. Bobrovnikov, J.A. Slavin, M. Sarantos: Paraboloid model of Mercury's magnetosphere. J. Geophys. Res. **113**, A12210 (2008). doi:10.1029/2008JA013368
6. H. Alfven, P. Carlqvist: Interstellar clouds and the formation of stars. Astrophys. Space Sci. **55**(2), 487–509 (1978)
7. W. Bednarek: TeV gamma-rays from accreting magnetars in massive binaries. MNRAS. **397**, 1420–1425 (2009)
8. W. Bednarek, J. Pabich: X-rays and γ-rays from cataclysmic variables: the example case of intermediate polar V1223 Sgr, MNRAS. **411**, 1701–1706 (2011)
9. E.S. Belenkaya: The jovian magnetospheric magnetic and electric fields: Effects of the interplanetary magnetic field. Planet. Space Sci. **52**, 499–511 (2004)
10. E.S. Belenkaya, I.I. Alexeev, V.V. Kalegaev, M.S. Blokhina: Definition of Saturn's magnetospheric model parameters for the Pioneer 11 flyby. Annal. Geophys. **24**, 1145–1156 (2006)
11. E.S. Belenkaya, I.I. Alexeev, M.S. Blokhina, E.J. Bunce, S.W.H. Cowley, J.D. Nichols, V.V. Kalegaev, V.G. Petrov, and G. Provan: IMF dependence of Saturn's auroras: modelling study of HST and Cassini data from 12–15 February 2008. Ann. Geophys. **28**, 1559–1570 (2010)
12. V. Beskin: Magnetohydrodynamic models of astrophysical jets. PHYS-USP. **53**(12), 1241–1278, 2010 (in Russian)
13. N.G. Bochkarev, A.I. Shapovalova: Variations of geometrical and physical characteristics of innermost regions of active galactic nuclei on time-scale of years. In: Proceedings of the International Astronomical Union, **2**, 327–328 (2006)
14. N.G. Bochkarev, C.M. Gaskell: The accuracy of supermassive black hole masses determined by the single-epoch spectrum (Dibai) method. Astron. Lett. **35**5, 287–293, 2009
15. M. Camenzind: In: Compact objects in astrophysics: White dwarfs, neutron stars and black holes, Astronomy and astrophysics library, ed. by G. Brner, A. Burkert, W. B. Burton, et al. Springer, Berlin Heidelberg New York (2007)
16. K.S. Cheng, K.N. Yu, K.Y. Ding: X-ray and gamma-ray emission from active galactic nuclei. Astron. Astrophys. **275** No. 1/AUG(I), 53–60 (1993)
17. A.M. Cherepashchuk: Highly evolved close binary stars. Space Sci. Rev. **74**(3–4), 313–324 (1995)

18. A.M. Cherepashchuk: X-ray nova binary systems. Space Sci. Rev. **93**(3–4), 473–580 (2000)
19. A.M. Cherepashchuk: Observational manifestations of precession of accretion disk in the SS 43 binary system. Space Sci. Rev. **102**(1–4), 23–35 (2002)
20. A.M. Cherepashchuk: Search for blackholes. PHYS-USP, **46**, 335–371 (2003)
21. K. Y. Eksi, M. Ali Alpar: Disks surviving the radiation pressure. Astrophys. J. **620**, 390–397 (2005). doi: 10.1086/425959
22. C. Fendt, J. Greiner: Magnetically driven superluminal motion from rotating black holes Solution of the magnetic wind equation in Kerr metric. Astron. Astrophys. **369**, 308–322 (2001)
23. J. Frank, A.R. King, D. Raine: Accretion power in astrophysics. Cambridge Univ. Press. Cambridge (1992)
24. Ghosh P., Lamb F. K: Accretion by rotating magnetic neutron stars. II - Radial and vertical structure of the transition zone in disk. Astrop. J. **232**, 259–276, (1979a)
25. Ghosh P., Lamb F.K.: Accretion by rotating magnetic neutron stars. III - Accretion torques and period changes in pulsating X-ray sources. Astrop. J. **234**, 296–316 (1979b)
26. Ginzburg, V.L.: On physics and astrophysics, Bureau Quantum, Moscow (1995)
27. Khodachenko, M.L., I. Alexeev, E. Belenkaya, H. Lammer, J.-M. Griessmeier, M. Leitzinger, P. Odert, T. Zaqarashvili, and H. O. Rucker: Magnetospheres of \Hot Jupiters": The importance of magnetodisks for shaping of magnetospheric obstacle. In press (2011)
28. Kuperus, M.: Magnetohydrodynamics of accretion disks, Computer Physics Reports **12**, No 4, 275–287 (1990)
29. Levine, D.A., D.F. Figer, M. Morris, and I.S. McLean: A circumstellar H_2O maser associated with the circumnuclear molecular disk at the Galactic Center? Astrop. J. **447**, L101–L104 (1995)
30. Livio, M.: Astrophysical jets: a phenomenological examination. Phys. Rep. **311**, 225–245 (1999)
31. Shakura, N.I., and R.A. Sunyaev: Black holes in binary systems. Observational appearence. Astron. Astrophys. **24** 337–355 (1973)
32. Suzuki, T.K.: Self-consistent simulations of Alfven waves driven winds from the Sun and stars. Space Sci. Rev. **158**, 339–363 (2011)
33. Tomsick John A., Kazutaka Yamaoka, Stephane Corbel, Philip Kaaret, Emrah Kalemci and Simone Migliari: Astrop. J. **707**, L87–L91 (2009)
34. Wang Y.-M.: Location of the inner radius of a magnetically threaded accreation disk. Astrop. J. **465**, L111–L113 (1996)
35. Zeldovich, Ya. B., Novikov, I.D.: The theory of the gravitation and stars evolution. Nauka. Moskow (1971)
36. Zhang, D and Z. G. Dai: Hyperaccreting discs around magnetars for gamma-ray bursts: Effects of strong magnetic fields. Astrop. J. **718**, No 2, (2010) doi: 10.1088/0004-637X/718/2/841
37. Zhao, X.P., and J.T. Hoeksema: The Magnetic Field at the Inner Boundary of the Heliosphere Around Solar Minimum. Solar Phys. **266**, 379–390 (2010) doi 10.1007/s11207-010-9618-0

Stochastic Properties of Solar Activity Proxies

Kristoffer Rypdal and Martin Rypdal

Abstract The sunspot number (SSN), the total solar irradiance (TSI), a TSI reconstruction, and the solar flare index (SFI) are analyzed for long-range persistence. The SSN, TSI, and TSI reconstruction are almost certainly long-range persistent with most probable Hurst exponent $H \approx 0.7$. The SFI process, however, is either very weakly persistent ($H < 0.6$) or completely uncorrelated.

1 Introduction

The idea of long-range persistence in the solar records, on short as well as long times scales, is not new. Mandelbrot and Wallis [1] applied rescaled-range (R/S) analysis to monthly sunspot numbers (SSN) and found the characteristic bulge on the $\log(R/S)$ vs. $\log\tau$ curve for time scales τ around the period of the sunspot cycle, but a common slope corresponding to a Hurst exponent of $H \approx 0.9$ in the ranges $3 < \tau < 30$ months and $30 < \tau < 100$ years. Ruzmaikin et al. [2] obtained similar results for the SSN, and for analysis extended to the time range $100 < \tau < 3,000$ years by using a ^{14}C proxy for cosmic ray flux. Since such behavior of the R/S-curve is reproduced by adding a sinusoidal oscillation to a fractional Gaussian noise with Hurst exponent H, both groups concluded that the stochastic component of the SSN is a strongly persistent fractional noise in the time range from months to millennia. Ogurtsov [3] combined SSN and SSN reconstructions with ^{14}C proxies to obtain H in the range 0.9–1.0 in the time range $25 < \tau < 3,000$ years by

K. Rypdal (✉)
Department of Physics and Technology, University of Tromsø, Tromsø, Norway
e-mail: kristoffer.rypdal@uit.no

M. Rypdal
Department of Mathematics and Statistics, University of Tromsø, Tromsø, Norway
e-mail: martin.rypdal@uit.no

Rypdal, K. and Rypdal, M.: *Stochastic Properties of Solar Activity Proxies*.
Astrophys Space Sci Proc. **33**, 227–232 (2012)
DOI 10.1007/978-3-642-30442-2_25, © Springer-Verlag Berlin Heidelberg 2012

means of R/S analysis and first and second order detrended fluctuation analysis (DFA(1) and DFA(2)). The statistical significance of the long-memory persistence hypothesis on time scales longer than the sunspot period has been questioned by Oliver and Ballester [4], using the so-called scale of fluctuation approach.

Renewed interest in long-range persistence has emerged from the debate on the connection between solar variability and climate change. One segment of this debate has focused on the detection of correlations and/or common statistical signatures between proxies of solar activity and climate signals on time scales of the sunspot period and shorter. Since the correlation appears to be quite weak, some works have drawn the attention to a possible "complexity-linking" which is proposed to be discernible by identification of a common long-range memory process represented by a common Hurst exponent H [5, 6]. This view was criticized by us in a recent Letter [7] where we point out that trends, like the sunspot cycle in solar signals, will create spuriously high Hurst exponents. For instance [6] (their Fig. 3B) obtain $H \approx 0.95$ for solar as well as global temperature signals. After such trends are accounted for, both solar signals and climate signals exhibit considerably lower Hurst exponents for the stochastic component of the signals.

2 Estimating Hurst Exponents from Data

The solar signals contain distinct periodicities, the most prominent being the 11-year solar cycle, and these trends will distort the result of the variogram or rescaled-range analysis. However, the detrended fluctuation analysis (DFA) [8], performs quite well on these data. The product of this analysis is the n'th order DFA fluctuation function $F^{(n)}(\Delta t)$, where Δt is the time scale [8]. If a fractional Brownian motion (fBm) with Hurst exponent $H \approx 0.5$ is superposed on a sinusoidal signal of comparable amplitude, variogram analysis will give an estimated Hurst exponent $H \approx 1$, while a third order DFA analysis (DFA(3)) will give $F^{(n)}(\Delta t) \propto \Delta t^H$ with H close to the Hurst exponent for the fBm. Thus, there are good reasons to assume that given sufficiently long data series DFA(3) would give an accurate estimate of the Hurst exponent for the underlying detrended stochastic process.

In Fig. 1a we have plotted the solar flare index (SFI), SSN and a total solar irradiance (TSI) reconstruction over the last four sunspot cycles, and an instrumental TSI (PMOD) composite for the last two cycles (all as daily averages). The thick smooth curves are moving averages. In order to extract the stochastic component the smoothed signal should be subtracted, but the signals are still strongly non-stationary in the amplitudes of the rapid fluctuations. The variance of the fluctuations around the local mean $y(t)$ is roughly proportional to $y(t)$, i.e. $\mathrm{Var}[x(t)|y(t) = y] \propto y$. This means that the mean- and amplitude-detrended signals $z(t) \equiv (x(t) - y(t))/\sqrt{y(t)}$, which is plotted in Fig. 1b, are approximately stationary. The variograms (squared DFA(0) fluctuation function) of the raw signals yield Hurst exponents in the range $0.88 < H < 0.97$ and correspond to the results

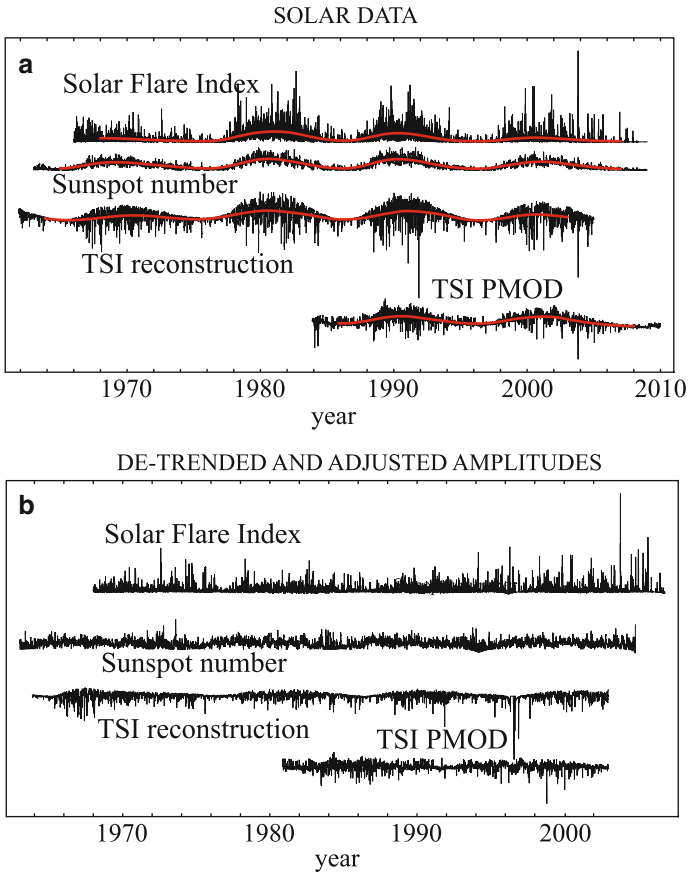

Fig. 1 (**a**) Sunspot number (SN), solar flare index (SFI), total solar irradiance (TSI) reconstruction, and the TSI PMOD composite. Smooth curves are gaussian moving averages with a 1-year standard deviation. (**b**) In this figure we have subtracted the smoothed signals from the original times series in order to de-trend the time series and then divided the detrended signals by the square root of the smoothed signals in (**a**). Prior to this amplitude adjustment, the origins for each of the signals are shifted to the minimal values of the smooth signals in (**a**)

obtained in Fig. 3B of [6]. The DFA(3) analysis, however, yields $0.55 < H < 0.67$. Results similar to the latter is obtained by computing variograms of the detrended signal in Fig. 1b.

3 A Stochastic Model for Assessing Uncertainty

The limited length of the observed data records makes it difficult to compute error bars in the estimates of Hurst exponents directly from the data. What we need to know is the PDF of estimated values $\hat{H}$ in an imaginary ensemble of realizations

of data sets of the same length as the observed record. Such an ensemble can be generated synthetically from a model that is assumed to have the same statistical properties as the observed data, including an hypothesized value of H that can be varied. From this ensemble one can construct a conditional probability density $p(\hat{H}|H)$ for obtaining an estimated value $\hat{H}$ for the Hurst exponent, given that the "true" exponent is H. Then, by means of Bayes' theorem we can obtain the conditional PDF $p(H|\hat{H})$, which gives us the probability of having a "true" Hurst exponent H provided we have estimated a value $\hat{H}$ from the observational data. The width of $p(H|\hat{H})$ gives us the error bar of our estimate.

We shall model $z(t)$ as a self-similar (in general non-Gaussian) process with self-similarity exponent H. By denoting this fractional noise process by $w_H(t)$, we can write $x(t) = y(t) + \sigma\sqrt{y(t)}\,w_H(t)$, where $y(t)$ is a 11-year-periodic oscillation with amplitude A, and $w_H(t)$ is a fractional non-Gaussian noise with unit variance. We assume that the observed signal is a realization of the stochastic model where $w_H(t)$ is a fractional noise with the measured distribution and with Hurst exponent $H \in [0, 1]$. We construct a uniform (all values of $H \in I \equiv [0, 1]$ are equally probable) sample space $\mathscr{S}$ of realizations of these processes. For each realization with a given H we measure (estimate) a value $\hat{H}$. In general $\hat{H} \neq H$. We can then, for instance, compute the conditional probability density $p(\hat{H}|H)$ from an ensemble of numerical solutions to the stochastic model where for each realization H is chosen randomly in the interval I. The conditional PDF $p(H|\hat{H})$ can also be computed directly from the ensemble or from Bayes' theorem: $p(H|\hat{H}) = p(\hat{H}|H)p(H)/p(\hat{H}$. Here $p(H)$ is by construction of $\mathscr{S}$ uniform on the unit interval I and hence $p(H) = 1$. However, $p(\hat{H})$ is not necessarily uniform and must be computed from the ensemble.

4 Results

In Fig. 2a (crosses) we show the mean estimated $\hat{H}$ computed by the DFA(3) method from ensembles of synthetic realizations of the SFI. $\hat{H}$ is estimated from DFA(3) applied to the synthetic $x(t)$ and the deviation from the straight dashed line indicates the systematic bias of the DFA(3) method. When the process is persistent ($H > 0.5$) the method performs quite well, with a slight overestimation of H when the process is strongly persistent ($H \to 1$). The circles (partly hidden by the crosses) are computed from DFA(3) applied to the fractional noise directly. The fact that the two curves fall on top of each other shows that the DFA(3) method removes the influence of the periodic trend. There is also a statistical spread in the estimated $\hat{H}$ indicated by the error bars. The spread in estimated $\hat{H}$ depends on the length of the synthetic data record which we have chosen equal to the observational record. The conditional PDF $p(H|\hat{H})$ can be computed from the same ensemble. In Fig. 2b the conditional cumulative distribution $P(H|\hat{H}) \equiv \int_{-\infty}^{H} p(H'|\hat{H})dH'$ is computed from the conditional PDF $p(\hat{H}|H)$ by means of the uniform sample space

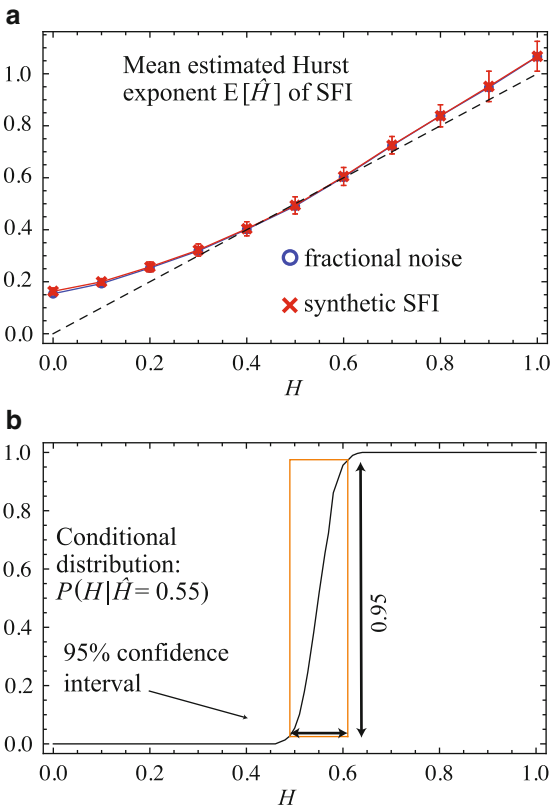

Fig. 2 (**a**) Ensemble mean $E[\hat{H}]$ of estimated Hurst exponent for SFI computed by the DFA(3) method. The crosses are computed from an ensemble of realizations generated from the stochastic model where the fractional noise $w_H(t)$ used in the model has Hurst exponent H and the PDF computed from the SFI time series. The circles (partly hidden by the crosses) are computed from DFA(3) applied to the fractional noise directly. The Gaussian statistical spread in the estimated $\hat{H}$ is given by the error bars. (**b**) The conditional cumulative distribution $P(H|\hat{H}) \equiv \int_{-\infty}^{H} p(H'|\hat{H})dH'$ computed from the conditional PDF $p(\hat{H}|H)$ by means of the uniform sample space and Bayes' theorem for $\hat{H} = 0.55$

Table 1 1. row: Hurst exponent $\hat{H}$ as estimated by DFA(3) from the observed time series. 2. row: The most probable Hurst exponents $\int H\, p(H|\hat{H})\, dH$ computed from the uniform sample space. 3. row: The 95% confidence intervals computed from the uniform sample space

	TSI reconstruction	TSI (PMOD)	Sunspot number	Solar flare index
$\hat{H}$	0.61	0.71	0.78	0.55
$\int H\, p(H\|\hat{H})\, dH$	0.62	0.70	0.73	0.54
95% confidence	$0.57 < H < 0.69$	$0.62 < H < 0.81$	$0.68 < H < 0.76$	$0.49 < H < 0.61$

and Bayes' theorem for $\hat{H} = 0.55$. From this distribution it is easy to compute the conditional mean $\mathbb{E}(H|\hat{H})$ (which is the best estimate for H given the observation $\hat{H}$) and the 95% confidence interval for this estimate. These are given in Table 1, and does not rule out the possibility that the SFI stochastic process is uncorrelated ($H = 0.5$). Note that $\mathbb{E}(H|\hat{H} = 0.55) = 0.54$, i.e. that the best estimate for H and the observation $\hat{H}$ are slightly different.

The mean estimated Hurst exponents and their 95% confidence intervals are summarized for all four proxies in Table 1. Except for the SFI this analysis indicates that there is a significant persistence in all solar activity proxies analyzed, but their

Hurst exponents are considerably lower than obtained by most previous authors. The largest H is found in the sunspot number, with the most probable value $H = 0.73$, and with 95% confidence $H < 0.76$.

References

1. Mandelbrot, B. B., and J. R. Wallis (1969), Global dependence in geophysical records, *Water Resor. Res.*, *5*, 321.
2. Ruzmaikin, A., J. Feynman, and P. Robinson (1994), Long-term persistence of solar activity, *Solar Phys*, *148*, 395.
3. Ogurtsov, M. G. (2004), New evidence for long-term persistence in the Sun's activity, *Solar Physics*, *220*, 93.
4. Oliver, R., and J. L. Ballester (1998), Is there memory in solar activity?, *Physical Review*, *58*, 5650.
5. Scafetta, N., and B. J. West (2003), Solar Flare Intermittency and the Earths Temperature Anomalies, *Phys. Rev. Lett.*, *90*, 248701.
6. Scafetta, N. and B. J. West (2005), Multiscaling Comparative Analysis of Time Series and Geophysical Phenomena, *Complexity*, *10*, 51.
7. Rypdal, M., and K. Rypdal, (2010), Testing Hypotheses about Sun-Climate Complexity Linking, *Phys. Rev. Lett.*, *104*, 128501.
8. Peng C-K, S. V. Buldyrev, S. Havlin, M. Simons, H. E. Stanley, and A. L. Goldberger (1994), Mosaic organization of DNA nucleotides, *Phys. Rev. E*, *49*, 1685.